Power Plant Degradation: A Modular Secondary Plant and Integrated Flow Accelerated Corrosion Model

by
Mark Johan van der Helm

B.S. Mechanical Engineering
University of Texas at Austin, 1994

M.S. Nuclear Engineering
Massachusetts Institute of Technology, 1996

Submitted to the Department of Nuclear Engineering
in partial fulfillment of the requirements for the degree of

Doctor of Philosophy in Nuclear Engineering
at the
Massachusetts Institute of Technology

February 2001

Author_____
Department of Nuclear Engineering
November 21, 2000

Certified by_____
Ronald G. Ballinger, Sc.D.
Professor of Nuclear Engineering and Materials Science and Engineering
Thesis Supervisor

Certified by_____
George E. Apostolakis, Ph.D.
Professor of Nuclear Engineering
Thesis Reader

Accepted by_____
Sow-Hsin Chen, Ph.D.
Chairman, Department Committee on Graduate Students

Power Plant Degradation: A Modular Secondary Plant and Integrated Flow Accelerated Corrosion Model

by
Mark Johan van der Helm
Submitted to the Department of Nuclear Engineering
on November 21, 2000 in partial fulfillment of the
Requirements for the degree of
Doctor of Philosophy in Nuclear Engineering

Abstract

Flow Accelerated Corrosion (FAC) is the most prevalent material degradation mechanism for low carbon steel in steam-water flow systems. The band of uncertainty in predictions of wear rate due to FAC spans one to two orders of magnitude. Such a wide range of uncertainty inhibits the ability to devise safe and economical repair and replacement schedules. The goal of this thesis is to reduce uncertainty of predictions of wear caused by FAC.

Reduction in the uncertainty in FAC wear rate predictions is achieved through the development of a new predictive FAC model, the incorporation of this model in a flow system analysis environment, and the use of this environment to identify improved methodologies for predicting FAC wear rate. The new FAC model is based on a published empirical model, published data, and physical mechanisms identified to be significant in the wear process. The new FAC model is shown to have less uncertainty for single phase lab data and single and two phase plant data.

The flow system analysis environment is an interactive program that calculates parameters relevant to the FAC phenomenon based on plant description. Functionality of this environment is validated for each of the four calculations it performs: thermodynamic, thermal hydraulic, chemistry, and degradation rate.

Additionally, this environment can be used to analyze contributions to uncertainty that are not yet identified. This environment was used to analyze the contribution to uncertainty from the current method of incorporating chemistry parameters in predictions of FAC wear. Based on this analysis, suggestions are made to improve these methods, thereby reducing prediction uncertainty and improving the knowledge necessary for safer and more economical plant operation.

Thesis Supervisor: Ronald G. Ballinger

Title: Associate Professor of Nuclear Engineering and Materials Science and Engineering

Acknowledgements

I would like to thank my advisor, Prof. Ronald Ballinger who has provided guidance for the thesis over the past four years. Additionally, I would like to thank Prof. George Apostolakis for being a reader for thesis. Prof. Peter Griffith's input to the project when it was in its infancy is also much appreciated.

I would like to thank those that monetarily supported the research. For the first two years, KEPCO support is appreciated. The continued support by the MIT Nuclear Engineering Department, specifically the efforts of Prof. Jeffrey Freidberg, Prof. Mujid Kazimi, Prof. Sidney Yip, and Prof. Michael Golay are certainly appreciated.

My thanks goes to those in the near vicinity of MIT: Rocco's advice and encouragement on running a marathon and a diner, Gus' willingness to browbeat his ice cream maker into Sluggo production regardless of the time of year and of course for having that fated flavor in the first place as well as the best coffee.

Special thanks goes to those I have befriended in my stay at MIT, and to which I owe the enjoyment I have had here in Boston. In regard to my good friend Tony, I will never forget ripping through Boston's nightlife and the unrelenting expectations of his friends and for Picante runs. The zest for life and love of the incorrigible Manuel will always be an inspiration to me. My thanks go to both Tony and Manuel for inviting me into their homes and introducing me to their families and their countries. Boston is not the only location that has solidified friendships: for the road trip to Montreal where I learned the true meaning of sharing, I must take my hat off to those who made it possible, Karen, Rebecca and Vanessa. My thanks go to Augustine (a.k.a. Gus, Augthe or Augy), for his revitalization of less meaningful verse and more meaningful Haus runs. My thanks go to my roommate, Cara, in appreciation of her fiery personality and her mastery of German cuisine. Her homestretch aid and conversations will not be forgotten. My thanks goes to Dave Grundy, for always being there for a beer or a Sam's run but most for living the quintessence of friendship. He holds the bar to which I aspire.

The love and support of my family has given me much appreciated strength in my endeavors. To Marijke Sage, Rebecca Berney, Michael van der Helm, Anneke Kaminski, Dicky van der Helm, and respective spouses, I will be forever grateful for their advice and ear through the troubled and good times. My thanks go to Nikolas and Eliana for reminding me of what life is all about.

Finally, I would like to especially acknowledge the person, Vanessa, who has shared this experience with me, the first of many. Her willingness to consult on decisions both big and small and her belief in and support of me were essential to the success of this thesis.

This thesis is dedicated to my parents, Dick and Louise van der Helm, who have taught me by example that everyday is an opportunity to learn and grow.

Table of Contents

List of Figures

List of Tables

Chapter 1. Introduction

Nuclear power accounts for 19% of the total electricity generation in the US. In replacing fossil fuel generated electricity, this power source corresponds to a significant saving of emitted carbon dioxide (on the order of the decrement in emissions agreed to by the administration in the Kyoto Protocol) which is the primary cause of the greenhouse effect (IPCC, 1996). Without relicensing nuclear power plants, approximately 40% of the current nuclear power capacity will be retired by 2020 (EIA, 1999). Keeping operating costs competitive with new sources of generation will drive these relicensing decisions. Proper management of material aging will lower the operating and maintenance costs making relicensing a viable option.

1.1. Description of the Problem

Flow Accelerated Corrosion (FAC), a type of material aging, has caused equipment failure and unexpected pipe rupture or leakage in numerous nuclear power plants. FAC is a phenomenon in which water flow accelerates dissolution of a continuously forming oxide layer at the inner metal surface. It is important to not only understand the mechanisms behind FAC and other wear phenomenon but to also give the plant operator the ability to quantify both the pipe thinning rate and the uncertainty in the rate in order to ensure safe economical operation.

FAC is only one of a number of pipe degradation phenomena resulting in material loss often referred to as Flow Induced Material Degradation (FIMD). In order to predict the wear of piping and components, one must understand the effect of FAC and other phenomena on material degradation. These FIMD phenomena include cavitation, FAC ,

abrasion corrosion, and droplet impingement. The combination of these phenomena have resulted in premature piping failures, extended outages for maintenance, and in a few cases catastrophic failures that have resulted in injury and fatalities (Chexal, *et. al.*, 1996). While FIMD is a generic problem in all steam power plants, it is especially troublesome in nuclear power plants due to the cost of maintenance. As a result, a considerable effort has been made by the industry to understand, model, and make plant chemistry modifications in order to mitigate the problem.

Because FAC is the most prevalent of these wear mechanisms, it is the focus of this thesis. When comparing wear predictions to real plant wear data, however, all types of FIMD may be contributing to the wear and are therefore discussed in this thesis and modeled to the extent possible based on the information available in the literature.

1.2. Previous Work

A number of models, both mechanistic and empirical, have been devised to estimate FAC rate based on pipe geometry, water chemistry, and thermal hydraulic parameters. Mechanistic models of the FAC process have the potential to provide more accurate predictions of the FAC rate since they consider the physics behind the process. Current mechanistic models describe FAC as a one dimensional transport process of iron from the metal to the bulk flow of water that is flowing perpendicular to the transport direction. Chemical species that are supplied by the bulk water flow travel in the direction opposite to the iron transport and also affect the transport process. While mechanistic models provide insight on these physical processes, current models are insufficient to provide accurate predictions of wear as none replicate all the trends found

in either laboratory or plant data nor do they incorporate the full range of independent parameters known to affect FAC.

Empirical models, based on available data, are necessitated to account for unidentified effects (which are therefore unquantified by mechanistic models) and to determine uncertainties in the FAC rate predictions. Current empirical models typically incorporate all independent parameters that are ascertained to affect the FAC rate. The model used as the current industry standard is empirical and has significant and unquantified uncertainty. The span of error in the ratio of predicted to measured wear rate is one to two orders of magnitude (Kastner, 1987).

1.3. Objectives

The goal of this thesis work is to reduce the uncertainty in the prediction of FAC rate. The approach to reducing this uncertainty may best be described by outlining the different sources that contribute to the uncertainty of a particular model namely

1. Parameter uncertainty
2. Equation set uncertainty
3. Incomplete condition information

Parameter uncertainty can be defined as differences between the estimated and actual conditions that a pipe or component is subjected to. For example, when collecting real data for pipe wear, one must estimate the conditions under which this wear occurred in order to input this into the model. However, the estimate of the conditions is likely to not be a true representation of the conditions that the pipe was actually subjected to. It is

because of this difference in the estimated and the actual conditions that parameter uncertainty results.

Two other types of uncertainty are distinguished, both of which are normally grouped together by others into a 'model' uncertainty. Model uncertainty is usually described in a plot of calculated outcome versus measured outcome for particular sets of conditions. It should be noted that often models will give a single calculated outcome that may correspond to several measured outcomes. The 'model' uncertainty may have two sources of uncertainty. The first source is that while the set of conditions is sufficient to accurately determine the outcome, the equation set of the model is inaccurate in translating a particular set of conditions (independent parameters), to the outcome, or the dependent parameter (in this case, wear rate). This source can be referred to as equation set uncertainty. The second source of uncertainty lies in the fact that the model as it is formulated, does not incorporate all the significant conditions that affect the outcome, so the calculated outcome will correspond to range of conditions that are not adequate to uniquely determine the outcome itself. This source can be referred to as incomplete condition information.

The approach to reducing uncertainty in FAC prediction focuses on these three sources of uncertainty. Literature on the FAC phenomenon indicates that there are at least eight parameters that affect FAC wear. However, information on all of these parameters for a reported measured wear rate are often sparse. Furthermore, parameters that are given are often system-averaged estimates based on limited plant information. The methods for determining the parameters were also often not clear, and definitely not consistent. This situation leads to significant parameter uncertainty.

In order to more accurately predict FAC rates, it was prudent to provide a more robust data set for the description of the local conditions affecting wear, which would therefore allow calculations to be performed in a consistent manner. To do this, a modular program was developed to calculate the known influential parameters of FAC throughout the plant from *first* principles. Through a modular approach, it is shown that is it possible to provide accurate parameter information, thereby reducing parameter uncertainty.

Developing a new FAC model reduced model uncertainty caused by equation set uncertainty. The new FAC model is based on a published empirical model (the Kastner model), published data, and physical mechanisms which were identified to be significant in the wear process. The new FAC model is shown to have less uncertainty for single phase laboratory data and single and two phase plant data. This new FAC model is integrated into the modular program described above, combining the improvements of the two approaches. Wear rates from this new integrated FAC model are then compared to those calculated were the original Kastner model integrated into the modular program. Predicted wear rates for the new FAC model relative to those for the original Kastner model shows that the new FAC model reduces the uncertainty. Because the data given for the plant is insufficient, specific parameters are not known but calculated by the modular program, and it is shown that parameter uncertainty reduction is significant using the new modular program.

Finally, the current method in which chemistry parameters are incorporated into the new FAC model is analyzed with the modular program. It is shown that using nominal chemistry parameters as input contributes significantly to the uncertainty in the

predicted FAC rate. Based on operating specifications for the plant and published data on typical ranges of these chemistry parameters, the modular program was used to determine the range of potential steady state wear rates possible during a cycle of plant operation. Quantifying the difference in a time integrated wear rate based on this range with the wear rate assuming nominal chemistry indicates the contribution to uncertainty from using nominal chemistry values. Based on this result, a new methodology for computing wear is suggested. In context of the uncertainty discussion above, an improvement in the model using the suggested new methodology (which uses time dependent chemistry parameters) addresses incomplete condition information. This exercise is but one example of the applications of this modular program. Section 7.2, Future Work, outlines other potential applications of the modular program for determining unidentified parameters that contribute to uncertainty.

1.4. Thesis Structure

To provide an overview of the presentation of this work, the following paragraphs provide a quick synopsis of the upcoming chapters. Chapter 2 reviews the general understanding of FAC as modeled by previous researchers and the relevant parameters identified to predict FAC rate to date. In this chapter, model development is discussed with respect to its relevance to the understanding of the FAC phenomenon. The advantages and disadvantages of the two main approaches to model development, empirical and mechanistic, are also described.

Chapter 3 describes the Secondary Power Plant Degradation Modular Modeling Environment (SPPDMME) upon which the Secondary Power Plant Degradation

Program(SPPDP, heretofore referred to as the modular program). Based on plant information this environment is designed to allow the modeling of a secondary system of interest. With this system model, the environment calculates unknowns that affect FAC rate based on physically known relationships allowing accurate determination of parameters known to affect degradation rate and parameters suspected of affecting the degradation rate. This environment, then, addresses the goal of reducing parameter uncertainty and uncertainty caused by incomplete condition information.

The discussion begins with the reasoning for designing the modular environment based on the broader goals of not only reducing uncertainty, but quantifying uncertainty as well. The modeling environment features are presented in context of the constraints of being able to model a wide range of plant designs described by a differing set of available information. Next, the component modules of the environment that are used to develop a secondary system model are described. Finally, technical details of the underlying calculations are described in terms of the parameter information flow between modules. The final form of this environment is a code programmed in Visual Basic®, the SPPDP. The following chapters show that the developed program can be used to determine both parameters known to affect FAC as well as provide a structure to determine parameters suspected to affect FAC wear.

Chapter 4 outlines the validation of the thermodynamic, thermal hydraulic, and chemistry calculation modules of the SPPDP by comparing the results to industry code results.

Chapter 5 describes the development of a new FAC model (NFM) based on the empirical Kastner model and physical understanding of FAC phenomenon. For each

modification, constraints, justification, and the results are discussed. Calculated wear rates from the generated NFM are then compared to data from the laboratory and plant. Reduction in wear uncertainty due to equation set uncertainty is shown with this new model.

Chapter 6 assesses the ability of the SPPDP and integrated NFM to determine parameters that affect FAC and predict FAC wear rates relative to measured FAC wear rates. Using results from previous section as a validated base case for nominal water chemistry conditions, the contribution to FAC wear prediction uncertainty from off-normal chemistry relative to overall model uncertainty is assessed.

Chapter 7 reviews the major conclusions made in the course of the thesis. Additionally, potential applications of the SPPDMME developed including the extension its capabilities to quantifying FAC wear rate uncertainty and modeling other operating conditions, flow systems, and chemistry related degradation mechanisms.

Chapter 2. Degradation Modeling Background

In order to improve model predictions of degradation rates, the uncertainty of these models must be reduced. To do this, it is important to understand the degradation mechanisms that potentially contribute to wear, the research aimed at explaining the underlying physical mechanisms, and the models then developed to predict this degradation. This background chapter reviews the major identified wear phenomena that affect piping for conditions that are typical of power plants. Following this description, models predicting the most prevalent of all wear phenomena, Flow Accelerated Corrosion (FAC), are discussed with the relevant parameters and physical processes involved. The knowledge gained from studying previous research and proposed models, dictates the approach needed for parameter calculations as described in Chapter 3 and possible improvements possible in the prediction of FAC rates as described in Chapter 5.

2.1. Types of Degradation

Four Flow Induced Material Degradation (FIMD) phenomena have been identified in the literature. These phenomena are FAC, cavitation, droplet impingement, and abrasion corrosion. Three phenomena, cavitation, FAC, and droplet impingement are more prevalent in secondary steam piping. Cavitation, abrasion corrosion, and are single phase phenomena; and abrasion corrosion, FAC, and droplet impingement are two phase phenomena.

2.1.1. Cavitation

Cavitation, solely a single phase flow phenomena, involves the repeated formation and collapse of vapor bubbles which upon collapse results in the generation of shock waves that cause material deformation and removal. Sharp, jagged surfaces characterize this form of wear damage. This phenomena is normally located downstream of control valves, orifices, pumps, expanders, and elbows, where local increases in the velocity of the cooling water causes static pressure reduction. Vapor collapse is then caused by the restoration of static pressure downstream of the component. The likelihood of such a phenomena occurring can be described through the cavitation factor that can be defined as:

$$C = \frac{\Delta P}{P_o - P_v(T_0)} \qquad \textbf{(Eq. 2-1)}$$

where

ΔP = pressure drop across the component

P_o = static pressure within component

$P_v(T_o)$ = saturation pressure at the fluid temperature within the component

A cavitation factor of less than 1/5 indicates the likelihood of cavitation. Proper prediction of cavitation requires specific knowledge and modeling of the component as it is a strong function of the component's geometry. Figure 2-1 shows the variety of bubble formation and collapse locations within a component or pipe (Kastner and Nedelko, 1991). It can be seen in this figure that a local decrease in pressure results in the formation of bubbles. A subsequent pressure increase can then result in the unstable collapse of the bubbles and the generation of locally high velocity fluid jets that can physically remove material.

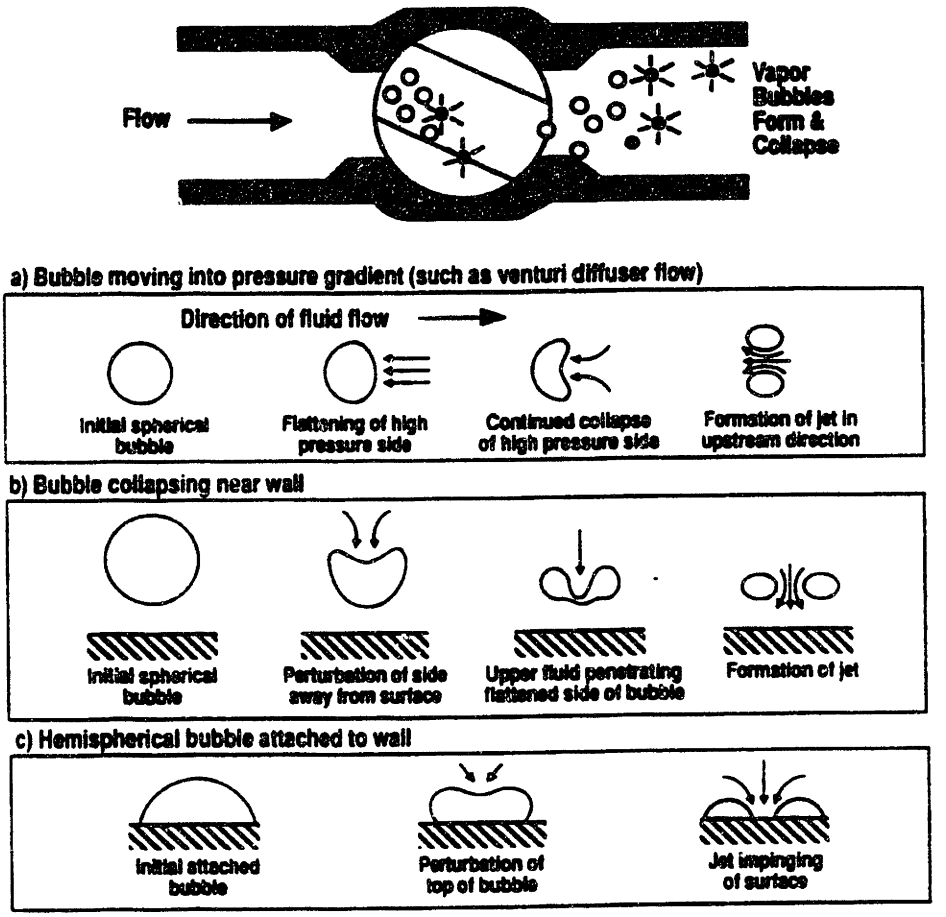

Figure 2-1. Forms of cavitation material degradation (Kastner and Nedelko, 1991).

2.1.2. Flow Accelerated Corrosion

Flow accelerated corrosion (FAC) in carbon steel piping systems is characterized by the simultaneous dissolution of iron from the iron oxide-fluid interface and the formation of an iron oxide film at the oxide-metal interface. Bulk flow plays a vital role in either providing a sink (gradient in concentration) for the dissolution products insuring the removal of these products. Under stagnant conditions, corrosion products concentrate in the aqueous solution, reducing the concentration gradient and hence the driving force for the corrosion process. Flow inhibits this concentration process and enhances the

concentration gradient. Figure 2-2 shows a schematic of a typical steady state material loss as a function of time assumed to exist for the FAC process under constant chemistry and thermal hydraulic conditions (Chexal, *et. al.* 1996), where FAC rate is shown to be proportional to time.

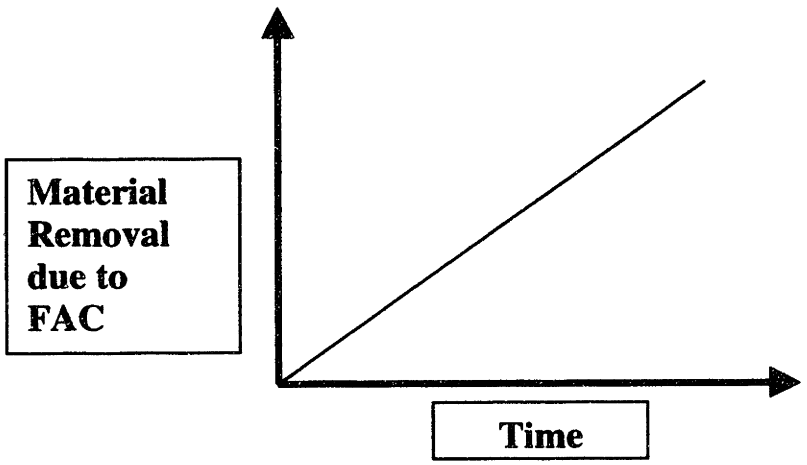

Figure 2-2. History characteristics of flow accelerated corrosion.

Wear patches often start as horseshoe or scallop shapes expanding to wide troughs with dimensions less than the pipe diameter (Kastner *et. al.*, 1990). Some two phase material degradation appears as 'tiger striping' occurring in bends and downstream from flow disruptions. The degradation often takes the form of separate patches on the dimensional order of the pipe diameter. These regions often experience significantly greater material loss than immediately adjacent sections. Tiger striping is a phenomenon that has yet to be adequately explained.

An additional acceleration of material removal may occur when rapid flashing of liquid water to vapor occurs. This phenomenon is aggravated by system pressure fluctuations. Increased fluid velocity, approaching sonic velocity, accelerates FAC (Kastner and Nedelko, 1991). This localized flashing may also result in striping the water of the chemicals affecting the corrosion film stability. The specific parameters and

physical processes included in a number of models of FAC will be discussed in more detail below.

2.1.3. Abrasion Corrosion

Abrasion corrosion involves the mechanical removal of the protective oxide film by particles within the flow as a result of their impingement on the oxide. Removal of the oxide followed by oxide reformation results in a continuous removal of material from specific sites. Figure 2-3 illustrates the typical time history of thickness reduction with a greater slope indicating oxide removal by impingement and a lesser slope indicating oxide reformation. The resulting process is quasi steady state.

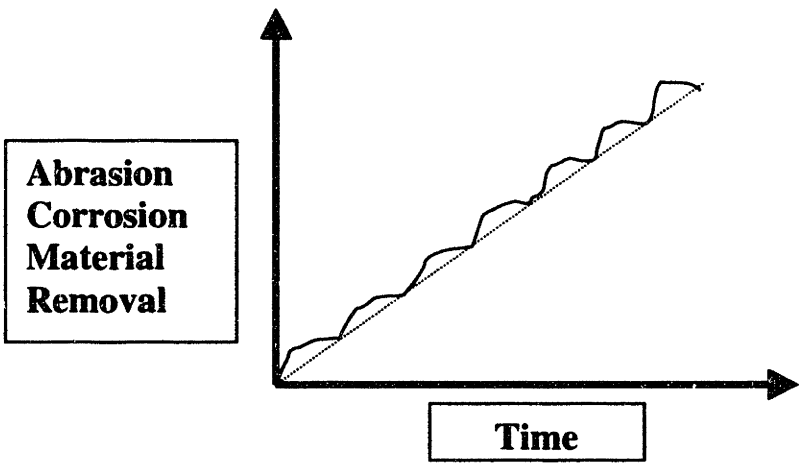

Figure 2-3. History characteristics of abrasion corrosion.

Figure 2-4 illustrates the respective velocity regimes where FAC and abrasion corrosion are dominant. Abrasion corrosion occurs at high velocities and results in a significant increase in material loss when compared to FAC loss rates occurring at lower velocities. Note the presence of a critical velocity above which abrasion corrosion occurs. Contributing factors to the abrasion corrosion rate include particle size and structure,

material toughness, and inclination of flow relative to the surface. Softer materials such as copper and brass alloys are more likely affected by abrasion corrosion (Chexal, 1996).

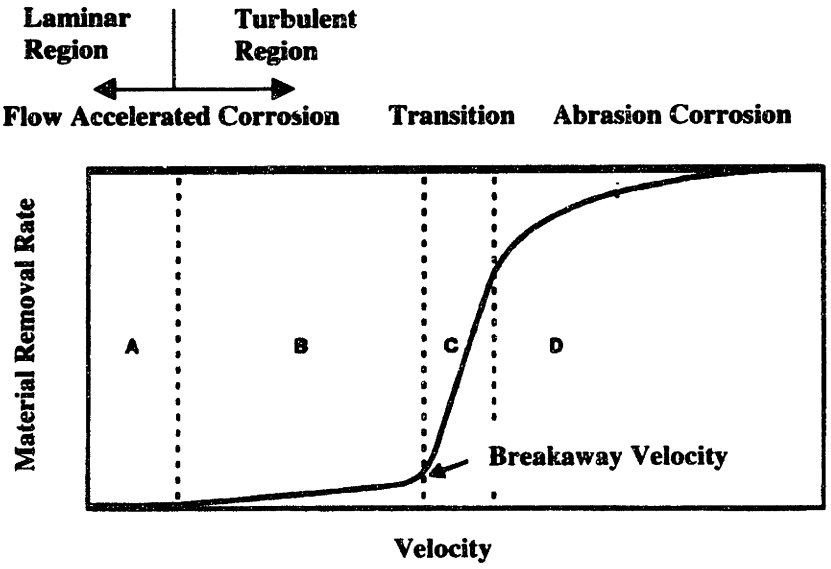

Figure 2-4. Material removal rate as a function of velocity for FAC and abrasion corrosion (Chexal *et. al.*, 1996).

2.1.4. Droplet Impingement

Droplet Impingement is a type of degradation for which two phase flow must exist. Entrained droplets from the liquid phase are propelled by the vapor phase at velocities that are significant enough to cause material fatigue. Keck measured a variety of droplet wear rates for a range of velocities and angles for two different geometries (Keck, 1987). By modifying a model suggested by Sanchez-Caldera (Sanchez-Caldera, 1984), incorporating data taken, and using Keller's geometric factors from the literature (Keller, 1974), two phase droplet velocity, entrainment fraction, and magnetite properties, Keck determined the wear coefficient using the following relation for material loss per unit area:

$$\dot{m}'' = \frac{K_{DI} \cdot \rho_f \cdot \dot{m}_{tot} \cdot (1-x) \cdot V_d^4 \cdot F_e \cdot F_h \cdot \rho_{ox}}{(IH \cdot \varepsilon_c)^2 \cdot A_c}, \qquad \textbf{(Eq. 2-2)}$$

where:

$\dot{m}''$ = wear rate per unit area [kg/m^2/sec],

K_{DI} = wear coefficient empirically derived,

ρ_f = fluid density [kg/m^3],

$\dot{m}_{tot}$ = total mass flow rate [kg/sec],

x = flow quality,

V_d = droplet velocity [m/sec],

F_e = entrained fraction,

F_h = fraction impacting surface,

ρ_{ox} = oxide density [kg/m^3],

IH = indentation hardness [N/m^2],

ε_c = critical strain to fracture,

A_c = characteristic wear area [m^2].

Droplet impingement exhibits two primary characteristics. The first is that material removal rates may be quite rapid. Second, damage due to droplet impingement is most often observed as 'sharp and jagged damage to a surface which is mostly metallically smooth' (Heitmann and Kastner, 1982).

2.2. Previously Proposed FAC models

A variety of models have been proposed to describe FAC, and can be classified as either empirical or mechanistic. Empirical models are based on a statistical fit to laboratory data trends, which are then modified as appropriate to match plant data. Mechanistic models establish a set of interrelated equations describing the physical processes occurring at particular locations within a proposed system. While empirical

models may fit data well, extrapolation of trends to the full function space may not be accurate. For example, the effect of velocity at low and high pH may be very different because of changes in oxide film stability. On the other hand, mechanistic models allow the investigator to incorporate correct physical trends, but they may produce a set of equations insufficient to numerically predict FAC wear rate or which do not include all parameters known to affect FAC wear. In the beginning of model development, mechanistic models provide insight into the phenomena and direction to experimentation. For final implementation, empirical models provide the necessitated numerical wear prediction with an attempt to include the currently identified influential parameters. Empirical models with adherence to physical trends provide a balance between the two approaches. The model developed in this thesis is such a model. Chapter 5 describes the development of the FAC model used in this thesis.

2.2.1. Empirical Models

Of the many models proposed to describe FAC, four will be briefly discussed in this section. The four models are those from Kastner (Kastner, 1987), Chexal-Horowitz , (CH), (Chexal *et. al.*, 1996), Sanchez-Caldera, (SC), (Sanchez-Caldera, 1984), and Bignold (Bignold *et. al.*, 1983). The Kastner and Chexal-Horowitz[1] models are empirical while the Sanchez-Caldera and Bignold[2] models are mechanistic. Table 1 shows the

---

[1] A third empirical model, part of the BRT-Cicero code, was developed at Electricite de France and is based on experimental data taken on the Cicero test loop (Chexal *et. al.*, 1996).

[2] A third mechanistic model, the Berge model, is similar in nature to the Sanchez-Caldera model but less complex.

variables that are included in each of these models. The Kastner model is the FAC model that serves as the basis of the commercial WALTHEC code produced by Siemens/KWU as a program to aid utilities in managing pipe degradation caused by FAC. The Kastner model is derived from both single and two phase flow data. Single phase flow data taken in the laboratory was used to derive the original empirical relationship. The derived relationships were then adjusted as needed to fit two phase plant data (Kastner, 1987). The laboratory data used in the Kastner model was generated at Siemens/KWU and the plant data used consists of approximately 6000 single and two phase data points (Chexal *et. al.*, 1996). The final Kastner model is a separable equation predicting material removal rate per unit area of the form

$$\dot{m}'' = F_1(v,T,aec)\cdot F_2(pH)\cdot F_3(O_2)\cdot F_4(G)\cdot F_5(x)\,, \qquad \textbf{(Eq. 2-3)}$$

which is a function of velocity (v), temperature (T), alloying element content (aec), pH, bulk oxygen content (O_2), geometry (G), and water quality (x), respectively.

Table 2-1. Comparison of models based on primary variables modeled. Note that (a) indicates a value included numerically but not varied experimentally, (b) indicates that Cr and Mo were considered together and, (c) indicates that Cr, Mo, and Cu were considered separately.

Parameter	Kastner	Chexal-Horowitz	Sanchez-Caldera	Bignold
pH	X	X	X[a]	X
Oxygen	X	X		
Velocity	X	X	X	X
Temperature	X	X	X	X
Alloy Chemistry	X[b]	X[c]		
Geometry	X	X	X[a]	X
Pipe Diameter		X	X[a]	X
Time	X			

A similar method was used in the derivation of the CH model which is the FAC model within the CHECWORKS code, developed by the Electric Power Research Institute (EPRI). The data used by EPRI includes 'pertinent' British, French and German lab data, U. S. plant data, and EPRI sponsored laboratory data (Chexal *et. al.*, 1996). The final form of the CH model is a separable equation of the form

$$\dot{m}'' = F_1(T) \cdot F_2(pH) \cdot F_3(aec) \cdot F_4(h) \cdot F_5(O_2) \cdot F_6(G) \cdot F_7(\alpha), \qquad \textbf{(Eq. 2-4)}$$

where h is the mass transfer coefficient and α is the void fraction of the flow.

Both the Kastner and CH model report better model predictions when compared to laboratory single phase data than when compared to all data within their respective databases. Figure 2-5 and Figure 2-6 show a comparison, respectively, of single phase lab data and both lab and plant data to the Kastner model. Figure 2-7 and Figure 2-8 show a comparison, respectively, of single phase lab data and both lab and plant data to the CH model. Data shown in Figure 2-5 and Figure 2-7 are a subset of that in Figure 2-6 and Figure 2-8, respectively. The outlying data, data for which the models predicts little wear yet actually experience significant wear, is of particular concern. As indicated from Figure 2-6 and Figure 2-8, the outlying data are likely data for which the influencing parameters are not well defined and not well controlled or the physical degradation mechanisms (e.g. the cause of tiger striping) are not well understood. One goal of this thesis is to improve the predictability of such wear rates.

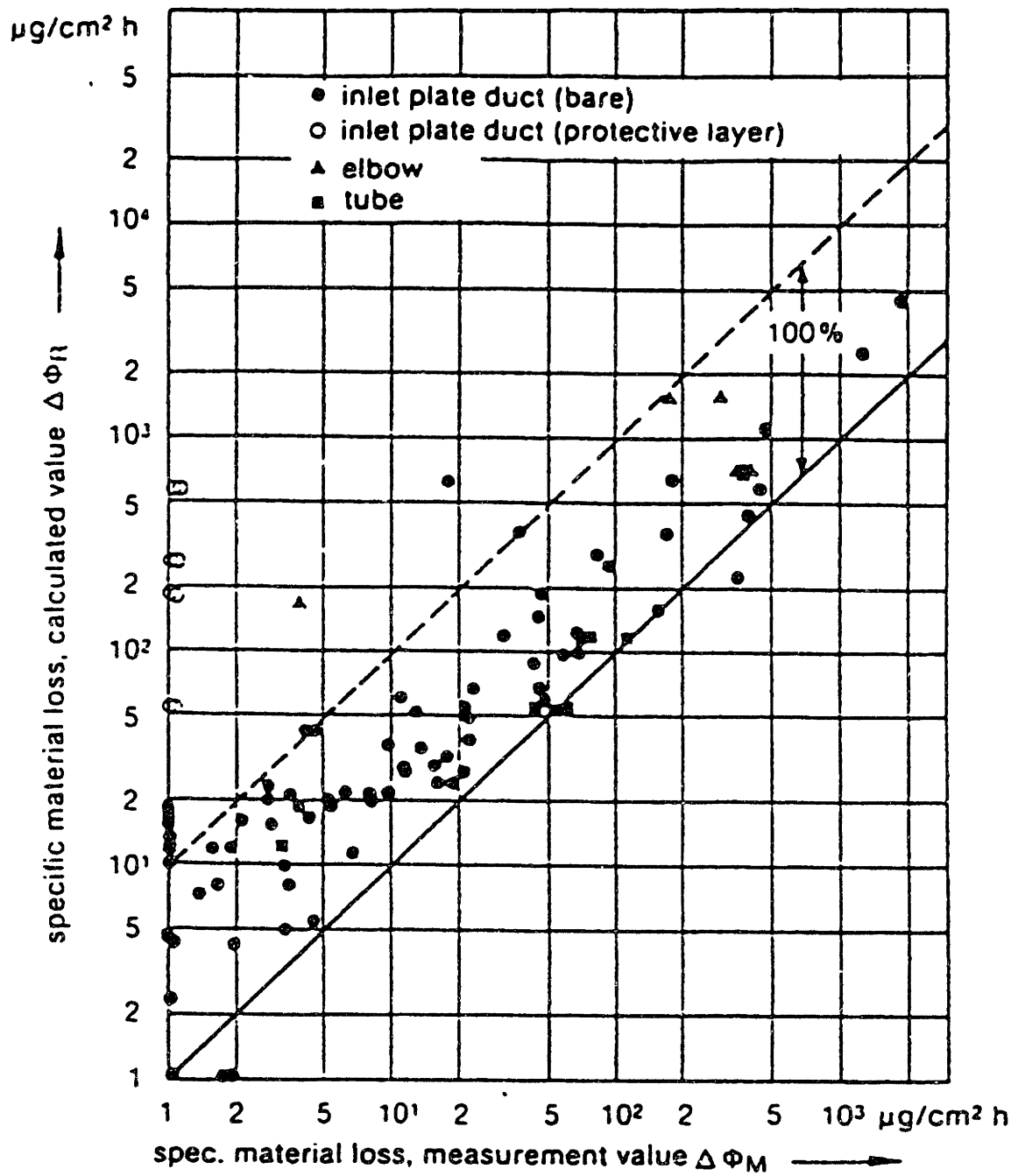

Figure 2-5. Comparison of predicted and measured material degradation by the Kastner model for single phase lab data (Kastner, 1987).

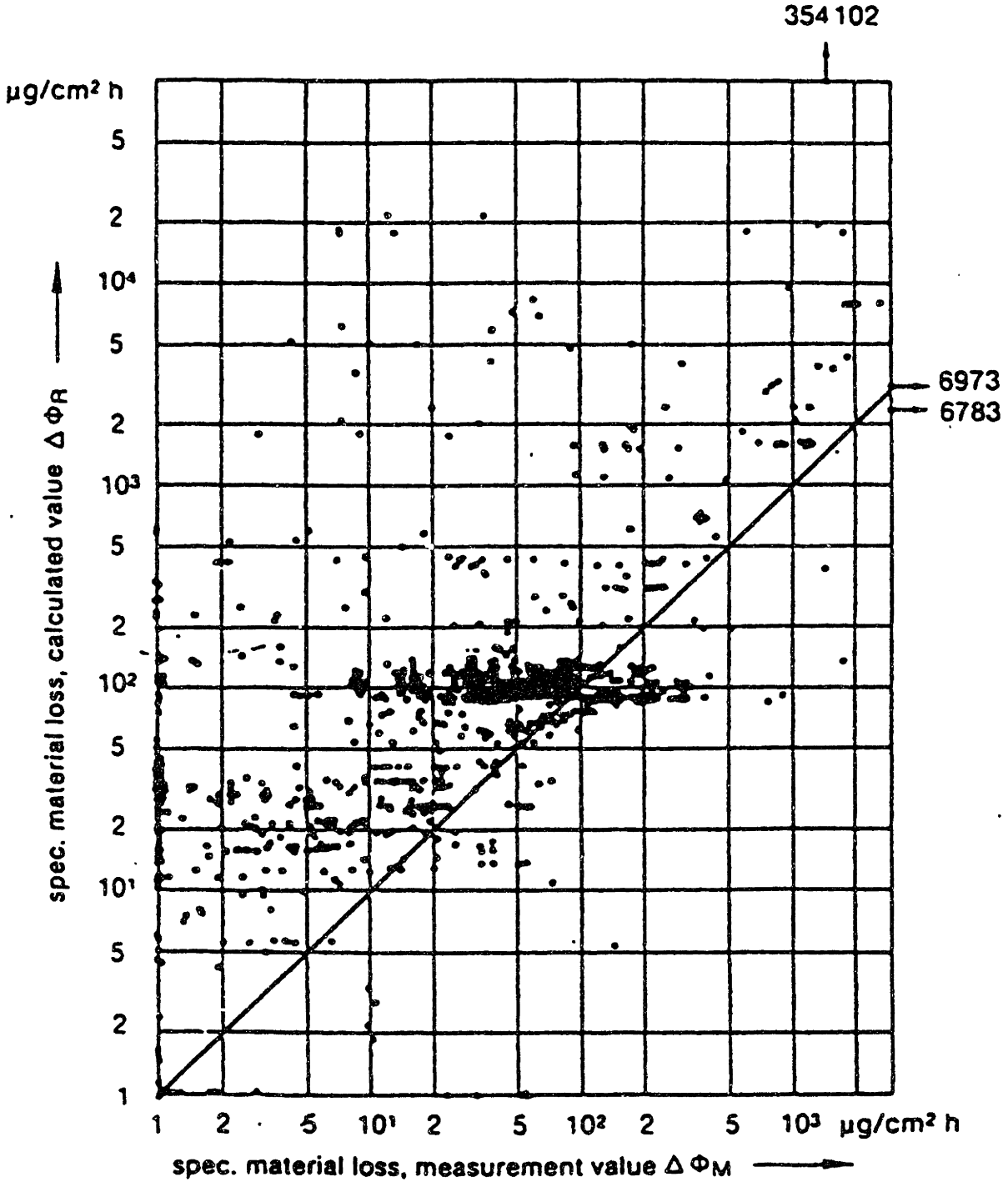

Figure 2-6. Comparison of predicted and measured material degradation by the Kastner model for single and two phase lab and plant data (Kastner, 1987).

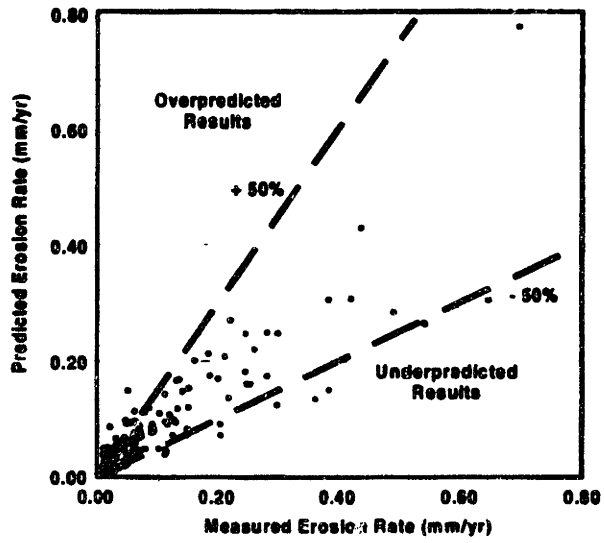

Figure 2-7. Comparison of predicted and measured material degradation by the Chexal-Horowitz model for single phase lab data (Chexal *et. al.*, 1996).

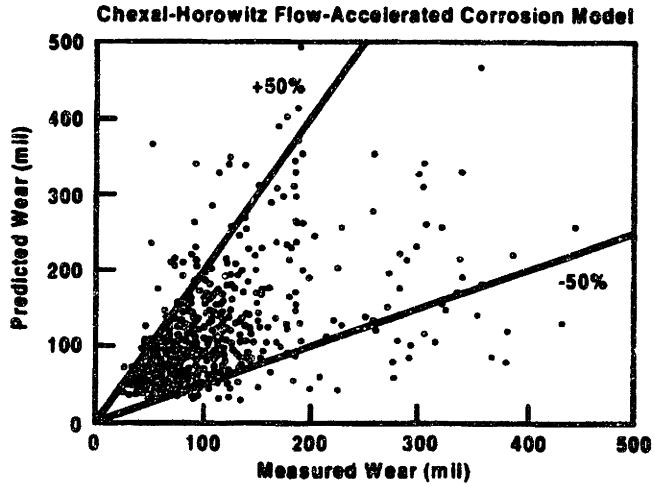

Figure 2-8. Comparison of predicted and measured material degradation by the Chexal-Horowitz model for single and two phase lab and plant data (Chexal *et. al.*, 1996).

2.2.2. Mechanistic Models

2.2.2.1. Sanchez-Caldera

Sanchez-Caldera models the FAC process as a coupled kinetically limited mass transfer process. The transfer rate of material from the pipe to the bulk fluid flow is modeled as a one dimensional steady state process. The process is assumed to take place in two steps: (1) kinetically limited dissolution of iron to produce ferrous ion followed by (2) mass transfer of the ferrous ion to the bulk flow by ion migration and conve :tion. Figure 2-9 shows a schematic of the model. The process can be modeled as a series of mass transfer processes through resistances to the transfer process as depicted in the "circuit" diagram at the base of Figure 2-9.

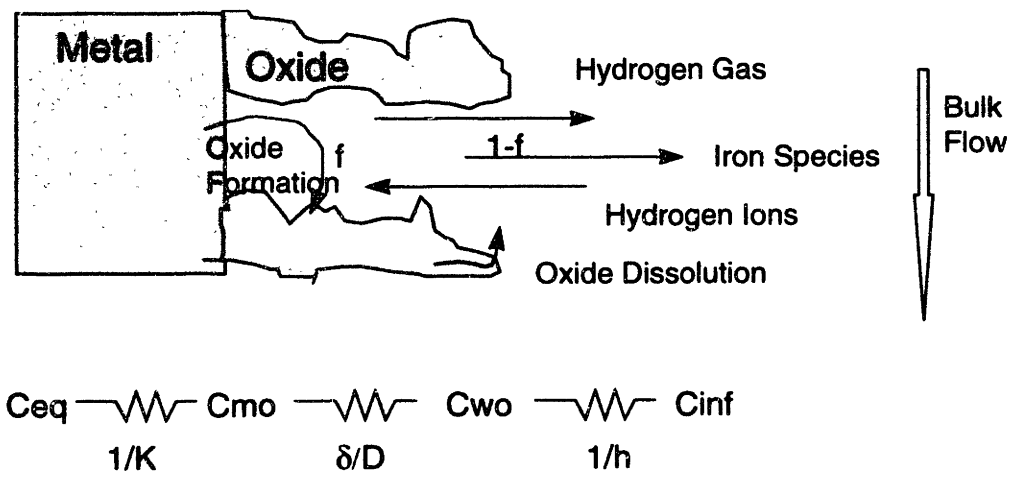

Figure 2-9. Schematic of the FAC process as described by the Sanchez-Caldera model (Sanchez-Caldera, 1984).

The metal dissolution to the metal-oxide interface is assumed to be first order with respect to concentration such that ferrous ion production at the metal-oxide interface is proportional to the difference between two concentrations, C_{eq} and C_{mo}, defined below. The relationship for material removal rate per unit area is then given by:

$$\dot{m}'' = K * (C_{eq} - C_{mo}) . \qquad \textbf{(Eq. 2-5)}$$

The proportionality constant, denoted K, is the reaction rate and is assumed to follow an Arrhenius Law:

$$K = Ae^{\frac{-E}{R \cdot T}} . \qquad \textbf{(Eq. 2-6)}$$

The constants A and E were determined by fitting the SC model to data. C_{eq} shown in Figure 2-9 corresponds to the equilibrium concentration of ferrous ion at the metal-oxide interface as described by the ferrous hydroxide formation reaction set (Sweeton and Baes, 1970):

$$Fe_3O_4 + 3 \cdot (2-b) \cdot H^+ + H_2 \longrightarrow 3 \cdot Fe(OH)_b^{2-b+} + (4-3 \cdot b) \cdot H_2O , \qquad \textbf{(Eq. 2-7)}$$

for $b = 0, 1, 2, 3$, and a given concentration of hydrogen ions and hydrogen gas at the interface. C_{mo} corresponds to the ferrous ion concentration that exists at the metal-oxide interface for a given concentration of hydrogen ions and hydrogen gas at the interface.

The mass transfer resistance controlled step consists of diffusion through an oxide layer to the oxide-fluid interface and convection to the bulk fluid. A competing pathway for ferrous ion removal at the metal-oxide interface is the production of magnetite, Fe_3O_4, according to the reverse of **Eq. 2-7**. This process creates the oxide layer. A fraction, f, of the ferrous ions at the metal-oxide interface are used in the formation of magnetite. The remaining fraction of ferrous ions, 1-f, are removed by the mass transfer step described above. Figure 2-9 shows the diffusion resistance through the oxide, δ/D, for transport from the metal-oxide interface to the water-oxide interface due to the concentration difference, $C_{mo} - C_{wo}$, at the two interfaces. In this resistance relation, δ is

the oxide thickness and D is the diffusion coefficient for ferrous ions through the oxide. The convection resistance, $1/h$, corresponds to the mass transfer from the water-oxide interface to the bulk fluid, due to concentration difference, $C_{wo} - C_{\inf}$, at the two interfaces. Hence, the bulk fluid motion enhances this mass transfer. The following relation describes the overall mass transfer:

$$\dot{m}'' = \frac{C_{eq} \cdot \theta(T)}{1/K + (1-f) \cdot \left[\frac{\delta}{D} + \frac{1}{h}\right]}, \qquad \textbf{(Eq. 2-8)}$$

where C_{eq} is assumed to much greater than C_{inf} and $\dot{m}''$ is the material removal rate per unit area. The porosity of the oxide on the metal-oxide interface is denoted by $\theta(T)$ and is assumed to be a function of temperature. As the porosity decreases available area for mass transfer decreases so that the overall iron dissolution rate decreases.

In a similar manner as described above, hydrogen ions are transferred to the metal-oxide interface from the bulk fluid and hydrogen gas is transferred from the metal-oxide interface to the bulk fluid. Assumptions are made about the bulk fluid hydrogen gas concentration and the hydrogen ion concentration is determined from measured pH values. The diffusion coefficients used to model the mass transfer processes correspond to that of hydrogen ions and gas in water.

At low temperatures, the production of ferrous ions at the metal-oxide interface is dissolution rate limited (i.e. a low value of K). At high temperatures, the oxide porosity decreases, thereby limiting the dissolution of the metal. The peak in FAC occurs near 150 °C (Sanchez-Caldera, 1984). Sanchez-Caldera matches his model parameters to the values determined in his experiments to evaluate constants in the model.

2.2.2.2. Bignold

The Bignold model (Bignold *et. al.*, 1983) is the only mechanistic model that considers the electrochemical aspects of the corrosion process. Noting the coupling of potential, ion concentration, and current of the oxidizing and reducing species, Bignold derives a relationship between FAC rate and the mass transfer coefficient. The mass transfer resistance (the inverse of the coefficient) operates in series with a kinetic resistance as in the SC model. As in the SC model, mass transfer resistance limits the process at high temperature and the kinetic resistance limits the process at low temperatures.

The Bignold model assumes a series process of (1) oxide formation at the metal-oxide surface, (2) oxide dissolution at the oxide-solution interface and (3) convection of ferrous ions and ferrous hydroxides, $Fe(OH)_b^{2-b+}$, to the bulk flow. In the last step, convection to the bulk flow is assumed to be rate limiting at high temperatures. Bignold considers the following set of reactions for the dissolution of magnetite:

$$Fe_3O_4 + 2 \cdot H^+ + H_2 + 2e^- \leftrightarrow 3 \cdot Fe(OH)_b^{2-b+} + 3 \cdot (2-b) \cdot OH^-, \qquad \textbf{(Eq. 2-9)}$$

for b=0,1, and 2. Bignold uses the Nernst equation to derive an expression that relates the half cell electrode potential, E, of the cathodic reactions to the total concentration of ferrous hydroxide species from the various reactions:

$$C_S = C_{eq}^o \cdot \left[H^+\right]^{2/3} \cdot e^{\frac{-2 \cdot F \cdot E}{3 \cdot R T}}, \qquad \textbf{(Eq. 2-10)}$$

where F is Faraday's constant, R is the gas law constant, T is absolute temperature, and the total ferrous species, C_S, is given by:

$$C_S = \sum_{b=0}^{2} Fe(OH)_b^{(2-b)+} . \qquad \textbf{(Eq. 2-11)}$$

Eq. 2-10 satisfies charge balance among the various ferrous hydroxides and ions produced by **Eq. 2-9**.

The Bignold model then assumes that the current, i_c, due to the cathodic discharge reaction of hydrogen ions in the production of hydrogen gas (which balances the total reaction of anodic dissolution of ferrous ions originating from the metal) is proportional to the exponential of the half cell electrode potential, E, of **Eq. 2-7**giving:

$$i_c = -F \cdot B(pH) \cdot e^{\frac{-F \cdot E}{R \cdot T}} , \qquad \textbf{(Eq. 2-12)}$$

where $B(pH)$ is a proportionality constant and is a function of pH as determined from experimental data. Bignold then balances this current with the convection limited dissolution of magnetite to derive a FAC rate proportional to the cube of the mass transfer coefficient. Bignold provides data to support this trend in FAC rate with mass transfer coefficient.

2.2.2.3. Limitations of Current Mechanistic Models

Neither the Bignold nor the SC model includes the effect of oxygen content of the fluid or alloy content of the metal. Neither model properly describes velocity effects at low temperatures. At low temperatures, experimental data show the FAC rate to be velocity dependent, which is not a characteristic of either mechanistic model. Because of

these limitations, the empirical Kastner model was chosen for further development as described in Chapter 5. Note that the Chexal-Horowitz model is not available in the open literature. Physical principles, experimental data, trend analysis provided by the investigators developing the models in this chapter are used to make the improvements.

Chapter 3. Secondary Plant Pipe Degradation Modular Modeling Environment

The goal of this thesis is to improve pipe degradation wear prediction in PWR secondary systems by reducing the uncertainty in predictions of FAC wear, the most prevalent form of pipe degradation in this system. The work in this thesis, however, is done in the broader context of not only reducing the uncertainty of wear predictions but with the intent to extend the work to quantify the uncertainty as well. This chapter gives a general description of the problem at hand, and then focuses on the specific solution, the creation of a Secondary Plant Pipe Degradation Modular Modeling Environment (SPPDMME) that was devised to achieve the thesis objectives. The chapter is divided into three sections. The first section describes the flow system calculation methodology created to meet the goals of this broader context based on known constraints. The second and third sections describe the result of this methodology applied to PWR secondary systems to predict pipe degradation rates, the SPPDMME. The second section specifically defines the environment structure in terms of subsystem (or section) boundaries (or interfaces) and information flow across these boundaries. Finally, the third section describes the specific calculations performed within each subsystem and the corresponding logic that controls the order of these calculations. The final form of this environment is a program coded in the Visual Basic® programming language that is used in later chapters of this thesis to determine pipe degradation rates.

3.1. Methodology

3.1.1. Goals

The focus of this thesis is on the improvement of pipe degradation wear predictions in PWR secondary systems by reducing the uncertainty in predictions of FAC wear. In this chapter, a broader set of goals than those addressed in the thesis are outlined in order to elucidate the potential applications of the concepts and models that are behind the Secondary Plant Pipe Degradation Program. These goals (the latter of which is addressed in the Section 7.2 Future Work) include:

1. Reducing uncertainty in the degradation rate prediction by
   - reducing parameter uncertainty by calculating parameters in a consistent manner,
   - reducing model inaccuracy by incorporating more physically based parameters and relations,
   - identifying and incorporating into wear predictions significant parameters that are not currently used in models,
2. Quantifying the uncertainty in the degradation rate prediction for specific sets of conditions

The reason for reducing uncertainty in degradation rates is self evident. The more confidence an engineer has in predicting a wear rate, the safer and more economonical are the decisions that that engineers makes for testing and maintenance activities. The reasoning behind quantifying uncertainty for specific independent conditions is that it provides information on the confidence of the prediction for that specific set of conditions based on how well it is supported by data and predictive models (Christensen, 1985). Such an approach provides more specific information than assigning an overall uncertainty to a wear prediction model as one could do by looking at Figure 2.6 of last chapter or by assigning an uncertainty for specific predicted wear ranges as suggested by

Smith (Smith *et. al.,* 1998). The additional information reflects that uncertainty varies for a particular wear rate depending on the conditions at the location where the wear is taking place. At a particular location, a condition set may have an uncertainty much larger than that of the average for a model indicating very little data for this condition set or a wide range in measured wear rates for this condition set. For a second location, the condition set may have an uncertainty much less than the average for a model indicating the opposite to be true. This information will have an impact on testing and maintenance activities that is location dependent. Quantifying uncertainty is further discussed in section 7.2. Future Work.

A review of the data from both laboratory experiments and plants demonstrates the necessity to develop a methodology for calculating the conditions affecting degradation at the locations where the wear was taking place based on descriptions of the plants provided by utilities. The development of an improved methodology would allow the determination of the local conditions that cause degradation, including both conditions that have been proven to cause degradation and those that have not yet been included in current predictive models. Furthermore, such a methodology could be used to generate a database for quantifying uncertainty with statistical techniques. For such statistical techniques, it is imperative that not only a significant amount of data be available, since the FAC phenomenon is known to be dependent on at least 8 parameters (see Table 2.1), but that all the data must be determined in a consistent manner.

3.1.2. Constraints and Requirements

In developing the methodology needed to translate plant descriptions into the local conditions that affect degradation rates, a number of constraints on plants and plant

information were realized. First of all, the plants to which the methodology was applied differed significantly in

1. Design of the energy conversion system,
2. The chemistry control system, and
3. Overall plant operation (e.g. startup and shutdown procedures)

Secondly, the available plant information:

1. from measurements is sparse,
2. is not the same set for each plant considered,
3. may be for only a specific type of operation (e.g. power level or blowdown percentage of feed flow), and
4. varies in the level of detail.

Based on the goals of the thesis and the constraints outlined, a more specific set of requirements for the methodology can be outlined:

1. Calculate conditions that affect degradation at location where degradation is actually occurring,
2. Perform these calculations based on fundamental physical relationships,
3. Perform calculations of parameters based on a single set of relationships,
4. Perform calculations at the level of detail necessitated by application or as possible based on plant information,
5. Perform calculations for a wide range of system designs (typical of the US fleet), and
6. Determine whether the input of information over or under constrains relationships.

A number of these requirements are elaborated before introducing the methodology devised to meet the requirements.

The first requirement can be explained based on the discussion of Chapter 2. A minimal set of parameters identified to affect degradation rate (specifically FAC) as listed in Table 2.1, must be calculated at each location where wear is to be predicted. Knowledge of what information is typically known about a flow system and the physical

relations describing the flow leads to a natural progression of the calculations that need to be performed at each location. This progression is illustrated in Figure 3-1. First of all, system configuration, flow rates, and heat input are used to calculate thermodynamic state parameters and mass flow rates. Secondly, thermodynamic results combined with piping size and orientation are used to determine liquid and vapor phase velocities. Thirdly, thermodynamic results are combined with information on chemistry additives, chemical ingress, air in-leakage, and component volumes in order to determine the pH and oxygen concentrations throughout the system. Finally, these local conditions are combined to determine local degradation rates based on predictive models (e.g. the models described in Chapter 2).

The second and third requirements, the performance of calculations based on fundamental physical relationships and on a single set of relationships, are instituted in order to ensure that the parameters that are calculated are as accurate as possible and are independent of plant design or operation in order to minimize parameter uncertainty. Furthermore, these requirements ensure that the parameters calculated are well characterized for the potential development of statistical prediction models based on these parameters.

The fourth and fifth requirements, the performance of calculations to the level of detail necessitated or possible and over a wide range of system designs, address the versatility constraints outlined above for both plant design and plant information. Because of the potential complexity of the system for which the calculations are being

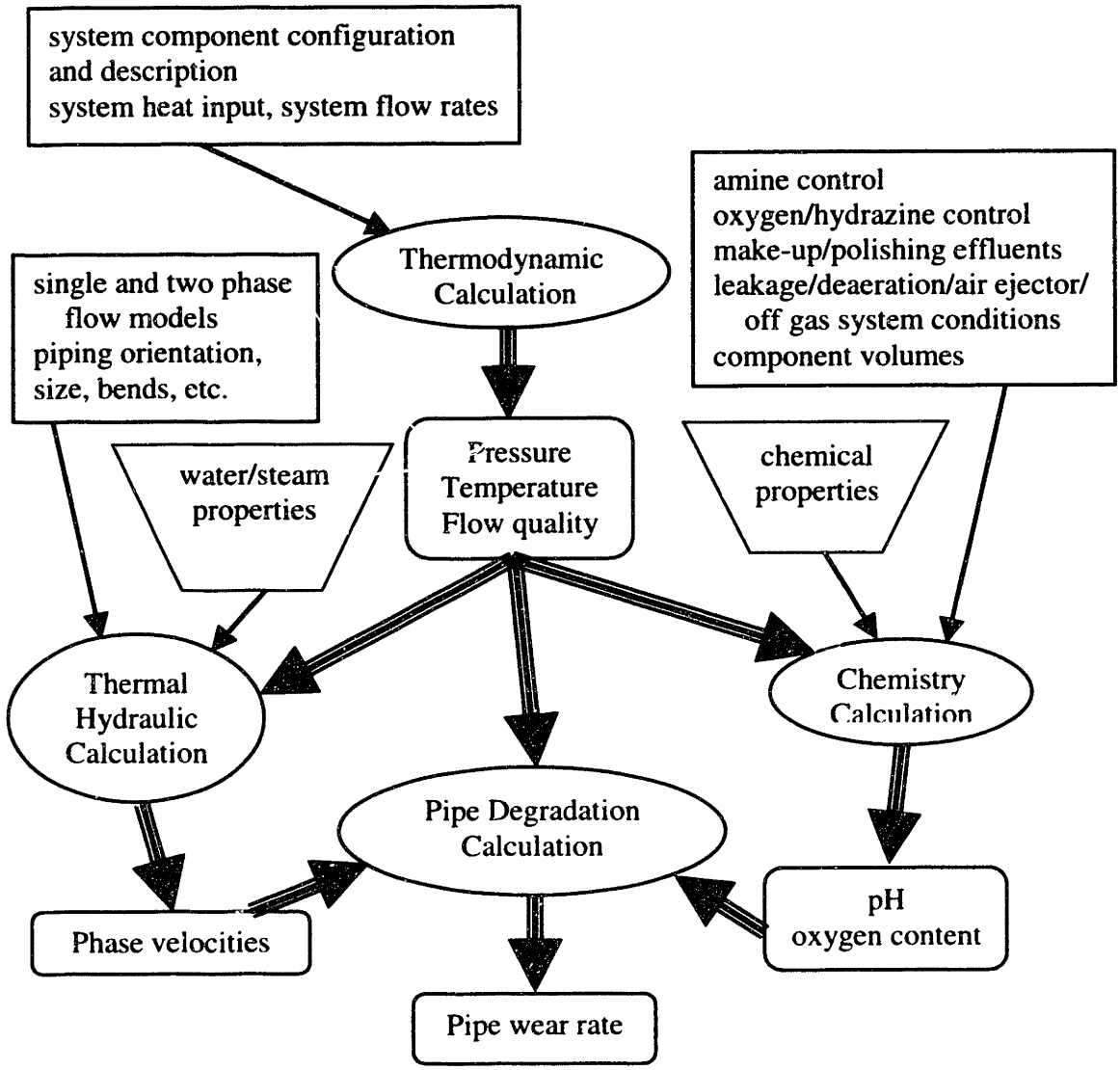

Figure 3-1. Flow of information for calculations required determining plant pipe degradation based on plant description.

performed and the input information quality (amount, accuracy, location, and completeness of the data) varies from system to system, it would be difficult for the information source (or likely sources) to be self aware of its own sufficiency to determine the unknown parameters. To overcome this difficulty, the sixth requirement, the determination of whether or not the input of information over or under constrains physical relationships, was introduced. In other words, the methodology is devised so that

it is responsible for determining if the system is over or under constrained by the input information thereby avoiding the necessity for the information source to make such an assessment.

3.1.3. Flow System Calculation Methodology

To address the requirements outlined in section 3.1.2, the author developed a flow system calculation methodology. This methodology consists of two fundamental concepts: a modular system concept and a sequential propagated calculation concept. The modular system concept involves breaking down the flow system and calculations into fundamental pieces (or modules) that can be combined in the necessary configuration in order to describe *any* variation of the flow system that is known to exist. As the number of modules chosen increases the amount of time needed to computationally describe each of these modules increases. As the number of modules chosen decreases, the variation in the flow systems that one can describe decreases. Therefore, an optimum number of modules exist depending on the application of the methodology. The key feature of these modules is that the set of interfaces that they share with other modules is identical so that the modules can be connected in any configuration. These interfaces consist of properties and signal flow, both of which will be described in later sections.

The sequential propagated calculation concept combines the necessity to sequentially perform calculations as displayed in Figure 3-1and propagate these calculations from location to location as information is input. Upon information input, relationships involving this input are checked in order to determine if unknown parameters for the relationship can be determined. If possible, these unknown parameters are solved and a similar check is performed on relationships involving these solved

parameters. The calculation, therefore, propagates and due to such feedback is self-consistent which makes this program novel to those currently used in the industry. When no more parameters can be solved based on this input, solved parameters are then displayed indicating that they have been determined from previous input. The same sequence of events, or propagation, occurs when information is removed. Such propagation provides feedback to the information source on the information needed (and not needed) and, in order to limit response time[3], requires efficiency in the order of sequential and propagated calculations. Inputting the information incrementally, propagating this information, and observing the results ensures the information does not over constrain the calculations and that sufficient information is supplied for a solution. The nature of the calculations (as outlined in section 3.3. SPPDMME Calculation Modules) determines the order of the sequential and propagated calculations which ensures limited response time in feeding back solved parameters.

Because the concepts in this methodology are abstract, they are best explained in conjunction with an example, specifically the application for this thesis. The remainder of this chapter concentrates on the specifics of how the flow system calculation methodology is applied to:

1. The PWR secondary system in the development of modules that correspond to components in this system and
2. Pipe degradation in the development of modules that calculate parameters specifically known to affect pipe degradation.

The resulting modules and calculation logic is referred to as the Secondary Plant Pipe Degradation Modular Modeling Environment (SPPDMME). This environment can be

[3] The time between input of information and methodology output of affected parameters.

used to model PWR secondary systems of interest. This environment is coded using the Visual Basic® (VB) programming language and is referred to as the Secondary Plant Pipe Degradation Program (SPPDP). VB is a based on Object Oriented Programming, a programming technique which is consistent with the modular concept of the SPPDMME. The technique is also versatile in its ability to issue program upgrades including new or improved modules (as outlined in future work) which would not conflict with previous versions of the program, a key aspect in the utilization of this program in industry. Furthermore, VB provides the building blocks for a Graphical User Interface (GUI). Such an interface is necessary for the features of this environment, wherein the environment provides feedback to the information source (or user) and prompts them on what additional information is necessary.

For further discussion of this environment, the information source will be referred to as the user who has an interactive role with environment. This user

1. Translates plant descriptive information into a plant model within this environment using the component modules within the environment,
2. Inputs plant parameter information known at specific locations,
3. Observes the environment response of calculated parameters based on the plant model and input information, and
4. Repeats step 2, if input information is insufficient to calculate the parameters of interest at the locations of interest.

Ideally, this user should be aware of the environment structure so that the best judgements and assumptions can be made about what plant information is to be used both to build a plant specific model and as input for known parameters. Such awareness of the environment should not be difficult though since the environment is designed to be user friendly.

The next two sections describe the component modules, calculation modules, and calculation logic of the SPPDMME which work together to meet the requirements for this methodology in the translation of plant descriptive information into parameters that affect pipe degradation at the location where the degradation is taking place. One aspect cannot be understood without understanding the others.

First, component modules represent a set of physically adjacent locations that can be joined with other modules in order to specifically create the arrangement of the secondary system being modeled. These component modules are described in section 3.2 and the interfaces they share with the rest of the environment outlined. Second, calculation modules are then outlined in section 3.3 in context of the specific models that they incorporate[4]. These calculation modules represent a set of equations used to determine unknown parameters based on known parameters at a single location and/or adjacent locations. In section 3.3.6, the reasoning for the calculation logic of the environment is provided. This calculation logic controls the order of sequential and propagated information flow across module interfaces. To aid the reader in understanding these elements of the environment, figures are provided from the GUI, the user interface of final form of the SPPDMME programmed in VB.

---

[4] Some confusion may exist on the use of 'models' and 'modeling' in the description of the SPPDMME. The SPPDMME is a modeling environment wherein a user can use the component modules of this environment to model the real secondary system of interest. Based on this plant model and the environment's calculation logic, the environment performs a set of calculations that are determined by the set of equations within each calculation module. This set of equations is also a model, a parameter model, for

3.2. SPPDMME Component Modules

Component modules are defined both by the information they contain as well as by the interfaces they share with the other elements of the SPPDMME. The discussion below first describes the component modules, then discusses the information flow and functions of the four interfaces that they share with other elements that interact with and within the environment.

3.2.1. General Description of Component Modules

Component modules represent a set of physically adjacent locations that can be joined with other modules in the arrangement of the specific secondary system being modeled. Component module definitions of the SPPDMME are determined by the physical components of *real* secondary systems and essentially, correspond to the typical components one would find in such secondary system. Table 3-1 lists the ten components available in this environment. These components are subdivided into sections (or control volumes). These sections have a range of the number of inlets and outlets that represent what one would observe for the real volumes they are intended to model.

A brief description of some of the more complicated components in Table 3-1 is given:

1. The Reheater is a separate module from the Moisture Separator in order to allow it to also be used to as a Heat Exchanger. To model a Heat Exchanger with the Reheater module, the user does not use the Tube Heating Stage 2.

---

determining unknown parameters. One of these parameter models, that predicting FAC wear rate, is the focus of Chapter 5.

Table 3-1. Listing of Significant Component Module Features.

Component Module	Section Name	# of Section Inlets	# of Section Outlets
Condenser	Shell	1-8	1
Drain Tank	Shell	1-7	1
Feedwater Heater	Shell Condensing	1-5	1
	Shell Drains Subcooling	1	1
	Tube	1	1
Junction	Shell	0-7	0-7
Moisture Separator	Shell	1	2
Piping System	Shell	1	1
Pump	Shell	1	1
Reheater/Heat Exchanger	Shell	1	1
	Tube Heating Stage 1	1	1
	Tube Heating Stage 2	0-1	0-1
Steam Generator	Shell	1	1-2
Turbine	Shell N+1 (N<6)[a]	1	2[b]

a - N refers to the number of extraction lines for the turbine.
b – The last section, the Shell N+1 Section, has only one outlet.

2. The Moisture Separator has two outlets representing the drain line and steam going into the Reheater. The range of possible numbers of inlets and outlets for other sections are based on expected maximum numbers of connections for these sections.

3. The Junction element is used to model flow splitting or convergence. A Junction that has zero inlets and some outlets acts as a source of fluid flow. A Junction with some inlets and zero outlets acts as a sink for fluid flow.

4. Table 3-1 lists 1 to 2 outlets for the Steam Generator. The 2 potential outlets represents the blowdown and steam exit necessitated for a recirculating steam generator. To model a Once Through Steam Generator, the user does not use the blowdown outlet.

The calculation modules are based on the inlet and outlet parameters of sections (see 3.3. SPPDMME Calculation Modules). Computationally, a section is treated as a lumped parameter control volume. Therefore, a section is defined based on calculation constraints and corresponds to the scale of locations for which properties are known. Inlet and outlet locations for a section, then, are adjacent locations. Because some components consist of separate fluid flow paths or fluid flow paths for which parameters internal to the component must be calculated, some components consist of more than one section (or control volume). Component module definitions are determined by the physical components of real secondary systems. Section definitions are determined based on calculation constraints.

As shown in Table 3-1, seven components consist of a single section (or control volume). Figure 3-2a) illustrates the typical relation between these components and their single section using the Piping System module as an example. The 'Inlet' and 'Outlet' arrows correspond to fluid flows in this figure. For these component modules, all sections match up to module interfaces and only a single fluid flow path exists. Though the Pipe System Module can have only one inlet and outlet, other single section modules may have numerous inlets and/or outlets.

Table 3-1 lists two components with three sections, the Feedwater Heater and Reheater/Heat Exchanger. Figure 3-2b) illustrates the Feedwater Heater module of the SPPDMME. This module corresponds to a two zone closed feedwater heater typically found in secondary systems of PWRs. Therefore, fluid in the shell passes through two sections, the Shell Condensing Section and Shell Drains Subcooling Section. The third

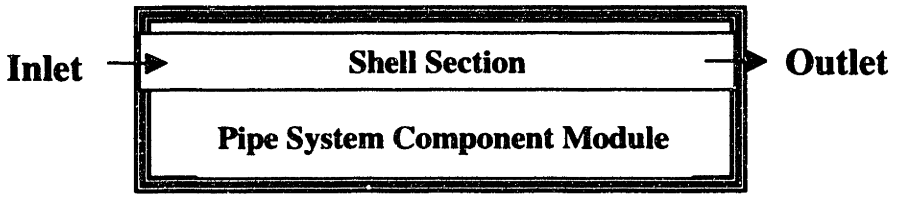

a. Pipe System Component - Section Relationship

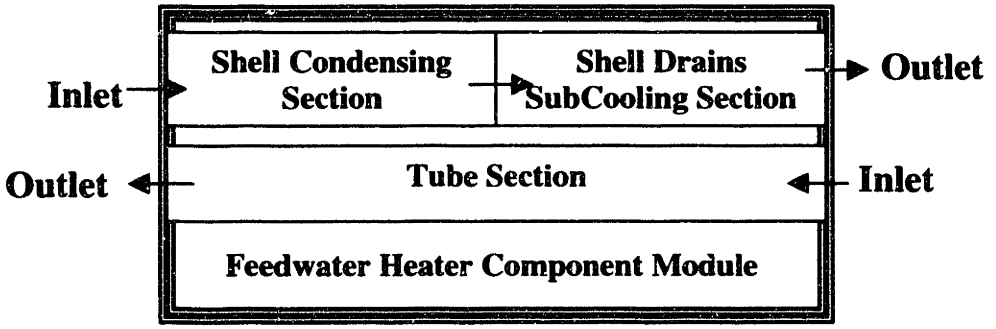

b. Feedwater Heater Component - Section Relationship

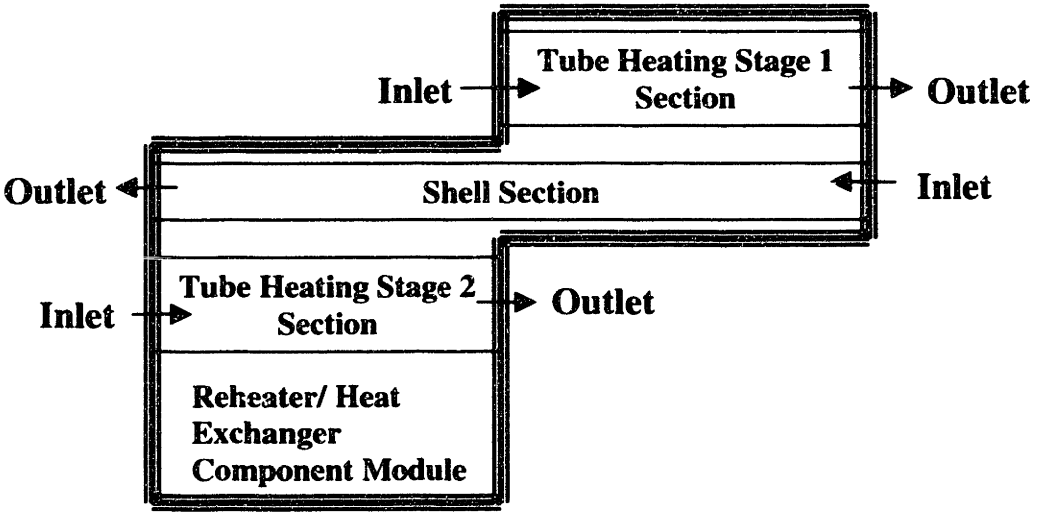

c. Reheater/Heat Exchanger Component - Section Relation hip

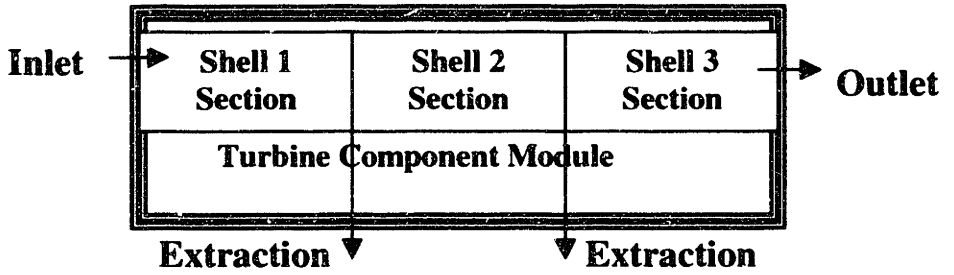

d. Turbine Component - Section Relationship

Figure 3-2. Relation of some component modules and their sections

section of the module is that for the tube fluid flow path. The Reheater/Heat Exchanger component module is shown in Figure 3-2c) and corresponds to a two stage reheater. In this case, three paths for fluid flow exist. If the module is used as a heat exchanger the Tube Heating Stage 2 Section is not used. For these later two modules, Figure 3-2 illustrates immediately adjacent fluid flow paths which exchange heat. The expressions used for this calculation are given in the next section.

Table 3-1 indicates that the turbine could have as many as 7 sections. Within the SPPDMME, as the user adds outlets, the number of sections is incremented for turbines with more than one outlet. As the user assigns pressures to these outlets the lowest is assumed to be the turbine outlet and the remaining are assumed to be extraction lines. For a turbine then, a section corresponds to the fluid flow paths between extraction lines. Each section (except the last) has two outlets, the extraction line flow and the flow to the next section. Figure 3-2d) illustrates an example turbine for which three outlets have been assigned (2 extraction, and one normal outlet) which results in 3 sections for the turbine.

To further describe the function of component modules within the environment, the interfaces these modules share with other elements are defined. As shown in Figure 3-3, component modules share 4 interfaces in the SPPDMME. These interfaces are described in terms of the information that crosses the interface and the functions that the interface performs. For this and the following figures, the arrows indicate the direction of information flow.

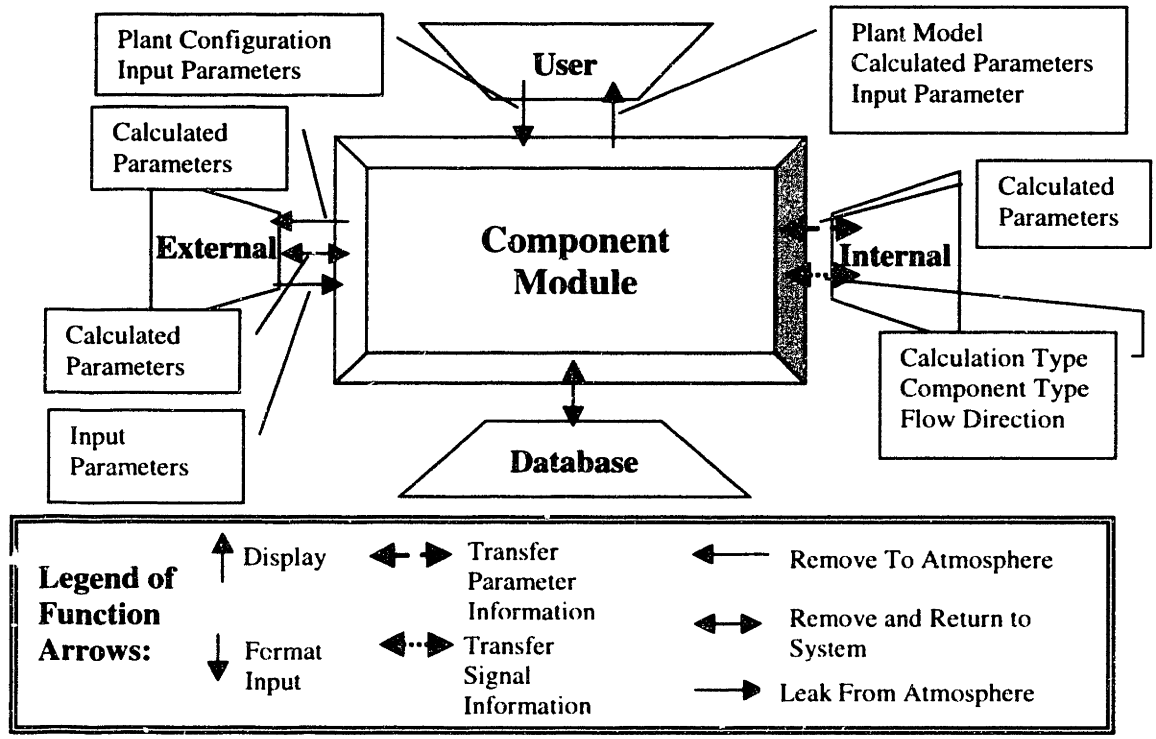

Figure 3-3. Schematic of four interfaces shared by component modules within the SPPDMME.

3.2.2. User Interface

The user interface provides the vital role of feeding back to the user what parameters have been calculated and identifying what information needs to be input. In this capacity, the interface functions can be specifically listed in terms of the two main actions, formatting input and displaying output. In formatting input the interface must:

1. Provide labeled locations for inputting information,
2. Provide instructions to user on how to input information,
3. Interpret input in familiar units, and
4. Provide feedback on incorrect or indecipherable input in the form of error messages.

Additionally, in displaying output the interface must:

5. Provide a visual display of the plant model developed within the SPPDMME,
6. Present results in familiar units, and

7. Differentiate between information that has been input and that which has been calculated.

Figure 3-3 illustrates the information flow across the user interface when performing these two functions.

To emphasize these functions two figures are given of the final form of this environment programmed in VB. The programmed interface consists of windows. The first figure, Figure 3-4, illustrates the programmed interface for building and displaying plant model information. In the interest of space, the window shown includes only a fraction of a plant model being developed, the high pressure steam system. This window can be broken down into its major areas: the buttons along the top, the workspace in the center, and the message bar at the bottom. By using the buttons to add components to the workspace, the user builds a plant model in this window by repositioning components and making connections as desired. This window then encapsulates the first, second, and fifth actions listed above.

An important restriction on the method required to develop a plant model is imposed within the SPPDMME. In connecting component modules, one must always use a Piping System module between component modules of any other type. Further, Piping System modules themselves cannot be connected together. This restriction can be seen in Figure 3-4 that illustrates the Piping System module icon, a straight black line with a blue box (or space in black and white) at its midpoint, that separates all other component module icons in the window. The black arrow on the line indicates the Piping System module's inlet and outlet (in reference to fluid flow). Physically, components may not necessarily be connected with piping. The Piping System module, however, can be modeled to have zero length to accurately model the physics of this situation. This

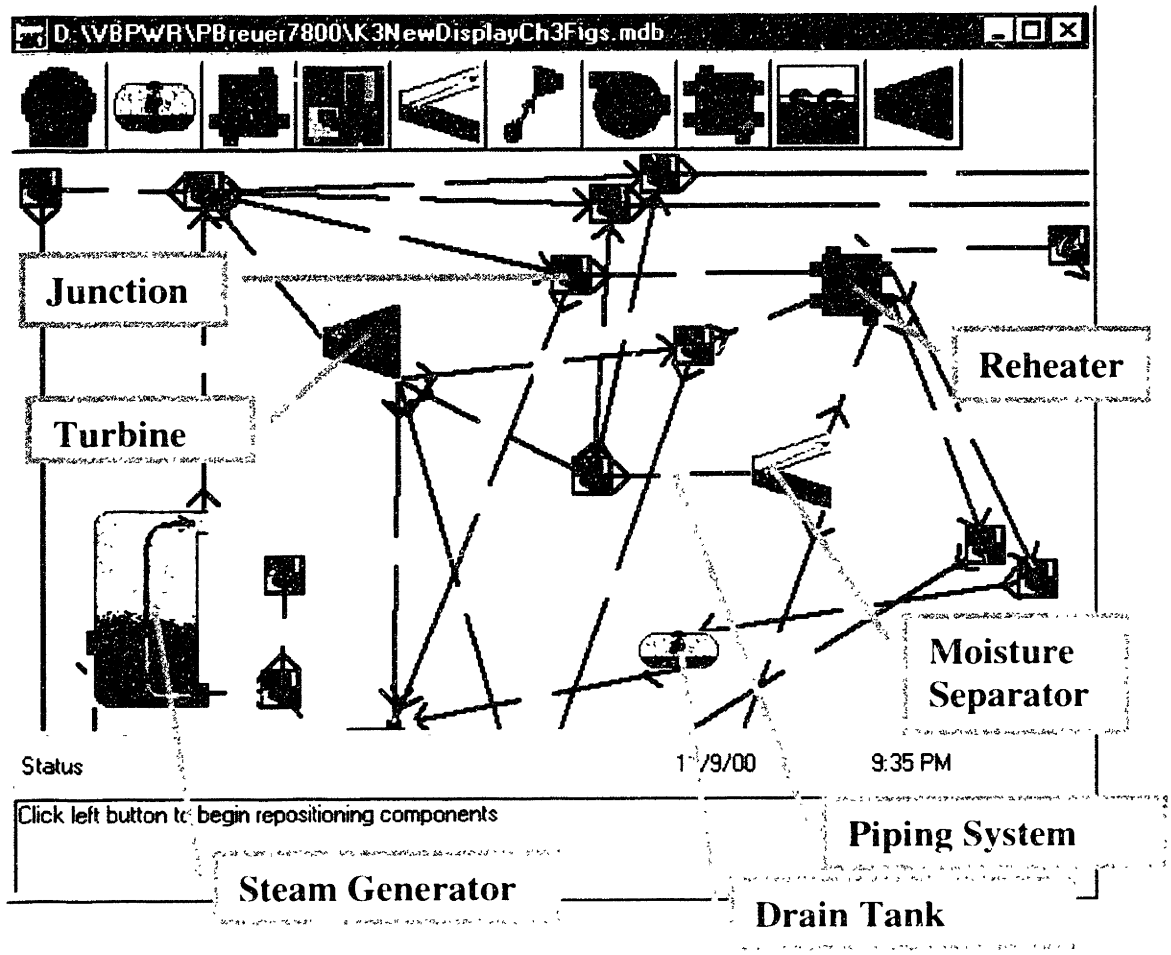

Figure 3-4. User interface for building and displaying the plant model as programmed in VB.

restriction is imposed so that all component modules (or more specifically their sections)have an associated inlet and outlet imposed by the connected Piping System module. The definition of inlet and outlet is used to interpret the direction of mass flow based on input by the user. An input of positive mass flow rate is interpreted as flow from inlet to outlet. An input of negative mass flow rate is interpreted as the opposite.

Figure 3-5 illustrates the programmed interface for a component module, in this case for a Piping System modeling a high pressure steam piping section. Attention is drawn to the textboxes in this window. Information above and beside these textboxes indicates the parameter information displayed and the units used for display. The user can

change the units of the display. The color of the numbers in the textbox indicates whether the information is input or calculated within the environment. The textbox also does not allow the input of non-numerical information. This window then encapsulates the first, third, fourth, sixth and seventh actions listed above.

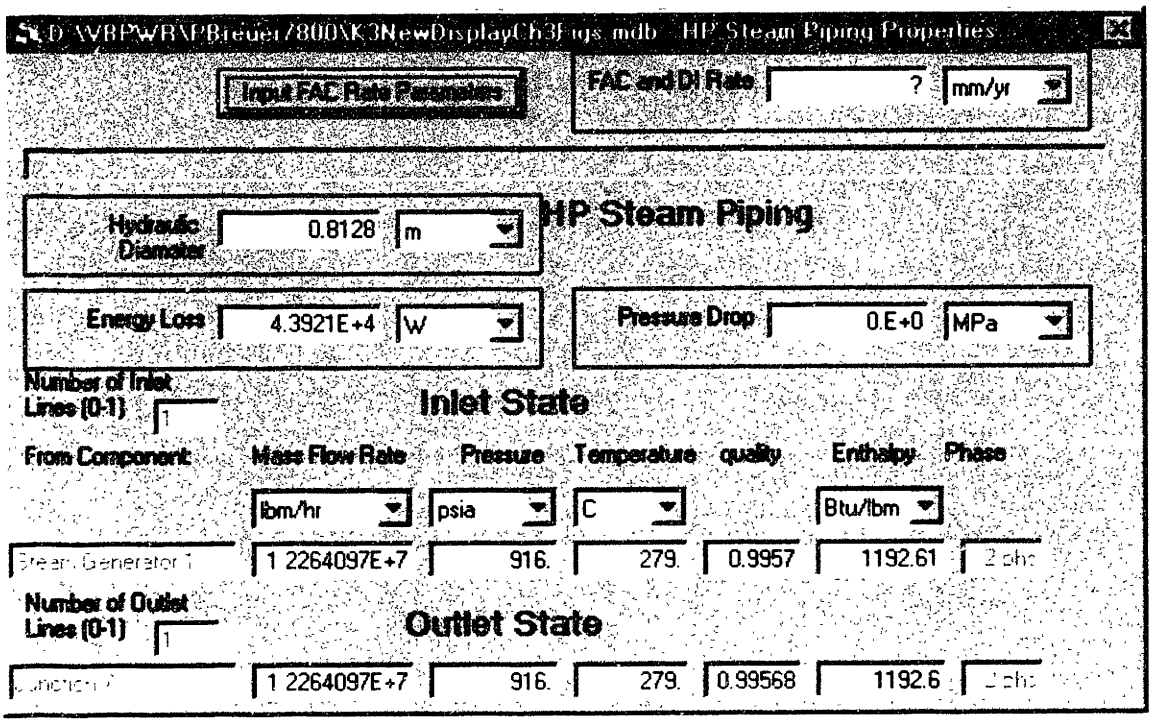

Figure 3-5. User interface for inputting and displaying plant parameter information as programmed in VB.

3.2.3. Internal Interfaces

Internal Interfaces are those that are shared between component modules. Two main information flows exist for this interface, calculated parameters and signals, as shown in Figure 3-3. The calculated parameters are the main results that this environment determines. The signal flow includes information on the type of calculation being executed, the components types joined at this interface, and the direction that the calculation that is being propagated relative to direction of fluid flow (as defined by the inlet and outlet). This signal information is used by the calculation logic of the program

to determine the next step of a sequential or propagated calculation. The relevance of this information will be made more apparent as the calculation modules and calculation logic are described in the next section.

3.2.4. External Interfaces

External interfaces represent ejectors, in-leakage, and vent lines in the PWR secondary system. These interfaces are external in their relation to the main fluid flow system. The physical interfaces that the external interfaces represent are distinct from internal interfaces in that gases other than steam may be a considerable volume fraction of the flow. (See the section on the Chemistry Calculation Module, 3.3.4, for more information on the assumptions of the physics of internal interfaces.) Because of this physical difference, the set of calculated parameters that cross this interface are different from the internal interfaces thereby making external interfaces distinct. The calculation logic controlling the information flow differs for these interfaces. Like internal interfaces, though, calculated parameters describing steam are still part of the information flow across external interfaces, as one would expect based on the physics of ejectors and vent lines.

Figure 3-3 illustrates the three functions of external interfaces that correspond to the three physical components or processes they represent. Ejectors remove gases to the atmosphere, vent lines transfer gases between components, and in-leakage represents air in-leakage into sub-atmospheric components of the secondary system. For the first two interfaces, information flow is that of calculated parameters. For the third, information flow is that input by the user.

Within the SPPDMME, these external interfaces are available for a subset of the sections of component modules. This subset reflects the presence within the secondary system of the components and processes these external interfaces represent. Table 3-2 lists all the component modules for which external interfaces can be modeled. Further, within Table 3-2 the specific sections of these component modules for which external interfaces can be modeled is indicated with a checkmark. Unlisted component modules have no external interfaces.

Table 3-2. Listing of External Interfaces modeled for each section within the SPPDMME.

Component Module	Section Name	External Interfaces Modeled		
		Ejector	Inleakage	Vent Line(s)
Condenser	Shell	✔	✔	✔
Drain Tank	Shell	-		✔
Feedwater Heater	Shell Condensing	-	✔	✔
	Shell Drains Subcooling	-	-	-
	Tube	-	-	
Reheater/Heat Exchanger	Shell	-	-	✔
	Tube Heating Stage 1	-	-	-
	Tube Heating Stage 2	-	-	-

3.2.5. Database Interface

The main functions of the database interfaceare reading information from and writing information to the database. Depending on what activity is occurring in the environment, the information that is being read and written varies. Figure 3-6 summarizes the read and write functions during four different activities. Note that when opening a new session and closing a session no database interaction occurs. All updating of new

information is done automatically as the user inputs new information and unknown parameters are calculated.

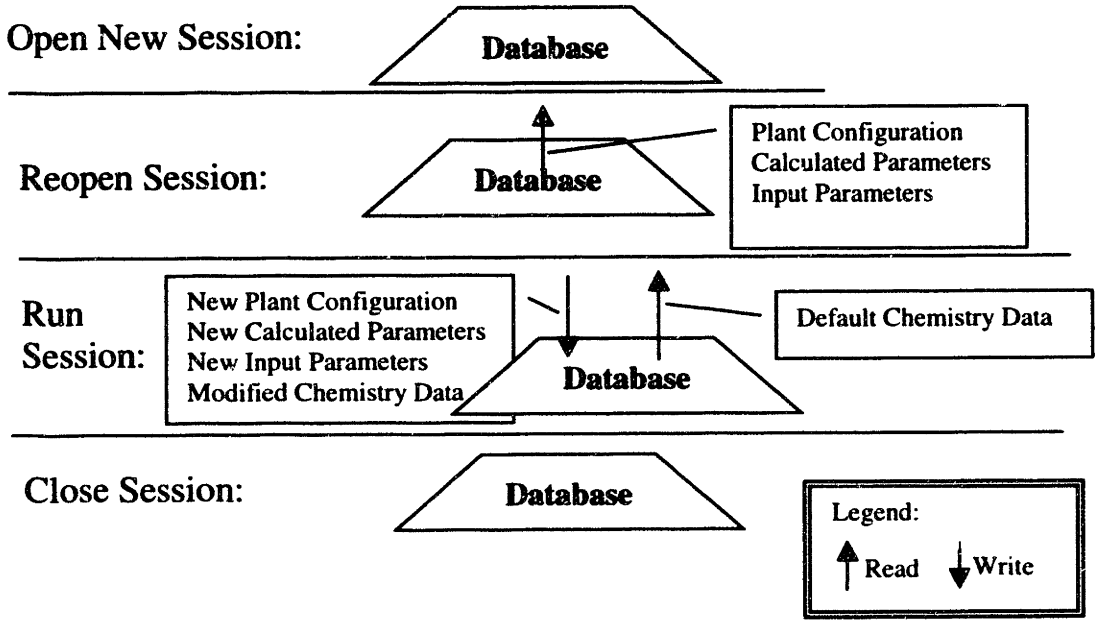

Figure 3-6. Database Interface functions and information flow during four different activities.

3.3. SPPDMME Calculation Modules

This section addresses the following two questions:

1. What set of equations are incorporated in the SPPDMME, and
2. How are these equations are solved within this modular environment.

Calculation modules are first described in terms of the general structure shared by the four calculation modules shown in Figure 3-1. The next four sections then describe the specific set of equations (or models) incorporated within each of these calculation modules. The last section ties in the relevance of the information flow across boundaries described above with the physical nature of the equation sets described below to explain the calculation logic in terms of propagated and sequential calculations without going into the details behind the logic.

3.3.1. General Description of Calculation Modules

A calculation module in the SPPDMME is defined by the parameter set it uses as input and the parameter set it calculates. The input and calculated parameter set may be similar parameters but differ in their location. Additional information such as the component module type to which the parameters correspond may affect the equation set used by a calculation module. Figure 3-7 provides a schematic of the general characteristics of a calculation module.

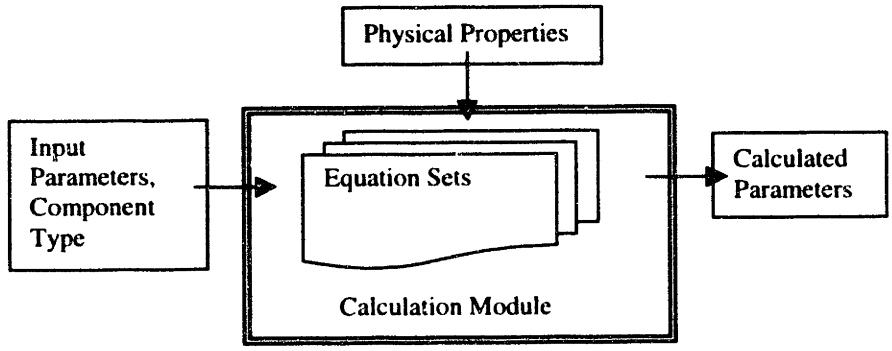

Figure 3-7. General Format of Calculation Module

The four calculation modules in the SPPDMME correspond to calculation steps shown in Figure 3.1 and are referred to as the following:

1. Thermodynamic module,
2. Thermal Hydraulic module,
3. Chemistry module, and
4. Pipe Degradation module.

The Thermal Hydraulic and Pipe Degradation modules calculate unknown parameters at a single location based on the known properties at that location. The Thermodynamic and Chemistry modules calculate unknown parameters at adjacent locations based on properties at adjacent locations. Recall that the sections within component modules

define adjacent locations. The Thermodynamic module can determine outlet parameters based on inlet parameters and vice versa. The Chemistry module can only determine outlet parameters based on inlet parameters.

Given this general description of the calculation modules, each module and the incorporated models will be discussed in further detail.

3.3.2. Thermodynamics

The Thermodynamic module relates the mass flow rate and state properties for the inlets and outlets of sections (i.e. between adjacent locations). Figure 3-8 illustrates that the input and calculated parameters of Figure 3-7 can be broken down into inlet, outlet, and section parameters, any of which can be input parameters or calculated parameters. Figure 3-8 can be expanded to show the parameters and equations sets that are referred to, as illustrated in Figure 3-9. The following discussion outlines the four equation sets of the Thermodynamic module and defines the symbols (representing parameters) illustrated in Figure 3-9.

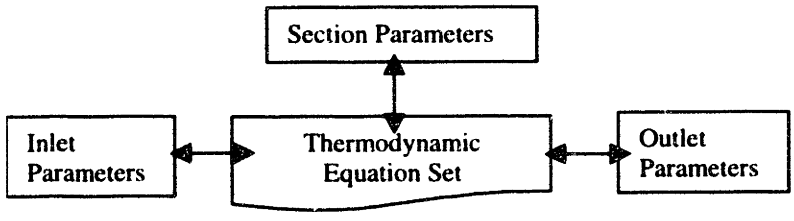

Figure 3-8. General format for Thermodynamic module equation sets.

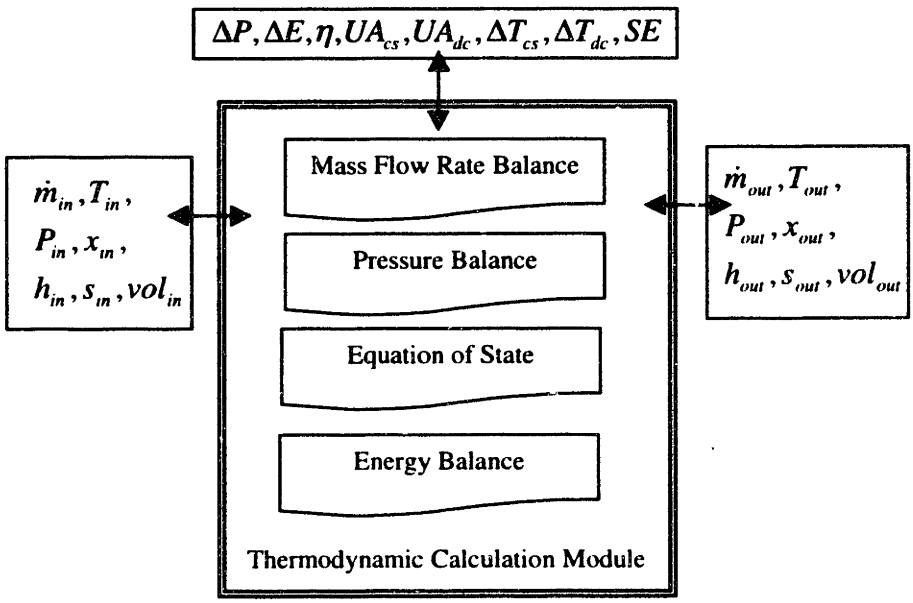

Figure 3-9. Expanded schematic of parameters and equation sets included in the Thermodynamic module.

3.3.2.1. Mass Balance

The most fundamental equation solved for each section is the mass balance,

$$\sum_{i=1}^{n_{in}} \dot{m}_{i,in} = \sum_{i=1}^{n_{out}} \dot{m}_{i,out} \qquad \textbf{(Eq. 3-1)},$$

where

$\dot{m}_{i,lctn}$ is the mass flow rate for connection i at location, *lctn*, and

n_{lctn} is the number of connections at location, *lctn*.

This equation determines the unknown inlet or outlet flow mass flow rate provided the remaining flow rates are known. As discussed above, the inlet and outlet connections of the Pipe System determine the direction of the flow. For a section for which the equation is under constrained (the number of connections exceeds the known mass flow rates by two or more), no calculation is performed. For a component for which the equation is over constrained a check of the values is performed. If the mass flow rates do not match,

an error message is generated. For component modules with more than one section, the mass balance is determined for each section separately. Figure 3-10 illustrates the subset of Figure 3-9 that is represented by this mass balance.

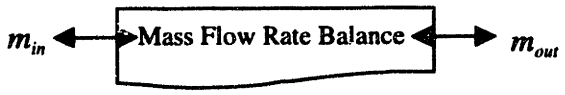

Figure 3-10. Mass balance information flow schematic.

3.3.2.2. Pressure Balance

The pressure balance is determined based on minimum inlet pressure, maximum outlet pressure, and the pressure drop across the section:

$$\min(P_{i,in}) = \max(P_{i,out}) + \Delta P \qquad \textbf{(Eq. 3-2),}$$

where

$P_{i,lctn}$ is the pressure for connection i at location, *lctn*, and

ΔP is the pressure drop for the section.

Figure 3-11illustrates the subset of Figure 3-9 that is represented by this pressure balance.

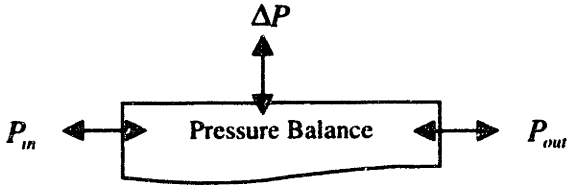

Figure 3-11. Pressure balance information flow schematic.

Note that the code does not determine pressure drop based on flow rate, pipe geometry, or pipe inclination. The reason is that while the user may have available information on pressure values at particular locations, the user may not have sufficient information on geometry needed to do the pressure calculations, specifically form loss information. The main impact of pressure on relevant degradation is its effect on the state

of the fluid flowing in the system. User information on whether the fluid is liquid, liquid/vapor, or vapor is more important.

3.3.2.3. Equation of State

At each location if two state values are known for the fluid flow the equation of state is used to determine the other state properties. Within the SPPDMME, the following combinations of parameters can be used to determine the other parameters:

1. Pressure and temperature,
2. Pressure and flow quality,
3. Pressure and enthalpy, and
4. Temperature and quality.

State properties are determined based on tables provided from the literature (Keenan and Keyes, 1992). Figure 3-12 illustrates the subset of Figure 3-9 that is represented by the equation of state. In Figure 3-9 the parameters listed relate to specific parameters, i.e.

P is the pressure,
T is the temperature,
x is the flow quality,
h is the specific enthalpy,
s is the specific entropy, and
vol is the specific volume.

Note from Figure 3-5 only the first four variables listed above are displayed to the user.

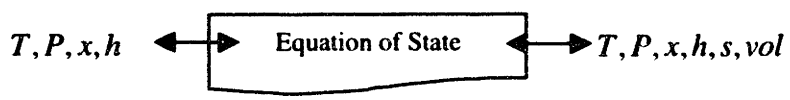

Figure 3-12. Equation of state information flow schematic.

3.3.2.4. Energy Balance

The energy balance equation of the Thermodynamic module is based on the following equation:

$$\sum_{i=1}^{n_{in}} \dot{m}_{i,in} \cdot h_{i,in} = \sum_{i=1}^{n_{out}} \dot{m}_{i,out} \cdot h_{i,out} + \Delta E \qquad \textbf{(Eq. 3-3),}$$

where, ΔE is the energy loss for the section. This equation is used to determine parameters for the section of the Steam Generator module. Figure 3-13 illustrates the subset of Figure 3.9 for this basic equation.

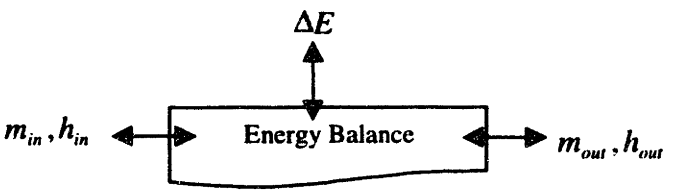

Figure 3-13. Energy balance information flow schematic.

The Thermodynamic module contains more specific equation sets for the remaining component modules as outlined in the following discussion.

3.3.2.4.1. Plenum Calculation

Recognizing that the exit enthalpy for most components will match for well-mixed flow, the following equation is derived:

$$\sum_{i=1}^{n_{in}} \dot{m}_{i,in} \cdot h_{i,in} = h_{exit} \cdot \sum_{i=1}^{n_{out}} \dot{m}_{i\ out} + \Delta E \qquad \textbf{(Eq. 3-4).}$$

This equation is used within the Thermodynamic module for component module sections that are modeled with matching exit enthalpy or component module sections with a single outlet. These modules include the Condenser, Drain Tank, Junction, Piping System, and

Reheater/Heat Exchanger. For the Reheater/Heat Exchanger module this equation is solved simultaneously for the sections exchanging heat.

3.3.2.4.2. Turbine

For determining the energy produced by a turbine **Eq. 3-3** is applied to the turbine component module as a whole. Previous to this calculation, the following equation is used for each section, i, within the turbine,

$$h_{out,i} = h_{in,i} - \frac{h_{in,i} - h(P_{out,i}, s_{in,i})}{\eta_i} \qquad \textbf{(Eq. 3-5),}$$

and for all sections except the last (i<imax), the following equations are used,

$$\dot{m}_{i+1} = \dot{m}_i - \dot{m}_{extraction,i} \qquad \textbf{(Eq. 3-6),}$$

$$h_{i+1} = \frac{\dot{m}_i \cdot h_{out,i} - \dot{m}_{extraction,i} \cdot h_{extraction,i}}{\dot{m}_{i+1}} \qquad \textbf{(Eq. 3-7),}$$

where, η_i is the isentropic efficiency of section i. Figure 3-14 illustrates the subset of Figure 3-9 that is represented by this equation set.

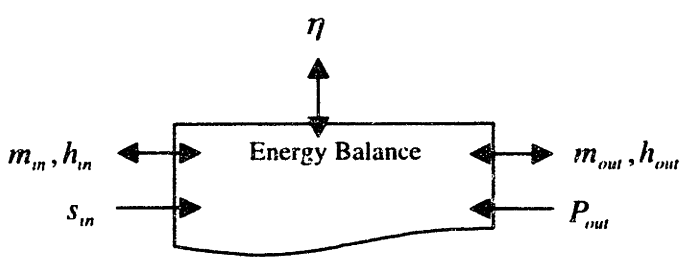

Figure 3-14. Turbine energy balance information flow schematic.

3.3.2.4.3. Feedwater Heater

The Thermodynamic module calculates the energy balance for the sections of this module simultaneously. To determine the combined inlet state (assuming well mixed

flow) for the set of connections to the shell condensing section, the following equations, similar to **Eq. 3-1**and **Eq. 3-4**, are used and expressed below in terms of the specific parameters for the Feedwater Heater module sections. These equations are:

$$\sum_{i=1}^{n_{in}} \dot{m}_{i,in} = \dot{m}_{shell} \qquad \textbf{(Eq. 3-8)}, \text{ and}$$

$$\sum_{i=1}^{n_{in}} \dot{m}_{i,in} \cdot h_{i,in} = h_{combined\_inlet} \cdot \dot{m}_{shell} \qquad \textbf{(Eq. 3-9).}$$

The remaining equations describing heat exchange between the Feedwater Heater module sections are solved simultaneously in order to determine unknown parameters. The energy balance between the two shell sections and the tube section is then given by:

$$\dot{m}_{tube} \cdot C_p \cdot (T_{out} - T_{in}) = \dot{m}_{shell} \cdot (h_{combined\_inlet} - h_{out}) \qquad \textbf{(Eq. 3-10)}$$

The heat transfer between the condensing section of the shell and the fraction of tube section that is exchanging heat with the condensing section is given by:

$$q_{cs} = \dot{m}_{tube} \cdot C_{p,tube} \cdot (T_{out,tube} - T_{mid,tube}) = \dot{m}_{shell} \cdot (h_{combined\_inlet} - h(P_{combined\_inlet}, x = 0)) \qquad \textbf{(Eq. 3-11)}$$

where

$C_{p,tube}$ is the heat capacity of the water is the tube section

$T_{mid,tube}$ is the temperature of the water entering the fraction of the tube section which exchanges heat with the condensing section, and

q_{cs} is the heat transfer from the condensing section.

The heat exchange effectiveness, ε_{cs}, is given by:

$$\varepsilon_{cs} = 1 - \exp\left(\frac{-UA_{cs}}{C_{p,tube} \cdot \dot{m}_{tube}}\right) \qquad \textbf{(Eq. 3-12)}$$

where UA_{cs} is the overall heat transfer coefficient area product for the condensing section.

This effectiveness can be related to the maximum heat exchange between the later fraction of tube section and condensing section, $q_{max,cs}$, by the following two expressions:

$$q_{max,cs} = \frac{q_{cs}}{\varepsilon_{cs}} \quad \textbf{(Eq. 3-13),}$$

$$q_{max,cs} = \dot{m}_{tube} \cdot C_{p,tube} \cdot (T_{saturation}(P_{combined\_inlet}) - T_{mid,tube}) \quad \textbf{(Eq. 3-14).}$$

Heat transfer between the shell drains cooling section and fraction of the tube section exchanging heat with the shell drains cooling section is modeled as counter current flow single pass heat exchange with the following relations in which subscript dc refers to parameters in the drains cooling section:

$$T_{in,shell} = T(P_{saturation,combined\_inlet}) \quad \textbf{(Eq. 3-15)}$$

$$q_{dc} = \dot{m}_{tube} \cdot C_{p,tube} \cdot (T_{out,tube} - T_{mid,tube}) = \dot{m}_{shell} \cdot C_{p,shell} \cdot (T_{in,shell} - T_{out,shell}) \quad \textbf{(Eq. 3-16)}$$

$$\varepsilon_{dc} = \frac{1 - \exp\left(\frac{-UA_{dc}}{C_{p,shell} \cdot \dot{m}_{shell}} \cdot \left(1 - \frac{C_{p,shell} \cdot \dot{m}_{shell}}{C_{p,tube} \cdot \dot{m}_{tube}}\right)\right)}{1 - \frac{C_{p,shell} \cdot \dot{m}_{shell}}{C_{p,tube} \cdot \dot{m}_{tube}} \cdot \exp\left(\frac{-UA_{dc}}{C_{p,shell} \cdot \dot{m}_{shell}} \cdot \left(1 - \frac{C_{p,shell} \cdot \dot{m}_{shell}}{C_{p,tube} \cdot \dot{m}_{tube}}\right)\right)} \quad \textbf{(Eq. 3-17)}$$

$$q_{max,dc} = \frac{q_{dc}}{\varepsilon_{dc}} \quad \textbf{(Eq. 3-18)}$$

$$q_{max,dc} = \dot{m}_{shell} \cdot C_{p,shell} \cdot (T_{in,shell} - T_{in,tube}) \quad \textbf{(Eq. 3-19)}$$

The calculation logic for these expressions is devised to solve for the UA_{cs} and UA_{dc} products and/or unknown inlet and outlet parameters. As is true for all equation sets the calculation logic determines if the parameters known for the Feedwater Heater module

over constrain or under constrain the set. Figure 3-15 illustrates the subset of Figure 3-9 that is represented by this equation set.

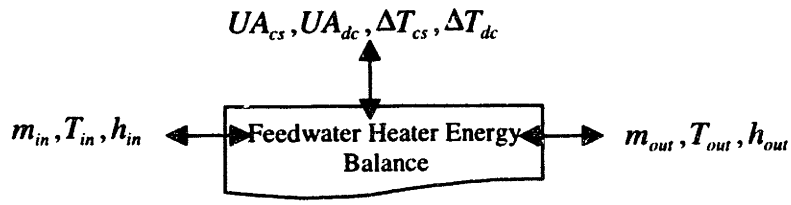

Figure 3-15. Feedwater Heater energy balance information flow schematic.

3.3.2.4.4. Pump

The Thermodynamic module calculates the energy balance for the Pump module based on the following equation:

$$h_{out} = h_{in} + \frac{h(P_{out}, s_{in}) - h_{in}}{\eta} \qquad \textbf{(Eq. 3-20)}$$

The information flow schematic for the pump would then be similar to that shown for the Turbine module in Figure 3-14.

3.3.2.4.5. Moisture Separator

The Thermodynamic module combines the energy balance and mass balance for the Moisture Separator module using the following equation set:

$$\dot{m}_{in} = \dot{m}_{st} + \dot{m}_{dr} \qquad \textbf{(Eq. 3-21),}$$

$$\dot{m}_{in} \cdot x_{in} = \dot{m}_{st} \cdot x_{st} \qquad \textbf{(Eq. 3-22),and}$$

$$SE = \frac{\dot{m}_{dr}}{\dot{m}_{in}(1 - x_{in})} \qquad \textbf{(Eq. 3-23),}$$

where

in refers to inlet

st refers to steam outlet

dr refers to drain outlet, and

SE refers to separation efficiency.

The separation efficiency is the percentage of moisture removed from the flow exiting from the high pressure turbine and is normally around 90% (Cohen, 1989). Figure 3-16 illustrates the subset of Figure 3-9 that is represented by this equation set.

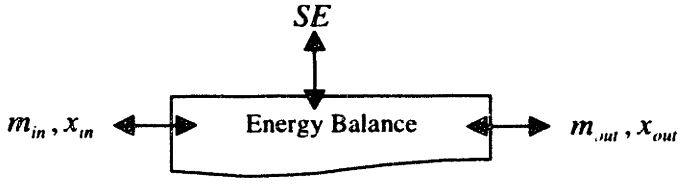

Figure 3-16. Moisture Separator mass and energy balance information flow schematic.

3.3.3. Thermal Hydraulics

The Thermal Hydraulics module relates the mass flow rate and thermodynamic state of the fluid flow to the liquid and/or vapor velocity for Piping System modules and the tube sections of the Reheater/Heat Exchanger and Feedwater Heater modules. The module then determines thermal hydraulic parameters at a single location based on known thermodynamic properties at that location. Figure 3-17 summarizes the information flow for this calculation module. The symbols of the figure (representing parameters) will be explained below in context of the equation sets in which they are used.

The section parameter input into the Thermal Hydraulic module highlights a significant feature of the SPPDMME, the ability of the user to model a number of parallel components with a single component. Secondary flow systems typically have a number of parallel flow paths (condensate, feedwater, moisture separation, etc.) that the user may

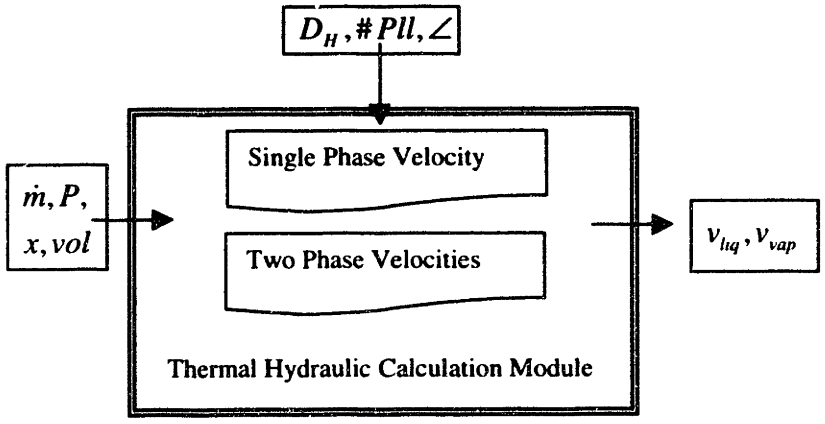

Figure 3-17. Thermal Hydraulic module information flow schematic.

or may not want to distinguish between in modeling the secondary system. Rather than input the same information for these similar paths, the user need only input the information once. For parallel flow paths that the user wants to model separately (to investigate differences that may affect degradation rate, for example), the user can add the additional necessary components using the Junction module to split and converge flow paths. Depending on the specific application, the user may partially model parallel trains using the Junction module.

3.3.3.1. Single Phase

The single phase velocity calculation determines the average velocity in the pipe or tube based on the input of hydraulic diameter, D_H, and the number of parallel flow paths for this pipe or tube, $\#Pll$. The calculation uses the specific volume calculated in the Thermodynamic module which results in

$$v_{liq} = \frac{\dot{m} \cdot vol_{liq}}{\#Pll} \cdot \frac{4}{\pi \cdot D_H^{\,2}} \qquad \textbf{(Eq. 3-24)}$$

for water flow and

$$v_{vap} = \frac{\dot{m} \cdot vol_{vap}}{\#Pll} \cdot \frac{4}{\pi \cdot D_H^{\,2}} \qquad \textbf{(Eq. 3-25)}$$

for steam flow. The hydraulic diameter for the Piping System module is the inner diameter of the pipe. The number of parallel flow paths for the Piping System module is the number of parallel components represented that module. The hydraulic diameter for the Reheater/Heat Exchanger and Feedwater Heater modules is the inner diameter of the tube. The number of parallel flow paths for the tube sections of the Reheater/Heat Exchanger and Feedwater Heater modules is the product of the number of tubes and the number of parallel components represented by that module. Figure 3-18 summarizes the subset of information flow from Figure 3-17 for this calculation.

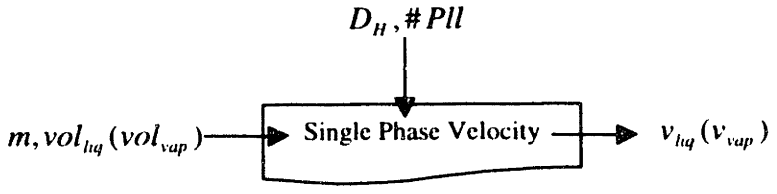

Figure 3-18. Single phase velocity equation information flow schematic.

3.3.3.2. Two Phase

The two phase velocity calculation determines the liquid and vapor velocity in the pipe or tube. The Thermal Hydraulic module performs the calculation in three steps determining parameters as shown in Figure 3-19. The first step is the calculation of the superficial vapor velocity, j_g, using

$$j_g = \frac{4 \cdot \dot{m}}{\pi \cdot D_H^{\,2}} \cdot \frac{vol_{vap}}{1 + \frac{1-x}{x}} \qquad \textbf{(Eq. 3-26)}$$

and the superficial liquid velocity, j_f, using

$$j_f = j_g \cdot \frac{1-x}{x} \cdot \frac{vol_{liq}}{vol_{vap}} \qquad \textbf{(Eq. 3-27)}$$

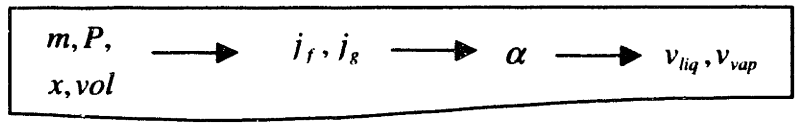

Figure 3-19. Two phase calculation steps for determining velocities.

The second step uses the Chexal-Lellouche void fraction correlation to determine the void fraction, α, based on the pipe orientation relative to vertical, $\angle$, and flow direction (Chexal, 1991). This correlation is based on the drift flux formulation first proposed by Zuber (Zuber, 1965). In the Chexal-Lellouche correlation the drift flux parameters are determined empirically throughout the various 2 phase flow regimes.

The main advantage of this correlation is its ability to replicate the trends of friction velocity for two phase flow. Because the FAC process is characterized by a concentration dependent dissolution of the metal, the impact of velocity on metal removal is through its affect on mass transfer. Thus, a two phase correlation that calculates velocities which trend with friction velocity is expected to provide better information for predicting the degradation rate than those used in the literature (Kastner, 1987). For a more in depth discussion of this argument, see section 5.1.3.

The third step is the calculation of liquid and vapor velocities based on the void fraction. Liquid velocity is given by

$$v_{liq} = \frac{\dot{m} \cdot 4 \cdot vol_{liq}}{\pi \cdot D_H^{\,2}} \cdot \frac{1-x}{1-\alpha} \qquad \textbf{(Eq. 3-28)}$$

The vapor velocity is given by:

$$v_{vap} = \frac{\dot{m} \cdot 4 \cdot vol_{vap}}{\pi \cdot D_H^{\,2}} \cdot \frac{x}{\alpha} \qquad \textbf{(Eq. 3-29)}$$

To summarize, Figure 3-20 illustrates the information flow for the two phase velocity equation set, a subset of Figure 3-17.

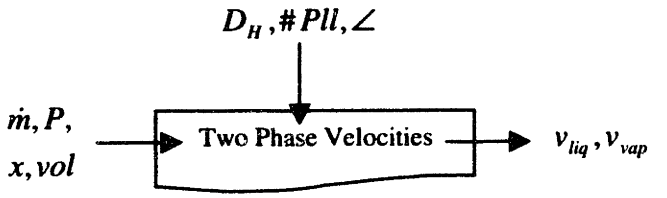

Figure 3-20. Two phase velocity equation set information flow schematic.

3.3.3.3. Advanced Thermal Hydraulic Modules

FAC has been observed in secondary components (or component sections) other than piping and tubes. These components include reheater shells (Chexal *et. al.*, 1996) , steam generator feed rings(Thailer *et. al.*, 1995), feedwater heaters shells (Bouchacourt, 1982), and pumps (LePrince, 1983). The determination of the local velocities affecting FAC for these components would require component modeling based on specific component information and calculations at the level of Computational Fluid Dynamics (CFD). A CFD module that determines the local velocities affecting FAC could be included in the SPPDMME in the future. Within the design of the current environment, if the velocities are known from such models of plant specific components, this information can be input directly and used to determine degradation rates.

3.3.4. Chemistry

In order to calculate those chemical parameters known to affect the FAC wear rate, pH and oxygen concentration, and investigate new parameters suspected to affect FAC and other degradation rates, specie concentrations must be determined at the locations where one intends to predict these degradation rates. To perform this function,

the Chemistry module of the SPPDMME relates mass flow rates, thermodynamic state, and inlet chemistry values to outlet chemistry values. As shown in Figure 3-21, this module consists of two equations sets. The first calculates chemical equilibrium at a single location. The second determines the decomposition and reaction rates of chemical species not at equilibrium as fluid flows through a component module. As a whole the Chemistry module calculates chemistry parameters at a single location and adjacent locations in the direction of the flow.

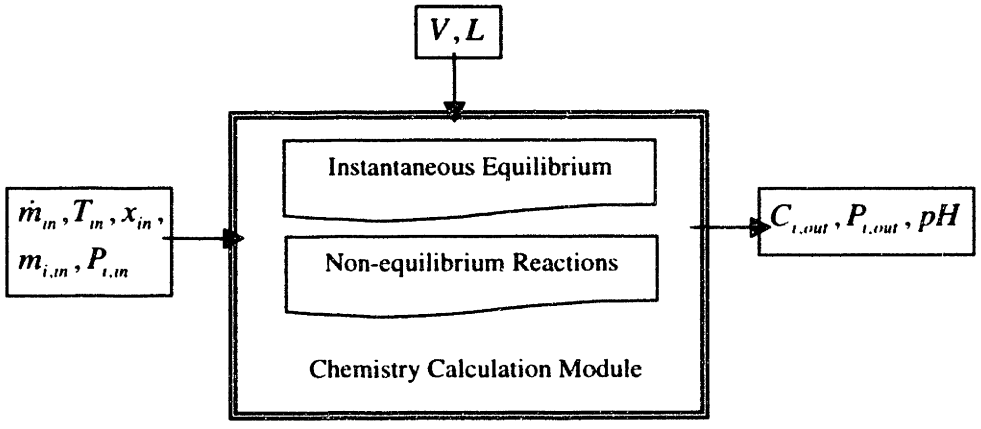

Figure 3-21. Chemistry Module information flow schematic.

3.3.4.1. Instantaneous Equilibrium

The Instantaneous Equilibrium calculation determines the balance of chemical species typically found in the secondary of a power plant. The calculation is considered instantaneous in that the time required to reach equilibrium is much quicker than that required for the fluid to pass through the component. The chemistry equilibrium calculation determines the partial pressure, P_i, and molality, m_i, of species i in components based on inlet conditions. These outlet values of partial pressure and molality are assumed to be the same for all outlets. Unlike the thermodynamic calculations, the determination of entering chemistry parameters based on exiting

parameters is not possible in the SPPDMME. This restriction is further explained in Section 3.3.5.

Two fundamental methods exist for solving chemical equilibrium problems:

a)Free energy minimization and

b)Direct solution of simultaneous chemical equilibria, mass balance equations, and a charge balance equation.

Because the latter of these two approaches is better suited for handling ion-ion interactions at higher temperatures (Cohen, 1989) and is more intuitive, the latter of these two approaches is used.

The Instantaneous Equilibrium calculation includes a charge balance, mole balances of all compounds present, the dissociation balance between the species, and the distribution of species between the vapor and liquid phases:

Charge Balance $$\sum_{i=1}^{N_{sp}} m_i \cdot Z_i = 0, \qquad \textbf{(Eq. 3-30)}$$

Compound Mass Balance $$\sum_{i=1}^{N_j} \left(n_i \cdot y_i^j\right) = \dot{N}_j, \qquad \textbf{(Eq. 3-31)}$$

Specie Dissociation $$\frac{m_{A^+} \cdot m_{B^-}}{m_{AB}} = K_{AB}(T), \qquad \textbf{(Eq. 3-32)}$$

Specie Distribution $$\frac{m_j}{P_j} = K_j^s(T), \qquad \textbf{(Eq. 3-33)}$$

where N_{sp} is the number species considered,

m_i is the molality of the specie i,

Z_i is the charge of specie i,

$K_i(T)$ is the temperature dependent dissociation coefficient of specie i,

N_j is the number of species in group j,

$\dot{n}_i$ is the entering total mole rate of specie *i*,

y_i^j is the number of compounds of type j in specie *i*,

$\dot{N}_j$ is the exiting total mole rate of group *j*,

$K_i^s(T)$ is the temperature dependent distribution coefficient for specie *i*,

P_i is the partial pressure of specie *i*.

Additionally, the entering flow rate of a specie *i* is given by:

$$\dot{n}_i = \frac{1}{R} \cdot \sum_{k=1}^{N_{in}} \left(P_{i,k} \cdot \frac{\dot{V}_k}{T_k} \right) + \sum_{k=1}^{N_{in}} (m_i \cdot \dot{m}_k), \qquad \textbf{(Eq. 3-34)}$$

and the exiting total mole rate of group j is given by:

$$\dot{N}_j = \sum_{k=1}^{N_j} \left(\frac{P_i}{R \cdot T_{out}} \cdot \sum_{k=1}^{N_{out}} \dot{V}_k + m_i \cdot \sum_{k=1}^{N_{out}} \dot{m}_k \right), \qquad \textbf{(Eq. 3-35)}$$

where

N_{in} and N_{out} are the number of component inlets and outlets, respectively,

$\dot{V}_k$ is the volume flow rate for exit k,

$\dot{m}_k$ is the mass flow rate for exit k, and

R is the gas constant.

The temperatures, mass flow rates, and volume flow rates in the above expressions are determined from thermodynamic calculations completed for the component. The effective volume of volatile species is assumed to be zero. In addition to specie concentrations and pressures, three pH values are computed:

hot pH $pH_{hot} = -\log(m_{H^+}(T))$ **(Eq. 3-36)**,

cold pH $pH_{cold} = -\log(m_{H^+}(25\,^{\circ}C))$ **(Eq. 3-37)**,and

neutral pH which is the hot pH assuming only water to be present. Hot pH is the value of the pH at the system temperature. Cold pH is the measured pH were the system cooled

to 25 C. For two phase flow, cold pH includes species and fluid mass from both the steam and water flows. Figure 3-22 summarizes the information flow for the Instantaneous Equilibrium equation set.

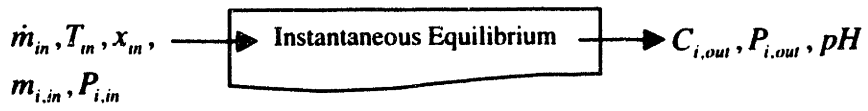

Figure 3-22. Instantaneous Equilibrium equation set information flow schematic

Table 3-3 lists the available species and equilibrium reactions considered. Appendix A.1 Equilibrium Chemistry Equations lists the full set of potential expressions included in the Instantaneous Equilibrium equation set. Appendix A.2 Equilibrium Chemistry Data lists the temperature dependent dissociation and distribution coefficients used for this equation set. For a particular calculation, not all the equations are used as not all species may be present. That is, within the Chemistry module, a check is made of which specie groups are present in the entering flow. This information is then used to determine the necessary subset of the equations to be solved. For any specie to be considered present the entering mole flow rate must be above a cutoff range (default set at 10^{-20} moles/sec). Note that the number of species in each group matches the number of necessitated equations to be solved so that the subset of equations remains properly constrained. Included in this entering specie subset are those specie groups that may be produced from the present specie groups either through reactions or decomposition. The potential of the production of a specie group is determined based on user (and default) input information that illustrates specie reactions and decompositions and their corresponding rates. (See section 3.3.4.2 Non-equilibrium Reactions for more detail on these reactions.)

Table 3-3. Species included in the Chemistry Module and the corresponding Instantaneous Equilibrium equation set.

Specie Group	Species	Equations Solved	Specie Group	Species	Equations Solved
Water	m_{H^+}, m_{OH^-}	CB[1],DS[2]	Morpholine	$m_{Morph}, P_{Morph}, m_{MorphH^+}$	MB[3], DT[4], DS
Ammonia	$m_{NH_3}, m_{NH_4^+}, P_{NH_3}$	MB, DT, DS	ETA	$m_{ETA}, P_{ETA}, m_{EtaH^+}$	MB, DT, DS
Carbonates	$P_{CO_2}, m_{CO_2}, m_{HCO_3^-}, m_{CO_3^{2-}}$	MB, DT, 2*DS	Hydrazine	$m_{N_2H_4}, P_{N_2H_4}, m_{N_2H_5^+}$	MB, DT, DS
Silicates	$m_{SiO_2}, m_{H_4SiO_4}, m_{H_3SiO_4^-}, m_{H_2SiO_4^{2-}}$	MB, DT, 2*DS	Ferrous Hydroxides	$m_{Fe^{2+}}, m_{FeOH^+}, m_{Fe(OH)_2}, m_{Fe(OH)_3^-}$	MB, 3*DS
Sulfuric Acid	$m_{H_2SO_4}, P_{H_2SO_4}, m_{HSO_4^-}, m_{SO_4^{2-}}$	MB, DT, 2*DS	Cupric Hydroxides	$m_{Cu^{2+}}, m_{CuOH^+}, m_{Cu(OH)_2}, m_{Cu(OH)_3^-}$	MB, 3*DS
Oxygen	P_{O_2}, m_{O_2}	MB, DT	Formic Acid	$m_{Form}, P_{Form}, m_{Form^-}$	MB, DT, DS
Nitrogen	P_{N_2}, m_{N_2}	MB, DT	Acetic Acid	$m_{Acet}, P_{Acet}, m_{Acet^-}$	MB, DT, DS
Hydrogen	P_{H_2}, m_{H_2}	MB, DT	Glycolic Acid	$m_{Glycol}, P_{Glycol}, m_{Glycol^-}$	MB, DT, DS

1- CB = Charge Balance
2- DS = Dissociation
3- MB = Mass Balance
4- DT = Distribution

Once the subset of reactions to be considered is determined, these non-linear expressions are solved numerically by first taking the natural logarithm of the chemical equilibrium equations such that the independent variables to be solved for are the natural logarithm of molalities and pressures. Numerically such an approach is more stable for computing variables which range over 20 orders of magnitude. These converted equilibrium expressions are then solved using a Newton-Raphson Method in which the Jacobian matrix is supplied explicitly.

The combination of these expressions may best be illustrated by example. If the program detects only ammonia species to be present, five simultaneous equations are solved. Note that water is always assumed to be present (except for Inleakage locations). For the default input, ammonia does not decompose (though it is a decomposition product) and does not react with other specie groups. Therefore, equilibrium concentrations are calculated from the dissolution and distribution of ammonia using the following set equations:

Charge Balance $$\sum_{i=1}^{N_{sp}} m_i \cdot Z_i = 0$$ **(Eq. 3-38),**

Water Dissociation $$m_{H^+}\, m_{OH^-} = K_{H_2O}(T)$$ **(Eq. 3-39),**

Ammonia Group Mass Balance $$\sum_{i=1}^{N_{NH_3}} \left(\dot{n}_i \cdot y_i^{NH_3} \right) = \dot{N}_{NH_3}$$ **(Eq. 3-40),**

Ammonia Dissociation $$\frac{m_{NH_4^+}\, m_{OH^-}}{m_{NH_3}} = K_{NH_3}(T)$$ **(Eq. 3-41),**and

Ammonia Distribution $$\frac{m_{NH_3}}{P_{NH_3}} = K^s_{NH_3}(T)$$ **(Eq. 3-42).**

The five unknowns that are solved by these equations are those shown in the Appendix A.1 corresponding to each of these equations, m_{H^+}, m_{OH^-}, m_{NH3}, m_{NH4^+}, and , P_{NH3}. Regardless of whether the flow was liquid, liquid/vapor, or vapor, the same set of equations would be solved. Because of the nature of the exit mass balance expression, **Eq. 3-35**, the computed exit mole rates of gaseous species in liquid flow will be zero as $\dot{V}_L$ is zero. By similar argument, the computed exit mole rates of aqueous species will be

zero as $\dot{m}_L$ is zero. Data listed in Appendix A.2 is interpolated to determine $K_{NH_3}(T)$ and $K^s_{NH_3}(T)$.

To illustrate the method used to input or view chemistry data, windows from the GUI, part of the VB code that is the final form of the SPPDMME, are shown. Figure 3-23 illustrates the window that pops up when the user selects to either view or input chemistry information. This form lists the potential specie groups for which the user can input and/or view information. Each group is positioned next to a checkbox. These specie groups correspond to those in Table 3-3. For specie groups that have been determined to be present and calculated for this physical location, the checkbox is selected but deactivated as is true for the "Water" checkbox in the window (note that water is always considered to be present, except for In-leakage connections). Specie groups with a deactivated, selected checkbox will automatically be viewed in the next window. For specie groups activated and for which the user would like to input concentration and partial pressure information, the user can select the associated checkbox. In the case shown in the figure, the "Ammonia" specie group has been selected and the species in this group will be available for the user to input chemistry information in the next window. After checking the desired boxes the user proceeds to the next window by selecting "Input".

Upon selecting "Input", the window in Figure 3-24 pops up on the screen. The user can input concentration and partial pressure information in the textboxes provided. The textboxes provided result from the selections in the previous window. For the species already calculated, the user can view but cannot change the chemistry information. In addition to concentration and partial pressure information this window lists the three pHs

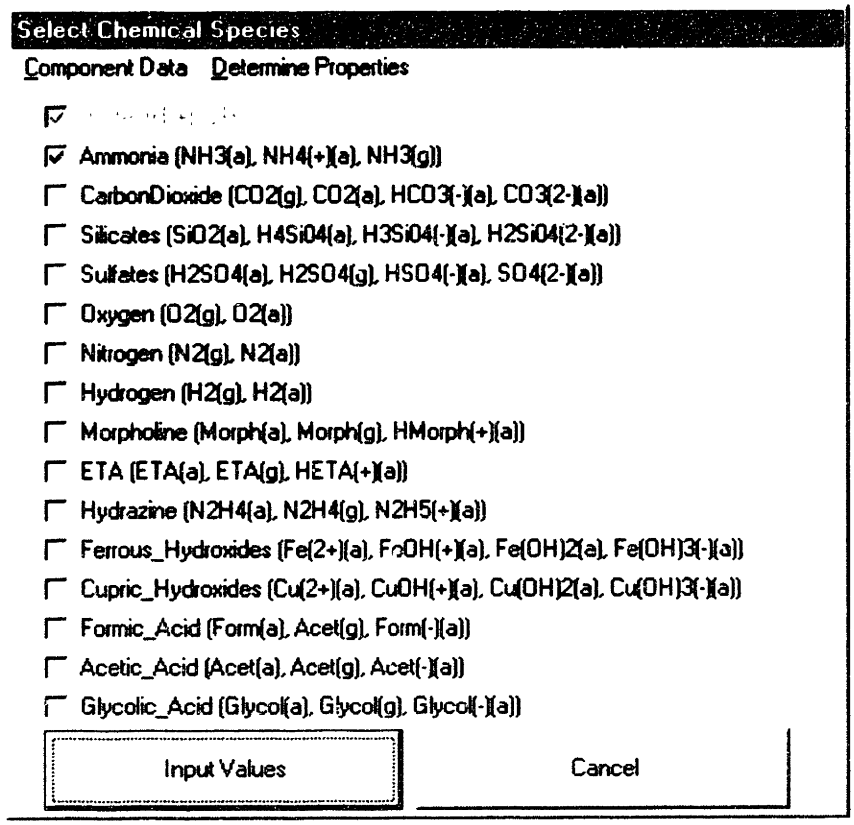

Figure 3-23. User interface for selecting which specie groups to input or display chemistry information.

calculated by the Instantaneous Equilibrium equation set and relevant thermodynamic information computed at this location. Again, note that the calculated information is color coded. Furthermore, neutral pH matches the hot pH, because chemistry information has been not yet been calculated for this location (as indicated by the lack of deactivated checkboxes in the previous window).

3.3.4.2. Non-equilibrium Reactions

Non-equilibrium chemical species are those which undergo reactions at rates which are on the order of the transport rates of the species through the plant. Of the species modeled in the Chemistry module, two amines (morpholine, and ethanolamine (ETA), hydrazine, and oxygen are involved in non-equilibrium reactions. These reactions

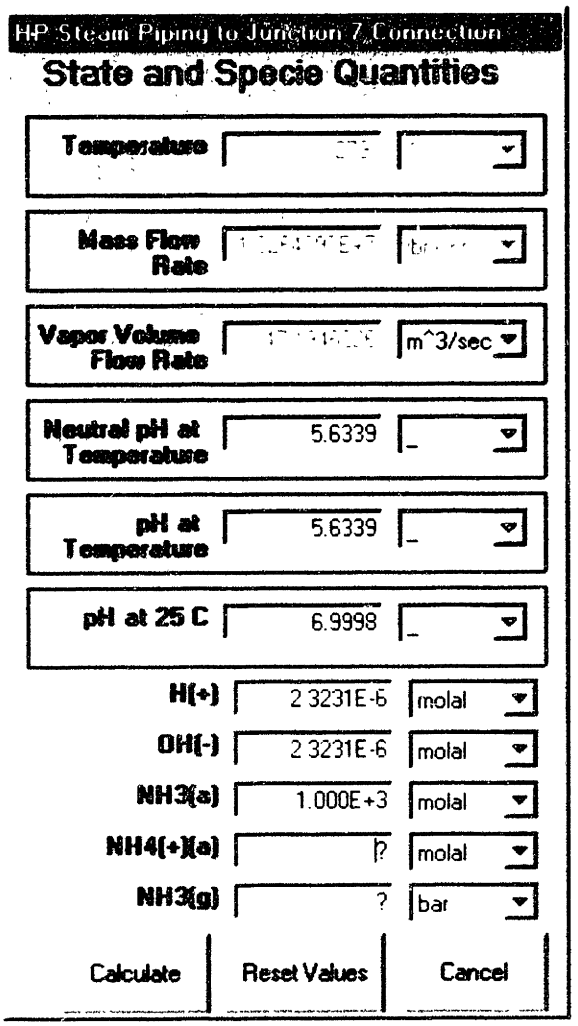

Figure 3-24. User interface for viewing and inputting chemistry information.

include amine decomposition, hydrazine decomposition, and hydrazine reaction with oxygen. The Chemistry module includes default parameters for each of these reactions. Because this calculation involves time dependent reactions, the volume of water in a component module section, V, or length of a Piping System, L, must be provided to solve the set of equations. These size values allow the determination of the time that the flow spends in a section, i.e. the residence time, t_{Res}. Figure 3-25 illustrates the resulting information flow schematic for this equation set.

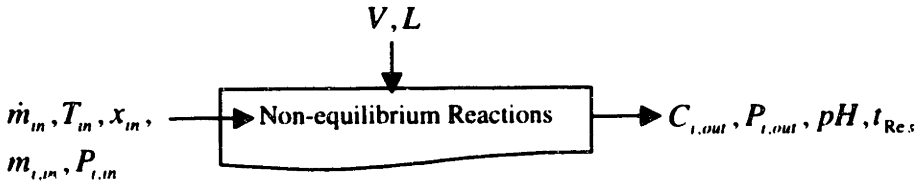

Figure 3-25. Non-equilibrium Reaction equation set information flow schematic.

Depending on the available literature data for a particular specie, the Chemistry module can interpret user input on specific reactions of a specie or an overall removal rate of a specie to determine a specie's reaction rates. In the first case, a number of reactions may be taking place simultaneously for a particular specie:

$$\frac{dC_i}{dt} = \sum_{n=1}^{N_{rxn}} k_n' \qquad \textbf{(Eq. 3-43)},$$

where

C_i is the reacting specie, i, concentration [ppb],

dt is the time increment for the reaction [sec],

k_n' is the reaction of type n for specie i [ppb/sec] and,

N_{rxn} is the number of reactions for specie i.

Each reaction is modeled as the product of the Arrhenius relation and the concentration of the species present with their corresponding orders as they affect the reaction rate,

$$k_n' = A_n \cdot \exp\left(\frac{-E_n}{R \cdot T}\right) \cdot \prod_{j=1}^{N_n} C_j^{a_j} \qquad \textbf{(Eq. 3-44)}$$

where

A_n is the probability factor of reaction, n $\left[\frac{ppb\wedge\left[\prod_{j=1}^{N_n} a_j\right]-1}{\sec}\right]$,

E_n is the activation energy of reaction, n [J/mole],

N_n is the number of reactants in reaction, n,

C_j is the concentration of reactant, j, [ppb], and

a_j is the order of reaction with respect to reactant j.

A particular reaction n may produce a number of products p. To determine the production rate of each product p of a reaction, the reaction rate for that reaction, k_n',is multiplied by the mole ratio of product p over reacting specie i in the balanced reaction, n.

This combination of reactions assumes that enough information is known about the individual reactions involved in reducing the concentration of specie i. However, if reaction rate information is limited, the Chemistry module can still determine removal and production rates for species. Input of an overall removal rate of a specie i and the type and corresponding percentage of products is sufficient information. In this case, the removal of a specie i is determined by **Eq. 3-43** for which the number of reactions, N_{rxn}, is one. The production rate of products is the product of this rate and the aforementioned input of percentages for each product. Thus, one can model specie loss and gain when exact knowledge of the reactions steps and types is not known.

Default parameters for the above two methods are based on literature data. For the reactions incorporated in the SPPDMME as default input, listed in Appendix B Non-Equilibrium Reaction Data, the default data for the reactions is also listed in Appendix B. Users may change these parameters or include additional reactions relevant to their particular problem. In a single time step, the Chemistry module logic limits the reduction of any specie in a reaction where the reaction rate is dependent on the concentration of that specie to 10% of its value. If a calculated concentration reduction exceeds 10% the time step is reduced. If the time step drops below a user specified lower limit (typically a fraction of a second), then the module logic allows a greater percentage in reduction in a single time step limited only by the amounts of reactant(s) available. At each time step,

the amount of species reacted and produced is added to their respective specie group masses. Before the reaction rate at the next time step is calculated, a new equilibrium value of molalities and partial pressures is determined by the equation set described in section 3.3.4.1 Instantaneous Equilibrium.

3.3.5. Material Degradation Rate

The Material Degradation Rate calculates the wear rate that would be occurring at the location where parameters are known due two phenomena: FAC and droplet impingement. For the other two FIMD phenomena, cavitation and abrasion corrosion, no models predicting wear were identified in the literature. Except in specific cases these two phenomena are not expected to be major contributors to wear. Figure 3-26 summarizes the information flow for this module. The symbols in the figure represent parameters defined in the locations were the two phenomena are described.

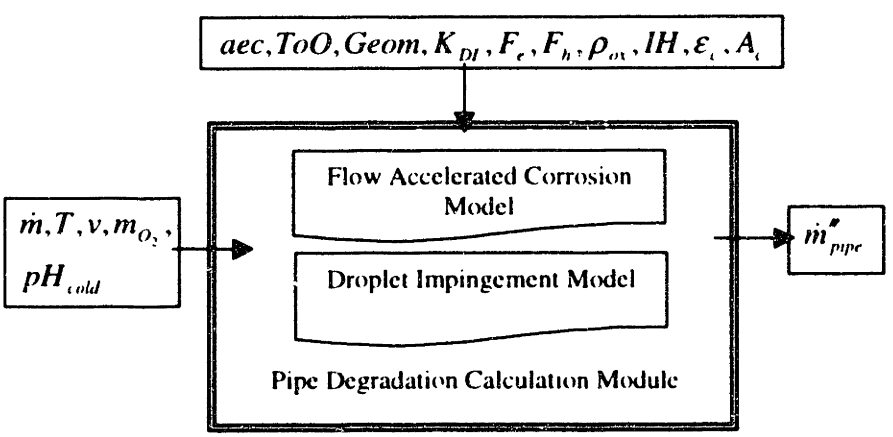

Figure 3-26. Material Degradation Rate module information flow schematic.

3.3.5.1. Flow Accelerated Corrosion

The FAC equation set is a new model developed for this thesis. The new FAC model is described in Chapter 5. Because the new model uses input parameters similar to

those described in Chapter 2, the focus of this discussion is on the specific window of the GUI developed for this equation set. In this window, the user inputs the additional information not calculated by modules previously described. Figure 3-27 illustrates the information flow for the FAC equation set. As shown in this figure the remaining information to be input is the alloying element content, *aec* , the time of operation for the component module section, *ToO* , and the geometry of piping section or tube, *Geom* .

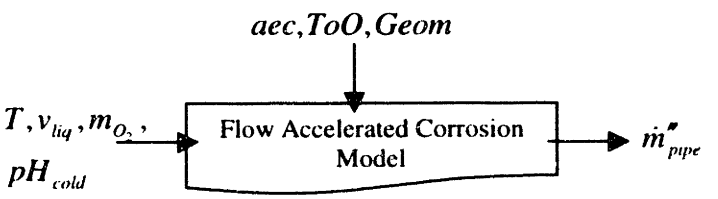

Figure 3-27. FAC equation set information flow schematic.

Figure 3-28 illustrates the window used to input this additional information. Note that other relevant information to the FAC model is also listed on the form but is deactivated (gray not black) and thus not available for user modification. The user may, however, change units of the displayed values as desired. Note also that for the example shown in the figure the oxygen concentration has not been calculated and is therefore represented with a '?'.

3.3.5.2. Droplet Impingement

The droplet impingement model used within the Pipe Degradation module is described in Chapter 2. Figure 3-29 puts this model in terms of the information flow discussion of this chapter. Appendix C. Droplet Impingement Default Data lists the values used for the parameters of this expression based on Keck's work (Keck, 1987).

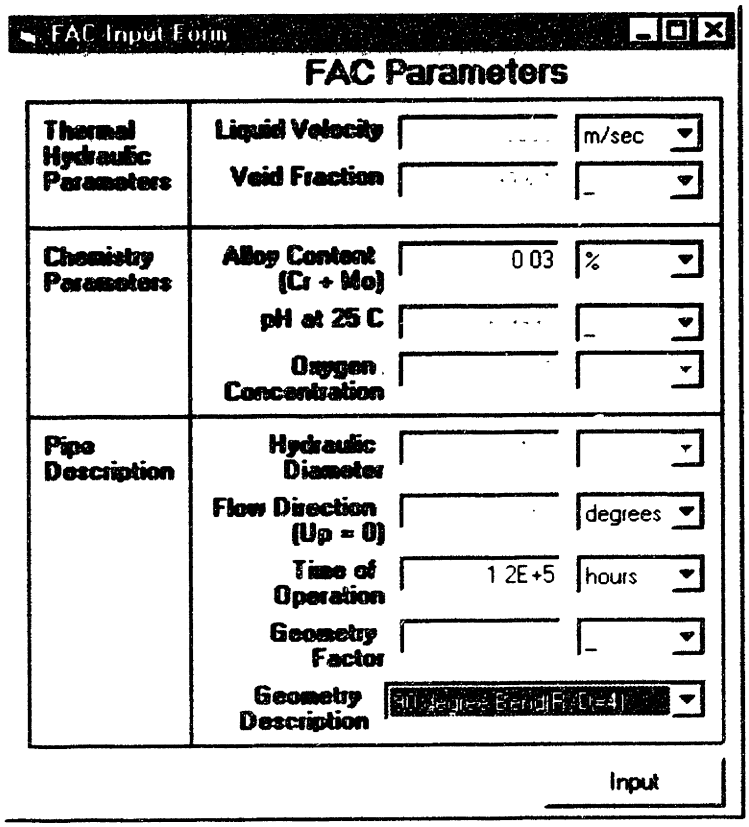

Figure 3-28. User interface for inputting FAC information.

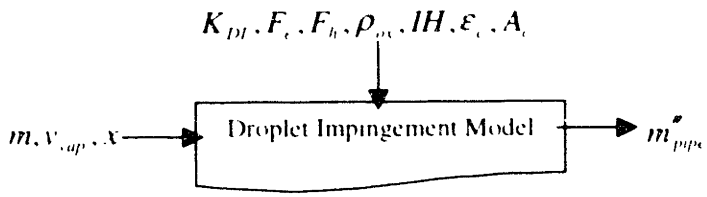

Figure 3-29. Droplet Impingement information flow schematic.

3.3.6. SPPDMME Calculation Logic

The calculation logic of the SPPDMME controls the order in which information transfers to component modules and the order in which calculation modules are called by these component modules. The logic must meet two competing constraints:

1. Propagate input (or removed) information to all parameters that that action affects, and
2. Limit the response time of environment in calculating affected parameters for an unlimited combinations of potential user actions

Meeting the first constraint might result in logic that performs redundant checks to determine whether parameters are affected by user changes. The second constraint might result in insufficient checks to determine affected parameters. This problem is partially solved by making all parameters 'situation aware'. 'Situation aware' means that each parameter contains information (in addition to its actual value) on the component modules, calculation modules, and input parameters by which this particular parameter has been or could be affected. The remaining part of the problem is solved by the calculation logic.

Using the information flow discussion and schematics provided above, this calculation logic can be explained in terms of its sequential and propagated aspects. As mentioned previously, the sequential aspects are straightforward. For the application in this thesis, the sequential calculation at a single location can be discussed in terms of the modules just discussed and illustrated in Figure 3-1. The thermodynamic module determines state variables and flow rates. The thermal hydraulic module determines phase velocities. The chemistry module determines pH and oxygen concentration. Finally, the degradation rate module determines the local wear rate based on the local conditions as determined by the results of the three previous modules.

As shown in the information flow schematics, only two of the four calculation modules, the Thermodynamic module and Chemistry module, calculate information at adjacent locations, and are therefore affected by the propagation aspects of the calculation logic. These schematics show that the Thermodynamic module can propagate calculations with or against the fluid flow (i.e. determine outlet conditions based on inlet conditions or outlet conditions based on inlet conditions). The Chemistry module can

propagate calculations only in the direction of flow. The physical reason for this restriction is that a single specie exiting a component module could be the product of a number of reactions. Because the specie contains no history information, it is impossible to determine its source and therefore impossible to determine the inlet amounts of the species based on the outlet amount of species.

Because the Chemistry module only propagates information in the direction of the flow and because of the typical values involved in the calculation, a problem of slow convergence arises. This slow convergence can be shown by a simple example illustrated in Figure 3-30. The figure illustrates a fluid flow system with a typical addition mechanism of a specie, injection, and a removal mechanism, leakage. Note that leakage embodies a common trait of removal mechanisms, the removal rate is proportional to the concentration of the specie in the flow. For the purpose of this discussion, let's assume

1. The user inputs information on the concentration of a species at the injection location, m_{inj},
2. In calculating the concentration of the specie of the system, m_{sys}, the Chemistry module propagation begins at location **A**,
3. The initial concentration of the specie in the system is 0, $m_{A0} = m_{C0} = 0$, and
4. The Thermodynamic module has propagated mass flow rate information such that, $\dot{m}_{inj} = \dot{m}_{leak}$.

For the propagation beginning at **A**, the concentration at **A** is $m_{A1} = 0$, and, traveling in the direction of the flow, the concentration at **C** is

$$m_{C1} = \frac{m_{inj} \cdot \dot{m}_{inj}}{\dot{m}_{inj} + \dot{m}_{sys}} \qquad \textbf{(Eq. 3-45).}$$

The leakage at **D** does not affect the concentration of the specie at **A** so that $m_{A,2} = m_{C,1}$. Were this new value at **A**, $m_{A,2}$, used as an estimate of the system specie concentration for the next iteration around the loop, one can see that a similar increment in the estimate of the concentration at **A** would be computed. A mass balance on the system shows that the actual specie concentration for the system is $m_{sys} = m_{inj}$. The increment in the estimate of this system concentration, however, is $\frac{m_{inj} \cdot \dot{m}_{inj}}{\dot{m}_{inj} + \dot{m}_{sys}}$, a small fraction of the actual solution, m_{inj}. Selecting a typical ratio of injection flow rate to system flow rate for a secondary system one can estimate this fraction to be 10^{-6}, resulting in an expected number of iterations necessitated to determine the system specie concentration of 10^6. Such convergence is extremely slow. When one considers, that the SPPDMME is designed to model 49 species and much more complicated flow systems, such a method is prohibitive.

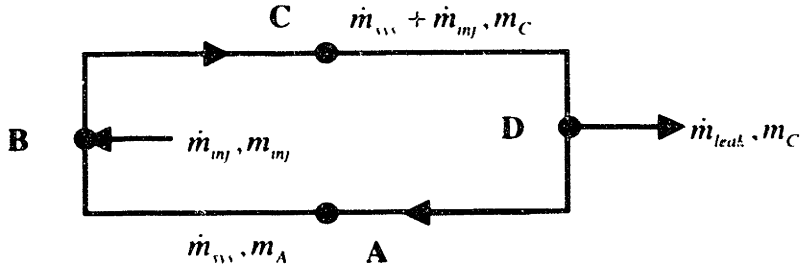

Figure 3-30. Schematic showing the potentially slow convergence of the Chemistry module.

This problem is solved by making a new estimate of the loop concentration for each loop iteration. The new estimate is based on the characteristics of the flow loop. A flow loop with n species is treated as a nonlinear system of n equations. Two common approaches for solving nonlinear systems of equations are included in the Chemistry

module. The first, the Newton method, uses the local convergence advantages of the Newton method with a global convergent strategy (Press, *et, al.*, 1995). The second, the Broyden method, is a multidimensional secant method (Press, *et, al.*, 1995). The user may select between these two methods, depending on which is the quickest. A general rule of thumb is: use the Newton method for more complicated flow systems with fewer species; use the Broyden method for simpler flow systems with numerous species.

The longer response time of the Chemistry module affects the propagation aspects of the calculation logic. To minimize the response time of the SPPDMME, all thermodynamic information is propagated throughout the modeled system first. Then the chemistry information is propagated throughout the system using the numerical routine selected by the user. Furthermore, the user can suspend the automated propagation of chemistry information that occurs after each user input. After a set of information has been input, the user can then restore chemistry information propagation.

3.4. Conclusions/Summary

As mentioned previously, the final form of this SPPDMME is a code programmed in the Visual Basic® (VB) programming language, the Secondary Plant Pipe Degradation Program (SPPDP). The database with which the program interfaces is a structure programmed in Microsoft Access®. The method of communicating with the database from VB is the Structured Query Language (SQL).

Because VB is based on the concept of Object Oriented Programming (OOP), the development of coded objects that have properties and react to events, it affords the necessary characteristics for coding the SPPDMME. Because of the method in which the

code is compiled, additional modules can de developed that will be compatible with earlier versions of the code. Furthermore, users can develop their own modules to use in the program provided they maintain the same interface structure (which can be done with copy and paste of the old structure).

Interfacing the SPPDP with Access® allows the user to save the information from a session including plant design, input parameters, and calculated parameters and close the session. By reopening the SPPDP, the user can open any previously saved sessions from Access®. In fact, the user can open a number of different sessions if so desired. The use of SQL ensures that the communication when saving information and retrieving information from the database is quick. In terms of future work, Access® is important in that it is a format that can be easily and quickly used by statistical models developed to determine degradation rates and degradation rate uncertainty.

As a synopsis of its capabilities, SPPDP performs the necessary calculations to determine, thermodynamic, thermal-hydraulic, chemistry, and pipe degradation parameters. The program is designed to do these calculations for plant descriptions of increasing complexity (as the user inputs more information, or breaks down systems into subsystems) while providing feedback to the user. The program performs calculations quickly, minimizes memory allocation, saves and retrieves information quickly from the database, and provides feedback to the user on input and needed information. The program is versatile, allowing a single component to model numerous parallel components (for all components) or numerous series components (for piping systems). The program can also handle minimal or an extreme amount of detail depending on the needs of the user. In essence, the program meets the requirements of the Secondary Plant

Pipe Degradation Modular Modeling Environment, the ideas upon which it is based. Chapter 4 provides various checks on some of the specific equation sets of the program. Chapter 5 focuses on the new FAC model used in the Pipe Degradation calculation module. Chapter 6 uses the program to predict pipe wear information for an example system for which there exists sufficient data to check the results.

Chapter 4. Secondary Plant Pipe Degradation Program Validation

For specific cases, calculations from the Secondary Plant Pipe Degradation Program (SPPDP), the program developed based on the Secondary Power Plant Degradation Modular Modeling Environment (SPPDMME), were compared to results from other codes to verify the accuracy of the SPPDP. This chapter details the results of these verifications for the first three of the four major calculations performed by the SPPDP. Chapter 5 describes the model used for the fourth calculation, degradation rate. Chapter 6 provides calculation results showing the accuracy of the SPPDP in modeling a PWR secondary system, specifically the Kori Unit 3 secondary system, and predicting degradation rate.

4.1. Thermodynamics

One important aspect of the SPPDP is that the underlying thermodynamic models in the SPPDP which balance mass flow rate, pressures, and enthalpies are straightforward to check component by component. This allows in-depth checks of the feedwater heater, reheater, and turbine components that combine heat transfer among numerous flows with thermodynamic balances, thereby ensuring calculation accuracy. Because of the nature of the SPPDP calculations to constantly update calculable information based on user input, the author not only determined that calculations were accurate but that they were not affected by what set of information the user inputs or what order the user inputs this information. Such consistency checks in the SPPDP are unique to this approach and ensure consistency of data input since calculable information is constantly readjusted.

Finally, results from simple secondary systems found in thermodynamic texts were compared to SPPDP calculations and showed good agreement (Cohen, 1989; Todreas and Kazimi, 1993; Howell and Buckius, 1992).

4.2. Thermal Hydraulics

The essential parameters used in the thermal hydraulic calculations that affect the degradation rate are the liquid velocity used for estimating FAC wear and the vapor velocity used for droplet impingement wear.

4.2.1. Single Phase Calculation

For most cases of single phase flow[5], the velocity is a straight forward relationship involving mass flow rate, water density, and hydraulic diameter (see section 3.3.3.1). Mass flow rate is well characterized as it is a measured value that is either input or computed from a mass balance calculation. Therefore, as long as the hydraulic diameter input into the SPPDP is the inside diameter of the pipe then the single phase velocities will be accurate.

4.2.2. Two Phase Calculation

As outlined in section 3.3.3.2, the Chexal-Lellouche void fraction model is the central calculation of the thermal hydraulics model for two phase flow (Chexal *et. al.*, 1991). This model determines void fraction based on the superficial liquid and vapor

[5] Some investigators have indicated that drain line flow lines in which one may expect single phase based on bulk thermal hydraulic conditions actually contains two phase flow

velocity. In order to verify that these calculations are properly incorporated into the SPPDP, SPPDP output of void fraction is compared to tabulated data for cases presented for the Chexal-Lellouche correlation (Chexal *et. al.*, 1991). Table 4-1 shows the values as calculated by the SPPDP and the results presented in the Chexal-Lellouche report. Slight differences in results are suspected to be caused by the fact that the incorporated correlation in the code is a more recent version than that in the report.

Table 4-1. Comparison of void fraction calculations for code incorporated into the SPPDP and results reported on the Chexal-Lellouche model for different pressures, hydraulic diameters and pipe orientations.

Case #	Pressure [bar]	Hydraulic Diameter [m]	Superficial fluid velocity [m/sec]	Superficial gas velocity [m/sec]	Angle with respect to vertical [deg]	Void Fraction SPPDP (Chexal et. al., 1991)
1	**68.95**	**.3048**	**1.524**	**3.048**	**0**	**0.590 (0.592)**
2	**68.95**	**.0152**	**1.524**	**3.048**	**0**	**0.587 (0.595)**
3	**68.95**	**.3048**	**1.524**	**3.048**	**0**	**0.530 (0.532)**
4	**68.95**	**.0152**	**1.524**	**3.048**	**0**	**0.502 (0.536)**
5	**1.01325**	**.3048**	**1.524**	**3.048**	**90**	**0.465 (0.460)**
6	**1.01325**	**.0152**	**1.524**	**3.048**	**90**	**0.464 (0.464)**
7	**1.01325**	**.3048**	**1.524**	**3.048**	**90**	**0.411 (0.393)**
8	**1.01325**	**.0152**	**1.524**	**3.048**	**90**	**0.401 (0.395)**

4.3. Chemistry

To demonstrate the accuracy of the Instantaneous Equilibrium Calculation (IEC) of the SPPDP, calculations were compared to an industry model produced by EPRI and incorporated into the MULTEQ code. Because pH is a major chemistry parameter affecting FAC, pH values were the outputs compared for the two models. Comparisons

---

with a corresponding increase in liquid velocity for pipes that are not "full" (Chandra, et. al., 1994).

were made for three amines (the pH control agent) modeled in the SPPDP, ammonia (NH_3), morpholine (C_4H_9NO), and ethanolamine (ETA, C_2H_7NO) for a range of temperatures, water quality, and amine, carbon dioxide, and hydrazine concentrations. Though both codes can compute equilibrium for the additions of numerous species, the amines plotted are those most commonly used in secondary plant chemistry. The addition of the bicarbonate ion, HCO_3, (lowering pH) and the hydrazine, N_2H_4, (increasing pH) were chosen as examples of common substances found in secondary plant chemistry. The range of concentrations plotted for these two additives is not necessarily indicative of what one would find in a typical PWR secondary system.

Figure 4-1. shows IEC and MULTEQ calculated pH values for a range of concentrations of added ammonia and bicarbonate ion for the temperatures a)25 °C b)150 °C and c)250 °C. For the same temperatures, Figure 4-2 shows the computed pH values for a range of ammonia and hydrazine concentrations. Figure 4-3 through Figure 4-6 show similar pH calculations for morpholine and ETA. Table 4-2 shows the error for each graph shown in these figures. It can be seen that agreement is on the order of 0.2% for each of these values. The major contributor to the differences calculated is disagreement in the reported dissociation products for the species modeled. That is, for some cases, the dissociation products used in the MULTEQ code could be guessed based on literature information (Cobble and Turner, 1992). In these cases, using this data in the IEC resulted in differences from the MULTEQ code on the order of the accuracy expected for the solution method used (see section 3.3.4.1 for information on the method). In general, error increases for substances that are less common and for which

there exists disagreement in data and at higher temperatures, where conditions for determining accurate data is more difficult.

Table 4-2. Percent difference in calculated pH using MULTEQ and IEC for Figure 4-1. through Figure 4-6.

	Ammonia		Morpholine		ETA	
Species added:	HCO3+	N2H4	HCO3+	N2H4	HCO3+	N2H4
Single Phase, T=50 °C	**0.09**	**0.09**	**0.12**	**0.14**	**0.17**	**0.14**
Single Phase, T=150 °C	**0.17**	**0.18**	**0.12**	**0.14**	**0.24**	**0.22**
Single Phase, T=250 °C	**0.16**	**0.14**	**0.05**	**0.07**	**0.61**	**0.45**

For the same 3 amines, pH was calculated for water quality of 0.206, 0.499, and 0.900. Comparison of MULTEQ and IEC calculations are plotted in Figure 4-7 through Figure 4-9. From these plots, two phase chemistry calculations can be seen to be not as accurate as single phase chemistry calculations. Furthermore, for calculations with noticeable differences, such as the morpholine plots, the difference increases as the quality increases. This trend implies that the major contributor to error is differences in reported data on the distribution of these substances between the gas and liquid phases. Table 4-1 summarizes the errors for the two phase pH results.

Table 4-3. Percent difference in pH calculated using MULTEQ and IEC for Figure 4-7. through Figure 4-9. shown above.

	Ammonia	Morpholine	ETA
Two Phase, Quality =0.206	**0.08**	**0.18**	**0.43**
Two Phase, Quality =0.499	**0.06**	**0.53**	**0.32**
Two Phase, Quality =0.900	**0.07**	**1.20**	**0.30**

Because comparisons between both single phase and two phase calculations result in differences that are caused by the data and not calculation methodology, further comparisons involving more species but using the same methodology can be expected to yield results which vary only by input data differences. It should be noted that users of

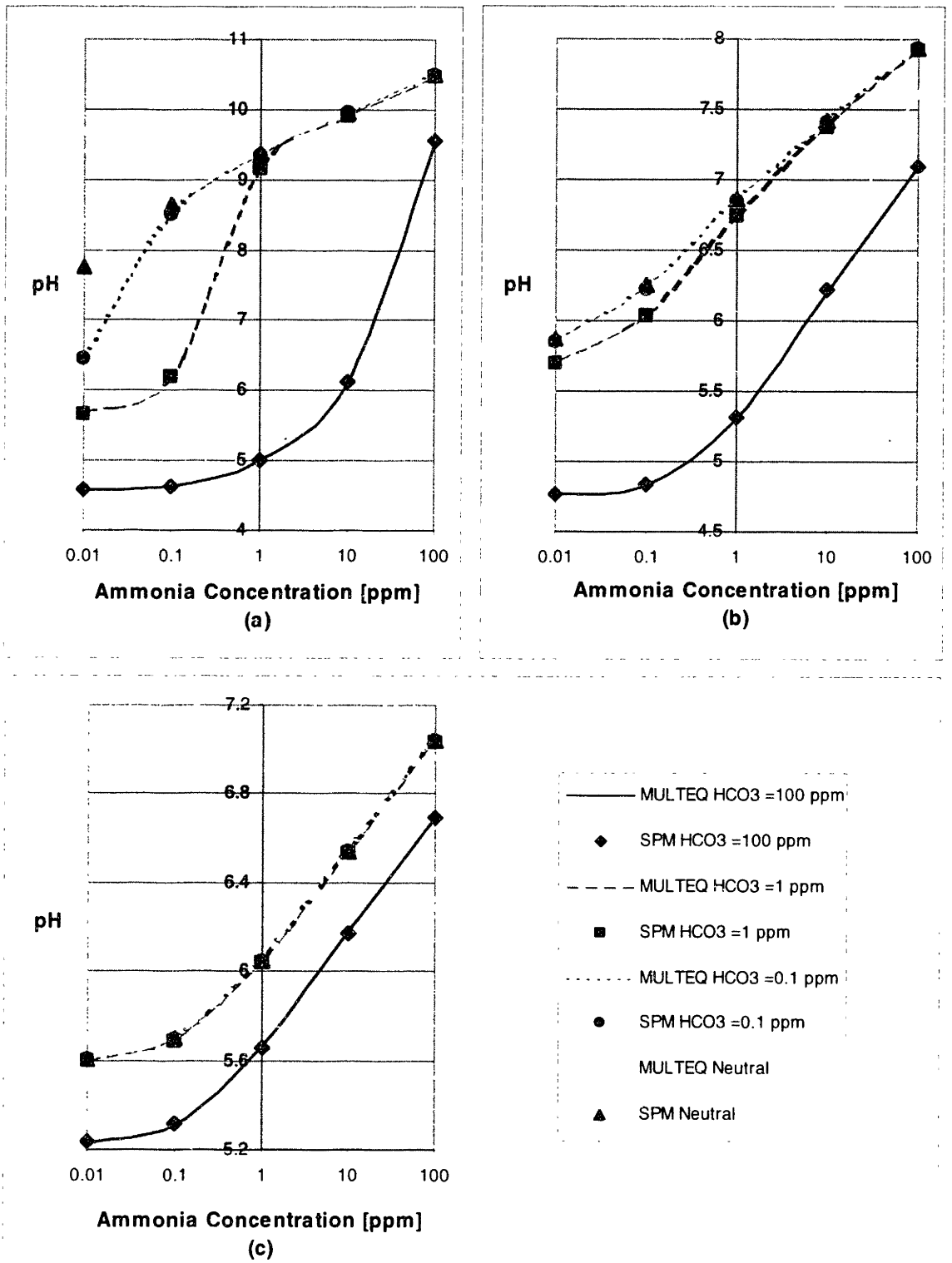

Figure 4-1. Comparison of single phase pH calculations between IEC and MULTEQ for ammonia with an acid (HCO3+) added at a) 50 °C, b) 150 °C, and c) 250 °C.

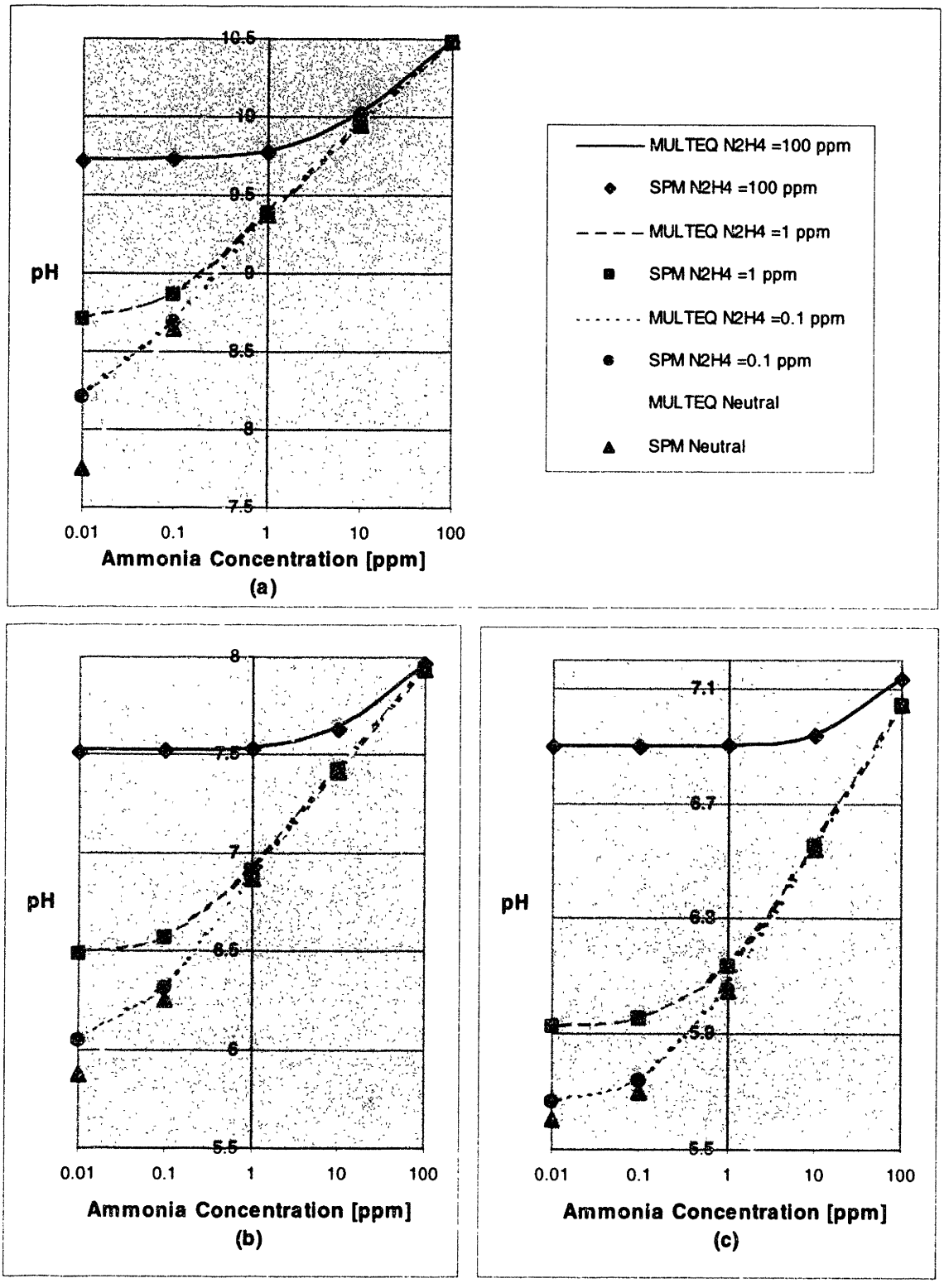

Figure 4-2. Comparison of single phase pH calculations between IEC and MULTEQ for ammonia with a base (N2H4) added at a) 50 °C, b) 150 °C, and c) 250 °C.

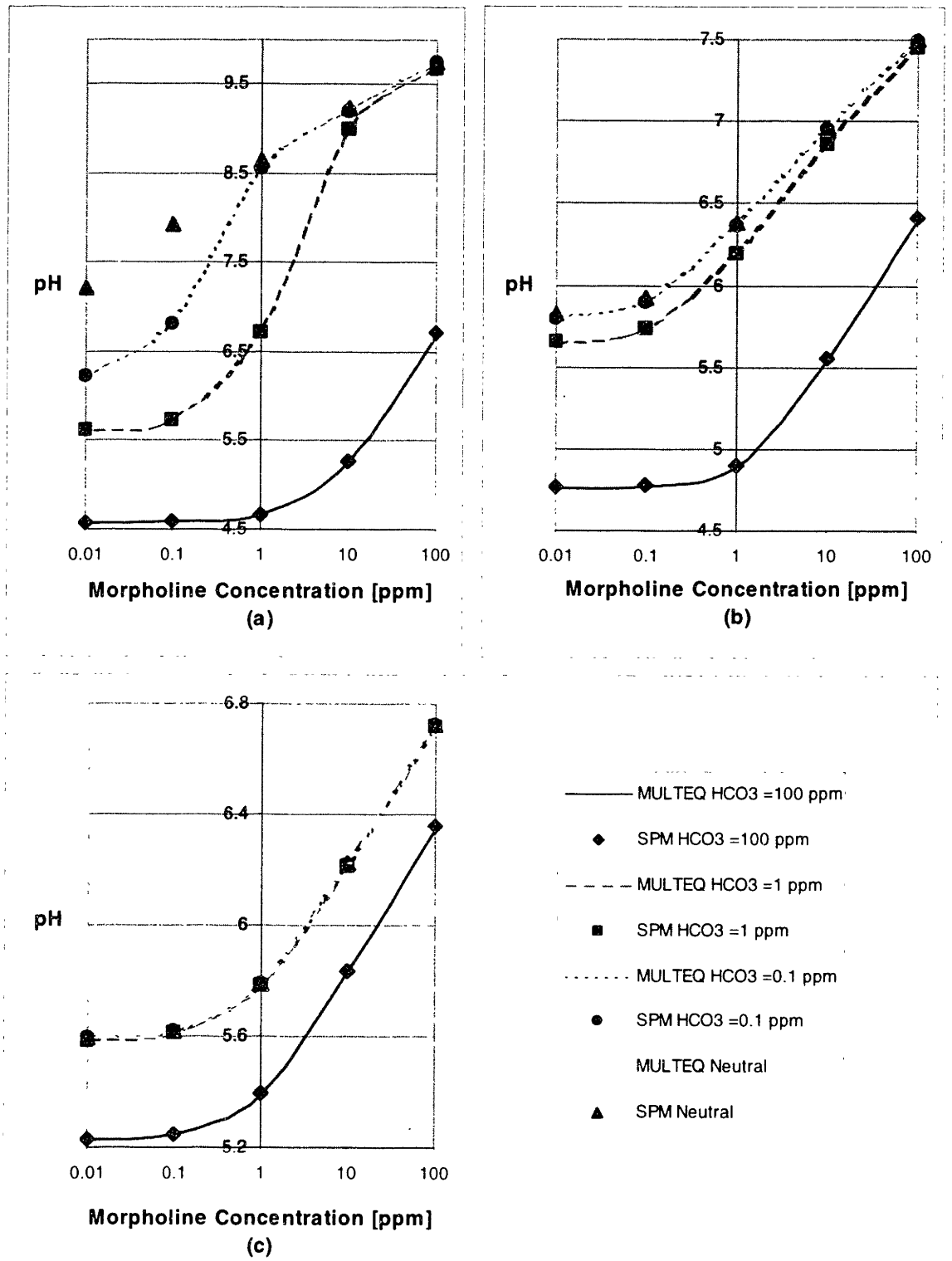

Figure 4-3. Comparison of single phase pH calculations between IEC and MULTEQ for morpholine with an acid (HCO3+) added at a) 50 °C, b) 150 °C, and c) 250 °C.

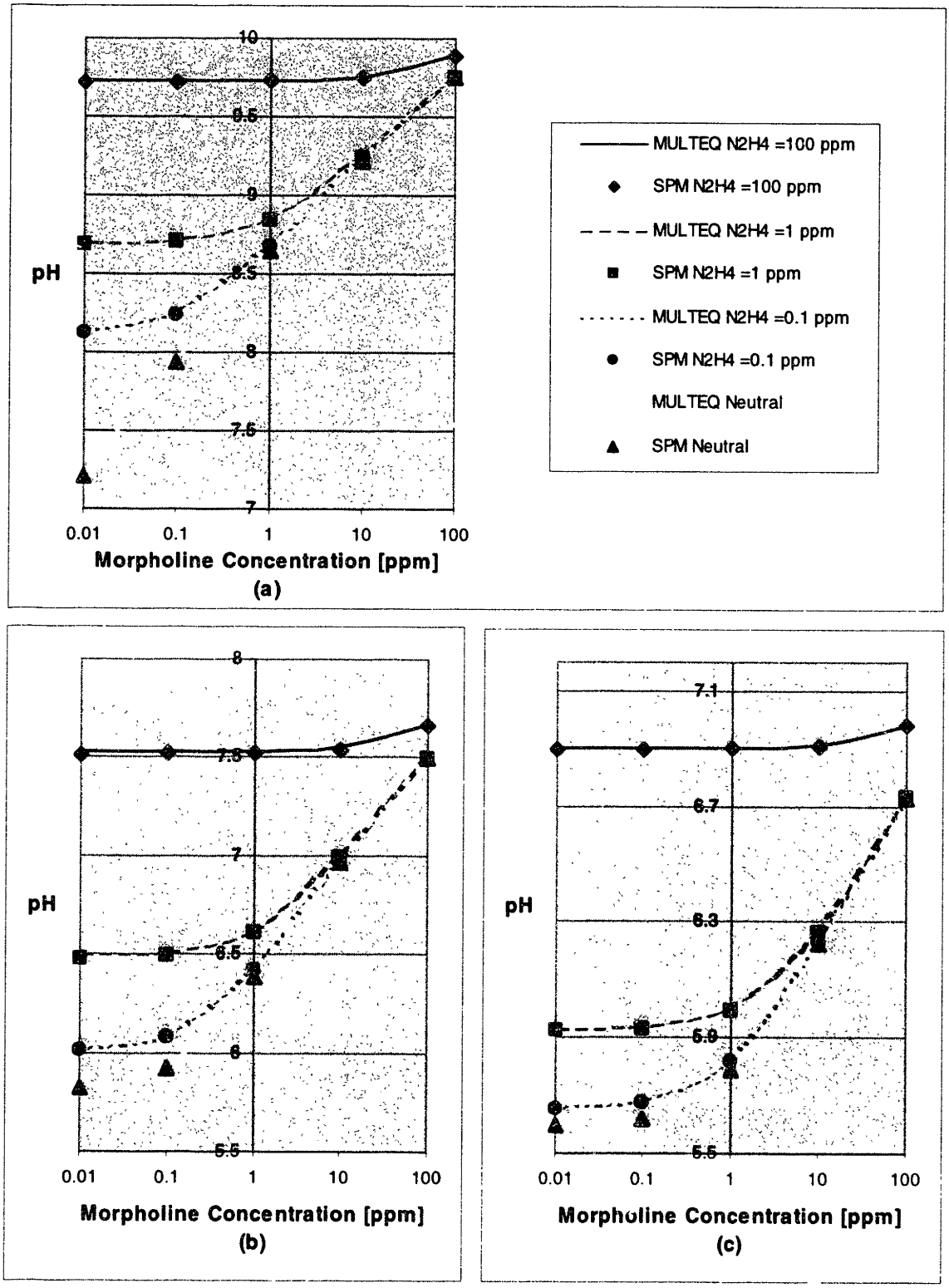

Figure 4-4. Comparison of single phase pH calculations between IEC and MULTEQ for morpholine with a base (N2H4) added at a) 50 °C, b) 150 °C, and c) 250 °C.

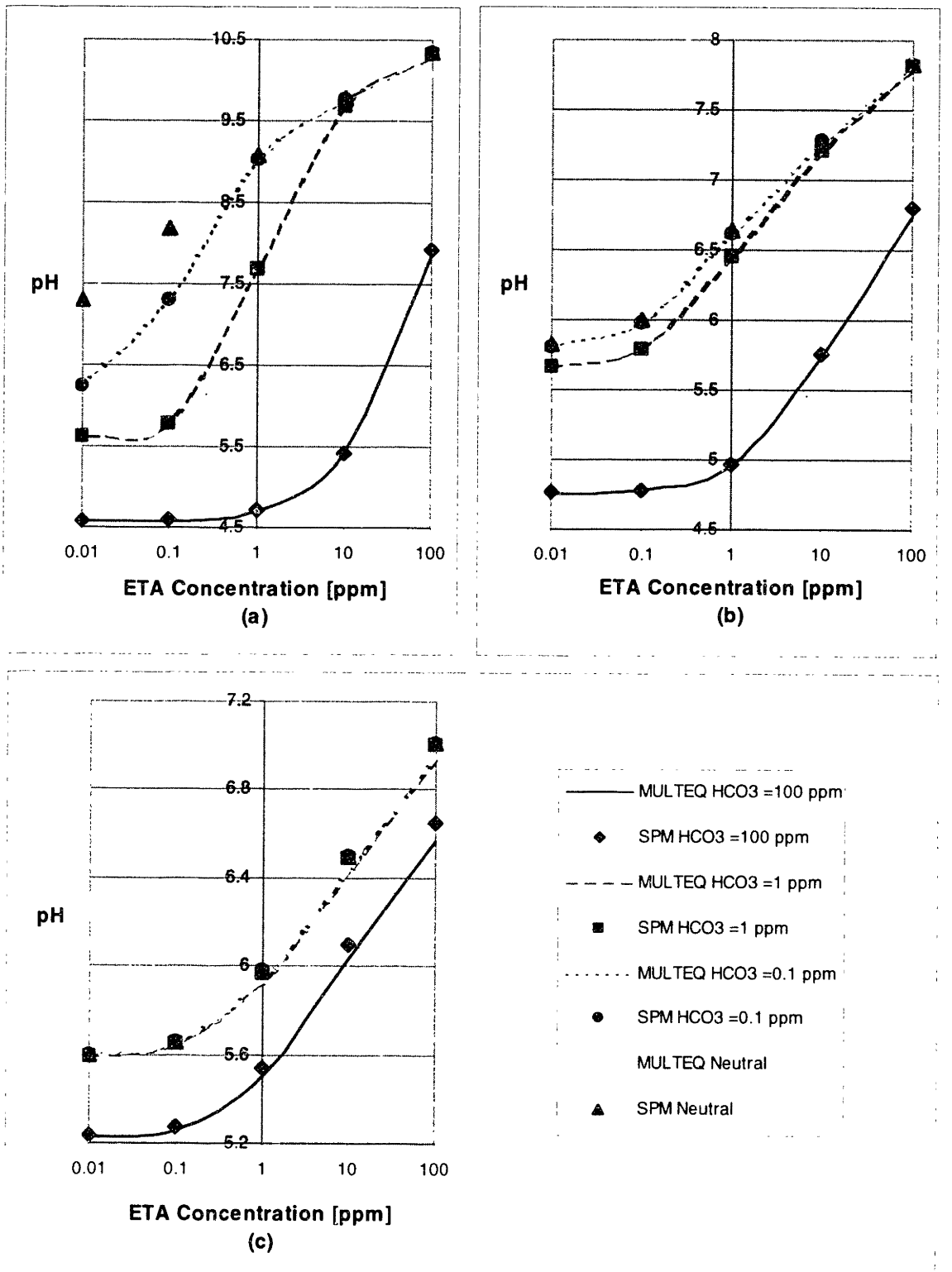

Figure 4-5. Comparison of single phase pH calculations between IEC and MULTEQ for ETA with an acid (HCO3+) added at a) 50 °C, b) 150 °C, and c) 250 °C.

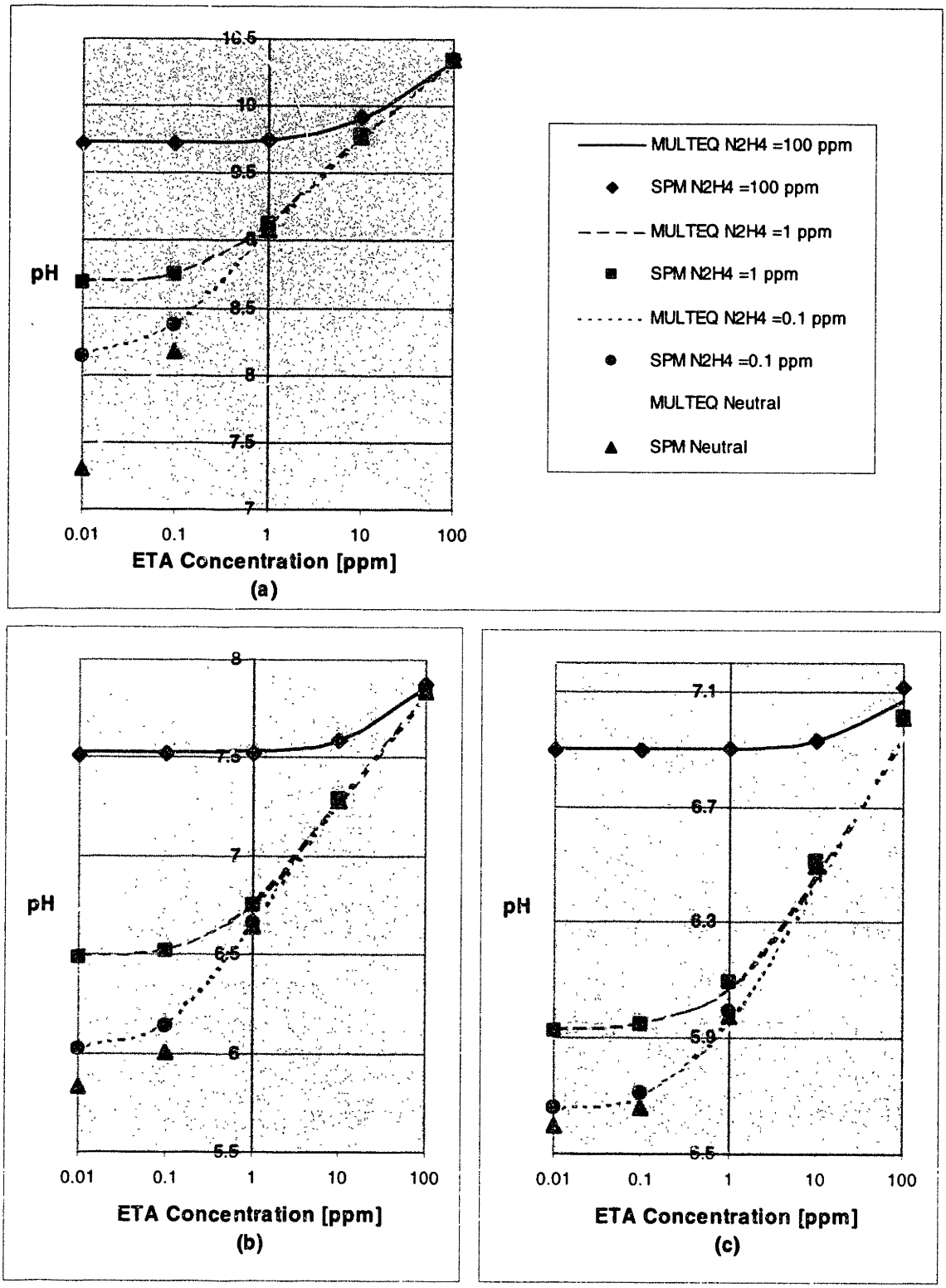

Figure 4-6. Comparison of single phase pH calculations between IEC and MULTEQ for ETA with a base (N2H4) added at a) 50 °C, b) 150 °C, and c) 250 °C.

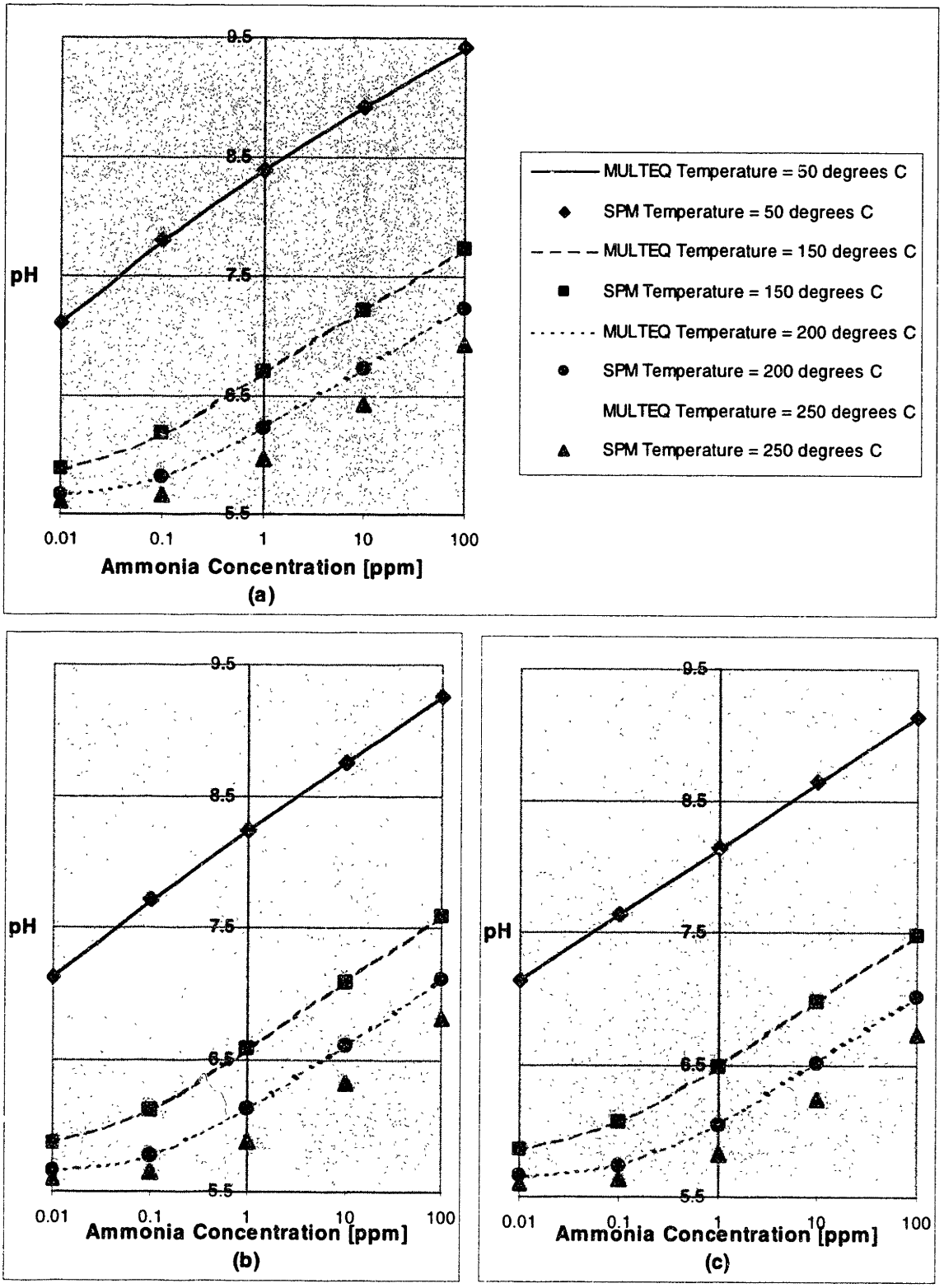

Figure 4-7. Comparison of two phase pH calculations between IEC and MULTEQ for ammonia at different temperatures for water qualities of a) 0.206, b) 0.499, and c) 0.900.

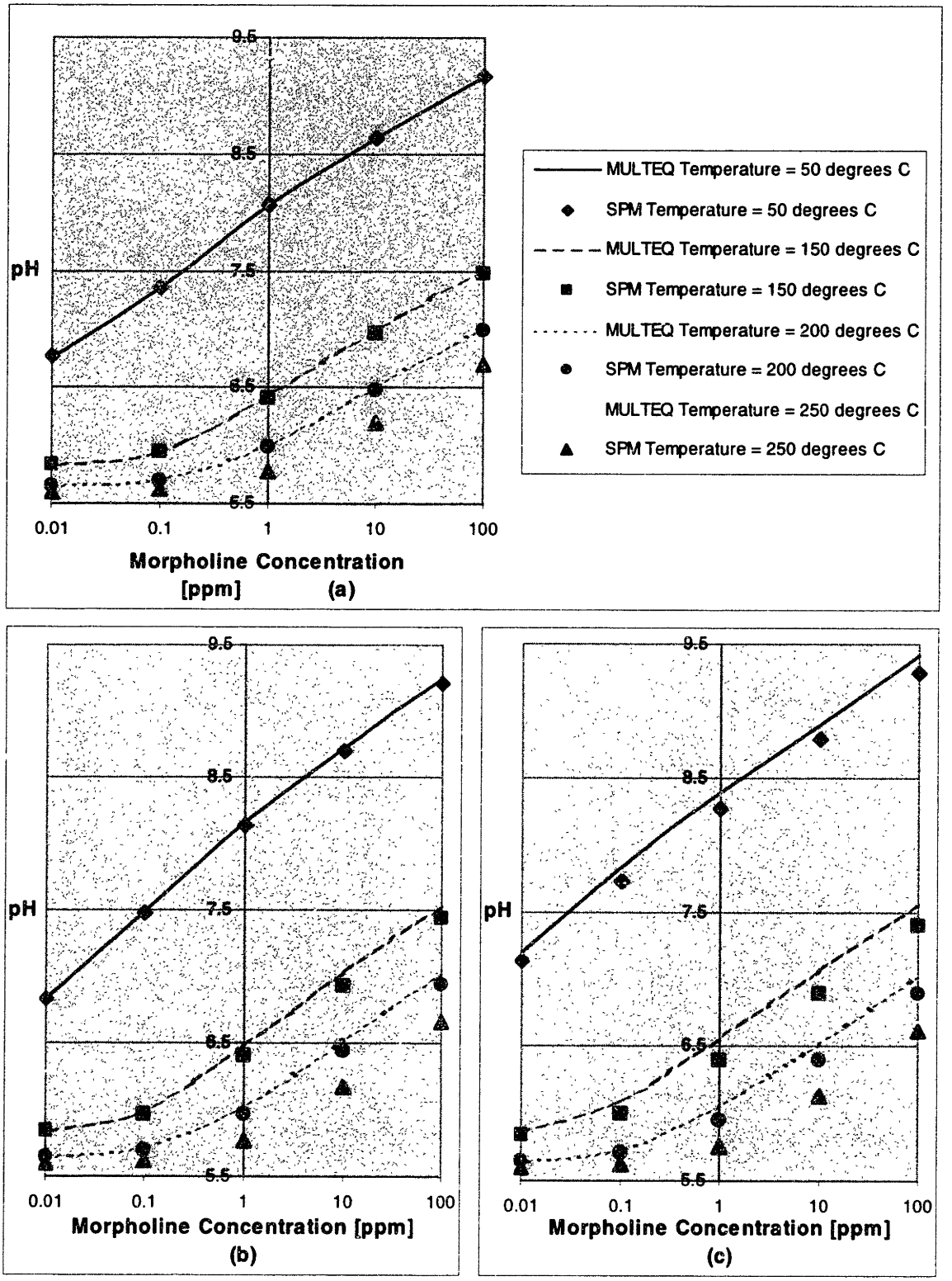

Figure 4-8. Comparison of two phase pH calculations between IEC and MULTEQ for morpholine at different temperatures for water qualities of a) 0.206, b) 0.499, and c) 0.900.

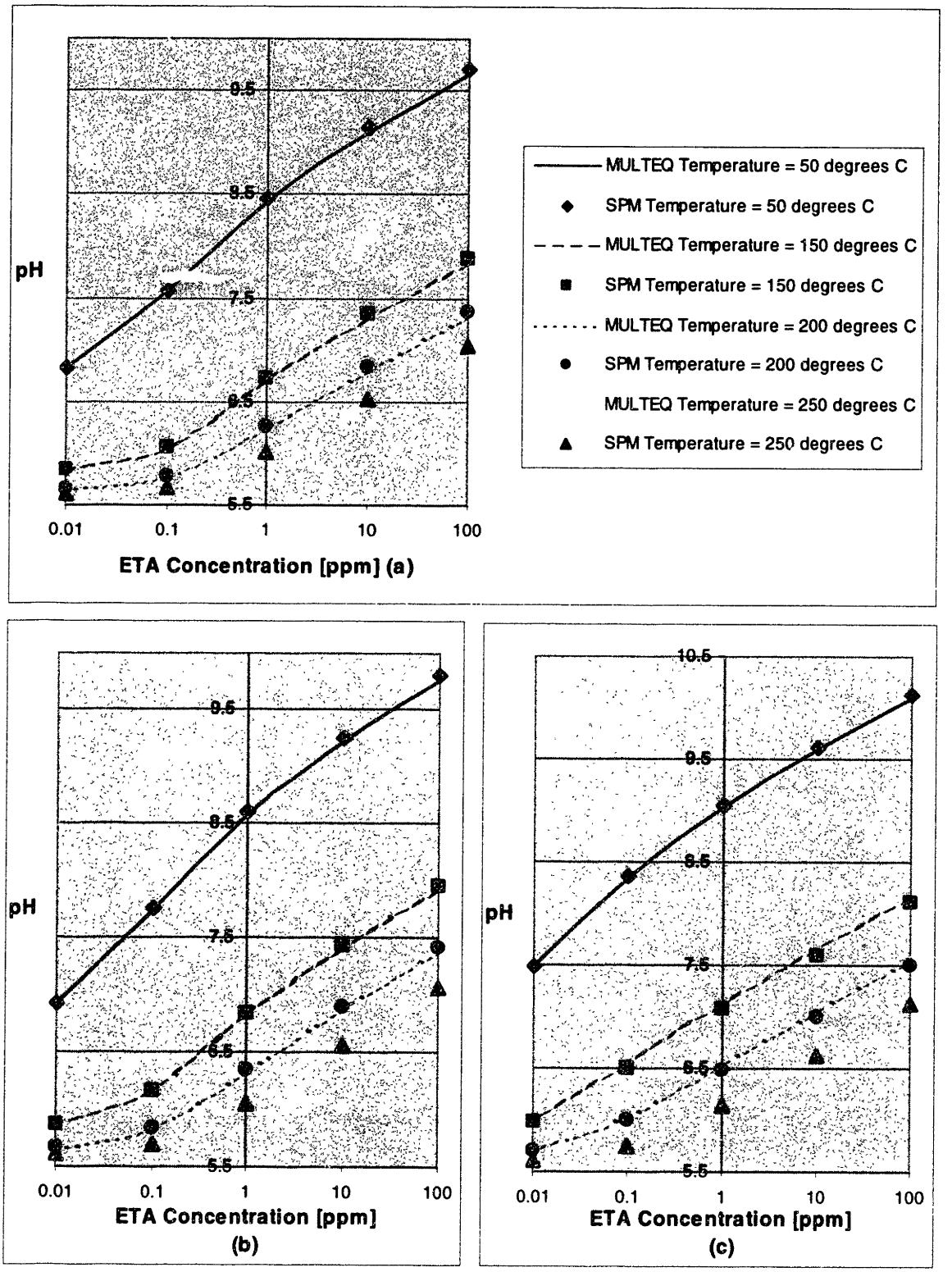

Figure 4-9. Comparison of two phase pH calculations between IEC and MULTEQ for ETA at different temperatures for water qualities of a) 0.206, b) 0.499, and c) 0.900.

the SPPDP may change input data on chemical species that is used in the IEC. Overall agreement of the SPPDP's IEC with the industry code, MULTEQ, is quite good. This accuracy is expected as both are based on similar physical principles.

Chapter 5. Flow Accelerated Corrosion Model

With the first three SPPDMME calculation modules discussed and verified, this chapter describes the main model used for the final calculation, degradation rate. The model discussed is used to predict Flow Accelerated Corrosion (FAC), the most prevalent of the four Flow Induced Material Degradation phenomena described in Chapter 2. The last section of Chapter 3 discusses the SPPDMME approach to modeling the other 3 degradation phenomena.

As outlined in Chapter 2, the advantage of an empirical model is that it provides a numerical prediction of wear rate dependent on all known significant parameters. The advantage of the mechanistic model is that it provides a prediction of wear rate whose validity is likely to extend to sets of conditions that have not been tested or verified. For the purpose of the SPPDP, the best model available in the literature, the Kastner model is combined with a physical understanding of the nature of the phenomenon gained from mechanistic models. Wear predictions of the resulting model, the New FAC Model, (NFM) are then compared to those of the Kastner model for experimental and plant data and to a second empirical model, the Chexal-Horowitz model, for published data. Having verified the NFM, the model is incorporated into the SPPDP.

5.1. Modifications to the Kastner Model

The models described in Chapter 2 culminate from significant research on the various parameters affecting the FAC rate. Understanding of the electrochemical and mass transfer principles incorporated into the mechanistic models described in that

chapter and analysis of literature and the functional dependencies incorporated in the empirical Kastner model indicate a number of modifications that can be made to improve the predictions of the Kastner model. These modifications include:

1) the decoupling of velocity and alloying element content at low alloying element content,
2) elimination of the effect of oxygen for bulk oxygen concentrations below a critical value,
3) an improvement in the two-phase correlation used to estimate liquid phase velocity, and
4) an adjustment of the cold pH factor to predict wear at higher values of pH.

A final modification ensures physically accurate trends at high and low temperatures. All modifications preserve the model's predictions outside the specified range of the variable being modified.

5.1.1. Decoupled Parameters: Pipe Alloying Element Concentration and Water Velocity

Modifying the effect of low alloying element content in the Kastner model was motivated by recognition that the Kastner model did not evenly fit Kastner experimental data at low alloy content, nor did it correlate well with published data of the Chexal-Horowitz model. Decoupling of the velocity and alloying element content effects, was based on information presented by other investigators and the fact that no experimental evidence of their coupling beyond the time of the film formation has been seen. Film formation is not modeled in the current version, because the model only addresses prediction of wear rate under constant conditions after film formation.

Two sources of experimental data exist on the effect of alloying element content on the FAC wear rate, experiments at Electricité de France (EDF) and Kastner's data

(Kastner *et. al.*, 1984). It should be noted that a third experimental study for two phase flow carried out at velocities not typical of those in a power plant will not be considered (Huijbregts, 1984). The experiments performed at EDF (Ducreux, 1982; Bouchacourt, 1988) consisted of single phase and two phase flow with water velocity at 56 m/sec and 60 m/sec, respectively. Based on the single phase experiments, Ducreux presented an expression for the increase in FAC wear rate resistance relative to a reference material for the statistically significant alloying elements: chromium, molybdenum, and copper (Ducreux, 1982). This data can be reanalyzed to determine an expression for the decrease in FAC rate due to these alloying elements as follows (Cragnolino *et. al.*, 1988):

$$F(aec) = \exp(-5.16 \cdot aec^*) \qquad \textbf{(Eq. 5-1)}$$

where

$$aec^* = Cr(\%) + 0.19 \cdot Mo(\%) + 0.40 \cdot Cu(\%) \qquad \textbf{(Eq. 5-2)}$$

Bouchacourt showed that the two phase data fit this expression (Bouchacourt, 1988). The expression used to fit experimental data derived by Kastner for the effect of alloying element content is discussed below.

Though a number of authors have implied the existence of potential coupling between velocity and alloying element content, none (except Kastner) include such a factor in the final predictive wear rate model (Chexal *et. al.*, 1996, Woolsey, 1988). Numerous mechanistic and empirical models use a separable factor to describe the alloying element effect, including the updated Berge model (as described in Chexal *et. al.*, 1996, pg 4-90), the BRT-Cicero model developed by EDF used to predict French power plants' FAC wear rate (Bouchacourt, 1987; Chexal *et. al.*, 1996, pg. 4-94), and the

Chexal-Horowitz model (see **Eq. 2-4**). A separable factor implies no coupling between alloying element content and velocity.

Figure 5-1 shows the Ducreux correlation plotted against the published data of the Chexal-Horowitz model normalized to match the published data point at negligible alloying element content (~0.025%). This normalization allows comparison of trends due to changes in alloying element content. Note that the Ducreux correlation only provides a prediction of trends for changes in alloying element content. For an increase in both molybdenum and chromium content, the correlation matches the published data at this low velocity (6.1 m/sec). Because the Ducreux correlation was based on data taken at higher velocities, one may assume that similar trends at this lower velocity implies the use of the Ducreux correlation as a separable factor in the Chexal-Horowitz model. That is the incorporated alloy content factor for the Chexal-Horowitz model is not velocity dependent.

The Kastner model couples the velocity and alloying element content. The alloying elements considered in the Kastner model are chromium and molybdenum as noted in Table 2-1. The Kastner model evenly weights these elements using the sum of their concentrations as an independent variable. In the above text, the Kastner model was generalized as a separable equation including a factor that depended on alloying element content, velocity, and temperature (see **Eq. 2-3**). Close examination of this factor shows that it can be further decomposed into three factors of the form:

$$F_1(v,T,aec) = F_1'(aec,T) \cdot F_1''(v,T) \cdot \exp(-v * aec). \qquad \textbf{(Eq. 5-3)}$$

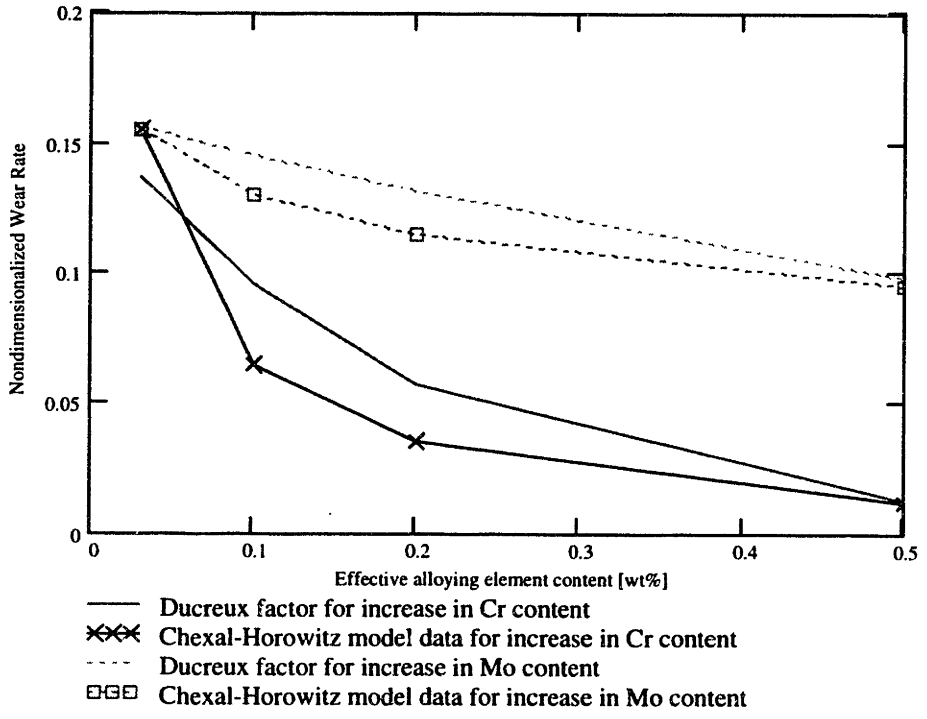

Figure 5-1. Comparison of Chexal-Horowitz published data for increase in Cr and Mo content at 300 °F against the Ducreux factor normalized to the same rate at negligible alloying element content. (Hydraulic diameter = 4", O_2 = 7ppb, v=20 ft/sec, cold pH = 7, geometry = 90 degree elbow.)

Analysis shows that the Kastner model matches Ducreux experimental data for the single phase test conditions (v = 56 m/sec and T = 180 °C) used. As expected, the Kastner model is also fitted to Kastner's single phase experimental data.

The majority of Kastner's data is for very high[6] alloying element content (80% of the data is for alloying element content greater than 0.25%[7], possibly more typical of German plants) with a velocity range of 5-39 m/sec. Because the Kastner data fit is heavily weighted by this relatively high alloying element content data, data fit at low

[6] 'Very high' refers to the fact that most researchers agree that an alloying element content greater than 0.10% is sufficient to inhibit FAC for single phase flow (e.g. Chexal *et. al.*, 1996, pg.4-85).

alloying element content is degraded. Because wear rate is most significant at these low alloying element contents, it is essential to model this region more accurately than at high alloying element content. Figure 5-2 shows the Kastner model wear predictions modeled against the experimental measured data. The low alloying element content data is not dispersed evenly within the scatter of the remaining data, indicating that at low alloying element content the model predicts too low of a wear rate.

Because of the arguments presented above, the Kastner model was modified for alloying element content less than 0.25%, so that the NFM form becomes:

$$F_1(v,T,aec) = F_1'(aec,T) \cdot F_1''(v,T) \cdot \exp(-C_{aec} \cdot aec) \quad aec < 0.25\% \quad \textbf{(Eq. 5-4)}$$

where *aec* is defined as for the Kastner model, and C_{aec} is a constant determined to be 4.0. This new factor combined with F_1', gives a similar relative decrease in FAC rate for alloying element content increasing from 0 to 0.25% as does the Ducreux relation (**Eq. 5-2**). Figure 5-3 shows a plot for various velocities of the NFM with and without this alloying element content modification. The y-axis is normalized to a FAC wear rate without this modification and with 0% alloying element content. Note that for the NFM, the relative change in FAC wear rate is not a function of velocity below alloying element content of 0.25% as it is above 0.25%.

5.1.2. Oxygen Effect as a Threshold

An extensive study by Woolsey has shown that above a critical concentration of bulk oxygen, the FAC wear rate is abruptly reduced (Woolsey, 1986). Oxygen

---

[7] The range of pipe alloying element content, <0.25%, is typical of US power plants.

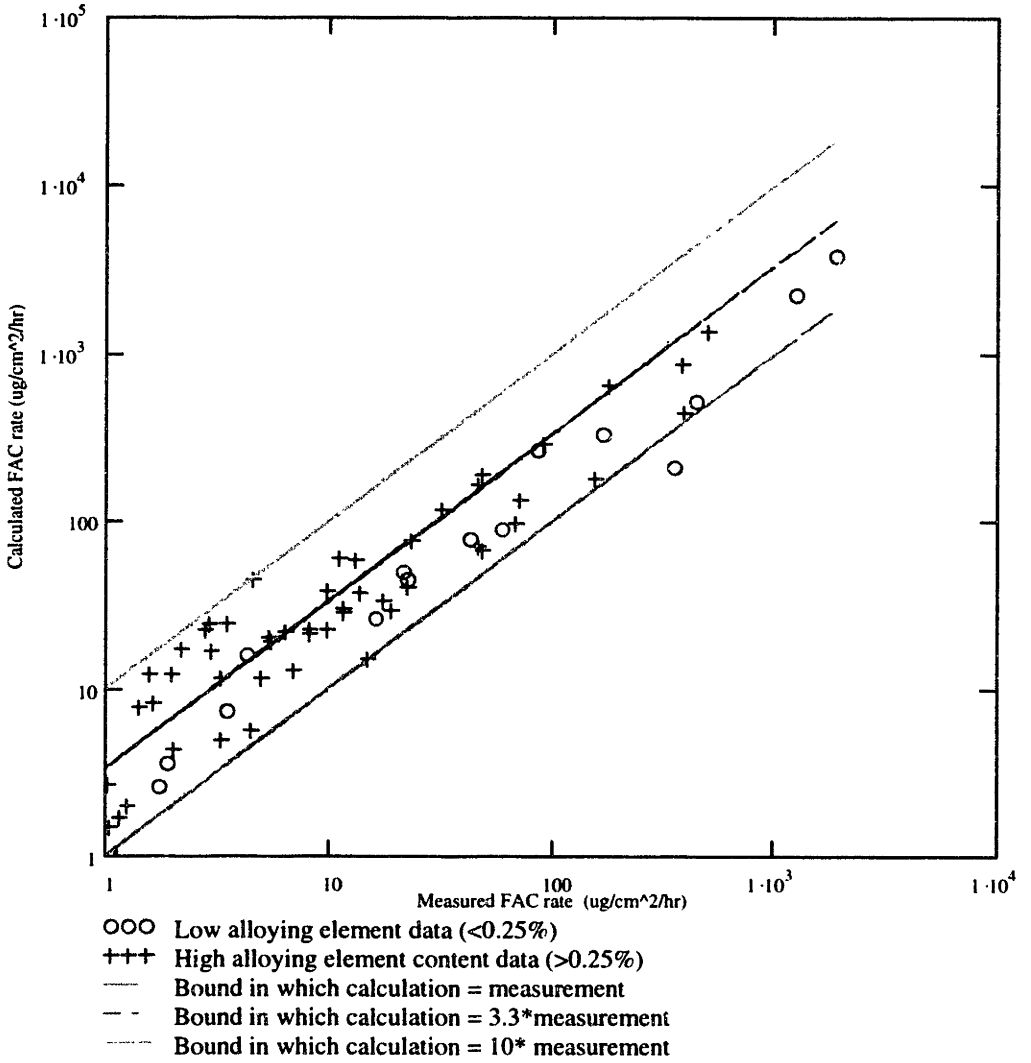

Figure 5-2. Plot of the Kastner model calculated FAC wear rate against measured FAC wear rate for Kastner experimental single phase data.

concentrations below this value have no effect on the FAC rate. The deaerated FAC rate and the mass transfer coefficient of the oxygen determine this critical bulk oxygen concentration. In the Woolsey experiments, the specimen potential was measured as well as the FAC wear rate.

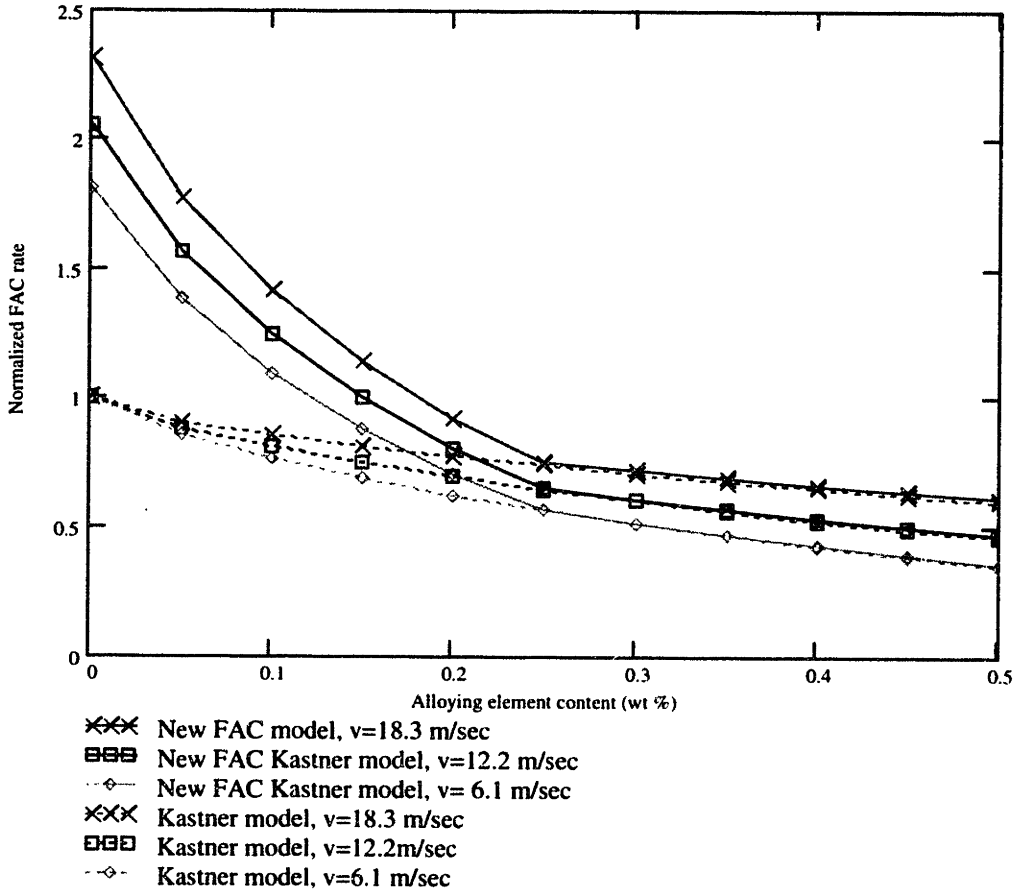

Figure 5-3. Comparison of the Kastner model to the NFM for a range of velocities. The y-axis is the FAC wear rate normalized to the value of the Kastner model at 0% alloying element content.

At low values of bulk oxygen concentration, it was found that the specimen electrochemical potential was low. Increases in bulk oxygen up until the critical concentration caused neither changes in potential nor in the FAC wear rates. At oxygen concentrations near the critical value, the specimen potential increases, and the FAC wear rate is abruptly reduced. These observations are consistent with the rate of oxygen reduction being controlled by the mass transfer of the oxygen to the surface. At low values of bulk oxygen concentration and low specimen potential, the hydrogen evolution reaction,

$$2 \cdot H^+ + 2e^- \longrightarrow 2 \cdot H_2 \qquad \textbf{(Eq. 5-5)}$$

is the major contributor to the cathodic process. This cathodic reaction is balanced by the anodic production of ferrous ions. At oxygen concentrations near critical, however, oxygen reduction,

$$\tfrac{1}{2}O_2 + H_2O + 2e^- \longrightarrow 2 \cdot OH^- \qquad \textbf{(Eq. 5-6)}$$

begins to compete with hydrogen evolution, raising specimen potential. An increase in specimen potential will increase the stability of the magnetite film thereby reducing the solubility of the magnetite film, reducing the metal dissolution process, and increasing the relative contribution of oxygen reduction to the cathodic reaction, which further increases the specimen potential. The process is, therefore, self-accelerating.

To determine the critical bulk oxygen concentration, then, one must equate the anodic and cathodic reactions by matching the charge transfer processes, deaerated FAC wear rate and the mass transfer rate of the oxygen:

$$n_{\frac{1}{2}O_2} \cdot \frac{\dot{m}''_{\frac{1}{2}O_2}}{MW_{\frac{1}{2}O_2}} = \frac{\dot{m}''_{Fe}}{MW_{Fe}} \cdot n_{Fe} \cdot Thrshld_{fctr} \cdot \frac{1}{Cnsrvtv_{Fctr}} \qquad \textbf{(Eq. 5-7)}$$

where

$$\dot{m}''_{\frac{1}{2}O_2} = h_{O_2} \cdot C_{O_2crit} \cdot \rho_{H_2O}\ , \qquad \textbf{(Eq. 5-8)}$$

n_x = the charge transferred per unit mole of material x [unitless]

$\dot{m}''_{Fe}$ = the deaerated FAC wear rate predicted per unit area [$mass_{Fe}$/area/time],

MW_x = molecular weight of species x [mass/mole],

C_{O_2crit} = the critical bulk oxygen concentration [ppb],

h_{O_2} = the mass transfer coefficient of oxygen [length/time], and

ρ_{H_2O} = the water density [$mass_{H2O}$/volume],

$Thrshld_{fctr}$ = the experimental factor found by Bignold (0.16 - 0.25)

$Cnsrvtv_{Fctr}$ = the median ratio of predicted wear to measured wear for the model used to determine the deaerated wear rate.

Note that the concentration of oxygen at the metal surface is assumed to be zero in **Eq. 5-8**. In addition, note that $n_{\frac{1}{2}O_2} = n_{Fe} = 2$, as shown in **Eq. 5-5** and **Eq. 5-6**. The effect of the $Thrshld_{fctr}$ factor is that the amount of oxygen necessary to induce the threshold phenomenon is about 4-6 times less than what would be required if the metal loss rate is equated to the mass transfer of oxygen to the surface. The $Cnsrvtv_{Fctr}$ factor accounts for the degree conservatism of the model used to calculate the deaerated FAC rate. For the Kastner model, this factor is caluculated to be 2.88. (see section 5.2.1.1 for this calculation.)

In applying this threshold concept to modify the Kastner model, one must determine the critical bulk oxygen concentration and compare this critical value to the value measured for the bulk flow. For a measured value below the critical value, the modified FAC wear rate is equal to the deaerated FAC wear rate. For a measured value above the critical value, the reduced FAC wear rate must be determined. In this derivation of a NFM, a measured value above the calculated critical value is computed using the oxygen factor of the Kastner model. In the context of **Eq. 2-3**, for a measured value below critical, the $F_3(O_2)$ factor is removed; and for a measured value above critical, the $F_3(O_2)$ factor is included. Figure 5-4 illustrates the resulting curve for the NFM as well as that for the Kastner model using the original oxygen factor.

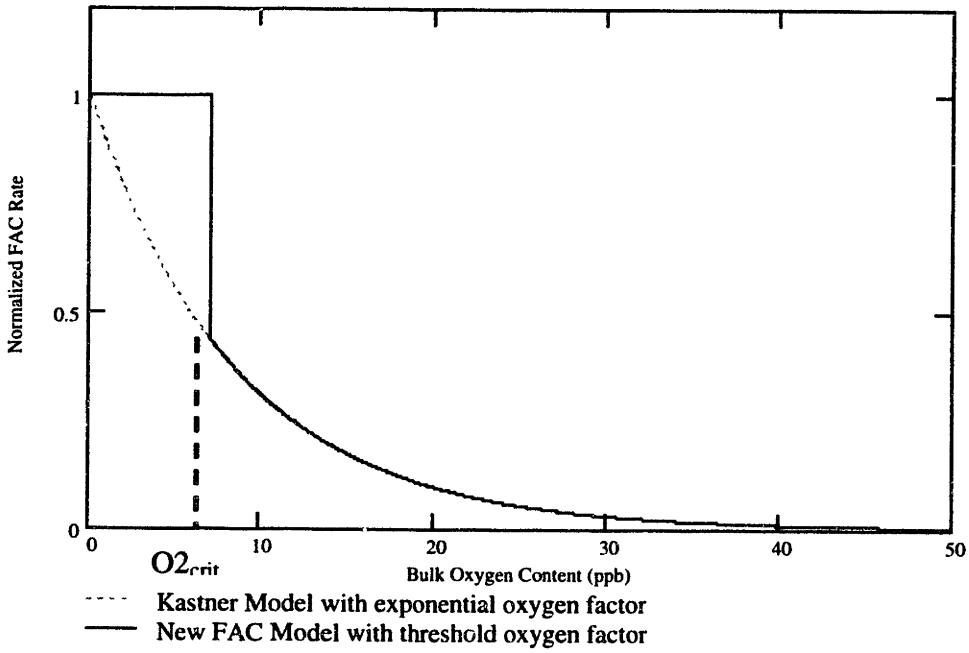

Figure 5-4. Comparison of FAC rate relative to deaerated conditions due to variation in the bulk oxygen concentration for the NFM and Kastner model. The critical oxygen concentration is determined as a function of the deaerated FAC rate and mass transfer coefficient of the oxygen.

To determine the critical bulk oxygen concentration, then, the deaerated FAC wear rate and mass transfer coefficient of the oxygen to the metal surface must be computed. **Eq. 5-7** and **Eq. 5-8** can be rewritten as

$$C_{O_2 crit} = \frac{\dot{m}''_{Fe}}{h_{O_2} \cdot \rho_{H_2O}} \cdot \frac{MW_{\frac{1}{2}O_2}}{MW_{Fe}} \cdot Thrshld_{fctr} \cdot \frac{1}{Cnsrvtv_{Fctr}} \qquad \textbf{(Eq. 5-9)}$$

A suggested correlation for h_{O_2} is given for fully developed flow as (Berger and Hau, 1977)

$$h_{O_2} = \frac{D_{O_2}}{D_H} \cdot (2 + c \cdot \mathrm{Re}^a \cdot Sc^{1/3}) \qquad \textbf{(Eq. 5-10)}$$

with

$$c = 0.0165 + 0.011 \cdot Sc \cdot \exp(-Sc), \qquad \textbf{(Eq. 5-11)}$$

$$a = 0.86 - \frac{10}{(4.7 + Sc)^3} \cdot Sc \cdot \exp(-Sc), \qquad \textbf{(Eq. 5-12)}$$

$$\mathrm{Re} = \frac{v \cdot D_H}{\nu} \text{ (the Reynolds number)}, \qquad \textbf{(Eq. 5-13)}$$

$$Sc = \frac{\nu}{D_{O_2}} \text{ (the Schmidt number)}, \qquad \textbf{(Eq. 5-14)}$$

where

D_{O_2} = the oxygen diffusion coefficient in water (Woolsey, 1986) [m^2/sec]

D_H = the hydraulic diameter[m]

v = the mean liquid velocity [m/sec]

ν = the dynamic viscosity of water [m^2/sec].

The deaerated FAC wear rate, $\dot{m}''_{Fe}$, is given by the NFM with no oxygen factor included.

Appendix D. New FAC Model summarizes the equations of the NFM.

5.1.3. Mass Transfer Effect Incorporated as the Friction Velocity

Ideally, any model, whether empirical or mechanistic, would use the mass transfer coefficient in the pipe as an input variable. The above discussion of the Sanchez-Caldera and Bignold mechanistic models indicates the importance of the mass transfer coefficient on the FAC wear rate. Two investigators specifically describe the FAC process as a mass transfer limited dissolution of the oxide surface (Bouchacourt, 1988; Bignold, 1988). As shown in **Eq. 5-10** through **Eq. 5-14**, the mass transfer coefficient is related to the mean

liquid velocity, the hydraulic diameter, and temperature (through the temperature dependence of the water and diffusing species properties).

One may then be motivated to convert the Kastner model to use the mass transfer coefficient as an input variable. The Kastner model, unfortunately, uses only velocity and temperature as input variables, neglecting the effect of hydraulic diameter (see Table 2-1). The motivation for using these two input variables is likely that an empirical model does not seek to utilize first principles in developing a curve fit. In fact, functional dependence is determined only by the fit to experimental data in which *a single* parameter is varied (Kastner and Riedle, 1986). Neglect of the effect of the hydraulic diameter in the Kastner model is likely due to the fact that this parameter was not varied in the single phase experiments upon which the model functional dependencies were determined. In the case of FAC wear rate in which temperature affects oxide solubility, pH, and mass transfer coefficient, using a single parabolic temperature factor (as is essentially done in the Kastner model) combines these multiple dependencies. A conversion of the Kastner model to use mass transfer coefficient as opposed to velocity as an input variable, would therefore require complete reformulation of the empirical model with respect to temperature as well. This reformulation was not possible since only approximately 120 data points were available to the author.

Application of the model to two phase flow provides a significant motivation for the conversion of the model so that the mass transfer coefficient rather than velocity is used as an input parameter. In two phase annular flow, (a flow regime typical of the two phase flow found in power plants), the relation between the mean liquid velocity and the mass transfer coefficient is not the same as that for single phase flow because of the

difference in the liquid velocity profile for annular flow. A model using mean fluid velocity as an input parameter is not likely to accurately predict the two phase flow FAC wear rate, which is a mass transfer controlled process. This fact almost certainly contributes to the increase in the data scatter between Figures 2-5 and 2-6, which depicts the Kastner model predictions against measurements for single and two phase flow, respectively. In contrast to mean fluid velocity, the friction velocity u^*, which is defined as:

$$u^* = \sqrt{\frac{\tau_w}{\rho}} \qquad \textbf{(Eq. 5-15)}$$

(where τ_w is the wall shear stress and ρ is the water density), characterizes the transport dimension for both single and two phase flow. A model using friction velocity as an input parameter as is done by Sanchez-Caldera, is likely to predict more accurately the two phase flow FAC wear rate. Like the mass transfer coefficient, the friction velocity includes the dependence upon hydraulic diameter and temperature. Like the mass transfer coefficient then, conversion of the Kastner model to incorporate friction velocity rather than mean fluid velocity would require complete reformulation of the model. (Note that the friction velocity does not characterize the mass transfer of a particular species; i.e. it does not depend on the diffusivity of a particular species. A model using friction velocity would necessarily need to include an additional factor including the ferrous ion diffusivity.)

A velocity modification of the Kastner model, however, is possible without complete reformulation of the model. The modification is only applicable to 2 phase flow. This modification involves using a different 2 phase flow void fraction correlation

(used to determine mean liquid phase velocity), the Chexal-Lellouche void fraction correlation (Chexal *et. al.*, 1991), with characteristics that better fit the problem at hand. The Kastner model is principally derived from single phase laboratory experiments (Kastner, 1987). To apply the Kastner model to two phase flow, the Kastner models uses a two phase correlation determining void fraction for annular flow based on water mass flux and quality (Rouhani, 1969). By calculating void fraction, the mean fluid velocity can be determined for the annular flow. This mean fluid velocity is used in the Kastner correlation as the bulk liquid velocity would be used for single phase flow.

The author noted, in comparing the two phase friction velocity, the mean fluid velocity calculated using the Rouhani correlation, and the mean fluid velocity calculated using the Chexal-Lellouche correlation (Chexal *et. al.*, 1991), that the Chexal-Lellouche correlation fit the trends of the friction velocity better than the Rouhani correlation over range of mass flux, quality and temperatures that are typical of PWR secondary cycles. For these three correlations, Figure 5-5 shows the relative change in velocity as a function of temperature for a typical value of mass flux and quality. The matching trend shown in the figure is typical throughout the range of mass flux, quality, and temperature investigated. This figure illustrates that the Chexal-Lellouche calculated fluid velocity matches the friction velocity curve better than the Rouhani calculated fluid velocity.

Therefore, the NFM uses the Chexal-Lellouche correlation to determine the fluid velocity instead of using the Rouhani. Like the Kastner model, the mean fluid velocity for 2 phase flow is used as would be the bulk fluid velocity for single phase flow. The advantage of the Chexal-Lellouche correlation is two fold:

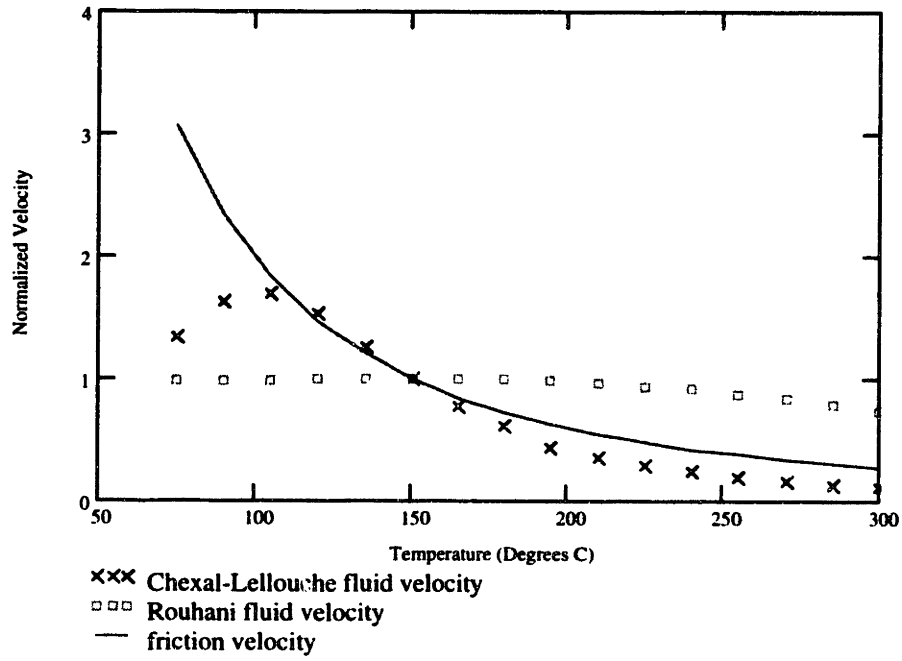

Figure 5-5. Friction velocity vs real velocity trends normalized to the value computed at 150 °C. Conditions for calculation are mass flux of 250 kg/m^2/sec and flow quality of 0.9, typical of an extraction steam line.

1) It computes a liquid velocity which similar in magnitude to what would be computed by the Rouhani correlation (i.e. they are both computing fluid velocities) and

2) It matches the trends of friction velocity for a wide range of 2 phase flow conditions.

Because fluid velocity determined by the Chexal-Lellouche correlation trends with friction velocity, the correlation is expected to better characterize the mass transfer process that the model is attempting to predict. Because the nominal value determined by the Chexal-Lellouche correlation is a mean fluid velocity, as is used for the single phase data upon which the Kastner model is developed, the correlation is not expected to introduce error.

5.1.4. Cold pH Factor

Both empirical models discussed in Chapter 2 use the cold pH (pH measured at

25 °C) as an input parameter to the model because that is the parameter typically measured and available from plant data. The pH that directly affects the corrosion rate, however, is the hot pH, or pH at the temperature of the fluid. For single phase flows cold pH corresponding to a specific hot pH differs depending on the amine used to control pH. For two phase flows, the cold pH measurement is the value of pH for mixture of the vapor and liquid at 25 °C. In this case, cold pH differs considerably from the hot pH in the liquid, because amines partition between vapor and liquid, and the degree of partitioning depends on the amine species..

Ideally, then one would rather correlate an empirical model based on the hot pH of the liquid. Since the SPPDP supplies this information as outlined in Chapter 3, the SPPDP could take advantage of this correlation to predict FAC rate with less uncertainty. Similar to arguments presented previously, the nature of the Kastner model and insufficient experimental data, however, prohibits this approach. Because the Kastner model is an empirical model, one cannot simply replace the current factor (a parabolic curve) with a physically based curve fit, even if the cold pH factor is separable[8].

---

[8] The reason for this is as follows. To create a physical model for a separable pH factor, one would need to base it on the physical quantity affecting FAC rate, the hot pH. Hot pH is a function of concentration, temperature, and amine type (and quality for 2 phase flow). Cold pH is a function of only concentration and amine type. A physical model proposing a separable hot pH factor would then correspond to a separable cold pH and temperature factor. The Kastner model includes only a separable cold pH factor implying that the incorporation of temperature effects, the difference between cold pH and hot pH, is implicit in the $F_i'(aec,T)\cdot F_i''(v,T)$ terms of **Eq. 5-3**. Furthermore, no physical explanation exists for the parabolic cold pH factor. Again, a replacement of the cold pH

A modification of the cold pH factor used by the Kastner model is necessary as presented here. For single phase flow, the Kastner predicts a cold pH value greater than 9.39 to be prohibitive of FAC. This prediction is in conflict with most other researchers. Modification of this separable factor is motivated by the observation that numerous researchers have reported FAC wear for cold pH values above 9.39. Furthermore, the Kastner model is based on data of which only about 15% is at cold pH other than 7.0 and only 5% is at a cold pH values greater than 9.39.

The modification of the cold pH factor incorporated into the NFM takes into account a number of constraints. It should:

a) cause minimal change in prediction rates at lower cold pH values,
b) use the same equation form as the original factor, and
c) fit the data of other researchers at higher cold pH values.

The first constraint ensures minimal change throughout the remaining pH range where the Kastner model is in agreement with published information from other researchers. The second constraint ensures that the new cold pH factor is consistent with the unmodified temperature factor that presumably accounts for the difference between hot and cold pH (see footnote 3). The final constraint is met as discussed below.

The Kastner model has a cold pH factor of the form:

$$F_2(pH) = 1 - 0.175 * (pH - 7)^2 . \qquad \textbf{(Eq. 5-16)}$$

The NFM replaces this cold factor with:

---

factor with a hot pH factor would require a complete reformulation of the empirical model. Insufficient data exists to reformulate the empirical model. If such data did exist,

$$F_2(pH) = 1 - 0.128 * (pH - 7)^2. \qquad \textbf{(Eq. 5-17)}$$

Figure 5-6 shows the effect of the adjustment on the pH factor. Note this adjustment has no effect at a pH value of 7. With the adjustment of the pH factor, a pH value of 9.79 is considered to be prohibitive of FAC. Chexal indicates that the cold pH controlled by ammonia which is prohibitive of FAC is 9.7 ±0.1 (Chexal, et. al. 1996). As the Kastner model is conservative, it makes sense that the predicted maximum cold pH devised is larger than that quoted. Because the Kastner model is based on single phase data with ammonia controlling the pH, and the cold pH is a function of the amine type, only data reported for single phase FAC with pH controlled by ammonia is used to verify this new factor. Table 5-1 compares the prediction of NFM to the data from 3 different investigators. In all cases the NFM is greater than that reported as is consistent with the conservative Kastner model philosophy. As will be explained in section 5.2.1.1, the conservatism of the NFM is calculated to be 2.88. The values of the NFM predicted over 'source' wear from Table 5-1 bound this mean indicating that the 0.128 factor of **Eq. 5-17** is a good estimate.

5.1.5. Low and High Temperature Correction

The final modification made to the Kastner model corrects a common negative characteristic of empirical models. Empirical models tend to make non physical predictions for sets of conditions outside the range of conditions to which they were fit, but within the range of conditions for which the model is intended to be valid. For the Kastner model, this occurs at high and low temperatures for changing velocity. At high

---

it would not be necessary to go through the process of improving the Kastner empirical

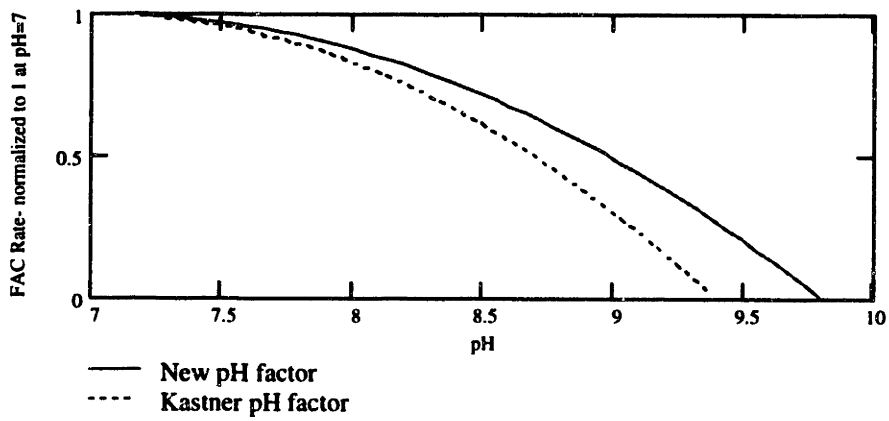

Figure 5-6. Change of cold pH factor in NFM based on literature data.

Source	Cold pH	Source FAC rate [10^{-3} in/yr]	Kastner Model FAC rate [10^{-3} in/yr]	NFM [10^{-3} in/yr]	Ratio of NFM /Source wear rate
Chexal-Horowitz Model	9.4	12	0.7	43.6	3.64
Bignold Experiment	9.5	7.87	0.4	13.7	1.74
Bouchacourt Experiment	9.6	1.04	0.8	1.77	1.71

Table 5-1. Comparison of NFM wear predictions with literature data for high values of cold pH using ammonia.

and low temperatures, the Kastner model predicts increasing wear for decreasing velocity. Experimental data and a physical understanding of the problem support the opposite trend, increasing FAC wear with increasing velocity regardless of temperature.

Figure 5-7 shows the Kastner model prediction of wear for two different alloying element concentrations, a range of velocities, and typical conditions for the remaining parameters. The graph shows that above 240 °C, increasing wear is predicted for

---

model.

decreasing velocity which is not consistent with experimental data. Below 60 °C the same trend is predicted. One can see that at 240 °C, under these typical conditions the wear predicted is still significant, near 50 μgm/cm^2/hr.

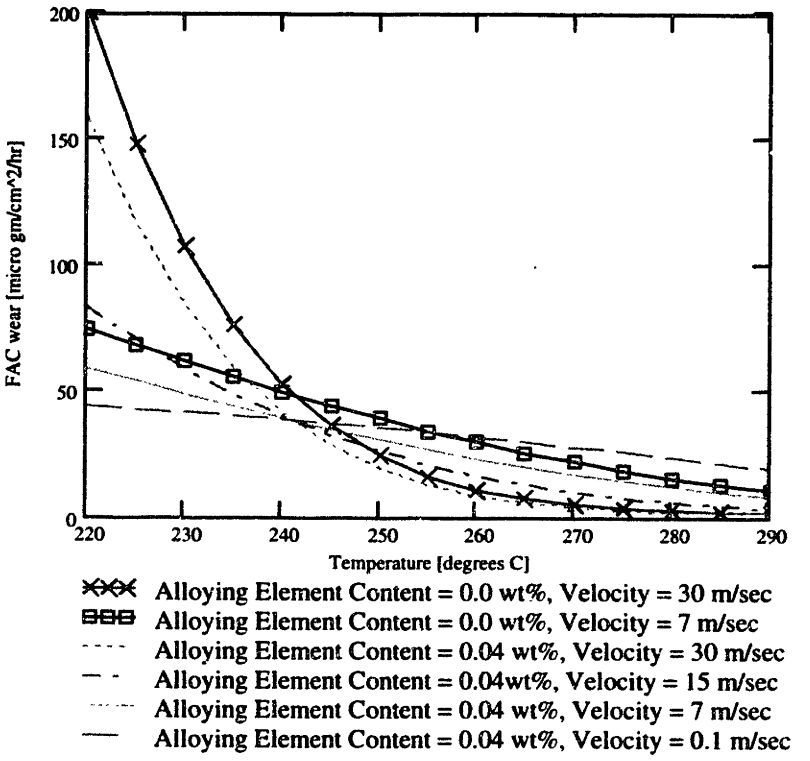

Figure 5-7. Kastner model prediction of FAC wear at high temperature for typical conditions: cold pH=9.4, 90° bend, deaerated ($O2 < O2_{crit}$), time of operation = 12 yrs.

The reason for this nonphysical trend is determined by analyzing the $F_1''(v,T)$ term of Eq. 5-4. At temperatures for which the derivative of this term with respect to velocity is negative (above 240 °C and below 60 °C), a modification of the was made. With increasing temperature between 150 °C, where FAC is predicted to peak, and 240 °C, the Kastner model predicts a lessening dependence of FAC on velocity. At about 240 °C, the FAC rate predictions are not dependent on velocity. The modification to Kastner

model assumes this characterstic is maintained, so that above 240 °C and below 60 °C the FAC rate is not dependent on velocity and is set to a nominal value of 15m/sec. Analytically, the NFM incorporates the following relation:

$$F_1''(v,T) = F_1''(v = 15m/\sec, T) \quad if \quad \frac{\partial F_1''(v,T)}{\partial v} < 0. \qquad \textbf{(Eq. 5-18)}$$

Figure 5-8 shows the resulting the result of this modification for the same set of conditions present in Figure 5-7.

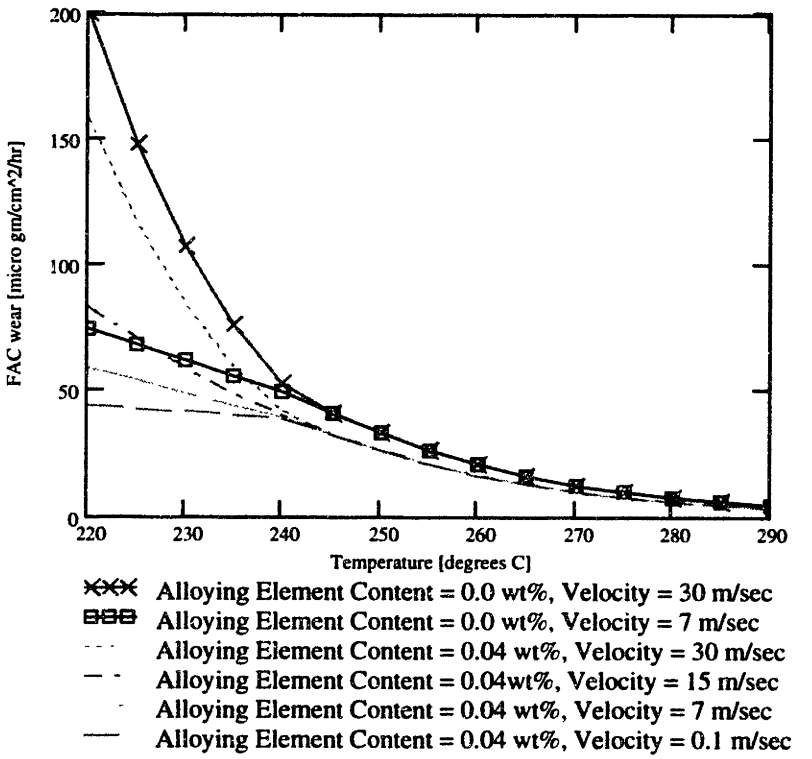

Figure 5-8. NFM prediction of FAC wear at high temperature for typical conditions: cold pH=9.4, 90° bend, deaerated ($O2 < O2_{crit}$), time of operation = 12 yrs.

5.2. Comparison to Other Models

To verify whether the NFM gives more accurate FAC wear rate predictions than the Kastner model, both were used to predict wear rate for Kastner's single phase experimental data, and two sets of data from US power plants. Additionally, the NFM predictions are compared to the published Chexal-Horowitz model predictions.

5.2.1. Kastner Model

The Kastner model is compared to the NFM for three data sets: Kastner's single phase laboratory data, Millstone Unit 2 single phase data, and Millstone Unit 3 two phase data.

5.2.1.1. Single Phase Laboratory Data

Kastner published single phase experimental data conditions and measured FAC rates (Kastner *et. al.*, 1984). Using this information, the NFM FAC rate predictions can be compared to measured wear data. Figure 5-9 illustrates this comparison. For single phase data only, the third modification affecting two phase flow does not take effect. One expects to see an increase in the predicted wear rate on average. The other modifications either increase the model wear rate prediction or do not change it. All points are now conservatively predicted though much fewer are immediately adjacent to the bound of calculated and measured wear equivalence. The data, however, have slightly less scatter using the NFM as shown below.

To compare the results of the two models, this scatter is quantified. First the ratio of calculated to measured wear is computed for each data point, i,

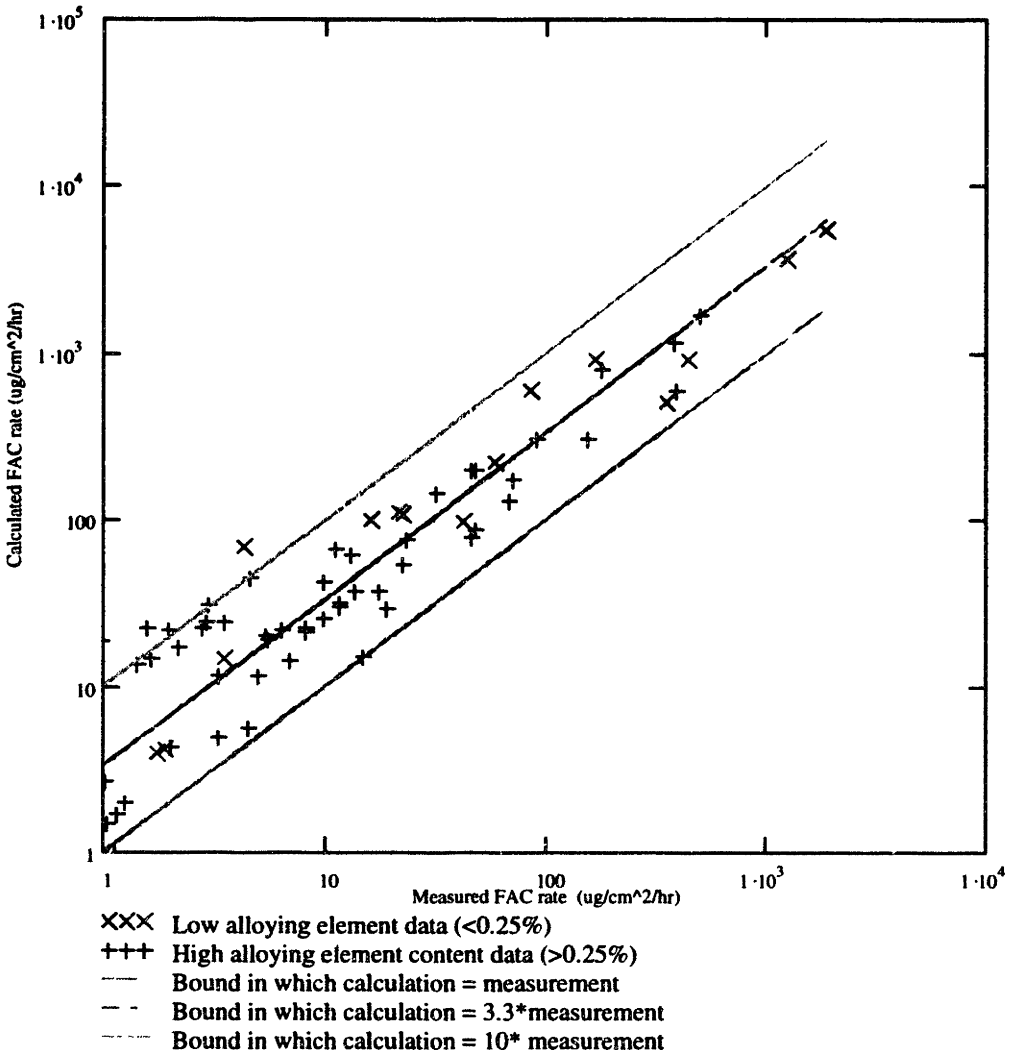

Figure 5-9. Plot of the NFM calculated FAC wear rate against measured FAC wear rate for Kastner experimental single phase data.

$$Rt_{C\_M_i} = \frac{\dot{m}''_{Fe,calculated_i}}{\dot{m}''_{Fe,measured_i}} \qquad \textbf{(Eq. 5-19).}$$

Second the mean of the natural logarithm of this ratio is computed,

$$\mu_{LN\_R} = \frac{\sum_{i=1}^{N} \ln\left[Rt_{C\_M_i}\right]}{N} \qquad \textbf{(Eq. 5-20).}$$

By taking the natural logarithm of the ratio, a calculated value that is twice the value of the measured value is weighed equal to a calculated value that is half the measured value. This mean characterizes the expected conservatism for the models and is used in later calculations of model accuracy. That is, regardless of the data the model should replicate this conservatism as closely as possible. To quantify the scatter, the standard deviation of the natural logarithm of the ratio is computed,

$$\sigma_{LN\_R} = \left[\frac{1}{N} \cdot \sum_{i=1}^{N} \left[\mu_{LN\_R} - \ln\left[Rt_{C\_M_i}\right]\right]^2\right]^{\frac{1}{2}} \qquad \textbf{(Eq. 5-21).}$$

The mean and standard deviation above calculated characterize a lognormal fit to the ratio of calculated to measured wear. By taking the exponential of the mean, one finds the median value of this distribution,

$$Mdn_{Rt} = \exp(\mu_{LN\_R}) \qquad \textbf{(Eq. 5-22).}$$

This median characterizes the typical proximity of calculations to measurements for each model (or conservatism). Finally, the value of the ratio of the 95th percentile value of this distribution to the median of this distribution is computed,

$$Rt_{span} = \frac{Rat_{C\_M\_95}}{Mdn_{Rt}} = \exp(1.645 * \sigma_{LN\_R}) \qquad \textbf{(Eq. 5-23).}$$

This value can be thought of as the value one would have to multiply and divide the median, Mdn_{Rt}, to span 90% of the lognormal distribution of $Rt_{C\_M_i}$.

For the wear calculations of both the NFM and the Kastner model and their corresponding measurements shown in Figure 5-9, the four values described by Eq. 5-20 through Eq. 5-23 are computed. Table 5-2 compares these values for all measured values

above 1 μg/cm^2/hr. The equivalent thickness reduction rate is 0.011mm/yr which is the lowest rate for which one should be concerned. At this rate, a 1 mm thick pipe would require 50yrs to be reduced to half of its thickness. As expected based on observations of Figure 5-9 and the changes made to generate the NFM, the NFM predictions have a greater median ratio, Mdn_{Rt}, than the Kastner model predictions. The increase in the median value is of little concern, because one could simply multiply by a factor less than one to reduce the conservatism of the model to level of conservatism desired. The spread of the data represented by, Rt_{span}, has decreased slightly for the NFM. This result is considered to be positive, because presumably the Kastner model is optimized on the Kastner laboratory data. The true advantage of the NFM is expected when it is extrapolated to conditions not well characterized by laboratory data, because the NFM incorporates more physically based trends. This improvement is shown in the following comparisons of plant data predictions.

Table 5-2. Statistical data comparing the results of the predictions of laboratory data for the Kastner model and NFM.

	μ_{LN_R}	σ_{LN_R}	Mdn_{Rt}	Rt_{span}
Kastner Model	0.919	0.604	2.51	2.70
NFM	1.057	0.588	2.88	2.63

5.2.1.2. Single Phase Millstone Unit 2 Data

The Kastner model and the NFM were both used to predict wear rates for a set of pipes from Millstone Unit 2. The pipes originate from potentially flashing systems such as the moisture separator drains, and saturated systems such as feedwater heater drains. The geometries are mostly 90° elbows with the exception of two reducers and one

straight pipe. For two data the alloying element content was unknown so it was assumed to be similar to that in other piping from the plant (Kupinski *et.al.*, 1993).

Figure 5-10 plots the predicted wear for both models against the measured wear for the pipes. The bounds on this figure indicate the range one would expect from the Kastner model. In general, though the wear predictions are not as conservative as one would expect for the Kastner model, the NFM gives better predictions than does the Kastner model. The blanket method refers to the method of determining a pipe thickness based on a set of UT tests over a grid. The blanket method involves determining the change in wall thickness over a user defined area of the pipe which includes some pipe at the original thickness. This area is then progressively moved over the complete set of UT data. Of the number of methods for determining a thinning rate, the blanket method is considered the most accurate.

To quantify the accuracy of the two models the mean and median are calculated using Eq. 5-20 and Eq. 5-22 above. Table 5-3 compares the conservatism of these models to that expected based on predictions of laboratory data described in the previous section. The NFM can be seen to have a median of the ratio of predicted to measured values, Mdn_{R_t}, much closer to that from single phase laboratory data than does the Kastner model. The NFM, then, extrapolates to this single phase plant data more accurately than the Kastner model.

5.2.1.3. Two Phase Millstone Unit 3 Data

The Kastner model and the NFM were both used to predict wear rates for a set of pipes from Millstone Unit 3. These piping samples originated from to parallel high

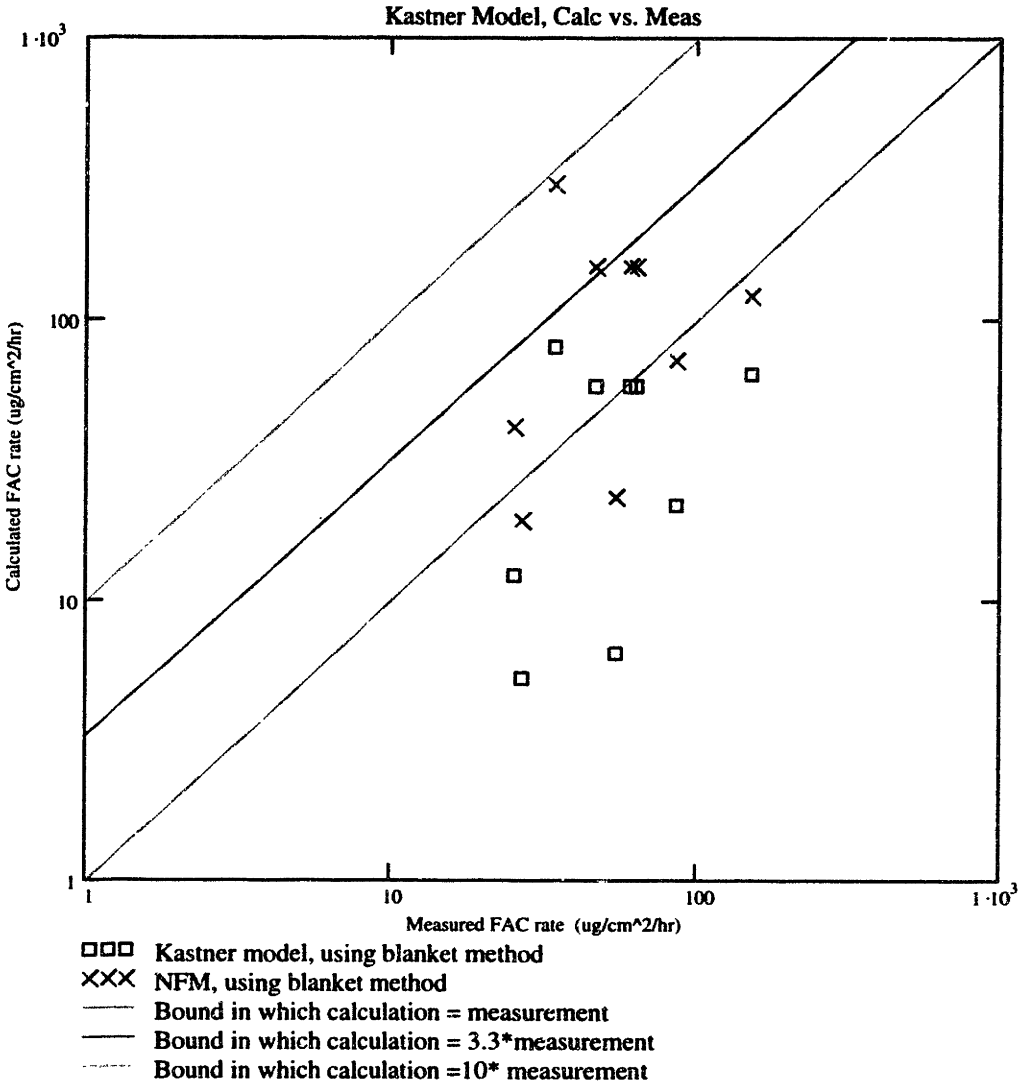

Figure 5-10. Plot of measured single phase plant data from Millstone Unit 2 against predicted wear as calculated with the Kastner model and the NFM.

Table 5-3. Comparison of statistical data for predictions by the NFM and Kastner model of single phase plant data from Millstone Unit 2.

	Kastner Laboratory Data		Millstone Unit 2 Data	
	μ_{LN_R}	Mdn_{Rt}	μ_{LN_R}	Mdn_{Rt}
Kastner Model	0.919	2.51	-0.643	0.526
NFM	1.057	2.88	0.453	1.573

temperature extraction steam lines with two phase flow of approximately 90% flow quality and mass flux of 700 kg/m^2/sec. The data consisted of straight pipes and 90° elbows. In the case of two phase flow the Kastner model designates the bulk oxygen concentration be set to zero. Therefore, only the alloying element content modification and two phase void fraction correlation change cause a change in results from the Kastner model.

Figure 5-11 plots the predicted wear for both the Kastner and the NFM against the measured wear for the pipes. The bounds on Figure 5-11 indicate the range one would expect from the Kastner model. The two clumps of data, one at higher wear rate than the other are reflective of the two different geometries for which wear is being predicted: elbows and straight pieces. The elbows experience greater wear. Figure 5-11 shows that the NFM fits the measured data better than the Kastner model, under-predicting only a single point and including the majority of the other points within the expected conservative bounds. The band method referred to in the plot is a second method for converting UT tests into a pipe wear rate. Determination of wear rate by this method involves computing the greatest variation in thickness for each band or circumference around the pipe. This method is conservative in that it results in a measured thinning rate larger than the actual thinning rate. The method does not readily distinguish between variation in wall thickness due to FAC wear and that from manufacturing. In Figure 5-11, note that the band method measurements are normally to the right of band method measurements. For a given predicted FAC wear rate, then, the band method results in a larger measured wear rate.

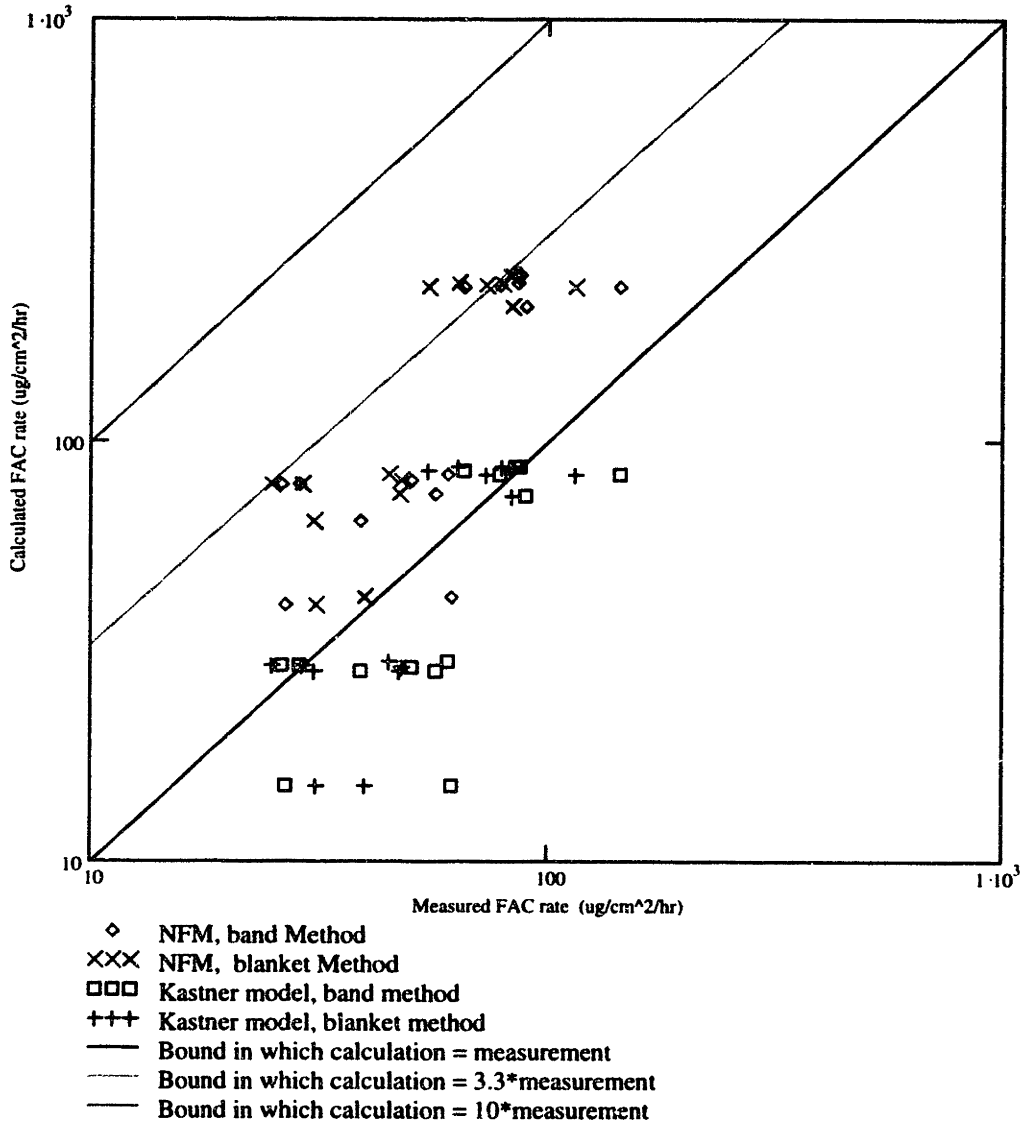

Figure 5-11. Plot of measured two phase plant data from Millstone Unit 3 against predicted wear as calculated with the Kastner and the NFM.

To quantify the accuracy of the two models for predicting this two phase plant data similar calculations are performed for the mean and median using Eq. 5-20 and Eq. 5-22 above. Table 5-4 compares the conservatism of these models to that expected based on predictions of laboratory data described in section 5.2.1.1. Again, the NFM can be seen to have a median of the ratio of predicted to measured values, Mdn_{R_I}, much closer

to that from two phase laboratory data than does the Kastner model. The NFM, then, extrapolates to this two phase plant data more accurately than the Kastner model.

Table 5-4. Comparison of statistical data for predictions by the NFM and Kastner model of two phase plant data from Millstone Unit 3.

	Kastner Laboratory Data		Millstone Unit 3 Data	
	μ_{LN_R}	Mdn_{Rt}	μ_{LN_R}	Mdn_{Rt}
Kastner Model	0.919	2.51	-0.446	0.640
NFM	1.057	2.88	0.553	1.738

5.2.2. Chexal-Horowitz Model

In this section, the NFM predictions are compared against a set of published Chexal-Horowitz model data (Chexal, et. al. 1996). Previous comparisons of the Kastner model results to the Chexal-Horowitz model results showed the Kastner model to typically predict a factor that was 2-4 below that of the Chexal-Horowitz model. Because the Kastner model is supposed to predict a conservative value, one may estimate the difference in the Kastner model and Chexal-Horowitz model to be about an order of magnitude. Because the modifications made to the Kastner model increase the calculated FAC wear rate, one would expect better matching to the Chexal-Horowitz data.

Figure 5-12 and Figure 5-13 show the model predictions for NFM and Chexal-Horowitz, respectively, for a range of chromium concentrations. The change in temperature is more peaked for the Chexal-Horowitz model as is true for the remaining comparisons. The peak value for the NFM is slightly greater than that for the Chexal-Horowitz model at low chromium concentration and a factor of 3 higher at high chromium concentration. Because of the modification of the alloy content dependence, it is not surprising that the NFM trends match better with the Chexal-Horowitz data.

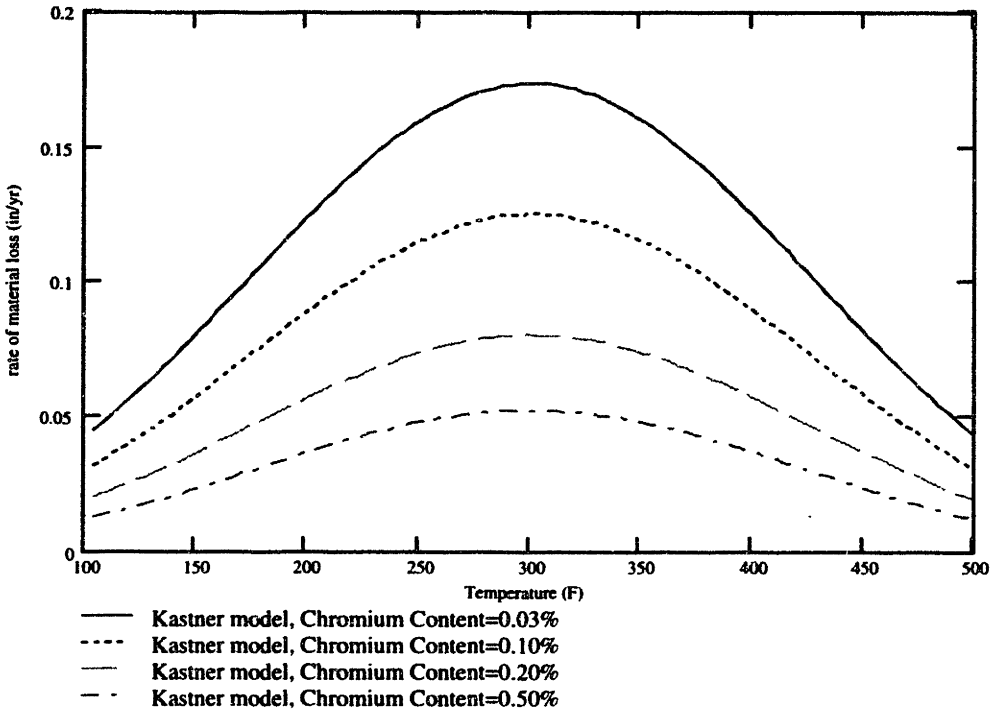

Figure 5-12. NFM predictions for variable chromium concentrations.

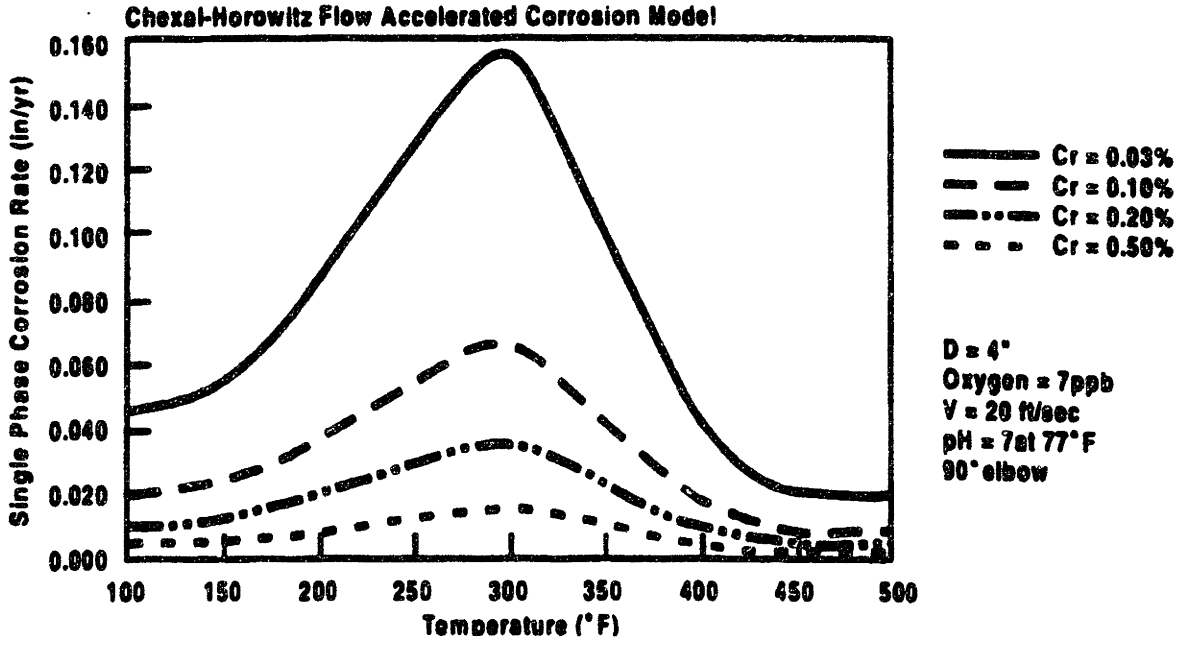

Figure 5-13. Chexal-Horowitz model predictions for effect of chromium concentration (Chexal *et.al.*,1996).

Figure 5-14 and Figure 5-15 show the model predictions for NFM and Chexal-Horowitz, respectively, for a range of molybdenum concentrations. The peak value for the NFM is slightly greater than that for the Chexal-Horowitz model at low molybdenum concentration. At high molybdenum concentrations, the Chexal-Horowitz model peak value is greater by about 80%. Recall that the Chexal-Horowitz model uses the Ducreux correlation for which the molybdenum concentrations is weigeted at 1/5 of chromium (see **Eq. 5-2**) while the NFM model weights both chromium and molybdenum evenly.

Figure 5-16 and Figure 5-17 show the model predictions for the NFM and Chexal-Horowitz, respectively, for a range of velocities. The peak value of the predicted FAC rate for the highest velocity is about 25% higher for the NFM and about 60% higher for the lowest velocity as compared to the Chexal-Horowitz model. The change in the FAC rate for this set of velocities is a stronger dependence for the Chexal-Horowitz model. The change in FAC rate with velocity of Figure 5-17 is approximately proportional to $v^{0.6}$ implying that the velocity is incorporated into the model as a mass transfer coefficient (see **Eq. 5-12**). In contrast, the velocity dependence of the NFM is $\exp(v)$ (see **Eq. 5-3**). Note the effect of the last modification at high and low temperatures removes the dependence on velocity at these temperatures all together.

Figure 5-18 and Figure 5-19 show the model predictions for NFM and Chexal-Horowitz, respectively, for a range of oxygen concentrations. Similar to the analysis before, the NFM model shows a larger drop over the range from 0 to 10 ppb, but both models essentially predict no wear beyond 30 ppb.

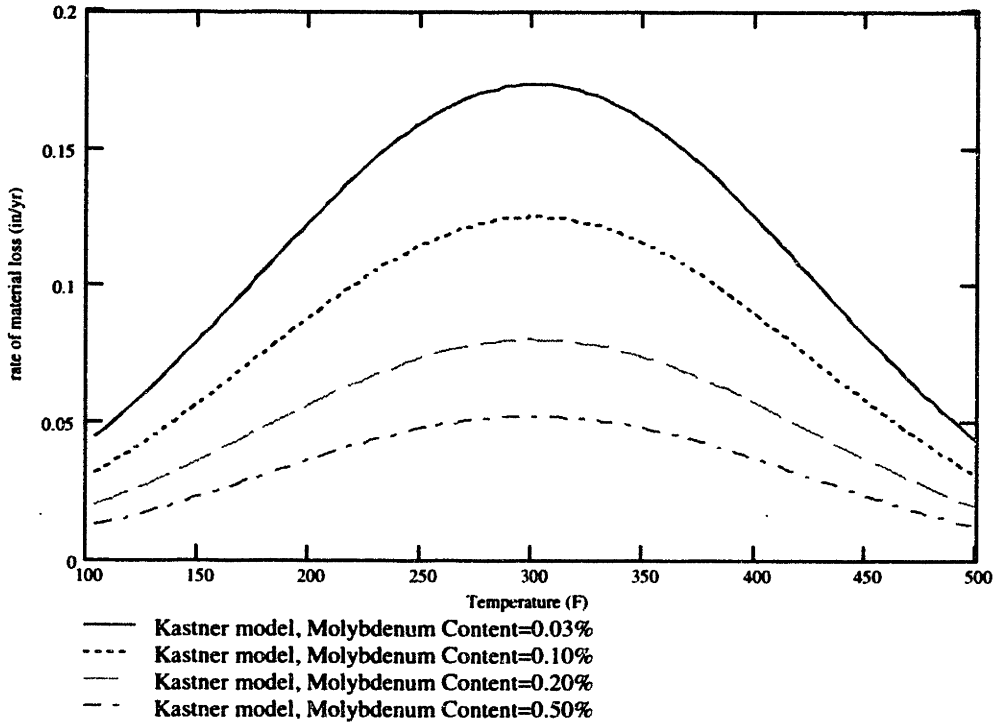

Figure 5-14. NFM predictions for variable molybdenum concentrations.

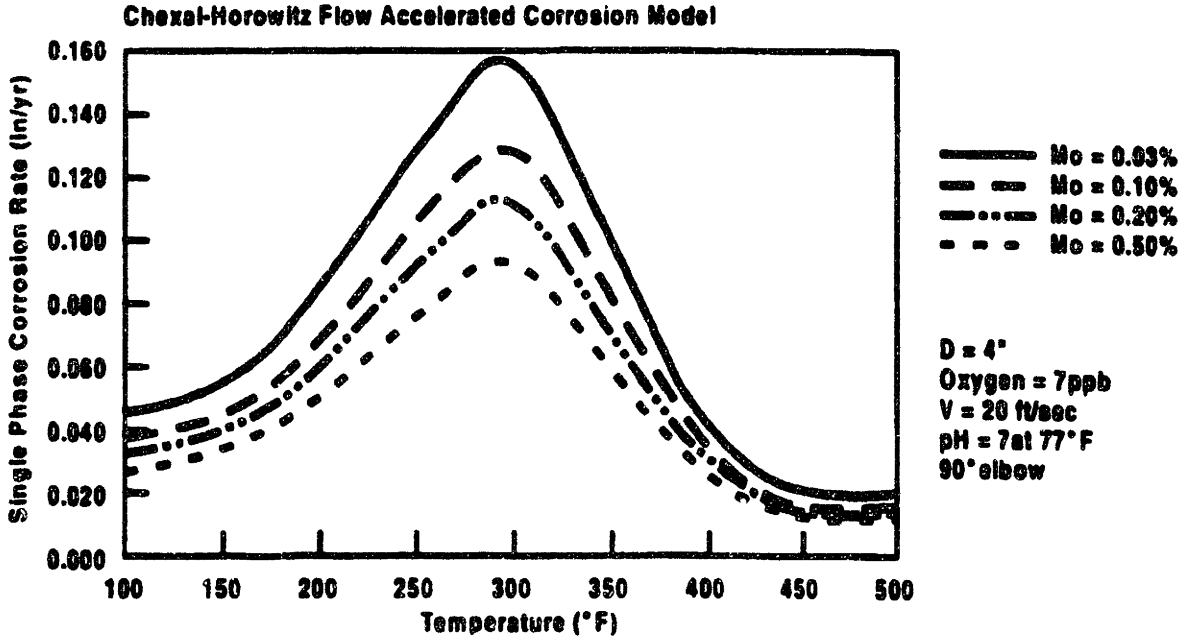

Figure 5-15. Chexal-Horowitz model predictions for effect of molybdenum concentration (Chexal *et.al.*,1996).

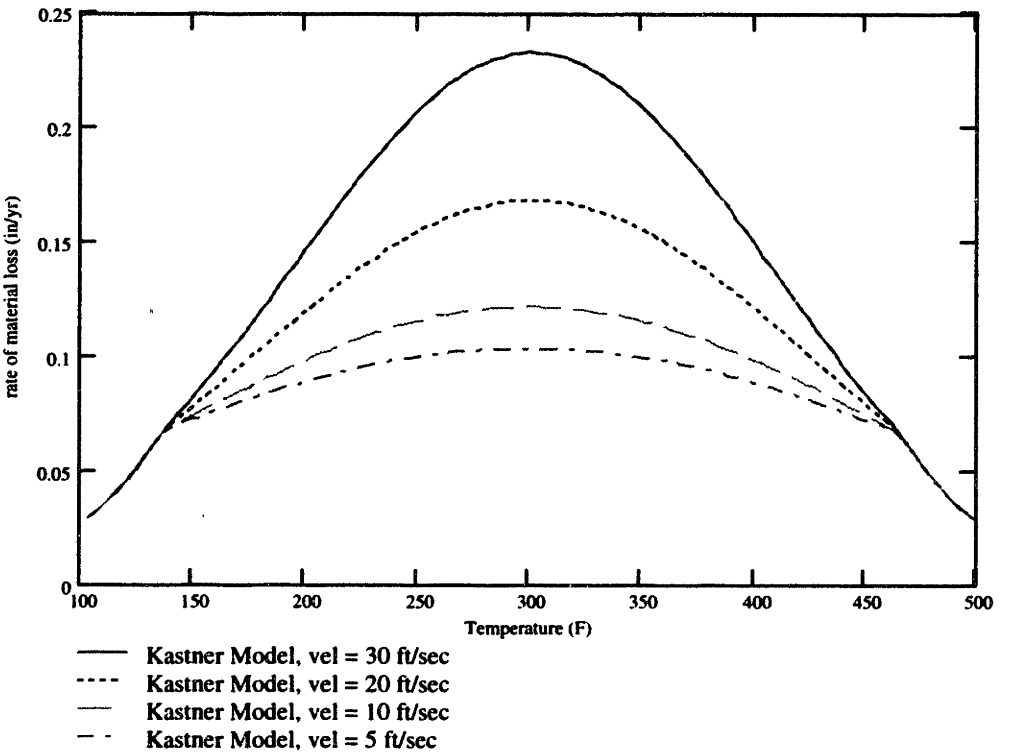

Figure 5-16. NFM predictions for variable velocities.

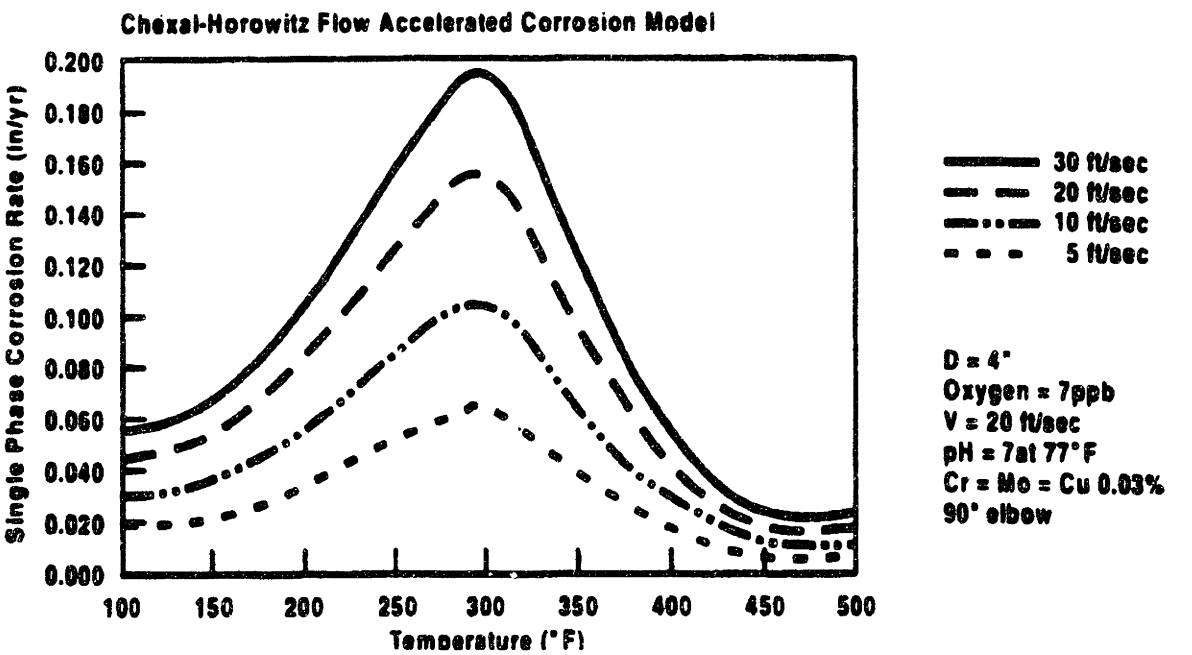

Figure 5-17. Chexal-Horowitz model predictions for effect of velocity (Chexal *et.al.*,1996).

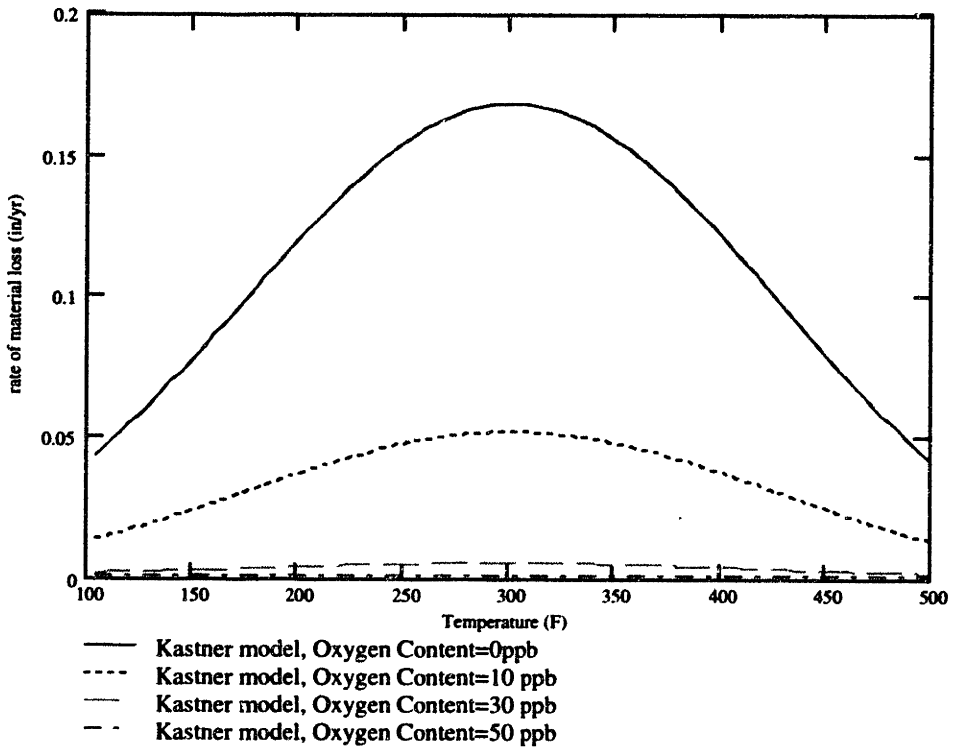

Figure 5-18. NFM predictions for variable oxygen concentrations.

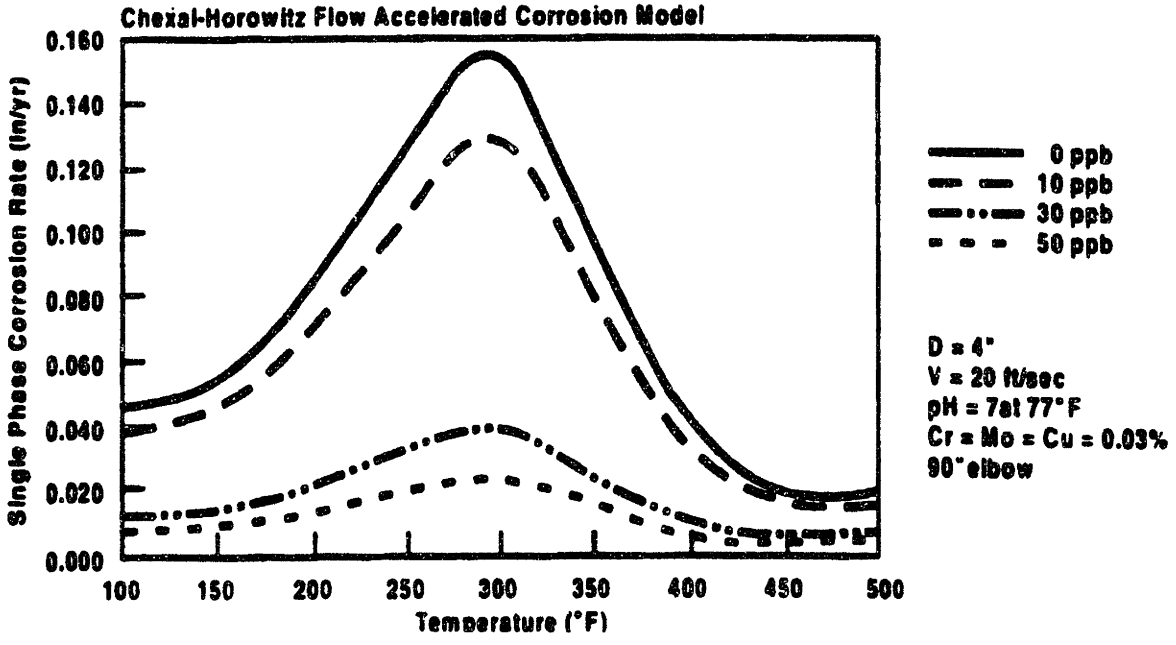

Figure 5-19. Chexal-Horowitz model predictions for effect ofdifferent oxygen concentrations (Chexal *et.al.*,1996).

Figure 5-20 and Figure 5-21 show the model predictions for NFM and Chexal-Horowitz, respectively, for a range of pipe diameters. Note that the NFM model does not use pipe diameter as an input parameter (see Table 2-1 or Figure 5-20). A likely contribution to the relatively high value of the Chexal-Horowitz model predictions as compared to other parameters (Figure 5-13 through Figure 5-20 and Figure 5-23 through Figure 5-25) is the small diameter pipe, 4in, used for the comparisons. Such a small pipe is not typical of power plant piping susceptible to single phase FAC[9]. Because the NFM model does not use the pipe diameter as input, the model is likely to only be conservative by a factor of 2 or 3 for larger pipes.

Figure 5-22 and Figure 5-23 show the model predictions for NFM and Chexal-Horowitz, respectively, for a range of cold pH values. At the peak value for low pH, the NFM predicts a value 80% greater than the Chexal-Horowitz model and at the high value for pH, the NFM mode predicts a value about 6 times larger. This indicates that over the range of pH from 8.7 to 9.39 the value of Chexal-Horowitz model is more sensitive to changes in pH value.

Figure 5-24 and Figure 5-25 show the model predictions for NFM and Chexal-Horowitz, respectively, for various piping geometries. The Chexal-Horowitz model predictions indicate a more complicated function is used as a to represent temperature than is used for the NFM model. At the peak value for the 180° turn, the NFM predicts a value larger by about 25%. At the peak value for the straight pipe, the Chexal-Horowitz model predicts a value larger by about 100%. Piping geometry of the NFM model is the

[9] Typical vent line piping from the tube side of reheaters to the high pressure feedwater heaters may be 4 inches in diameter, but this flow is two phase at high quality.

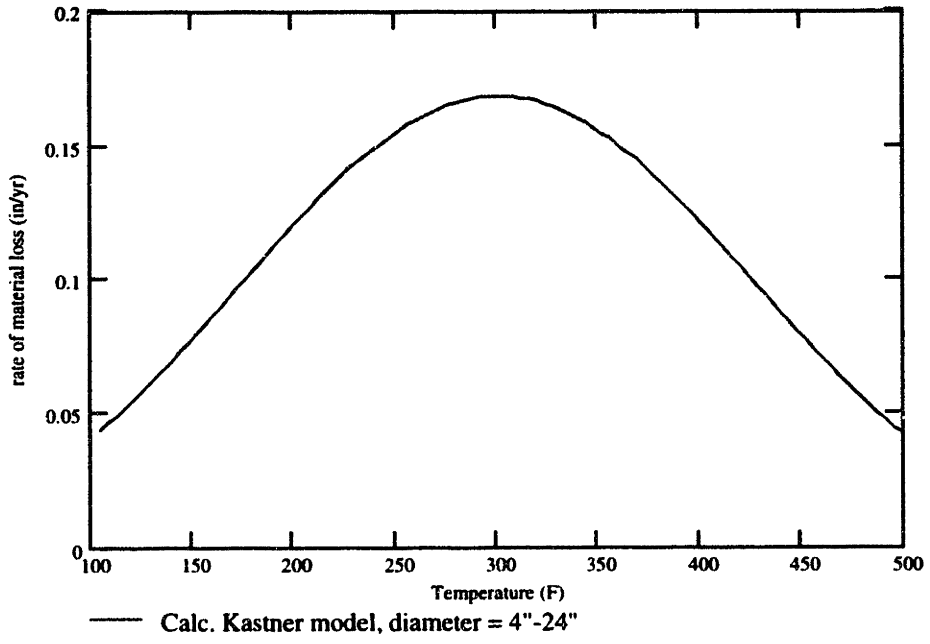

Figure 5-20. NFM predictions for variable pipe diameters.

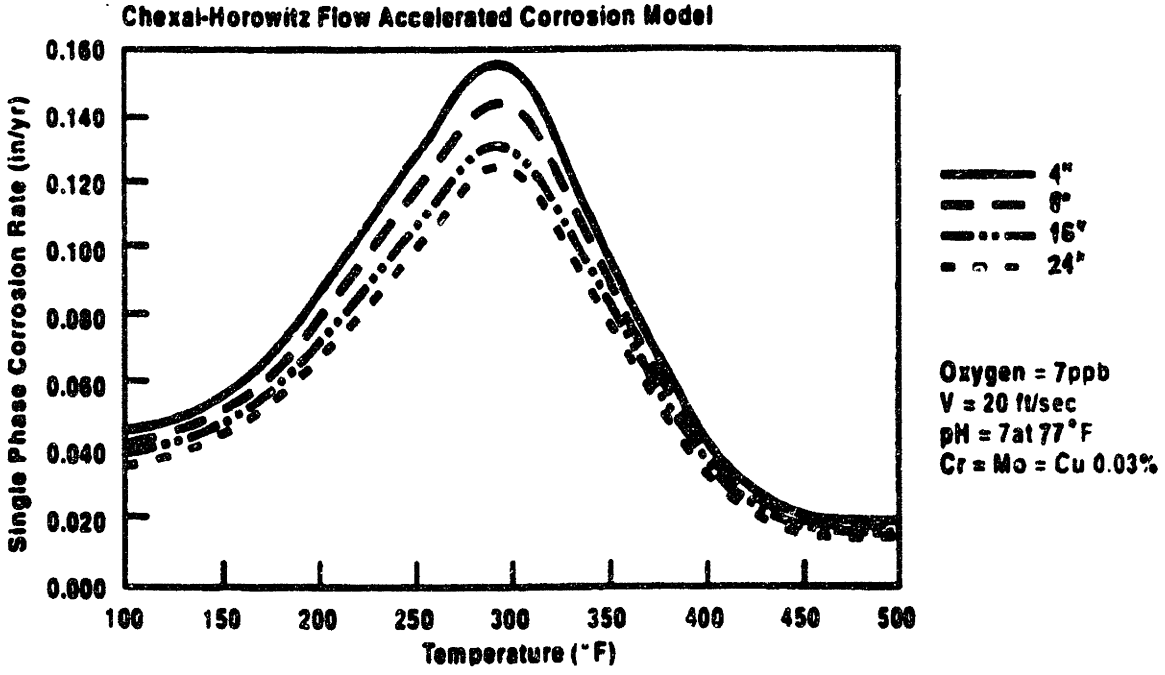

Figure 5-21. Chexal model predictions for effect of pipe diameter (Chexal *et.al.*,1996).

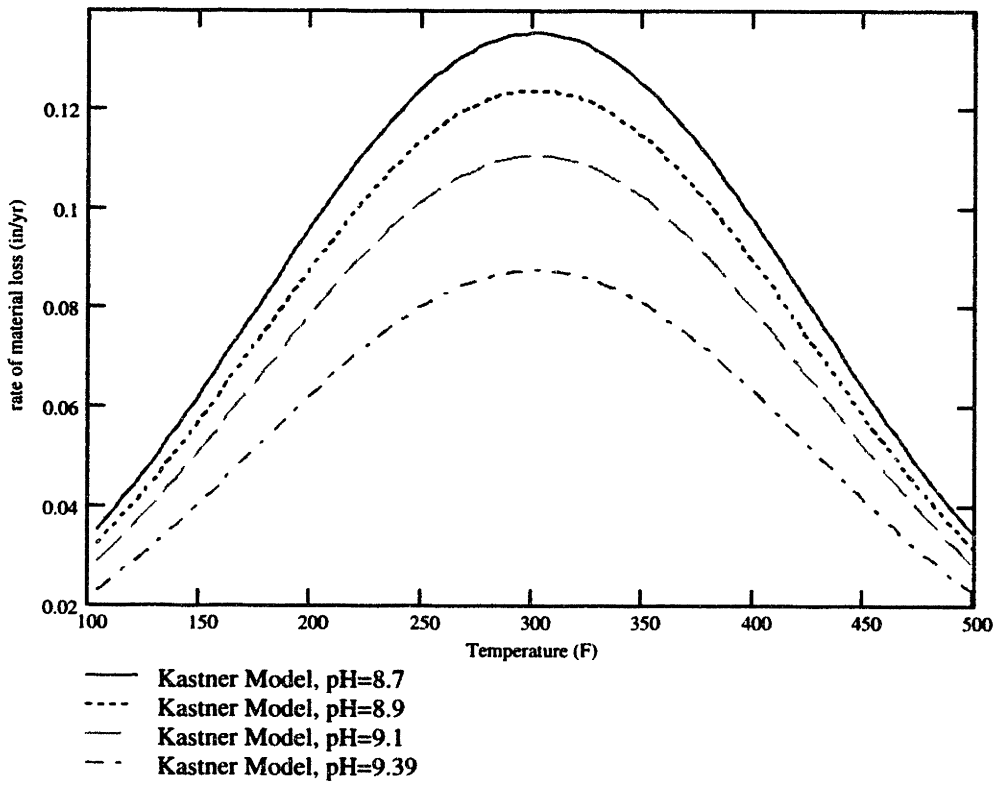

Figure 5-22. NFM predictions for variable pH values.

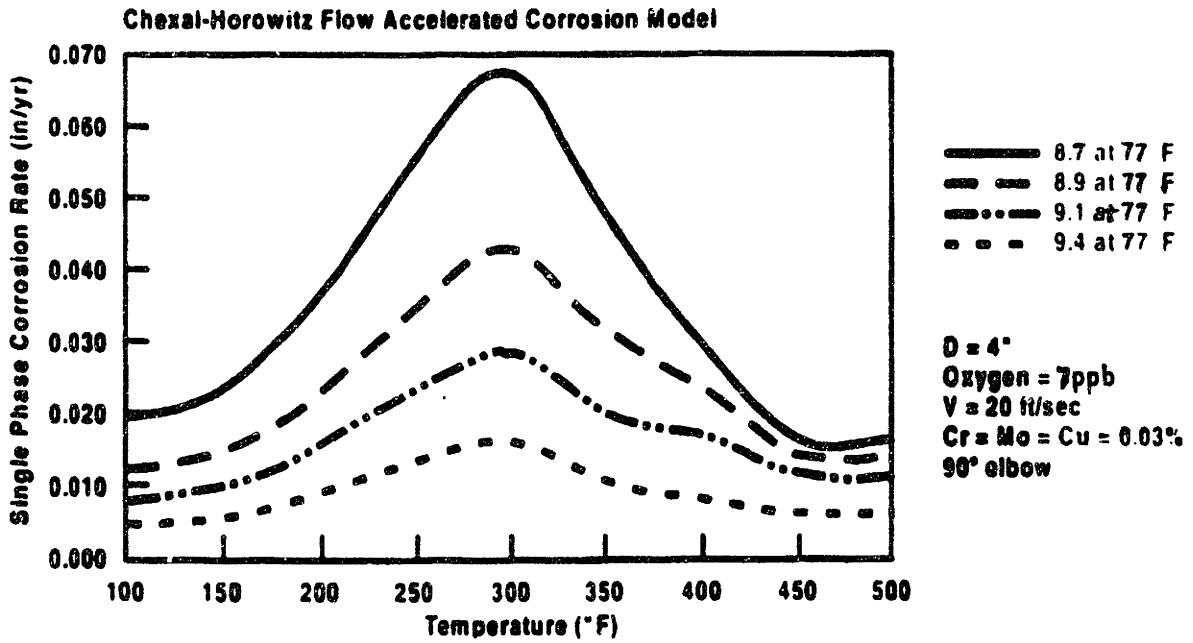

Figure 5-23. Chexal-Horowitz model predictions for effect of pH (Chexal *et.al.*,1996).

least developed of the independent variables and is expected to vary significantly when compared with other models.

Overall, the NFM compares well with the published Chexal-Horowitz model. The conservative NFM model typically predicts larger wear rates than the Chexal-Horowitx model, though not always as large as one might expect. Discrepancies can often be explained by the specific conditions being modeled.

In summary, from the physical understanding of the FAC wear process, five modifications have been made to the empirical Kastner model. The modifications include:

1) decoupling of velocity and alloying element content at low alloying element content,
2) elimination of the effect of oxygen for bulk oxygen concentrations below a critical value,
3) an improvement in the two-phase correlation used to estimate liquid phase velocity,
4) an adjustment of the cold pH factor to predict wear at higher values of pH, and
5) the removal of velocity dependence at high and low temperature to ensure physically accurate trends.

This resulting NFM was then shown to better predict Kastner's lab single phase data, Millstone Unit 2 single phase data, and Millstone Unit 3 two phase data. Finally, the NFM was compared against published data for the Chexal-Horowitz model and shown to have good agreement. The NFM, as described in Appendix D. New FAC Model, is incorporated into the SPPDP to predict FAC wear rate.

These results show the advantage gained in predicting FAC wear rate by incorporating into the model the physical principles that underlie the process. The author recognizes the need for checking this NFM against a greater amount of data to increase confidence that the changes are accurate. With more data it would also be possible to

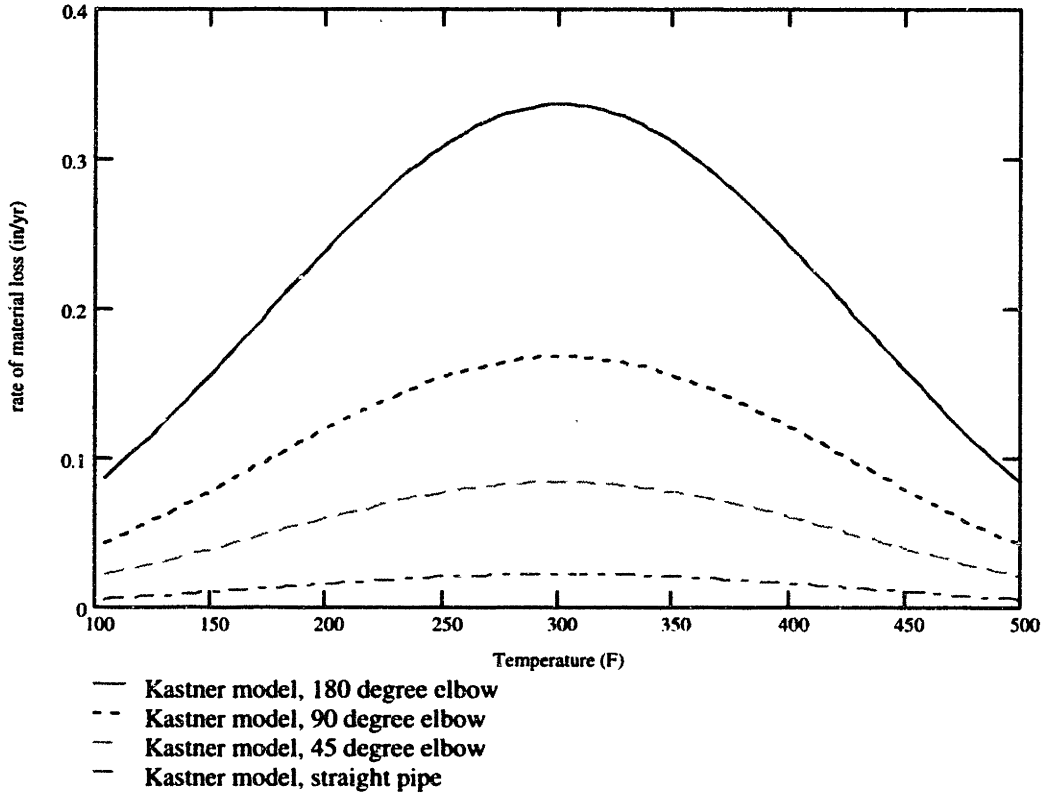

Figure 5-24. NFM predictions for variable piping geometries.

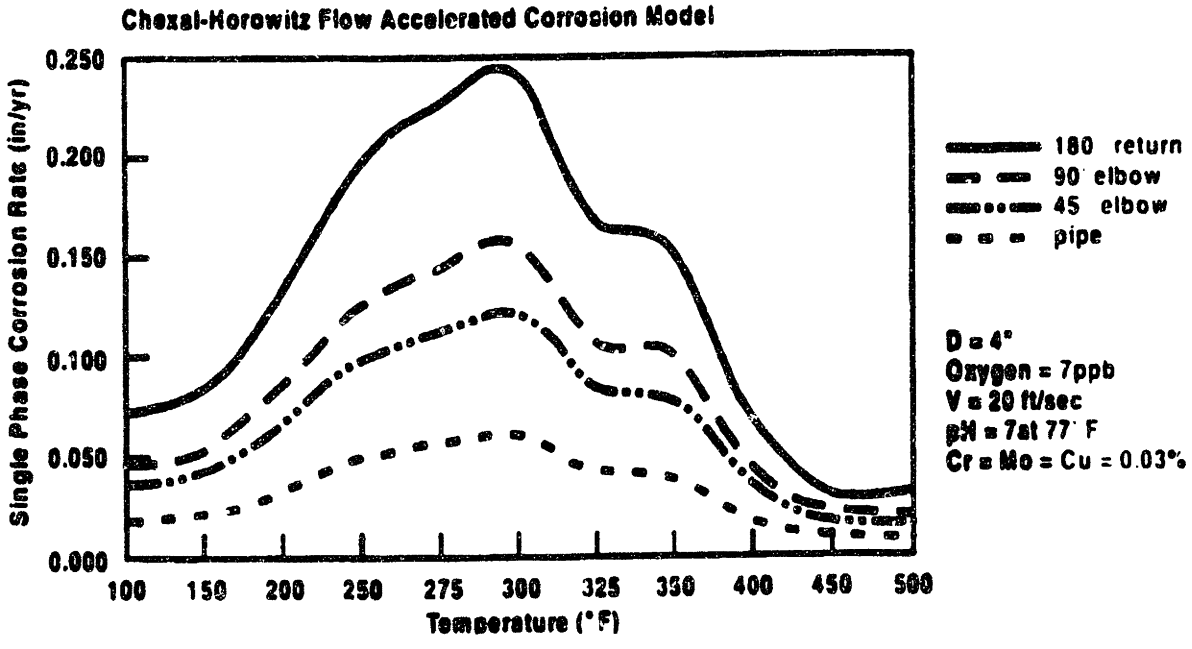

Figure 5-25. Chexal-Horowitz model predictions for effect of pipe geometry (Chexal *et.al.*,1996).

reformulate the Kastner model in terms of friction velocity or mass transfer coefficient, both of which characterize the transport layer. More data would also allow reformulation of the model with hot pH as an input parameter indicating the true hydrogen ion activity. Both endeavors are left for future work when significant amounts of data are available.

Chapter 6. Results and Discussion

To show reduction in uncertainty when predicting FAC wear and investigate potential sources of uncertainty in this prediction, the Secondary Plant Pipe Degradation Program (SPPDP) is used to model the secondary system of a power plant. The modular and technical features of the SPPDP can be best demonstrated by using the program to model a specific plant. While individual plant components modeled in the SPPDP were validated separately to ensure all possible inputs resulted in correct calculations (see Chapter 4), modeling a plant provides validation of the SPPDP's ability to model an entire system properly. Because of the amount of available information for Kori Unit 3, this plant is used to demonstrate the ability of the code to model thermodynamic, thermal hydraulic, and chemistry conditions for the secondary side of a power plant. Specifically, those parameters that are known to affect the FAC wear rate are computed. Upon calculating these parameters, wear rate predictions are made for different locations in Kori Unit 3 and compared to measured values with good agreement.

Using the Kori Unit 3 plant modeled in SPPDP as a base case, the contribution to uncertainty of the current method for incorporating chemistry parameters is investigated. This analysis shows considerable contribution to wear prediction uncertainty from postulated off-normal chemistry conditions. Recommendations on wear prediction methodology that can minimize this uncertainty are given.

6.1. Modeling Kori Unit 3: Nominal Operating Conditions

The process of building a system model in the SPPDP necessitates a significant amount of information. The information used for input into the SPPDP to model the Kori Unit 3 secondary system came from five sources:

1) a heat balance (HB) diagram developed in the design of the power plant which provides nominal mass flow rate and thermodynamic state information for the major fluid flows at various locations throughout the plant (see Figure 6-1),
2) piping and instrumentation (P&I) diagrams of the secondary system which provide information on mass and signal flows that are included in measurement and chemistry control, and information on parallel components connections,
3) isometric drawings of the pipes which provide specific information about pipe diameter, orientation with respect to gravity, and geometry,
4) plant specific chemistry calculations and average cycle measurements of chemical species concentrations at particular locations within the secondary, and
5) measured pipe wear rate data at 45 specific locations in the secondary system.

The HB diagram was primarily used for input and validation of the thermodynamic calculations. P&I diagrams and isometric drawings were used for input of piping segment information relevant for the thermal hydraulic calculation. The chemistry data was used to validate pH calculations at particular locations in the plant. The wear data is used to assess the accuracy of the developed model.

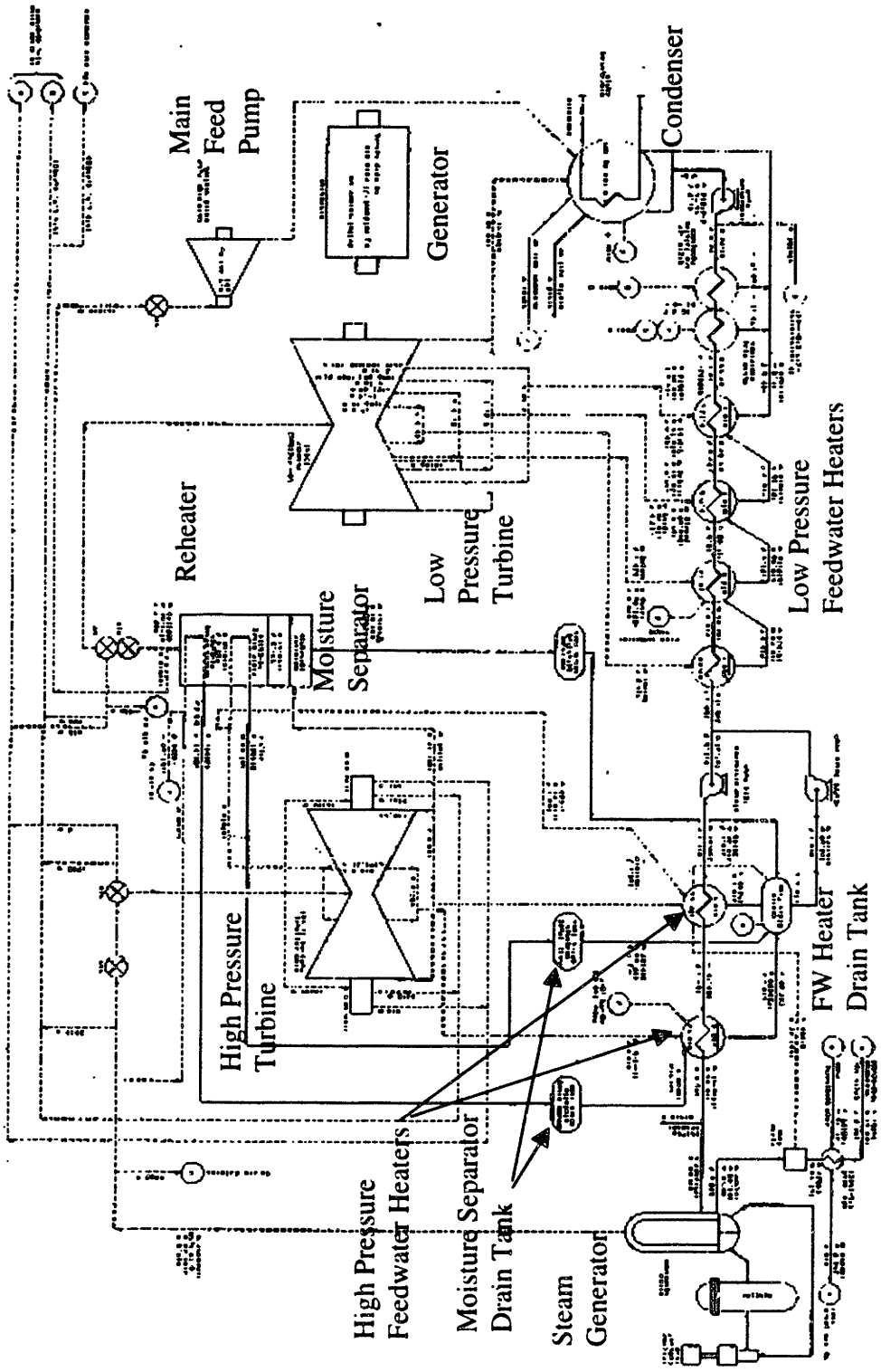

Figure 6-1. Heat Balance Diagram of Kori Unit 3 Secondary at 100% load, 1% steam generator blowdown, and 0.5% system makeup flow.

6.1.1. Thermodynamics

The HB diagram used to provide input for modeling the Kori Unit 3 secondary system is for 100% load, 1% steam generator blowdown, and 0.5% system makeup, typical conditions for this plant used to provide base load electricity and operate within EPRI recommended chemistry guidelines. Overall the agreement with thermodynamic information provided on Kori Unit 3 is very good. Differences in temperature and enthalpy are typically less than .01% and can be attributed to round off error and slight differences in state property relations used. Figure 6-2 shows the Kori Unit 3 secondary system as it represented in the SPPDP.

Because the mass flow rate information provided in the HB diagram is detailed for the major liquid flows, good agreement exists for the condensate and feedwater subsystem flow rates. For the high pressure (HP) turbine and associated reheaters, drain tanks, and feedwater heaters (FWHs) 5 and 6, the vent lines are included in the mass balance. For the low pressure(LP) FWHs 3 and 4, however, the energy increase of the condensate on the tube side is less than the energy decrease of the heating flow from extraction lines. Further, the P&I diagram shows vent lines for these two FWHs. While including these vent lines has a minor effect on the thermodynamics, their effect is significant on ensuring sufficient heat transfer in removing noncondensibles from the shell and on chemistry in removing volatile amines (reducing pH) and oxygen from the drain lines. For these reasons vent lines were included in modeling FWHs 3 and 4, even though they are neglected on the HB diagram. Table 6-1 lists the HB diagram mass flow rates and modeled mass flow rates using SPPDP.

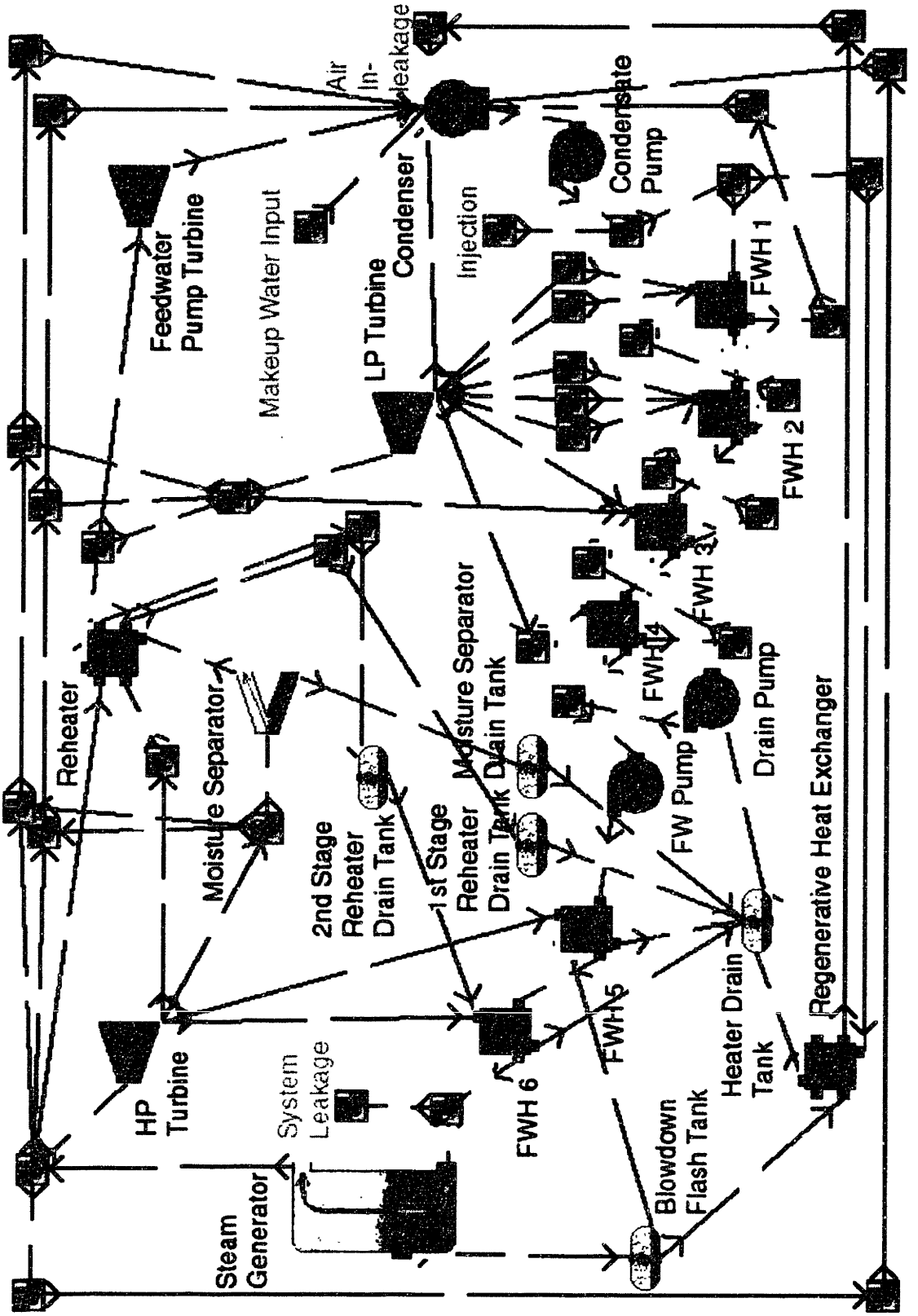

Figure 6-2. Model of Kori Unit 3 developed using the SPPDP indicating the external chemistry interfaces of the secondary system.

Table 6-1. Comparison of mass flow rates and tube and shell temperature differences calculated by SPPDP and indicated on the HB diagram (in parentheses) for the low pressure feedwater heaters 1-4 of Kori Unit 3.

SPPDP Value (HB Value)	Feedwater Heater #			
	1	2	3	4
Drain Mass Flow Rate [lb/hr]	1808515 (1818365)	1432965 (1442815)	1027320 (1037170)	557484 (561984)
DT Condensing Section [°F]	4.8 (5.0)	4.8 (5.0)	4.8 (5.0)	5.0 (5.0)
DT Drains Cooling Section [°F]	9.5 (10.0)	9.5 (10.0)	9.8 (10.0)	19.9 (10.0)

A comparison of component efficiencies and the system power output also shows good agreement between SPPDP calculations and HB information. Table 6-2 lists the component efficiencies computed for the turbines and pumps. All pump efficiencies are close to that information listed on the HB diagram and the computed efficiencies for the Low and High Pressure Turbines are reasonable values.

Table 6-2. Comparison of component efficiencies and system power produced calculated by SPPDP and indicated on the HB diagram for turbines and pumps of the system.

	Component Isentropic Efficiency [%]		Component Power [MW]	
	SPPDP	HB	SPPDP	HB
High Pressure Turbine [MW]	82	-	330.68	-
Low Pressure Turbines [MW]	82.25	-	673.32	-
Main Feedwater Pump Turbine [MW]	75	75	10.911	10.689
Condensate Pumps [MW]	86.56	85	5.0748	-
Heater Drain Pumps [MW]	85.95	85	0.9673	-
Feedwater Pumps [MW]	84.79	85	10.689	-
Generator Efficiency [%]	-	-	-	98.92
Generator Output [MW]	-	-	987.17	989.90
Heat Rate [BTU/kWhr]	-	-	9600	9626

Table 6-2 also lists SPPDP calculations of the energy produced by the turbines and the energy consumed by the pumps. Computing the generated electric energy at the generator terminals based on these SPPDP calculations again shows good agreement with HB diagram information. The error in the computed generator output power is 0.28% and the error in the computed heat rate is 0.27%. The error in the reported Main Feedwater Pump Turbine (MFPT) power is 1.99%. The MFPT power listed exactly matches the power consumed by the Feedwater Pumps so this 1.99% difference is likely to be caused by the fact that the HB diagram value reported includes mechanical losses and the SPPDP calculation does not.

6.1.2. Thermal Hydraulics

The essential parameters calculated in the thermal hydraulic calculation that affect the degradation rate are the liquid velocity used for estimating FAC wear and the vapor velocity used for estimating droplet impingement wear. As indicated section 3.3.3, the input to this calculation includes mass flow rate, steam quality, and pipe internal diameter. Pipe internal diameters are taken from the isometric drawings. No velocity information was supplied for Kori Unit 3, so validation of those velocities calculated against measurements is not possible. Liquid and vapor velocities computed for the locations where FAC wear measurements have been supplied are listed in Appendix F. Kori Unit 3 Raw Data.

6.1.3. Residence Time: Component Volumes and Piping System Lengths

In order to perform time dependent Non Equilibrium Reactions for a system modeled in the SPPDP, one must supply information on pipe lengths and component

volumes. (see section 3.3.4.2). This information is necessary to determine the amount of time species spend in the various components, referred to as residence time, which affects the extent of species removed and produced in reactions.

The pipe lengths used for the Kori Unit 3 system are taken from the isometric drawings. Information of component volumes in Kori Unit 3 is not readily available. Estimates on FWH shell and tube volumes are based on throughput times as indicated in the literature (Jonas, 1988) and FWH schematics given in the Heat Exchange Institute (HEI) design recommendations (HEI, 1979). Appendix E. Kori Unit 3 Component Volume Calculations provides the set of expressions used to determine volumes for three sections of the FWHs: the tube section, the condensing section, and the drain cooling section. The latter two of these sections comprise the shell section, referred to section 3.2.1. Moisture Separator volume is determined in a similar manner from drawings provided in the literature (Cohen, 1989). Condenser volume is based on HEI recommendations that the hotwell be able to contain full power flow for 1minute and assuming the hotwell is approximately 1/3 full during normal operation (HEI, 1978). Steam generator volume is determined from information on a typical Westinghouse Model F design (EPRI, 1985). Reheater tube volumes and drain tank volumes are estimates. Residence times for Junctions, Turbines, and Pumps are approximated to be zero. Appendix E provides the assumptions, equations, and references used to determine the remaining component volumes. Table 6-3 summarizes the results from Appendix E giving, state information, the component volumes, the number of similar components modeled in parallel (based on P&I diagrams), and the resulting computed residence time by the SPPDP.

Table 6-3. Summary of component volumes and residence times computed for the Kori Unit 3 secondary system.

Component (Section)		Pres-sure [psia]	Temper-ature [°F]	Component Volume [m^3]	Number of Parallel Components	Residence Time [sec]
Condenser		0.735	92	63	1	59.15
Feed-water Heater 1	Tube	430	94	3.80	3	10.76
	Condensing	2.22	130	0.757	3	9.83
	Drain Cooling	2.22	103	1.67	3	21.75
Feed-water Heater 2	Tube	375	125	3.30	3	9.24
	Condensing	5.71	168	0.658	3	10.65
	Drain Cooling	5.71	135	1.45	3	23.67
Feed-water Heater 3	Tube	375	163	3.36	3	9.19
	Condensing	20.1	228	0.669	3	14.68
	Drain Cooling	20.1	173	1.47	3	33.19
Feed-water Heater 4	Tube	375	223	3.45	3	9.14
	Condensing	62.2	375	0.687	3	26.79
	Drain Cooling	62.2	243	1.51	3	61.09
Feed-water Heater 5	Tube	1140	369	7.30	2	8.25
	Condensing	171.6	318	1.45	2	25.8
Feed-water Heater 6	Tube	1140	364	7.70	2	8.12
	Condensing	400.4	445	1.52	2	11.53
	Drain Cooling	400.4	374	3.34	2	26.88
Steam Generator		1140	440	60	3	86.78
Flash Tank		907	533	0.5	1	28.38
First Stage Reheater Drain Tank		412.7	448	2.5	4	179.94
Second Stage Reheater Drain Tank		913.5	534	4.5	4	197.07
Moisture Separator Drain Tank		176	371	4.5	2	52.53
Feedwater Heater Drain Tank		171.6	369	36.0	1	60.15
Moisture Separator		180.6	373	28	2	41.35
Reheater	First Stage Tube	425.2	451	.05	4	3.44
	Second Stage Tube	916	534	.05	4	1.93

For Table 6-3, temperatures and pressures refer to inlets of components (or sections) except for the FWH Drain Cooling section for which outlet values are listed.

Further, condensate pressures listed in the table are not exact. Because these pressures are not computed by the SPPDP and because they do not significantly affect the calculations performed to predict the degradation rate, there was no need to reevaluate the pressures.

The condensate and feedwater subsystems require the most accurate residence time information. Because of the nature of chemistry control used in Kori Unit 3 (see 6.1.4 Chemistry), modeling these subsystems and the corresponding source terms accurately is sufficient for modeling the parameters currently identified to affect the FAC rate. Combining the pipe and component transit times for theses subsystems results in a total transit time between condenser and stream generator of 2 minutes for the model of Kori Unit 3. This transit time matches well with that reported in the literature (Jonas, 1988).

6.1.4. Chemistry

As is typical of PWRs, Kori Unit 3 uses All–Volatile Treatment (AVT) chemistry control (EPRI, 1993). For Kori Unit 3, pH control is provided by ammonia and the deoxygenated environment is achieved by hydrazine injection. As mentioned previously, the two main chemistry parameters affecting FAC are the pH and oxygen concentration. Therefore chemistry modeling of Kori Unit 3 using the SPPDP includes hydrazine, ammonia (as well as other decomposition products of hydrazine), and oxygen.

Chemistry modeling can best be described in terms of the source and sink processes that affect these various chemistry groups. Hydrazine is injected after the condensate pumps, reacts with oxygen in the condensate and feedwater subsystems, and predominantly decomposes to ammonia before returning to the condenser. Ammonia is

injected after the condensate pumps as well and removed via system leakage and air ejection from the condenser. Ammonia is produced by hydrazine decomposition to a lesser extent than it is removed, thus requiring injection. As a relatively volatile amine, ammonia partitions predominantly into the vapor phase as it is transported through the two phase portions of the secondary.[10]

The major source of oxygen ingress is air inleakage into components operating below atmospheric pressure. For Kori Unit 3 at 100% power, the subatmospheric components modeled by the SPPDP are the condenser and the first two feedwater heaters. Potential oxygen ingress may also come from makeup water fed into the condenser. Available measurements of oxygen concentration only indicate concentrations exiting the condenser, for which it is not possible to discern the amount of oxygen coming from makeup water as opposed to air inleakage. For the purpose of predicting FAC, the important parameter to match to measurements is the exiting condenser concentration. Therefore, the model of Kori Unit 3 simply assumes that the oxygen concentration comes solely from air inleakage, the major source for most plants. Beyond the steam generator oxygen exists predominantly in the vapor phase because of its high volatility. The resulting concentration in the liquid portion of two phase flows is too low to provide protection against FAC beyond the steam generator.

Figure 6-2 shows the model generated in the SPPDP indicating the locations for chemical injection, air inleakage, system leakage, and system makeup water input in red.

---

[10] The volatility of ammonia relative to other amines used in other PWRs and modeled in the SPPDMME including morpholine and ETA result in a lesser portion of the amine in the liquid flow, reducing the pH protection necessary to inhibit FAC.

Note that though the system leakage is modeled to occur only after the last feedwater heater. This leakage actually occurs throughout the condensate and feedwater subsystems, but no error occurs in computing reaction rates by assuming it occurs at a single location. Reaction rates are based on species concentration. The concentrations are not affected by leakage flow because leakage removes species at the same concentration as the bulk flow thus not affecting bulk concentration.

Chemistry data provided for Kori Unit 3 indicates that the nominal operating conditions include feedwater cold pH (measured at 25 ° C) equal to 9.4 and condenser exit oxygen concentration less than 10 ppb. An air inleakage value of 6 SCFM was assumed based on limits indicated by the HEI to maintain such low oxygen concentrations in the condensate. For a nominal value of typical condenser ejection flow rate of 750 lb/hr the resulting exit condenser oxygen concentration is 8.0 ppb. Values of ammonia and hydrazine injection were adjusted and the model of Kori Unit 3 run until steady state values of 9.4 for feedwater cold pH and 55 ppb for condensate hydrazine were achieved. (Note that the most recent EPRI guidelines recommend a condensate hydrazine concentration greater than three times the oxygen concentration.)

With the known measurements of water chemistry met, attention is turned to checking the accuracy of the SPPDP calculations for the rest of the Kori Unit 3 model. To adequately predict FAC wear rate, the secondary system cold pH and the condensate and feedwater oxygen concentrations must be calculated accurately. The following sections provide validation of these calculations.

6.1.4.1. System pH Validation

In order to validate the chemistry calculation for the model of the Kori Unit 3 secondary system, SPPDP results are compared against chemistry information provided by the utility for the same system. Additional information on this data indicates that though the run is for 100% power, the thermodynamic conditions used differ from those used in developing the plant model in the SPPDP in terms of both flow rates and thermodynamic state. Because not enough information is given to determine the entire secondary system state used as input for this data, it is not modeled in the SPPDP. Instead, the model based on the HB diagram is used to compare results with expectations that trends will still match. Despite differences in thermodynamic state, the SPPDP results match well with those of the utility data provided and certainly follow the same trend.

Differences in calculations between SPPDP and data provided by the utility may exist because the data given does not specify the exact location in the component to which the calculation correspond. The most significant differences in the data exist for the FWH shell side values of hot pH (with the exception of FWH 5). The location in each component to which the CW values refer is not clear. The SPPDP value shown in Table 6-4 for each "Feedwater Heater Shell Side" is the value calculated at the drains cooling section exit. Because of changes in temperature through the drains cooling section, hot pH increases by as much as 0.6 pH units. Therefore, SPPDP values are larger than those reported from the utility data, but not by more than 0.6 pH units so that the inlet and outlet SPPDP values bound the reported utility value. Values calculated for FWH Shell Side 5 do not differ, because this FWH does not have a drains cooling section. A similar explanation exists for differences in data for the tube sides of FWHs 5 and 6. In this case,

the SPPDP value given is for the exit of the FWH tube. Because the temperature is increasing, the value of hot pH decreases by 0.3 pH units through the tube section. Therefore, the value calculated by the SPPDP code is less than that reported in the utility data, but not by more than 0.3 pH units. Again the SPPDP inlet and outlet values bound the reported utility values.

Table 6-4. Comparison of SPPDP results for modeled secondary system with utility data for operation at 100% power. For two phase lines the cold pH reported is for the mixture of steam and water. The concentrations and hot pH are for the water phase only. For superheated steam no amine concentration or hot pH is reported as no water phase is present.

	Cold pH SPPDP(Utility)	Hot pH SPPDP(Utility)	Ammonia [ppm] SPPDP (Utility)
Steam Generator Blowdown Line	9.03 (9.01)	5.79 (5.77)	0.28 (0.28)
Steam Generator Outlet Steam	9.36 (9.38)	5.80 (5.77)	0.28 (0.29)
High Pressure Extraction Line #1	9.37 (9.38)	5.87 (5.87)	0.28 (0.24)
HP Extraction Line #2	9.37 (9.38)	8.05 (8.00)	0.28 (0.18)
Moisture Separator Drain Line	8.96 (8.95)	6.13 (6.13)	0.23 (0.23)
Low Pressure Extraction Line #1	9.40(9.38)	-	-
Low Pressure Extraction Line #2	9.39 (9.40)	7.03 (6.99)	0.21 (0.22)
Low Pressure Extraction Line #3	9.40 (9.40)	7.59 (7.58)	0.20 (0.20)
Low Pressure Extraction Line #4	9.40 (9.40)	8.03 (8.02)	0.18 (0.19)
#1 Feedwater Heater Tube Side	9.39 (9.37)	8.62 (8.62)	1.08 (0.96)
#2 Feedwater Heater Tube Side	9.39 (9.37)	8.13 (8.12)	1.08 (0.96)
#3 Feedwater Heater Tube Side	9.39 (9.40)	7.50 (7.51)	1.08 (1.06)
#4 Feedwater Heater Tube Side	9.39 (9.40)	6.95 (6.97)	1.08 (1.06)
#5 Feedwater Heater Tube Side	9.36 (9.40)	6.45 (6.52)	0.98 (1.06)
#6 Feedwater Heater Tube Side	9.36 (9.40)	6.12 (6.20)	0.98 (1.06)
#1 Feedwater Heater Shell Side	9.36 (9.38)	8.94 (8.62)	0.89 (0.97)
#2 Feedwater Heater Shell Side	9.38 (9.38)	8.49 (8.13)	0.95 (0.97)
#3 Feedwater Heater Shell Side	9.40 (9.40)	8.02 (7.52)	1.03 (1.07)
#4 Feedwater Heater Shell Side	9.41 (9.40)	7.32 (6.97)	1.06 (1.07)
#5 Feedwater Heater Shell Side	9.40 (9.40)	6.51 (6.52)	1.02 (1.07)
#6 Feedwater Heater Shell Side	9.39 (9.40)	6.43 (6.20)	0.99 (1.07)
#1 Reheater Drain Line	9.39 (9.38)	5.87 (5.87)	0.24 (0.24)
#2 Reheater Drain Line	9.39 (9.38)	5.80 (5.77)	0.28 (0.28)
#1 Drain Tank	9.02 (9.01)	6.05 (5.77)	0.16 (.028)
#2 Drain Tank	9.32 (9.30)	6.43 (6.41)	0.77 (0.73)

6.1.4.2. Condensate and Feedwater Oxygen Concentration Validation

Non Equilibrium Reaction results for hydrazine in the model of Kori Unit 3 in the SPPDP are compared with Figure 6-3(Chexal *et. al.*, 1996). Figure 6-3 shows the typical trends for the amount of oxygen removal and ammonia production through the condensate and feedwater subsystems of a PWR plant. Because the transit time from condenser to steam generator is not given for the figure, one cannot make direct numerical comparisons with the SPPDP results. Comparison of trends in oxygen reduction and ammonia production, however, can be expected to match.

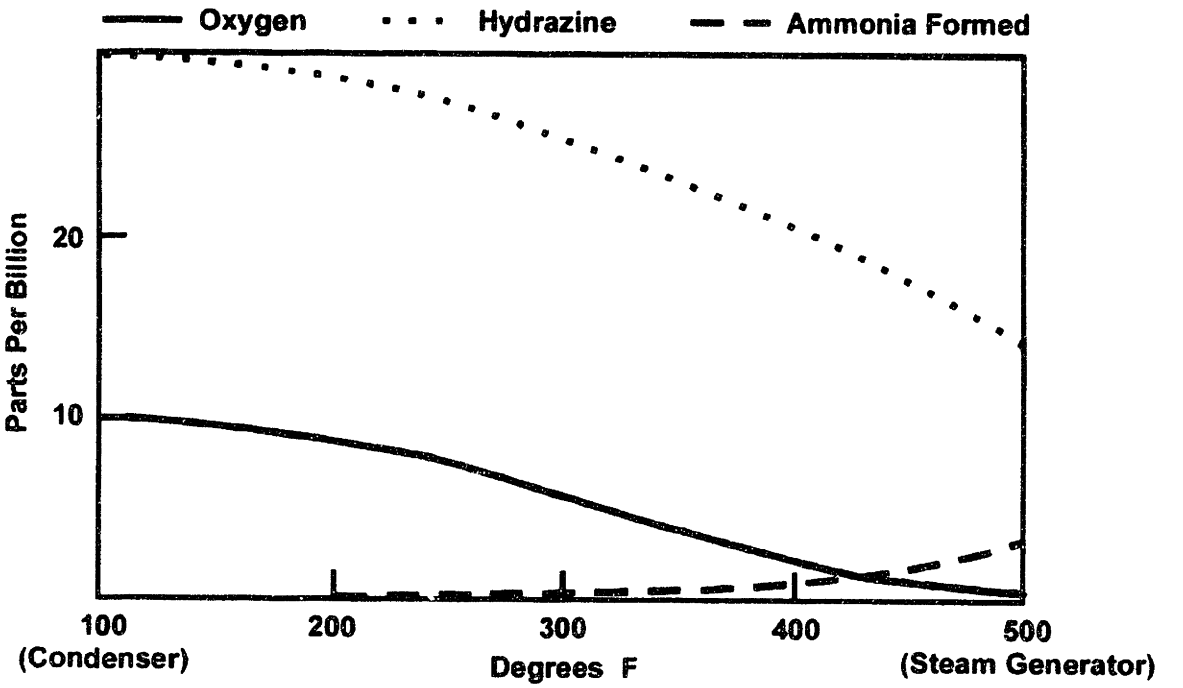

Figure 6-3. Hydrazine reaction with oxygen and decomposition to hydrazine in the condensate and feedwater subsystems.

For a condensate hydrazine concentration, Figure 6-3 shows oxygen reduction from 10 ppb at the condenser to 1 ppb at the steam generator entrance. For a condensate hydrazine concentration of 55 ppb, the SPPDP calculates an oxygen reduction from 8.0 ppb to 1.2 ppb at respective locations. Figure 6-3 also shows minimal ammonia

production (<1 ppb) from hydrazine decomposition below 300 °F. At the outlet of FWH 4 (at 290 °F), the SPPDP calculates an increase in ammonia concentration of 0.32 ppb. Beyond 300 °F, Figure 6-3 shows ammonia production of 3.5 ppb. The ammonia production computed for the model of Kori Unit 3 in SPPDP is 2.2 ppb. For higher concentration of condensate hydrazine and equal total transport time, one would expect a greater amount of ammonia production and oxygen reduction. Because the values given in Figure 6-3 are greater than the SPPDP results, one can conclude that the transit time used to develop the figure is longer. In any case, the general trends of production and removal shown in the figure match well with calculations of the SPPDP.

6.1.5. FAC Wear Rate Predictions vs Measurements

To test if the SPPDP can be used to accurately predict FAC wear rate, one must compare FAC wear predictions from the code to measured data for the plant modeled. For Kori Unit 3 measured wear rates for piping locations marked on the isometric diagrams were provided by the utility. When all information affecting wear is eitner computed by the SPPDP or supplied as input, the code will automatically compute predicted wear (see section 3.3.5).

In addition to the thermodynamic, thermal hydraulic, and chemistry data calculated by the SPPDP, two additional parameters must be supplied to predict the FAC wear using the SPPDP. These factors are the time of operation for and the alloying element content of the piping segments being worn. Based on plant cycle information provided by the utility, the time of operation for the plant at the time the wear measurements was taken to be 12.66 years. It is assumed that the piping at locations for

which wear measurements are given have not been replaced since the beginning of operation for the plant. The alloying element content (the sum of chromium and molybdenum concentrations) for all piping segments is unknown. The value assumed for all locations is 0.03% based on nominal values measured for other power plants. Because this value is unknown for each segment it is expected to contribute to uncertainty in wear predictions.

At locations in the Kori Unit 3 model in which sufficient information is supplied, wear predictions are made by the SPPDP. For the 45 locations at which wear predictions are supplied by the utility, Figure 6-4 shows a log log plot of the wear measured against the wear predicted using two different methods. The first method is the prediction of FAC wear with the Kastner Model integrated into the SPPDP. The second method is the wear prediction using the integrated new FAC model described in Chapter 5. A clear improvement in prediction accuracy is seen for the new FAC model prediction.

Table 6-5 lists the mean and standard deviation (**see Eq. 5-20** and **Eq. 5-22**) of the lognormal distribution characterizing the ratio of predicted wear to measured wear using these two methods. For the new FAC model, the mean is almost identical to that found for the single phase laboratory data of section 5.2.1.1. indicating its accuracy. For the modified Kastner model, the mean is much lower than that found when predicting laboratory data. The scatter of the ratio of predicted to measured wear is also considerably less for the new FAC model. These results indicate the increased accuracy and significantly reduced uncertainty of the new FAC model. Appendix F. Raw Data Calculated for Kori Unit 3 lists the raw data computed by the SPPDP code and used to predict wear rates for the 45 measured locations in Kori Unit 3.

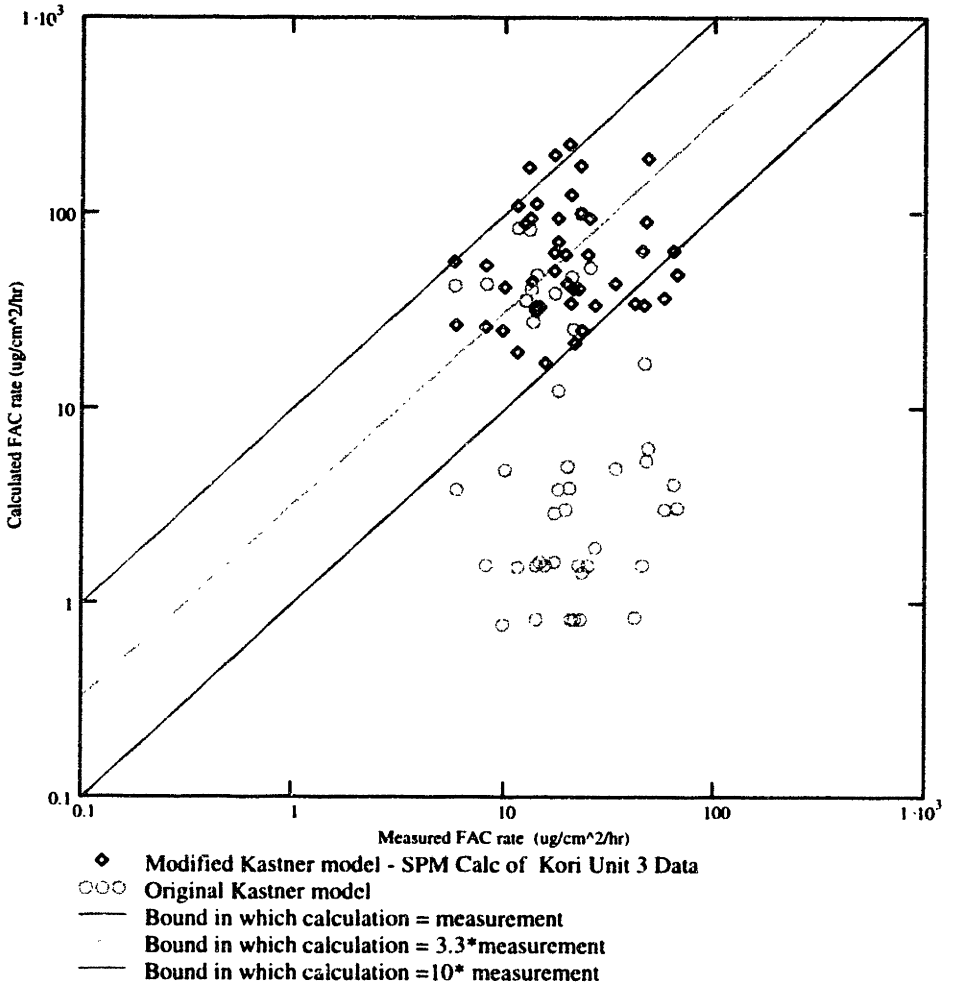

Figure 6-4. Plot of measured wear rates for the Kori Unit 3 secondary system against predicted wear rates using the Kastner Model and the new FAC model.

Table 6-5. Mean ratio of calculated wear to measured wear for the original Kastner model and MKKWM. The standard deviation is normalized to that mean ratio.

	μ_{LN_R}	σ_{LN_R}	Mdn_{Rt}	Rt_{span}
Kastner Model	-1.257	1.729	0.285	17.19
New FAC Model	1.057	0.817	2.861	3.834

For the reported nominal chemistry for Kori Unit 3, SPPDMME gives better results than were previously possible from information in the literature. These results still show uncertainty in predicted verse measured wear rates. This uncertainty, however, is

much lower than that produced from previously reported models. Further, the standard deviation computed for the Kori Unit 3 data is not as low as that found in Chapter 5 for single phase data. The expected reason for this is that the percentage of alloying elements at each location is unknown and this percentage contributes significantly to model uncertainty (Ardillon, 1994), so the larger value of uncertainty is expected.

6.2. Investigation of Off Normal Chemistry Effect on FAC Rate

As shown in Figure 2.6 and Figure 2.8, FAC model wear predictions plotted against measured wear rates, and in .he previous section for the SPPDP, a large scatter exists in the ratio of predicted against measured data. Regardless of the model used for prediction, the deviation ranges over at least an order of magnitude. Further progress can be made to reducing uncertainty predictions of FAC wear rate predictions by investigating those parameters that have not yet been identified to affect FAC or investigating the relevance of how currently modeled parameters are incorporated. In addition to providing a more accurate estimate of degradation rate, the SPPDP can be used to investigate these contributions to model uncertainty.

The SPPDP was devised to investigate model uncertainties either caused by unidentified significant parameters or improper combination of the parameters already incorporated in the model. This section gives the results of an investigation of cold pH and oxygen concentration are incorporated in the current SPPDMME formulation. The investigation shows that using nominal values for chemistry parameters over the lifetime of the plant is a significant contributor to the uncertainty in the prediction rate.

6.2.1. Chemistry and Time Features of FAC

A number of points are important to consider in comparing the incorporation of the chemisty parameters in the predicting a time averaged wear value against the events that actually contribute to the time average wear rate[11].

As previously described in Chapter 5, the chemistry parameters, cold pH and oxygen concentration, are incorporated differently in the new FAC model than in the Kastner model. The new FAC model uses a modified pH factor to compute the wear rate assuming no oxygen is present. This deaerated wear rate is then compared to the transport of bulk oxygen to the corroding surface. If the supply of oxygen to the surface is sufficient to inhibit the wear rate, i.e. larger than the necessitated threshold set by the deaerated FAC rate, it is incorporated in the model as an exponential factor. For values of oxygen concentration and pH constant over a sufficient amount of time, this model is expected to accurately predict the resulting constant wear rate. In the current implementation, nominal values for either the service life or the most recent operating cycle are input for pH and oxygen concentration. During plant operation, however, the values of oxygen concentration and pH vary from hour to hour. Because of the threshold

---

[11] There exists a time parameter in the Kastner model which does not differ in the new FAC model. This parameter is a single input of the time of operation for the piping segment being worn. For the first 12 years the factor decreases from 1.0 to 0.8. In the remaining years, the factor increases from 0.8 reaching 2.25 after 30 years of life. Literature data shows little physical justification for this time factor trend. Insufficient information exists, however, to change it. Further, it is not clear in the Kastner formulation, whether this time factor has been validated for times of operation longer than 12 years.

effect, nominal values of these parameters are not likely to yield the lifetime averaged or cycle averaged wear rate.

In addition, numerous investigators recognize that the required time for corrosion film destruction can be much less (on the order of hours) than that required for corrosion film reformation. In discussion of chemistry transients, Jonas notes, "Destruction of passivity can occur quite rapidly; repair and recovery are much slower processes." (Cohen, 1989). Kastner reports film formation times of 200 hours (8 days) (Kastner, 1987). Sanchez-Caldera reports film formation times of 150 hours, about 6 days (Sanchez-Caldera, 1984). Bignold and Woolsey show the importance of chemistry history on current wear rates (Bignold and Woolsey, 1980). Therefore, off normal chemistry operation occurring only for a few hours can have impact on the wear rate for the ensuing days.

Finally, current typical operating conditions for pH and oxygen concentration for plants such as Kori Unit 3 are chosen based on EPRI guidelines. Current guidelines specify a maximum suggested condensate oxygen concentration of 10 ppb before corrective action must be taken, but no lower limit (EPRI, 1993). As shown in the next section, currently advised oxygen levels are on the oxygen threshold with the potential for slight changes in oxygen concentration to cause large oscillations in the steady state wear rate. Oxygen concentrations above 30 ppb are required before corrective action must be taken in conjunction with reduced power.

Information supplied by Kori Unit 3 utility indicate that older guidelines are used for determining pH. These EPRI guidelines specify a final feedwater pH range for all-ferrous systems with condensate polishers in operation (such as Kori Unit 3) of 9.0 to 9.6

for which no corrective action need be taken. At pHs below 9.0 corrective action should be taken but reduction in power is not required.

In summary investigation into a history effect of the chemistry parameters can be justified by the following observations:

1) the sensitivity of wear calculation in the range of reported oscillations of pH is significant. This pH value determines the deaerated wear rate which affects the threshold oxygen concentration,
2) the time of corrosion film destruction is significantly shorter than the time of corrosion film reformation,
3) current typical operating chemistry conditions result in wear conditions near the oxygen threshold, and
4) the current EPRI PWR Secondary System Guidelines provide only an upper bound on suggested oxygen concentration (FAC wear worsens for lower oxygen concentrations) and a large range in allowed pH

In essence, input of a single averaged parameter throughout the service life of the degrading piping segment is insufficient. These observations motivate the quantification of uncertainty in the wear rate prediction caused by the history effect of chemistry parameters.

6.2.2. Calculated Uncertainty Caused by a History Effect of Chemistry Parameters

The SPPDP is used to investigate the history effect of the chemistry parameters and the resulting effect on wear prediction uncertainty. Because no additional parameters are being investigated, the model of Kori Unit 3, described in Section 6.1. is used without the necessity for inputting additional plant information. For the same 45 wear locations used in the previous section, wear rate is determined for a set of postulated off normal chemistry conditions. These conditions and their likelihood are determined based on plant and literature information. Because the SPPDP calculates steady state system pH and

species concentration based on the system sinks and sources and specie reactions, the set of chemistry conditions was achieved through an iterative process. The postulated range of final feedwater cold pH and condenser outlet oxygen concentrations are met by adjusting injection and air inleakage flow rates, respectively, in the Kori Unit 3 model.

The set of off normal chemistry conditions used is listed in Table 6-6 with the associated probability of operating in that condition. No continuous chemistry data was available for a plant of similar design, so the set of conditions are based on the following sources:

1) Kori Unit 3 information on the range of blowdown pHs for operating cycles prior to 1996,
2) feedwater chemistry report which lists the average and minimum pHs and oxygen concentrations for 31 plants (Jonas, 1988),
3) Millstone Unit 3 information on feedwater pHs for operating cycles prior to 1997, and
4) discussions with plant chemistry personnel (Jones, 2000)

Table 6-6. Postulated off normal chemistry conditions, feedwater pH value and condenser exit oxygen concentration, with their associated and combined likelihood.

pH Value / O2 (Pr) Value [ppb] (Pr)	8.6 (.02)	9.0 (.05)	9.2 (.12)	9.3 (.17)	9.4 (.47)	9.5 (.10)	9.6 (.05)	9.7 (.02)
29 (.02)	0.0004	0.001	0.0024	0.0034	0.0094	0.002	0.001	0.0004
16 (.05)	0.001	0.0025	0.006	0.0085	0.0235	0.005	0.0025	0.001
12 (.07)	0.0014	0.0035	0.0084	0.0119	0.0329	0.007	0.0035	0.0014
8 (.49)	0.0098	0.0245	0.0588	0.0833	0.2303	0.049	0.0245	0.0098
6 (.20)	0.004	0.01	0.024	0.034	0.094	0.02	0.01	0.004
4 (.12)	0.0024	0.006	0.0144	0.0204	0.0564	0.012	0.006	0.0024
2 (.05)	0.001	0.0025	0.006	0.0085	0.0235	0.005	0.0025	0.001

Probabilities of operating at the each pH value and oxygen concentration are specified separately. Because these parameters are controlled by different physical

processes, the combined probability is computed assuming independence of the parameters. In general operating conditions requiring no corrective action according to EPRI guidelines were given heavier weight than those requiring corrective action. Due to lack of data on film destruction rates, no history dependent corrosion film relation has been developed for the study. Instead, the mismatch in film destruction rates and film reformation rates is reflected in heavier weighting of the lower values of pH and oxygen concentration (both of which correspond to higher wear rates).

As is expected, oxygen concentration does not affect wear rate as pH decreases (increasing the deaerated corrosion rate) and bulk oxygen concentration decreases (decreasing the available oxygen to passivate the surface) below the threshold value corresponding to this deaerated corrosion rate. For the entire set of chemistry conditions, Table 6-7 shows whether the calculated corrosion rate is at the deaerated (D) value for three locations. At nominal chemistry conditions the wear for these three locations is low, medium, and high. It can be seen that for low wear under nominal conditions the pH value and oxygen concentration must drop lower for the calculated wear to be at the deaerated value. This threshold trend exists for all wear locations in the condensate and feedwater. Beyond the steam generator, oxygen concentration is always too low to affect the wear rate.

Table 6-7. Designation of whether bulk oxygen concentration is sufficient to affect wear rate (denoted X for oXygenated) or not (denoted D for Deaerated) for the analyzed set of chemistry conditions at three wear locations. For oxygenated conditions bulk oxygen affects the wear rate because it is above the threshold.

PH Value / O2 Value [ppb]	8.6	9.0	9.2	9.3	9.4	9.5	9.6	9.7
29	X	X	X	X	X	X	X	X
16	X	X	X	X	X	X	X	X
12	X	X	X	X	X	X	X	X
8	X	X	X	X	X	X	X	X
6	D	X	X	X	X	X	X	X
4	D	D	X	X	X	X	X	X
2	D	D	D	D	D	X	X	X

a)Low Wear Rate

PH Value / O2 Value [ppb]	8.6	9.0	9.2	9.3	9.4	9.5	9.6	9.7
29	X	X	X	X	X	X	X	X
16	X	X	X	X	X	X	X	X
12	D	X	X	X	X	X	X	X
8	D	D	D	X	X	X	X	X
6	D	D	D	D	D	X	X	X
4	D	D	D	D	D	D	X	X
2	D	D	D	D	D	D	D	X

b) Medium Wear Rate

PH Value / O2 Value [ppb]	8.6	9.0	9.2	9.3	9.4	9.5	9.6	9.7
29	D	X	X	X	X	X	X	X
16	D	D	D	D	D	X	X	X
12	D	D	D	D	D	D	X	X
8	D	D	D	D	D	D	D	X
6	D	D	D	D	D	D	D	X
4	D	D	D	D	D	D	D	D
2	D	D	D	D	D	D	D	D

c) High Wear Rate (Location 12)

Figure 6-5 shows calculated wear for the same locations. In general, the wear increases as the pH value and oxygen concentration decreases. The threshold indicated in Table 6-7 is reflected in each part of Figure 6-5 where wear rate reduces quickly with little change in the chemistry parameters. Just as in Table 6-7 the higher the deaerated wear, the larger the bulk oxygenation concentration at threshold. Appendix G. Kori Unit 3 Off Normal Chemistry Data shows this information for all calculated single phase locations. Note that for piping segments with 2 phase flow, the input pH for the new FAC model is 7.0 regardless of the actual cold pH. Further, due to the large volatility of oxygen, the oxygen liquid concentration is well below the threshold value. Therefore, for locations with 2 phase flows, there will be no change in the predicted wear rate for this set of chemistry conditions. This prediction by the new FAC model is not supported by data[12], but is a feature carried over from the Kastner model.

For each wear location, this calculated wear can be plotted against its probability of occurrence as listed in Table 6-1. Figure 6-6 shows typical histograms of wear rate for the three wear locations used in the previous two figures. As expected, they show a distribution peaked at midrange values of wear with tails at higher and lower wear rates caused, correspondingly, by lesser and greater values of both pH and oxygen concentration.

---

[12] The main motivation for using heavier amines to control pH, such as morpholine or ETA, is their relatively low volatility (when compared with ammonia) which ensures better corrosion control in the liquid phase. A number of utilities uses these less volatile

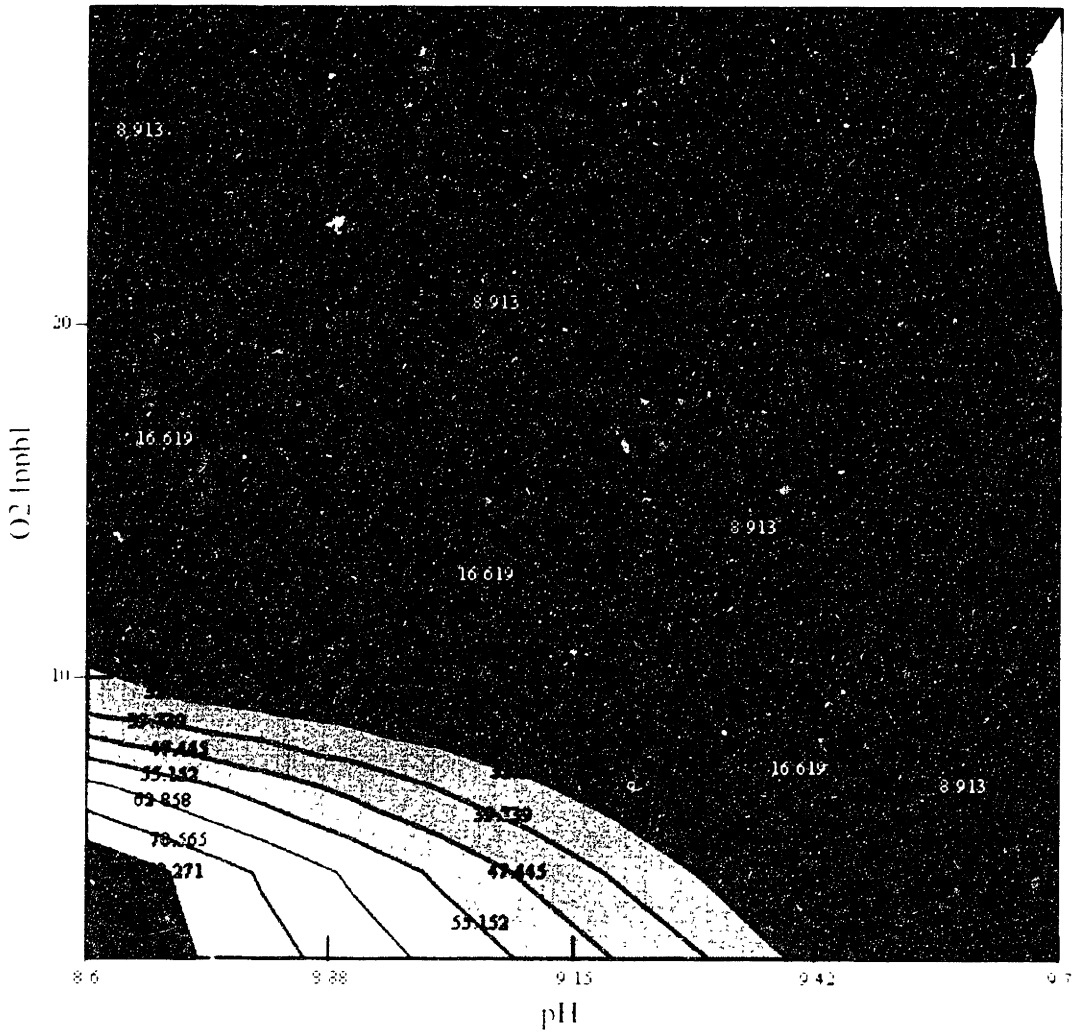

6-5 a)Low Wear Rate

amines indicating that the corrosion rate in piping with 2 phase flow is affected not only by the pH but by the type of amine used to control pH

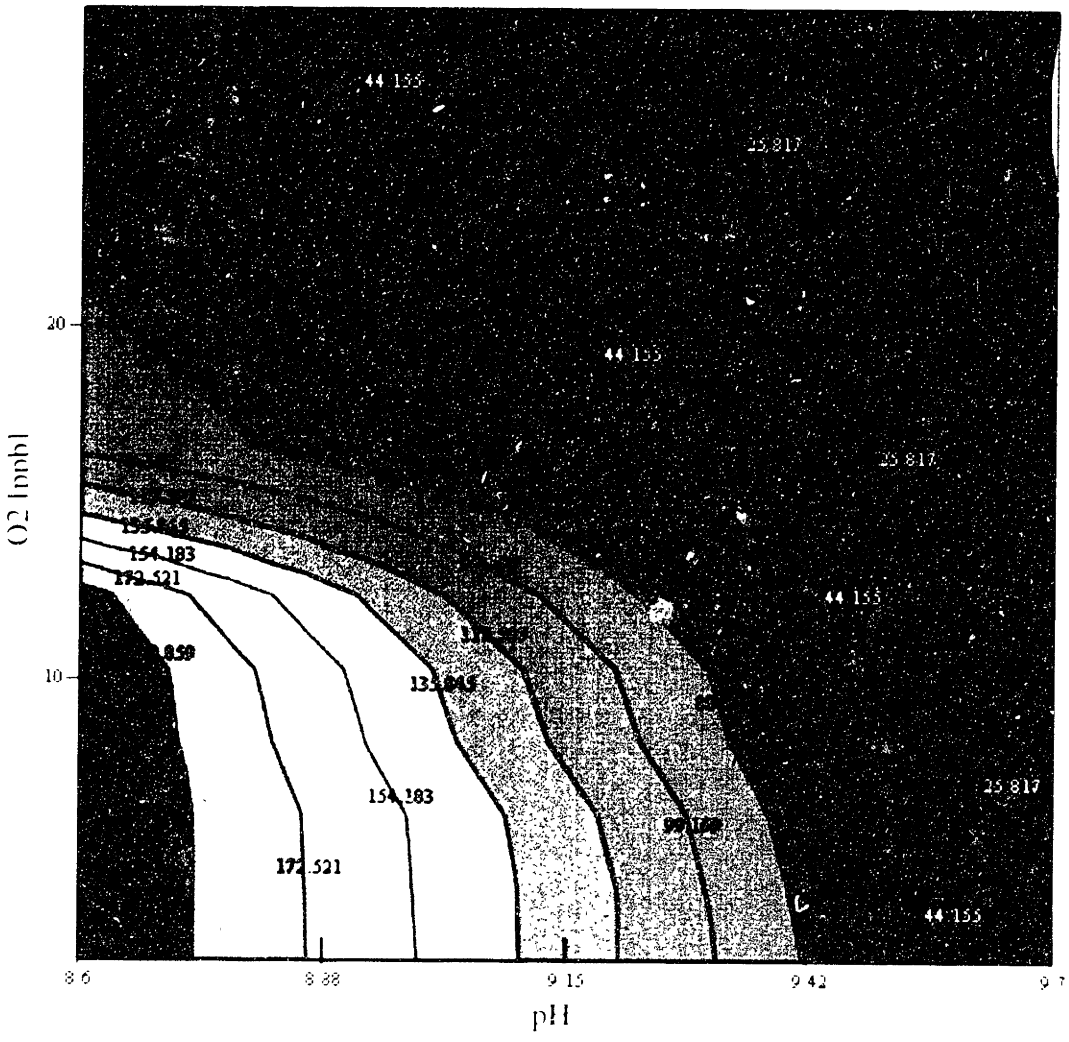

6-5 b)Medium Wear Rate

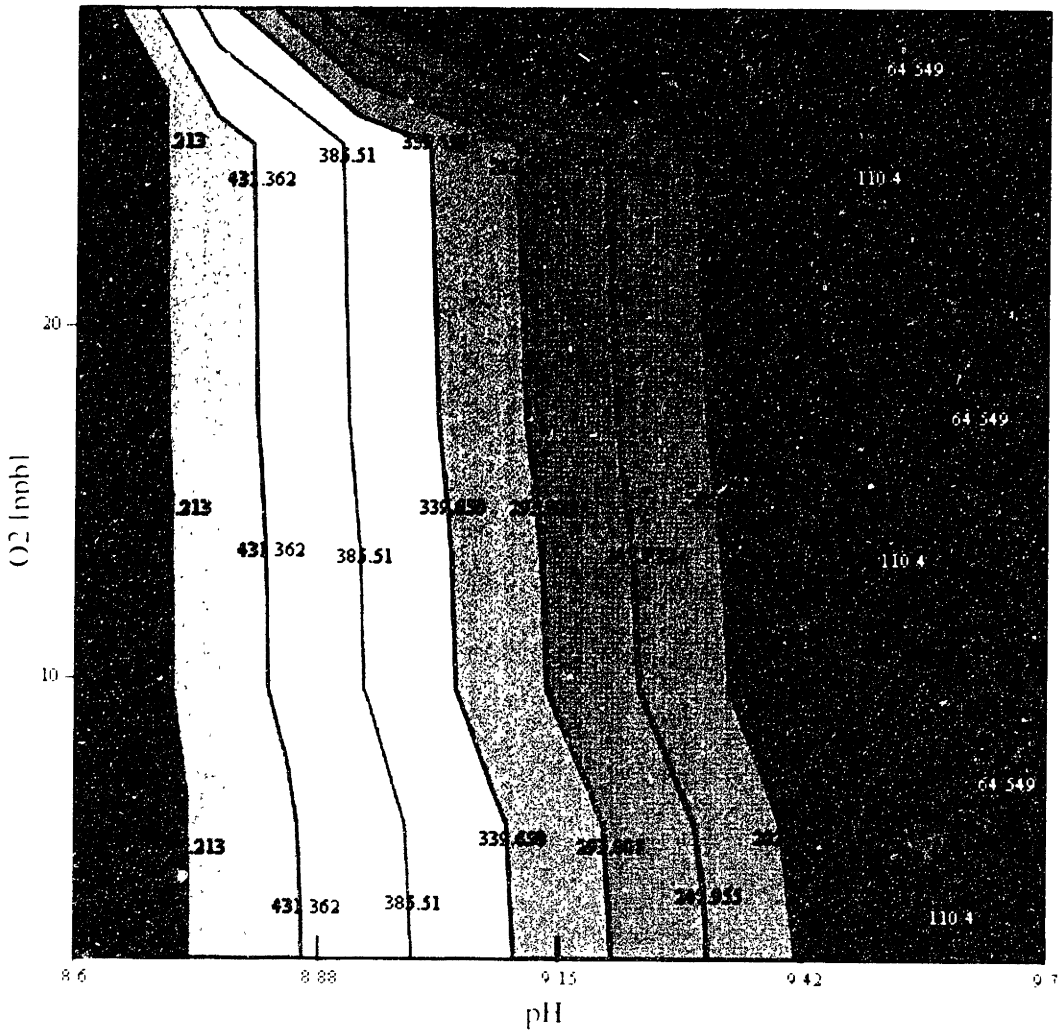

c)High Wear Rate

Figure 6-5. Contour plot of calculated wear for the analyzed set of chemistry conditions at three wear locations.

To assess the contribution to uncertainty from these off normal chemistry conditions, the distribution of potential chemistry conditions is sampled for short time intervals (on the order of an hour and much less than an operating cycle or the plant lifetime) assuming each to be an independent event. This is an approximation to the actual plant operation for which chemistry while change continuously. Wear rates are assigned for that period according to that which has been computed for the sampled set of

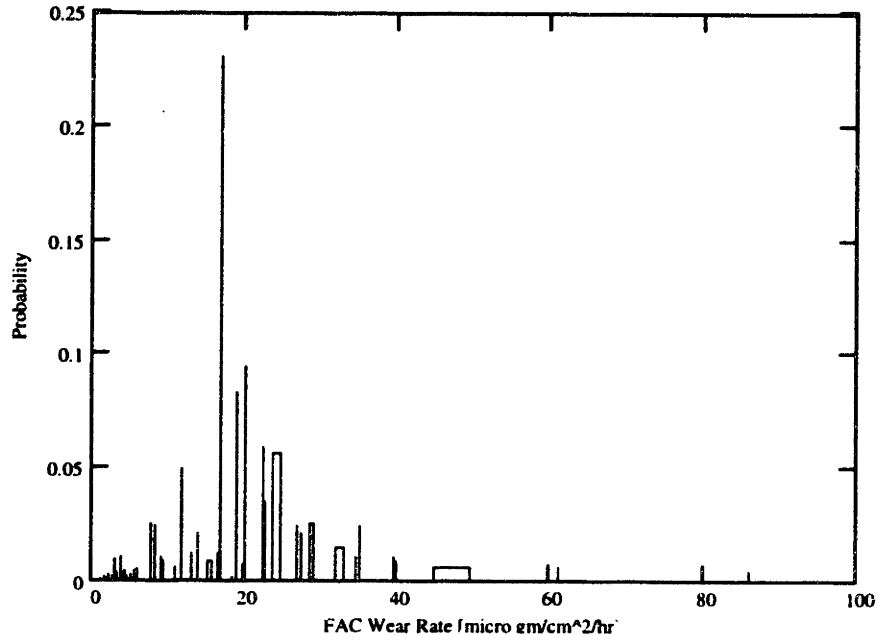

a) Low Wear Rate

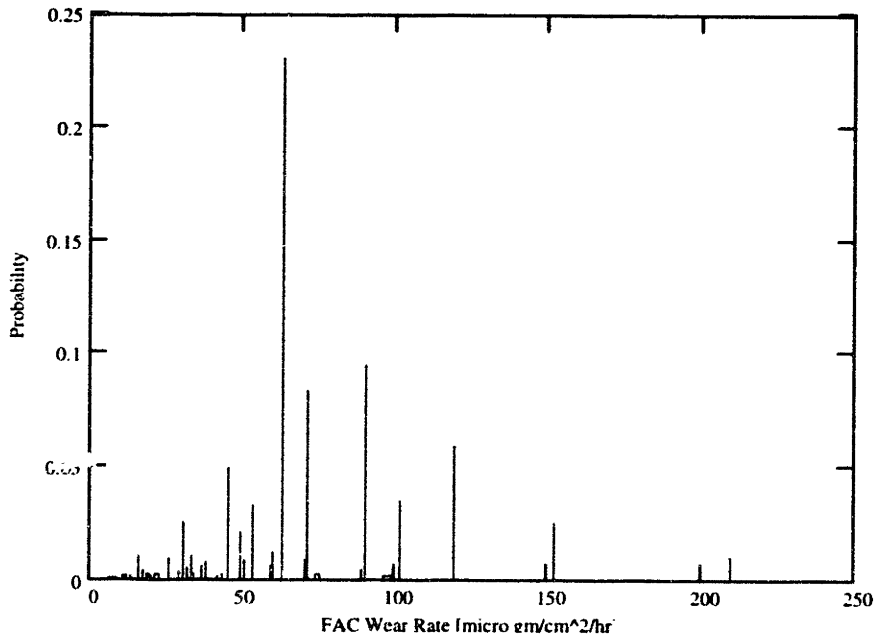

b) Medium Wear Rate

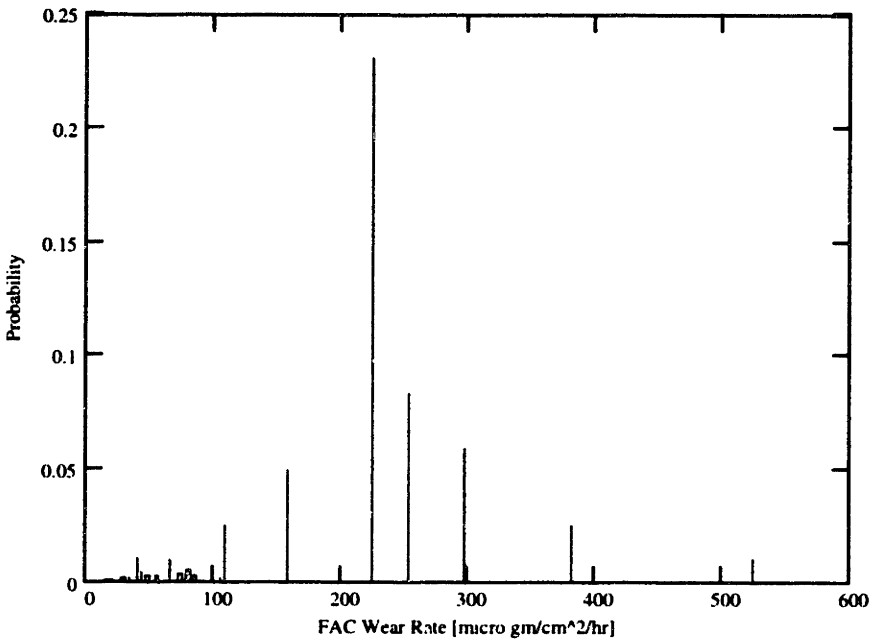

c) High Wear Rate

Figure 6-6. Typical histograms of SPPDP predicted wear rates for the model of Kori Unit 3 for the entire set of chemistry conditions analyzed.

conditions. By integrating these wear rates over the period of interest (e.g. an operating cycle) and dividing by that period, one calculates an integrated wear rate. Provided sufficient number of samples are taken, which is true in this case because of the number of hours in an operating cycle, the resulting integrated wear rate for the assumed set of plant conditions will be the mean wear rate for the distributions at each location. This integrated wear rate can be compared to the wear rate that would result from inputting the nominal chemistry conditions (as computed in section, 6.1.5 FAC Wear Rate Predictions vs Measurements).

For the feedwater and condensate subsystems, this difference reflects oscillations in both pH and oxygen concentration conditions. Wear rates in the remaining single phase systems including drain lines for the moisture separators, the heater drain tank, and

the FWHs are affected only by changes in the pH conditions. As explained earlier, locations with 2 phase flow are not predicted to be affected by this set of chemistry conditions because the volatile oxygen is typically below the threshold concentration and the pH value is assumed to be zero. For this purpose of this analysis, then, locations with 2 phase flow are omitted.

The statistical parameters (using **Eq. 5-20** and **Eq. 5-22**) are computed for two groupings of locations: the feedwater and condensate subsystem locations (affected by pH and O2 changes – 19 locations) and all single phase locations (averaging in all affected locations - 35 locations). Table 6-8 lists the results. These calculations are performed with the results from the nominal conditions of section 6.1.5 and the off normal conditions of this section. By comparing the results from these two groupings of conditions, one can see that the inclusion of the effects of off normal chemistry results in an increase in the median ratio. The increase for the first grouping of locations (which includes only locations affected by both pH and oxygen changes), 0.26 or 15%, is greater than that increase for the second grouping of locations (which includes all affected locations), 0.21 or 9%, indicating that the oxygen parameter is in itself a significant contributor. This increase is an improvement because this median ratio is approaching the value of 2.88 expected for the new FAC model as established in section 5.2.1.1 (this section shows the results of the new FAC model in predicting Kastner laboratory data). This approach to 2.88 is true for both groupings of locations with the median value over all single phase reaching 2.59. As this median approaches the value of 2.88 the uncertainty of the model reduces. Therefore, off normal chemistry is a significant contributor to the reported uncertainty of the model specifically in the condensate and

feedwater subsystems and in general for all single phase locations. Recall that the Kori Unit 3 system analyzed has significant uncertainty caused by the fact that alloying element content for all locations is unknown and therefore estimated for these calculations. With this uncertainty removed, then, analyzed difference in nominal and integrated wear rates would be a larger portion of the calculated uncertainty.

Table 6-8. Lognormal Mean and corresponding Median of the ratio of predicted to measured wear for locations affected by off normal water chemistry.

	Nominal Chemistry Conditions		Off Normal Chemistry Conditions	
	μ_{LN_R}	Mdn_{Rt}	μ_{LN_R}	Mdn_{Rt}
Condensate and Feedwater Locations	0.548	1.73	0.674	1.96
All Single Phase Locations	0.866	2.38	0.952	2.59

6.2.3. Recommended Methodology for History Effect Into Wear Rate Prediction

Having established that current practice of using lifetime or operating cycle nominal chemistry values for computing FAC to be not sufficient for determining accurate wear rates, a methodology for improving these techniques is fairly evident. Combining the developed SPPDP with plant data measured over much shorter periods (averaged over periods on the order of an hour) and integrating the computed wear rates for these periods over the time of interest will give a more accurate estimate of wear rate. For previous operation of plants historical chemistry data will be needed. For current operation, real time measured plant data can be used to not only predict wear rate, but to modify operation by weighing in this information. In both cases, the SPPDP computes the changing wear based on changing input chemistry data and already input system

information with relative ease. This method is in keeping with the future intent of SPPDMME, to provide real time calculations of the numerous degradation processes occurring, providing a more comprehensive set of information from which one can make decisions.

Overall wear can be reduced by continually monitoring the effects of plant chemistry operation on degradation rates. Current EPRI guidelines designate only an upper bound on condensate oxygen concentration to minimize corrosion product transport. FAC increases for decreasing bulk oxygen concentration, precipitously so for oxygen concentration decreasing just below the threshold value. For plants with successful chemistry control of their secondary systems, a lower bound on condensate oxygen concentration or different injection of hydrazine (the oxygen scavenger) may be justified. This lower bound will be plant specific but can be determined by the using the SPPDP.

In this chapter, the SPPDP modular and technical features were tested with success by demonstrating the SPPDP's ability to predict pipe wear for the Kori Unit 3 plant. The prediction of this wear was shown to have lower uncertainty than codes currently available in the literature. Second, the code was used to analyze significant contributors to wear rate prediction uncertainty by modeling plant off normal chemistry conditions. Based on this analysis, recommendations were made to reduce FAC wear rate and FAC wear rate prediction uncertainty. This exercise exhibits the potential of the developed environment to aid in improving plant operation and maintenance activities by supplying more accurate predictions of degradation rates and serving as a method to investigate unidentified causes for degradation.

Chapter 7. Conclusions and Future Work

7.1. Conclusions

The goal of this thesis was to improve the methodology for predicting wear caused by Flow Induced Material Degradation mechanisms. This objective was achieved by reducing the uncertainty associated with the prediction of Flow Accelerated Corrosion (FAC) phenomenon, the most prevalent of these degradation mechanisms. In reducing uncertainty, three sources were addressed as described in Chapter 1: parameter uncertainty, model inaccuracy, and incomplete condition information (the latter two of which are typically grouped into model uncertainty).

To achieve this goal, a flow system analysis methodology was developed to translate plant information into parameters that affect wear at the location in which the wear is taking place. Such a methodology not only meets the requirements of the thesis but lays the groundwork for future improvements in wear prediction methodology. The combined set of goals met by this methodology include:

1. Reducing uncertainty in the degradation rate prediction by
- reducing parameter uncertainty by calculating parameters in a consistent manner,
- reducing model inaccuracy by incorporating more physically based parameters and relations, and
- identifying and incorporating into wear predictions significant parameters that are not currently used in models.
2. Quantifying the uncertainty in the degradation rate prediction for specific sets of conditions.

The flow system methodology was conceived recognizing two major constraints, the wide range of plant designs that the methodology must accomodate and the variability in

the quality (amount, accuracy, location/completeness) of the data available to describe the flow system of interest. This flow system analysis methodology consists of two fundamental concepts: a modular system concept and a sequential propagated calculation concept. The modular system concept involves breaking down the flow system and calculations into fundamental pieces (or modules) that can be combined in the necessary configuration in order to describe the variations of the flow system that are known to exist. The key feature of these modules is that the set of interfaces that they share with other modules is identical so that the modules can be connected in any configuration. The sequential propagated calculation concept determines the method that information is fed back during analysis. The ability to feedback calculated information based on system design and parameter information allows one to determine what additional information must be supplied in the analysis.

This methodology was applied to the secondary system of a PWR to determine pipe degradation results in the Secondary Plant Pipe Degradation Modular Modeling Environment (SPPDMME). Chapter 3 described the component modules and calculation modules of this environment in terms of their capabilities individually as well as their combined capabilities to meet the following requirements:

1. Calculate conditions that affect degradation at locations where degradation is actually occurring,
2. Perform these calculations based on fundamental physical relationships,
3. Perform calculations of parameters based on a single set of relationships,
4. Perform calculations at the level of detail necessitated by application or as possible based on secondary system information,
5. Perform calculations for a wide range of system designs (typical of the US fleet), and
6. Determine whether the input of information over or under constrains relationships.

Component models were defined in terms of the physical components they model as well as the information flow across their interfaces. Calculation modules were defined in terms of the set of equations (or models) they incorporate, the information they require for input, and the information they can calculate. The final form of this environment is the Secondary Plant Pipe Degradation Program (SPPDP), a program coded in the Visual Basic® programming language.

The SPPDP and its modules were applied to a number of data sets, to assess the impact of the program on reducing prediction uncertainty. First, the calculation modules within the SPPDP were shown in Chapter 4 to accurately predict thermodynamic, thermal hydraulic, and chemistry parameters known to affect FAC rate. In Chapter 6, the SPPDP was used to calculate these parameters at the locations where the wear is taking place for an example system, the secondary side of the Kori Unit 3 plant. This application exhibits the integrated modular and technical concepts incorporated in the SPPDP as described in Chapter 3. The resulting accurate parameter calculation at the location of wear described in Chapter 6 reduces parameter uncertainty.

Second, development of a empirical new FAC model (the NFM, which is incorporated into the SPPDP as part of a calculation module) based on the empirical Kastner model reduced model inaccuracy by incorporating changes that reflect physical properties of the phenomenon and data on FAC wear in the literature. The changes include:

1. the decoupling of velocity and alloying element content at low alloying element content,
2. the elimination of the effect of oxygen for bulk oxygen concentrations below a critical value,

3. an improvement in the two-phase correlation used to estimate liquid phase velocity,
4. an adjustment of the cold pH factor to predict wear at higher values of pH, and
5. the removal of velocity dependence at high and low temperature to ensure physically accurate trends.

The NFM was shown to have slightly improved accuracy over the Kastner model when compared using Kastner single phase laboratory data. Because the Kastner model is optimized for this single phase data, only slight improvement can be expected. Because of the incorporated changes, however, the NFM is expected to show significant improvement when extrapolated to regions for which the model has not been optimized. This expectation is born out in further comparisons to data.

Comparisons to single phase and two phase plant data from Millstone Unit 2 and 3, respectively, showed the NFM to provide more accurate predictions than the Kastner model. The NFM wear predictions were also compared to the Chexal-Horowitz model, used widely by the US utility industry, with good agreement for a wide range of conditions. Finally, the NFM was integrated into the SPPDP as a calculation module. In the first half of Chapter 6, wear predictions for the integrated NFM were compared to those that would be produced were the Kastner model integrated in the SPPDP. Wear predictions from integrating the NFM generated more accurate results than an integrated Kastner model would have, again indicating improved accuracy of the NFM.

Last, to address wear rate uncertainty caused by incomplete condition information, the SPPDP was used to investigate additional information that may be relevant to improving the prediction FAC wear rate. Specifically, the method in which chemistry parameters are included in the prediction of FAC rate was investigated. The current method for determining FAC wear rate based on nominal chemistry conditions

was shown to contribute to model uncertainty. Using the SPPDP to model the secondary side of Kori Unit 3 for a range of chemistry conditions typical of an operating cycle, a time integrated wear rate is calculated. This time integrated wear rate is shown to reduce model prediction uncertainty. Therefore, the incomplete condition information is the time dependent chemistry conditions. A new methodology using the SPPDP is suggested that incorporates this information. This investigation is just one of many applications anticipated for the SPPDP in improving methods for determining degradation rates of plant components. A number of further investigations are discussed in the next section.

7.2. Future Applications of the SPPDP

This thesis has laid the necessary groundwork for continued improvements in predicting FAC and other degradation rates for a number of phenomena in the development of an investigative program, the SPPDP. As is typical for such endeavors, the work generated a number of ideas for what the next steps could be for both the application of this investigative program as well as the systems and degradation mechanisms it could be used to investigate.

As outlined in the previous section one of the goals of the methodology used to develop the SPPDP was to quantify the uncertainty in FAC rate prediction for a specific set of conditions. In this endeavor, the SPPDP can be used to model numerous power plants predicting wear throughout the secondary side. The wear data and conditions determined by the SPPDP can be combined with statistical techniques to quantify wear uncertainty (Christensen, 1985). The SPPDP provides a consistent method for determining these conditions. Further the determination of these conditions is based on

first principles of thermodynamics and transport. These two characteristics ensure limited parameter uncertainty used as input for the developed statistical models.

In order to develop statistical models to quantify uncertainty, a set of plants should be selected that have a range of operating design and characteristics that are representative of the industry. Modeling these plants using the SPPDP and combining the results with statistical techniques to quantify uncertainty requires collaboration with industry. This collaboration would include the following steps in the development of statistical models:

1) Work with plant personnel at each plant to obtain the necessary plant data and plant design information,
2) Model the selected power plants to develop a large and robust set of data describing the conditions that lead to FAC wear,
3) Combine data with statistical techniques to develop a model that determines not only the wear rate but the uncertainty in that value, and
4) Integrate wear rate and wear rate uncertainty results into current risk informed inservice inspection and inservice testing methodologies developed by EPRI and Westinghouse Owner's Group to improve the safety and cost of plant operation (Balkey *et. al.*, 1998).

The major difference is that instead of current methods of supplying an overall value of wear uncertainty for FAC wear, the new statistical model will provide a condition specific wear rate uncertainty.

Based on research conducted during the course of this thesis there are a number of conditions or factors *known* to affect FAC but are not included in the NFM devised in this thesis. These conditions include:

1) the mass transfer coefficient,
2) the hot pH in single phase flow and either cold or hot pH in two phase flow, and
3) the surface chemistry where the oxide is being formed and where the oxide is being dissolved in the flow.

The first two factors are computed by the SPPDP. Including these factors would improve the FAC prediction. Further, the use of statistical techniques enables one to determine if a particular condition is statistically significant in affecting wear and if so for what subset of the other conditions this significance exists. There exist some conditions or factors *suspected* to affect FAC wear for some subset of conditions that are not included in the NFM devised in this thesis. Such factors include:

1) specific conductivity,
2) electrochemical potential,
3) porosity of magnetite solution and oxide kinetics,
4) film dynamics and stability,
5) accelerated removal with large scale roughness typical of tiger striping,
6) pipe joining affects such as number of welds and fit-up,
7) potential for a partially filled drain line,
8) entrance effect causing greater wear at entrance of a pipe with lower alloying element content, and
9) organic acid effects caused by buildup from amine decomposition.

The second major application of the SPPDP is the extension of the program to investigate additional flow systems and flow system conditions. The effects on FAC rate of operating conditions such as startups and shutdowns, power transients, and chemistry excursions can be determined. With further development of the program to model additional components, other flow systems, such as BWRs and fossil-fueled plants can be analyzed to determine FAC wear. Because the calculations performed by the SPPDP are based on first principles of transport, other degradation or chemistry related problems can be modeled with the SPPDP. The modular characteristic of the program allows modeling of these additional degradation mechanisms to be easily integrated. Finally, because of

the calculations of thermodynamics and chemistry, the SPPDP can be used as a teaching or design tool for the secondary side of a PWR.

References

Alexander, J.H., Howard, F.H. and Luu, L. "MULTEQ: Equilibrium of an Electrolytic Solution with Vapor-Liquid Partitioning and Precipitation- Volume 1: User's Manual (revision 2)," **RPS407-30**, Electric Power Research Institute, Palo Alto, CA, July, 1992.

Al-Haydari, Y.K., Saleh, J.M. and Matloob, M.H. "Adsorption and Decomposition of Hydrazine on Metal Films of Iron, Nickel, and Copper," *The Journal of Physical Chemistry*, **89**, n.15, pp.3286-3290, 1985.

Ardillon, E. and Bouchacourt, M. "Probabilistic Evaluation of Flow-Accelerated Corrosion in French PRW," *Pressure Vessel and Piping*, **283**, pp.69-77, 1994.

Balkey, K.R., Art, R.J. and Bosnak, R.J. "ASME Risk-Based Inservice Inspection and Testing: An Outlook to the Future," *Risk Analysis*, **18**, n.4, pp.407-421, 1998.

Berger, F.P. and Hau, K., *Heat and Mass Transfer*, **20**, p.1185, 1977.

Bignold, G.J, and Woolsey, I.S. "Hysteresis Effects in Response of Mild Steel Circuits to Changes in Water Chemistry," *Proceedings of the Second Meeting on Water Chemistry of Nuclear Reactors*, British Nuclear Engineering Society, London, England, pp.25-30, 1980.

Bignold, G.J. *et. al.* "Mechanistic Aspects of Erosion-Corrosion under Boiler Feedwater Conditions," *Proceedings of the Third Meeting on Water Chemistry of Nuclear Reactors*, British Nuclear Engineering Society, London, England, pp.219-226, 1983.

Bishop, B.A. "Westinghouse Structural Reliability and Risk Assessment (SRRA) Model for Piping Risk Informed Inservice Inspection," **WCAP-14572**, Westinghouse Electric Corporation, Pittsburgh, PA, October, 1997.

Bouchacourt, M. "*Corrosion-Erosion des aciers dans l'eau sous pression a 180 °C: essais sur tubes*," EDF Report, Ref.:HT/PV D 591 MAT/T.42. February, 1992.

Bouchacourt, M. "Flow Assisted Corrosion in Power Plants – Part 1: The EDF Research Program," Proceedings of the International Atomic Energy Agency's Specialist's Meeting on Corrosion and Erosion Aspects of the Pressure Boundary Components of Light Water Reactors, Vienna, Austria, 1988.

Bouchacourt, M. "Identification of Key Variables: EDF Studies," *Electric Power Research Institute's Workshop on Erosion Corrosion of Carbon Steel Piping*, Washington D.C., April, 1987.

Chandra, S., Klisiewicz, J.W. Schonenberg, R.Y. and Habicht, P.R. "The Examination of Pipe Components Degraded Due to the Erosion/Corrosion Phenomenon," *Pressure Vessel and Piping*, **285**, pp.17-24, 1994.

Chexal, B. "Corrosion in Power Plant Piping," *Presentation at MIT Nuclear Engineering Department Seminar Series*, Cambridge, MA, Sept. 16, 1996.

Chexal, B. *et. al. Flow Accelerated Corrosion in Power Plants*, Electric Power Research Institute, Pleasant Hill, CA, 1996.

Chexal, B., Lellouche, G., Horowitz, J., Healzer, J. and Oh, S. "The Chexal-Lellouche Void Fraction Correlation for Generalized Applications," **NSAC-139**, Electric Power Research Institute, April, 1991.

Christensen, R. "SPEAR-BETA Fuel Performance Code System- Volume 1: General Description," **RP700-3**, **RP971-1**, **RP971-2**, Electric Power Research Institute, Palo Alto, CA, April, 1982.

Christensen, R. "Entropy Minimax Multivariate Statistical Modeling- I: Theory," *International Journal of General Systems*, **11**, pp.231-277, 1985.

Cobble, J.W. and Turner, P.J. " PWR Advanced All-Volatile Treatment Additives, By-Products, and Boric Acid," **RPS409-02**, Electric Power Research Institute, Palo Alto, CA, July, 1992.

Cohen, P., editor, *The ASME Handbook on Water Technology for Thermal Power Systems*, The American Society of Mechanical Engineers, New York, NY, 1989.

Cragnolino, G. *et. al.*"Review of Erosion-Corrosion in Single-Phase Flows," **NUREG/CR-5156, ANL-88-25**, April, 1988.

Dalgaard, S.B. and Sanford, M.O. "Review of the Hydrazine/Oxygen Reaction Kinetics," presented during *Corrosion:* **81/15** *National Association of Corrosion Engineers*, Toronto, Ontario, April, 1981.

Ducreux, J. "Theoretical and Experimental Investigation of the Effect of Chemical Composition of Steels on their Corrosion Erosion-Corrosion Resistance," Paper 19 presented to the *Specialist's Meeting on Corrosion-Erosion of Steels in High Temperature Water and Wet Steam*, Les Renardières, France, May, 1982.

Energy Information Administration (EIA), "Annual Energy Outlook: With Projections to 2020," *Office of Integrated Analysis and Forecasting*, Washington D.C., www.eia.doe.gov/oiaf/aeo/index.html, December 1999.

EPRI PWR Secondary Water Chemistry guidelines Revision Committee, "PWR Secondary Water Chemistry Guidelines- Revision 3," **RP2493**, **RPS401**, Electric Power Research Institute, Palo Alto, CA, May 1993.

EPRI Steam Generator Project Office Staff, *Steam Generator Reference Book*, Electric Power Institute, Palo Alto, CA, 1985.

Gilbert, R. and Lamarre, C. "Thermal Stability of Morpholine Additive in the Steam-Water Cycle of CANDU-PHW Nuclear Power Plants," *The Canadian Journal of Chemical Engineering*, **67**, August, pp.646-651, 1989.

Guppy, J.G. "Super System Code (SSC, Rev. 2): An Advanced Thermohydraulic Simulation Code for Transients in LMFBRs," **NUREG/CR-3169, BNL-NUREG-51650**, April, 1983.

Heat Exchange Institute Committee, *Standards for Closed Feedwater Heaters* (Third Edition), Heat Exchange Institute, Cleveland, OH, pp.8-28, 1979.

Heat Exchange Institute Committee, *Standards of the Heat Exchange Institute: Condenser Section* (Second Edition), Heat Exchange Institute, New York, NY, pp.1-43, 1978.

Heitmann, H.G. and Kastner, W. "Erosion-Corrosion in Water-Steam Cycles-Causes and Counter Measures," *VGB Kraftwerkstechnik*, **64,** n.5, pp.1023-1029, 1984.

Horowitz, J.S., Chexal, B. and Goyette, L.F. "A New Parameter in Flow-Accelerated Corrosion Modeling," *Pressure Vessel and Piping*, **368**, pp.63-68, 1998.

Howell, J.R. and Buckius, R.O, *Fundamentals of Engineering Thermodynamics* (Second Edition), McGraw-Hill, New York, NY, 1992.

Huijbregts, W.M.M. "Erosion-Corrosion of Carbon-Steel in Wet Steam," *Materials Performance*, **23**, pp. 39-45, 1984.

Intergovernmental Panel on Climate Change. *Climate Change : The IPCC Scientific Assessment*, Cambridge University Press, New York, NY, 1997.

Jonas, O. "Erosion-Corrosion of PWR Feedwater Piping Survey of Experience, Design, Water Chemistry, and Materials," **NUREG/CR-5149, ANL-88-23**, March, 1988.

Jones, V. Personal communication, Chemistry Engineer at Millstone Unit 2 1991-1999, March, 2000.

Kastner, W. "Erosion Corrosion-Experiments and Calculational Model," Electric Power Research Institute's Workshop on Erosion-Corrosion of Carbon Steel Piping-Nuclear and Fossil Plants, Washington D.C., April 14-15, 1987.

Kastner, W. *et. al.* "Erosion Corrosion in Power Plants- Decision Making Tools for Counteracting Material Degradation," *VGB Kraftwerkstechnik*, **70**, n.11, pp.806-815, 1990.

Kastner, W. *et. al.* "Erosion Corrosion in Power Plants– Research Work, Plant Experience, and Predictive Code," *Third International. Top-Meeting on Nuclear Power-Plant Thermal Hydraulics and Operation*, **NUPTHO-3**, **2**, Seoul, Korea, November 14-17, ppB5-41 to B5-48, 1988.

Kastner, W. *et. al.* "Experimental Investigations on Material Loss Due to Erosion-Corrosion," *VGB Kraftwerkstechnik*, **64**, n.5, pp.411-423, May, 1984.

Kastner,W. and Nedelko,L. "Erosion Corrosion in Nuclear Power Plant Piping, Part 1 to 3," *Symposium: Plant Life Extension (PLEX) of Nuclear Power Plants*, Madrid, Spain, April 24-26, 1991.

Kastner,W. and Riedle, K. "Empirical Model for the Calculation of Material Losses Due to Erosion Corrosion," *VGB Kraftwerkstechnik*, **64**, n.12, pp1023-1029, 1986.

Keck, R.G. "Prediction and Mitigation of Erosive-Corrosive Wear in Steam Extraction Piping Systems," PhD Thesis, MIT, Cambridge, MA, 1987.

Keenan, J.H. and Keyes, B.S. *Steam Tables: Thermodynamic Properties of Water*, (Reprint Edition) Krieger Publishing Company, Malabar, FA, 1992.

Keller, V.H. "Erosion-Corrosion in Damp Steam Turbines," *VGB Kraftswerkstechnik*, **54**, p.292, 1974.

Kupinski, M., Chandra, S. and Habicht, P.R. "Analysis of Moisture Separator Reheater Drain Line Rupture at Millstone Point Unit 2," *Pressure Vessel and Piping*, **259**, pp.193-200, 1993.

LePrince, J.M. "Essais d'Erosion-par l'eau chaude sous pression de materieaux pour corps de pompes alimentaires. – Synthese-," EDF Report, Ref.:P.33/224/8.22. December, 1983.

MacArthur, A.D. "Evaluation and Improvement of PWR Secondary-System Oxygen Control Measures," **NP-3020, S104-1**, July, 1983.

Mahini, R.T., Chexal, B. and Horowitz, J.S. "Developing Predictive Models for Cavitation Erosion," *Pressure Vessel and Piping*, **259**, pp.189-192, 1993.

Press, W.H., Teukolsky, S.A., Vetterling, W.T., and Flannery, B.P., *Numerical Recipes in C: The Art of Scientific Computing* (Second Edition), Cambridge University Press, Cambridge, England, 1995.

Rouhani, Z. "Modified Correlations for Void and Two-Phase Pressure Drop," **AE-RTV-841**, 1969.

Sanchez-Caldera, L.E. "The Mechanism of Corrosion-Erosion in Steam Extraction Lines of Power Stations," PhD Thesis, MIT, Cambridge, MA, 1984.

Shenberger, D.M., Zupanovich, J.D. and Walker, J.L. "Loop Testing of Alternative Amines for All-Volatile Treatment Control in PWRs," **RPS409-11**, Electric Power Research Institute, Palo Alto, CA, June, 1992.

Smith, C. L., Apostolakis, G. E., Kao, T. M., and Shah, V. "Incorporating Aging Effects into Probabilistic Risk Assessment," presented at the Water Reactor Safety Meeting, Washington D.C., September, 1998.

Stultz, S.C. and Kitto, J.B., editors., *STEAM: Its Generation and Use* (Fortieth Edition), The Babcock and Wilcox Company, Barberton, OH, 1992.

Sweeton, F.H. and Baes, C.F., *Journal of Chemical Thermodynamics*, **2**, p.49, 1970.

Thailer, H. J. and Dalal, K. J., Goyette, L. "Flow Accelerated Corrosion in Steam Generators," presented at the Pressure Vessel & Piping Conference, Honolulu, July, 1995.

Todreas, N.E.and Kazimi, M.S., *Nuclear Systems I: Thermal Hydraulic Fundamentals*, Taylor and Francis, New York, NY, 1993.

Woolsey, I.S. "Assessment and Avoidance of Erosion-Corrosion Damage in PWR Feedpipework," Proceedings of the International Atomic Energy Agency's Specialist's Meeting on Corrosion and Erosion Aspects of the Pressure Boundary Components of Light Water Reactors, **IWG-RRPC-88-1**, Vienna, Austria, pp.60-66, 1988.

Woolsey, I.S. *et. al.* "The Influence of Oxygen and Hydrazine on the Erosion-Corrosion Behavior of Electrochemical Potentials of Carbon Steel under Boiler Feedwater Conditions," *Proceedings of the Fourth Meeting of Water Chemistry of Nuclear Reactors*, British Nuclear Engineering Society, London, England, pp.337-344, 1986.

Zuber, N. and Findlay, J. A. "Average Volumetric Concentration in Two-Dimensional Flow," Trans. ASME., J. of Heat Transfer, pp.453-468, November, 1965.

Appendix A. Chemistry Equilibrium

A.1 Chemistry Equilibrium Equations

The following equations are used in the Instantaneous Equilibrium Model.

Eq.	Equ. Type	Equation Formulation	Symbol	Name
1.	Charge Balance	$\sum_{i=1}^{Nsp} m_i \cdot Z_i = 0$	m_{H^+}	Hydrogen
2.	Water Dissociation	$m_{H^+}\ m_{OH^-} = K_{H_2O}$	m_{OH^-}	Hydroxide
3.	Ammonia Mass Balance	$\sum_{i=1}^{N_{Nh_3}} m_i \cdot n_i^{NH_3} = C_{NH_3}$	m_{NH_3}	Ammonia aq
4.	Ammonia Dissociation	$\frac{m_{NH_4^+}\ m_{OH^-}}{m_{NH_3}} = K_{NH_3}$	$m_{NH_4^+}$	Ammonium
5.	Ammonia Distribution	$\frac{m_{NH_3}}{P_{NH_3}} = K_{NH_3}^s$	P_{NH_3}	Ammonia g
6.	Carbon Mass Balance	$\sum_{i=1}^{N_C} m_i \cdot n_i^C = C_C$	P_{CO_2}	C. Dioxide g
7.	Carbon Dioxide Distribution	$\frac{m_{CO_2}}{P_{CO_2}} = K_{CO_2}^s$	m_{CO_2}	C. Dioxide aq
8.	Carbon Dioxide Dissociation	$\frac{m_{H^+}\ m_{HCO_3^-}}{m_{CO_2}} = K_{CO_2}$	$m_{HCO_3^-}$	Bicarbonate
9.	Bicarbonate Dissociation	$\frac{m_{H^+}\ m_{CO_3^{2-}}}{m_{HCO_3^-}} = K_{HCO_3^-}$	$m_{CO_3^{2-}}$	Carbonate
10.	Silicon Mass Balance	$\sum_{i=1}^{N_{Si}} m_i \cdot n_i^{Si} = C_{Si}$	m_{SiO_2}	Quartz

Eq.	Equ. Type	Equation Formulation	Symbol	Name
11.	Quartz Solubility	$\frac{m_{H_4SiO_4}}{m_{SiO_2}} = K_{SiO_2}$	$m_{H_4SiO_4}$	Silicic Acid
12.	Silicic Acid Dissociation	$\frac{m_{H^+}\, m_{H_3SiO_4^-}}{m_{H_4SiO_4}} = K_{H_3SiO_4^-}$	$m_{H_3SiO_4^-}$	Bisilicate
13.	Bisilicate Dissociation	$\frac{m_{H^+}\, m_{H_2SiO_4^{2-}}}{m_{H_3SiO_4^-}} = K_{H_3SiO_4^-}$	$m_{H_2SiO_4^{2-}}$	Silicate
14.	Sulfur Mass Balance	$\sum_{i=1}^{N_S} m_i \cdot n_i^S = C_S$	$m_{H_2SO_4}$	Sulfuric Acid aq
15.	Sulfuric Acid Distribution	$\frac{m_{H_2SO_4}}{P_{H_2SO_4}} = K^s_{H_2SO_4}$	$P_{H_2SO_4}$	Sulfuric Acid g
16.	Sulfuric Dissociation	$\frac{m_{H^+}\, m_{HSO_4^-}}{m_{H_2SO_4}} = K_{H_2SO_4}$	$m_{HSO_4^-}$	Bisulfate
17.	Bisulfate Dissociation	$\frac{m_{H^+}\, m_{SO_4^{2-}}}{m_{HSO_4^-}} = K_{HSO_4^-}$	$m_{SO_4^{2-}}$	Sulfate
18.	Oxygen Mass Balance	$\sum_{i=1}^{N_O} m_i \cdot n_i^O = C_o$	P_{O_2}	Oxygen g
19.	Oxygen Distribution	$\frac{m_{O_2}}{P_{O_2}} = K^s_{O_2}$	m_{O_2}	Oxygen aq
20.	Nitrogen Mass Balance	$\sum_{i=1}^{N_N} m_i \cdot n_i^N = C_N$	P_{N_2}	Nitrogen g
21.	Nitrogen Distribution	$\frac{m_{N_2}}{P_{N_2}} = K^s_{N_2}$	m_{N_2}	Nitrogen aq

Eq.	Equ. Type	Equation Formulation	Symbol	Name
22.	Hydrogen Mass Balance	$\sum_{i=1}^{N_H} m_i \cdot n_i^H = C_H$	P_{H_2}	Hydrogen g
23.	Hydrogen Distribution	$\frac{m_{H_2}}{P_{H_2}} = K_{H_2}^s$	m_{H_2}	Hydrogen aq
24.	Morpholine Mass Balance	$\sum_{i=1}^{N_{Morph}} m_i \cdot n_i^{Morph} = C_{Morph}$	m_{Morph}	Morpholine aq
25.	Morpholine Distribution	$\frac{m_{Morph}}{P_{Morph}} = K_{Morph}^s$	P_{Morph}	Morpholine g
26.	Morpholine Dissociation	$\frac{m_{MH^+} \, m_{OH^-}}{m_{Morph}} = K_{Morph}$	m_{MorphH^+}	Morpholine ion
27.	ETA Mass Balance	$\sum_{i=1}^{N_{ETA}} m_i \cdot n_i^{ETA} = C_{ETA}$	m_{ETA}	ETA aq
28.	ETA Distribution	$\frac{m_{ETA}}{P_{ETA}} = K_{ETA}^s$	P_{ETA}	ETA g
29.	ETA Dissociation	$\frac{m_{EtaH^+} \, m_{OH^-}}{m_{ETA}} = K_{ETA}$	m_{EtaH^+}	ETA ion
30.	Hydrazine Mass Balance	$\sum_{i=1}^{N_{N_2H_4}} m_i \cdot n_i^{N_2H_4} = C_{N_2H_4}$	$m_{N_2H_4}$	Hydrazine aq
31.	Hydrazine Distribution	$\frac{m_{N_2H_4}}{P_{N_2H_4}} = K_{N_2H_4}^s$	$P_{N_2H_4}$	Hydrazine g
32.	Hydrazine Dissociation	$\frac{m_{N_2H_5^+} \, m_{OH^-}}{m_{N_2H_4}} = K_{N_2H_4}$	$m_{N_2H_5^+}$	Hydrazine ion
33.	Ferrous Ion Mass Balance	$\sum_{i=1}^{N_{Fe^{2+}}} m_i \cdot n_i^{Fe^{2+}} = C_{Fe^{2+}}$	$m_{Fe^{2+}}$	Ferrous Ion

Eq.	Equ. Type	Equation Formulation	Symbol	Name
34.	Ferrous 1st Hydrolysis	$\frac{m_{H^+}\, m_{FeOH^+}}{m_{Fe^{2+}}} = K_{FeOH^+}$	m_{FeOH^+}	Ferrous Hydroxide+
35.	Ferrous 2nd Hydrolysis	$\frac{m_{H^+}^{\ 2}\, m_{Fe(OH)_2}}{m_{Fe^{2+}}} = K_{Fe(OH)_2}$	$m_{Fe(OH)_2}$	Ferrous Hydroxide
36.	Ferrous 3rd Hydrolysis	$\frac{m_{H^+}^{\ 3}\, m_{Fe(OH)_3^-}}{m_{Fe^{2+}}} = K_{Fe(OH)_3^-}$	$m_{Fe(OH)_3^-}$	Ferrous Hydroxide-
37.	Cupric Ion Mass Balance	$\sum_{i=1}^{N_{Cu^{2+}}} m_i \cdot n_i^{Cu^{2+}} = C_{Cu^{2+}}$	$m_{Cu^{2+}}$	Cupric Ion
38.	Cupric 1st Hydrolysis	$\frac{m_{H^+}\, m_{CuOH^+}}{m_{Cu^{2+}}} = K_{CuOH^+}$	m_{CuOH^+}	Cupric Hydroxide+
39.	Cupric 2nd Hydrolysis	$\frac{m_{H^+}^{\ 2}\, m_{Cu(OH)_2}}{m_{Cu^{2+}}} = K_{Cu(OH)_2}$	$m_{Cu(OH)_2}$	Cupric Hydroxide
40.	Cupric 3rd Hydrolysis	$\frac{m_{H^+}^{\ 3}\, m_{Cu(OH)_3^-}}{m_{Cu^{2+}}} = K_{Cu(OH)_3^-}$	$m_{Cu(OH)_3^-}$	Cupric Hydroxide-
41.	Formic Mass Balance	$\sum_{i=1}^{N_{Form}} m_i \cdot n_i^{Form} = C_{Form}$	m_{Form}	Formic Acid aq
42.	Formic Acid Distribution	$\frac{m_{Form}}{P_{Form}} = K^s_{Form}$	P_{Form}	Formic Acid g
43.	Formic Dissociation	$\frac{m_{H^+}\, m_{Form^-}}{m_{Form}} = K_{Form}$	m_{Form^-}	Formate
44.	Acet Mass Balance	$\sum_{i=1}^{N_{Acet}} m_i \cdot n_i^{Acet} = C_{Acet}$	m_{Acet}	Acetic Acid aq
45.	Acetic Acid Distribution	$\frac{m_{Acet}}{P_{Acet}} = K^s_{Acet}$	P_{Acet}	Acetic Acid g

Eq.	Equ. Type	Equation Formulation	Symbol	Name
46.	Acetic Dissociation	$\frac{m_{H^+}\, m_{Acet^-}}{m_{Acet}} = K_{Acet}$	m_{Acet^-}	Acetate
47.	Gycol Mass Balance	$\sum_{i=1}^{N_{Gycol}} m_i \cdot n_i^{Gycol} = C_{Gycol}$	m_{Gycol}	Gycolic Acid aq
48.	Gycolic Acid Distribution	$\frac{m_{Gycol}}{P_{Gycol}} = K^s_{Gycol}$	P_{Gycol}	Gycolic Acid g
49.	Gycolic Dissociation	$\frac{m_{H^+}\, m_{Gycol^-}}{m_{Gycol}} = K_{Gycol}$	m_{Gycol^-}	Gycolate

A.2 Chemistry Equilibrium Data

The following tables list the negative natural log of the temperature dependent dissociation and solubility coefficients used in the SPPDP. The equation to which they correspond in section A.1 above is listed in the first column along with the reference from which the data is taken. To determine values at temperatures not listed in the table, linear interpolation of these coefficients is used.

Table A-1. Negative natural log of coefficients for equations 4 through 16 at temperatures from 25 °C to 150 °C (Cohen, 1989).

Equation	Temperature (°C)					
	25	50	75	100	125	150
4	4.752	4.732	4.772	4.856	4.976	5.128
5	-1.761	-1.288	-0.894	-0.564	-0.283	-0.044
7	1.47	1.72	1.89	2	2.06	2.09
8	6.366	6.311	6.343	6.433	6.569	6.742
9	10.327	10.177	10.129	10.151	10.23	10.353
11	4.19	3.76	3.4	3.11	2.86	2.66
12	9.82	9.5	9.27	9.1	8.98	8.9
13	13.92	13.41	13.04	12.75	12.54	12.39
15	-15.49	-13.15	-11.04	-9.36	-7.38	-5.76
16	-2	-2	-2	-2	-2	-2

Table A-2. Negative natural log of coefficients for equations 4 through 16 at temperatures from 175 °C to 300 °C (Cohen, 1989).

Equation	Temperature (°C)					
	175	200	225	250	275	300
4[a]	5.311	5.525	5.77	6.047	6.355	6.694
5[a]	0.162	0.341	0.495	0.63	0.748	0.852
7[a]	2.1	2.06	2.02	1.96	1.89	1.81
8	6.948	7.188	7.467	7.763	8.098	8.465
9	10.518	10.72	10.959	11.233	11.543	11.887
11	2.48	2.34	2.21	2.11	2.02	1.95
12	8.85	8.85	8.89	8.96	9.07	9.22
13	12.31	12.27	12.27	12.32	12.42	12.56
15	-4.2	-2.7	-1.19	0.33	1.93	3.55
16	-2	-2	-2	-2	-2	-2

Table A-3. Negative natural log of coefficients for equations 17 through 32 at temperatures from 25 °C to 150 °C (Cohen, 1989).

Equation	Temperature (°C)					
	25	50	75	100	125	150
17	1.987	2.342	2.712	3.083	3.472	3.843
19	2.896	3.03	3.095	3.11	3.085	3.031
21	3.165	3.293	3.353	3.361	3.33	3.27
23	3.087	3.131	3.135	3.108	3.059	2.991
25	-3.87	-2.96	-	-1.63	-	-0.753
26	5.505	5.309	-	5.178	-	5.278
28	-5.153	-4.182	-	-2.692	-	-1.637
29	4.418	4.394	-	4.514	-	4.745
31	-5.47	-4.64	-3.93	-3.31	-2.76	-2.28
32	6.005	5.842	5.744	5.693	5.677	5.691

Table A-4. Negative natural log of coefficients for equations 17 through 32 at temperatures from 175 °C to 300 °C (Cohen, 1989).

Equation	Temperature (°C)					
	175	200	225	250	275	300
17	4.221	4.605	5.003	5.419	5.859	6.324
19	2.951	2.857	2.747	2.627	2.499	2.364
21	3.186	3.085	2.971	2.845	2.712	2.57
23	2.914	2.827	2.728	2.627	2.521	2.412
25	-	-0.173	-	0.208	-	0.449
26	-	5.549	-	5.965	-	6.512
28[a]	-1.141[b]	-0.86	-	-0.281	0.052[c]	0.163
29[a]	4.953[b]	5.083	-	5.539	5.871[c]	6.191
31	-1.84	-1.46	-1.1	-0.78	-0.49	-0.22
32	5.737	5.813	5.92	6.058	6.23	6.434

a- (Cobble and Turner, 1992)

b- Data at 180 °C not 175 °C

c- Data at 286 °C not 275 °C

Table A-5. Negative natural log of coefficients for equations 34 through 49 at temperatures from 25 °C to 150 °C (Cohen, 1989).

Equation	Temperature (°C)					
	25	50	75	100	125	150
34	9.31	-	-	7.4	-	6.53
35	20.57	-	-	16.4	-	14.5
36	29.4	-	-	24.6	-	22.4
38	8	-	-	6.34	-	5.59
39	17	-	-	13.6	-	12.1
40	27.8	-	-	23.3	-	21.3
42	-3.66	-3.03	-	-2.07	-	-1.38
43	3.73	3.79	3.86	3.94	4.04	4.15
45	-3.93	-3.22	-	-2.18	-	-1.47
46	4.76	4.79	4.86	4.95	5.06	5.18
48	-5.813	-4.932	-	-3.532	-	-2.477
49	3.83	3.848	-	3.983	-	4.192

Table A-6. Negative natural log of coefficients for equations 34 through 49 at temperatures from 175 °C to 300 °C (Cohen, 1989).

Equation	Temperature (°C)					
	175	200	225	250	275	300
34	-	5.86	-	5.35	-	4.92
35	-	13	-	11.8	-	10.9
36	-	20.7	-	19.3	-	18.2
38	-	5.02	-	4.57	-	4.22
39	-	10.9	-	10	-	9.2
40	-	19.7	-	18.4	-	17.4
42	-	0.87	-	-0.48	-	-0.18
43	4.28	4.43	4.6	4.79	5.02	5.26
45	-	-0.97	-	-0.62	-	-0.38
46	5.33	5.49	5.67	5.87	6.1	6.36
48	-	-1.66	-	-1.011	-	-0.487
49	-	4.475	-	4.847	-	5.325

Appendix B. Non-Equilibrium Chemical Reaction Data

The default chemical reactions coded in the SPPDP are the decomposition of morpholine, ethanolamine (ETA), and hydrazine and the reaction of hydrazine with oxygen. The default reaction rate information for the SPPDP is listed in this appendix. The reaction rate information provided in this thesis is based on Eq. 3-44 provided in the main text:

$$k_n^i = A_n \cdot \exp\left(\frac{-E_n}{R \cdot T}\right) \cdot \prod_{j=1}^{N_n} C_j^{a_j} \qquad \textbf{(Eq. B-1)}$$

The morpholine decomposition rate and products are based on information in the literature (Gilbert and Lamarre, 1989). In terms of the equation above:

A_n = 2.19*10^6 pbb/sec, and
E_n = 131.9 *10^6 J/mole, and
a_j = 1 for C_j corresponding to the concentration of morpholine in ppb.

The decompostion products of morpholine are assumed to split evenly between ETA, acetic acid, and glycolic acid. In terms of the equation above the decomposition of ETA is (Shenberger, 1992) determined by the following constants:

k_n = 5.87*10^-6 pbb/sec, and
a_j = 1 for C_j corresponding to the concentration of ETA in ppb.

The decompostion products of ETA are assumed to split evenly between ammonia, acetic acid, and glycolic acid. The decomposition of glycolic acid to formic acid is estimated with the following constants:

k_n = 1*10^-2 pbb/sec, and
a_j = 1 for C_j corresponding to the concentration of glycolic acid in ppb.

Hydrazine both decomposes and reacts with oxygen. The constants of the decomposition reaction,

$$H_4N_2 \Rightarrow 2NH_3 + H_2 + N_2 \qquad \textbf{(Eq. B-2),}$$

are (MacArthur, 1993):

A_n = 67.989 pbb/sec, and
E_n = 3.993 *10^4 J/mole, and
a_j = 1 for C_j corresponding to the concentration of hydrazine in ppb.

The constants for the reaction with oxygen,

$H_4N_2 + O2 \Rightarrow 2H_2O + N_2$ **(Eq. B-3),**
are (Dalgaard and Sanford, 1981):

A_n = 3.059 (pbb^-0.5)/sec, and
E_n = 2.547*10^4 J/mole, and
a_j = 1/2 for C_j corresponding to the concentration of hydrazine in ppb.
a_j = 1 for C_j corresponding to the concentration of oxygen in ppb.

Appendix C. Droplet Impingement Default Parameters

The default input parameters for the droplet impingement correlation are based on literature (Keck, 1987). The equation for droplet impingement, **Eq. 2-2**, is provided again in this appendix:

$$\dot{m}'' = \frac{K_{DI} \cdot \rho_f \cdot \dot{m}_{tot} \cdot (1-x) \cdot V_d^4 \cdot F_e \cdot F_h \cdot \rho_{ox}}{(IH \cdot \varepsilon_c)^2 \cdot A_c} \qquad \textbf{(Eq. C-1).}$$

The default data for these parameters defined in Chapter 2 and used in the SPPDP is as follows:

$K_{DI} = 1.5*10\text{^}{-7}$

V_d = SPPDP calculated vapor velocity [m/sec],

$F_e = 1$,

$F_h = 1$,

$IH = 650 \frac{N}{mm^2}$,

$\varepsilon_c = 0.03$, and

A_c = 1.5 * d^2, where d is the diameter of the pipe in meters.

Appendix D. New FAC Model Equations

The final new FAC model with the five changes detailed in Chapter 5 and incorporated into the Secondary Plant Pipe Degradation Modular Modeling Environment is the following:

For $C_{O_2} < C_{O_2 crit}$

$$\dot{m}''_{Fe,deaer} = 6.25 \cdot Geom \cdot \left\{B \cdot e^{N \cdot v} \cdot \left[1 - 0.128 \cdot (pH - 7)^2\right] \cdot 1.8 + 1\right\} f(t), \qquad \textbf{(Eq. D-1a)}$$

For $C_{O_2} > C_{O_2 crit}$

$$\dot{m}''_{Fe} = 6.25 \cdot Geom \cdot \left\{B \cdot e^{N \cdot v} \cdot \left[1 - 0.128 \cdot (pH - 7)^2\right] \cdot 1.8 \cdot e^{-0.118 \cdot C_{O_2}} + 1\right\} f(t) \qquad \textbf{(Eq. D-1b)}$$

where

$$C_{O_2 crit} = \frac{\dot{m}''_{Fe,deaer}}{h_{O_2} \cdot \rho_{H_2O}} \cdot \frac{MW_{\frac{1}{2}O_2}}{MW_{Fe}} \cdot Thrshld_{fctr} \cdot \frac{1}{Cnsrvtv_{Fctr}} \qquad \textbf{(Eq. D-2)}$$

$$h_{O_2} = \frac{D_{O_2}}{D_H} \cdot (2 + c \cdot \mathrm{Re}^a \cdot Sc^{1/3}) \qquad \textbf{(Eq. D-3a)}$$

$$Cnsrvtv_{Fctr} = \dot{m}''_{Fe,predict} / \dot{m}''_{Fe,measure} \qquad \textbf{(Eq. D-3b)}$$

with

$$c = 0.0165 + 0.011 \cdot Sc \cdot \exp(-Sc), \qquad \textbf{(Eq. D-4)}$$

$$a = 0.86 - \frac{10}{(4.7 + Sc)^3} \cdot Sc \cdot \exp(-Sc), \qquad \textbf{(Eq. D-5)}$$

$$\mathrm{Re} = \frac{v \cdot D_H}{\nu} \text{ (Reynolds number)}, \qquad \textbf{(Eq. D-6)}$$

$$Sc = \frac{\nu}{D_{O_2}} \text{ (Schmidt number)}. \qquad \textbf{(Eq. D-7)}$$

Defining terms as:

D_{O_2} = the oxygen diffusion coefficient in water (Woolsey, 1986) [m^2/sec],

D_H = the hydraulic diameter[m],

v = the fluid mean velocity [m/sec],

ν = the dynamic viscosity of water [m^2/sec]

$Thrshld_{Fctr}$ = the threshold correction factor found experimentally = 0.165 (Woolsey, 1986)

$Cnsrvtv_{Fctr}$ = the average conservatism predicted by the model = 2.88 (see Chapter 5)

The expression in equations D-1a and D-1b are given by:

$$B = -10.5 * \sqrt{aec} - 9.375 \cdot 10^{-4} \cdot T^2 + 0.79 \cdot T - 132.5, \qquad \textbf{(Eq. D-8)}$$

$$N = C - \frac{4}{v} \cdot aec - 1.275 \cdot 10^{-5} \cdot T^2 + 1.078 \cdot 10^{-2} \cdot T - 2.15 \quad \text{for } 0<\text{aec}\leq 0.25\%, \textbf{(Eq. D-9a)}$$

$$C = \frac{1}{v} - 0.0875 \cdot 0.25 \qquad \textbf{(Eq. D-9b)}$$

$$N = -0.0875 \cdot aec - 1.275 \cdot 10^{-5} \cdot T^2 + 1.078 \cdot 10^{-2} \cdot T - 2.15 \quad \text{for } 0.25\%<\text{aec}\leq 0.5\%, \textbf{(Eq. D-10)}$$

$$N = (-1.29 \cdot 10^{-4} \cdot T^2 + 0.109 \cdot T - 22.07) \cdot 0.154 \cdot e^{-12 \cdot aec} \quad \text{for } 0.5<\text{aec}\leq 5\%, \textbf{(Eq. D-11a)}$$

$$N = N(v = 15 m/\sec, T, aec) \quad if \quad \frac{\partial (Nv)}{\partial v} < 0 \qquad \textbf{(Eq. D-11b)}$$

$$f(ToO) = C_1 + C_2 \cdot ToO + C_3 \cdot ToO^2 + C_4 \cdot ToO^3 \qquad \textbf{(Eq. D-12)}$$

with

$C_1 = 0.9999934$

$C_2 = -0.3356901 \cdot 10^{-6}$

$C_3 = -0.5624812 \cdot 10^{-10}$,

$C_4 = 0.3849972 \cdot 10^{-15}$

where $\dot{m}''_{Fe}$ = material loss rate per unit area [μg/cm^2/hr],

k_c = geometrical factor,

pH = pH value (negative log of the hydrogen ion concentration),

C_{O_2} = bulk oxygen content [ppb],

aec = total content of chromium and molybdenum in steel [%],

ToO = time of operation [hours]

T = temperature [K] (Kastner and Riedle,1986).

The geometry factors used in the modified model are the same as those of the original model (Kastner and Riedle, 1986). Further, for a FAC rate calculated below 1 μg/cm^2/hr, set the FAC rate equal to 1 μg/cm^2/hr.

In piping containing two phase flow, the liquid velocity is a function of void fraction, α:

$$v_{film} = \frac{G}{\rho_l} \cdot \frac{1-x}{1-\alpha} \qquad \textbf{(Eq. D-13)}$$

where G = mass flux [kg/m^2/sec],

x = water flow quality,

ρ_l = water density [kg/m^3],

α = void fraction given by the Chexal-Lellouche void fraction correlation (Chexal *et. al.* 1991).

Note that for two phase flow, the bulk oxygen concentration in the liquid film is assumed to be zero due to the partitioning coefficient of oxygen and the pH is set to neutral or 7.

To account for material degradation downstream of a component such as a bend, pump, etc., the following increase in geometrical factor is used:

$$\Delta k_{c,A} = k_{c,A} \cdot e^{-C\frac{z}{D}} \qquad \textbf{(Eq. D-14)}$$

where z is the axial distance downstream of component, D is the pipe diameter, $k_{c,A}$ is the unaffected downstream geometry factor, and C is based on an estimation of axial distance along the pipe for which the component affects the flow. As a function of quality, the

ratio of axial distance to pipe diameter for which the component affects downstream FAC is given by:

$$\left(\frac{z}{D}\right)_{max} = 30 + 20 \cdot \cos(2 \cdot \pi \cdot (x - 0.5)). \qquad \textbf{(Eq. D-15)}$$

The maximum of this expression is at a quality value of 0.5. For multiple components within this maximum value, the potential for getting an unreasonably high geometry factor exists. Therefore, the geometry factor is limited to that found for stagnation point flow (Kastner *et. al.*, 1988).

Appendix E. Component Volumes

E-1. Estimating the volume of the tube and shells of the Feedwater Heaters (FWH) for Kori Unit 3.

The calculations in this Appendix are done for a vector of values which correspond to these six FWHs. Values are listed in the order in which condensate and feedwater flow throught the components. Values corresponding to FWH 1 are the listed in the first row and values for FWH 6 are listed in the last row.

The following estimates of condensate and feedwater residence time in FWHs 1-6 are made based on literature data (Jonas, 1988). This values of time correspond to the residence time of fluid on the tube side of the FWH.

$$HTr\_Time := \begin{pmatrix} 0.18 \\ 0.155 \\ 0.155 \\ 0.155 \\ .14 \\ .14 \end{pmatrix} \cdot min$$

For the purpose of this calculation two parameters are assumed for all feedwater heaters: the velocity in the tubes and the overall heat transfer coefficient. The velocity (vel) assumed is a nominal value, 7*ft/sec, which does not affect the final determination of volume of either the tube or shell sections but provides reasonable values for parameters computed in the process of determining these volumes. The overall heat transfer coefficient (U_{CS}) is a nominal value given in the literature (Stultz and Kitto, 1992).

Assuming:

$$vel := 7 \cdot \frac{ft}{sec}$$

$$U_{cs} := 250 \cdot \frac{BTU}{hr \cdot ft^2 \cdot F}$$

The number of FWHs is denoted with i 0 thru 5 corresponding to FWH1 thru FWH6.

$$i := 0..5$$

The following values are known for the tube and shell side of the FWHs from the SPPDP model of Kori Unit 3.

Pressure on the tube side is:

$$p_{tube} := \begin{pmatrix} 375 \\ 375 \\ 375 \\ 375 \\ 950 \\ 950 \end{pmatrix} \cdot psi$$

Temperature on the tube side is:

$$T_{tube} := \begin{pmatrix} 110 \\ 144 \\ 193 \\ 256 \\ 341 \\ 402 \end{pmatrix} \cdot F$$

Pressure on the shell side is:

$$p_{shell} := \begin{pmatrix} 2.22 \\ 5.71 \\ 20.1 \\ 62.2 \\ 171.6 \\ 400.4 \end{pmatrix} \cdot psi$$

Temperature on the shell side is:

$$T_{shell} := \begin{pmatrix} 129 \\ 167.5 \\ 228 \\ 295 \\ 369 \\ 444 \end{pmatrix} \cdot F$$

Mass flow rate on the tube side is:

$$mfr_{tubes\_tot} := \begin{pmatrix} 8.307 \\ 8.307 \\ 8.307 \\ 8.307 \\ 12.4 \\ 12.4 \end{pmatrix} \cdot 10^6 \cdot \frac{lb}{hr}$$

Mass flow rate on the shell side is:

$$mfr_{shell\_tot} := \begin{pmatrix} 1.818 \\ 1.44 \\ 1.037 \\ .562 \\ .786 \\ 1.73 \end{pmatrix} \cdot 10^6 \cdot \frac{lb}{hr}$$

Number of parrallel components represented by each FWH is:

$$Prll := \begin{pmatrix} 3 \\ 3 \\ 3 \\ 3 \\ 2 \\ 2 \end{pmatrix}$$

Product of the FWH overall heat transfer coefficient and area for the condensing section is:

$$UA_{cs\_tot} := \begin{pmatrix} 4.93 \\ 5.487 \\ 6.747 \\ 7.15 \\ 9.79 \\ 11.4 \end{pmatrix} \cdot 10^7 \cdot \frac{BTU}{hr \cdot F}$$

Mass flow rate in the tubes for each parallel FWH is:

$$mfr_{tubes_i} := \frac{mfr_{tubes\_tot_i}}{Prll_i}$$

Mass flow rate in the shell for each parallel FWH is:

$$mfr_{shell_i} := \frac{mfr_{shell\_tot_i}}{Prll_i}$$

Density of the water in the shell based on tabulated properties of the specific volume of the liquid (stm_vcl) is:

$$\rho_{shell_i} := \frac{1}{stm\_vcl\left(\frac{P_{shell_i}}{psi}, \frac{T_{shell_i}}{F}\right) \cdot \frac{ft^3}{lb}}$$

Density of the water in the tube based on tabulated properties of the specific volume of the liquid (stm_vcl) is:

$$\rho_{tube_i} := \frac{1}{stm\_vcl\left(\frac{P_{tube_i}}{psi}, \frac{T_{tube_i}}{F}\right) \cdot \frac{ft^3}{lb}}$$

Product of the FWH overall heat transfer coefficient and area for the condensing section for each parallel FWH is:

$$UA_{cs_i} := \frac{UA_{cs\_tot_i}}{Prll_i}$$

Condensing section surface area is:

$$A_{surface\_cs} := \frac{UA_{cs}}{U_{cs}}$$

$$A_{surface\_cs} = \begin{pmatrix} 6.107 \times 10^3 \\ 6.797 \times 10^3 \\ 8.358 \times 10^3 \\ 8.857 \times 10^3 \\ 1.819 \times 10^4 \\ 2.118 \times 10^4 \end{pmatrix} m^2$$

Cross sectional area of the tubes for two passes in the condenser shell is:

$$A_{xs\_tubes_i} := \frac{mfr_{tubes_i}}{\rho_{tube_i} \cdot vel} \cdot 2$$

$$A_{xs\_tubes} = \begin{pmatrix} 0.33 \\ 0.333 \\ 0.338 \\ 0.348 \\ 0.814 \\ 0.85 \end{pmatrix} m^2$$

Assuming a pitch-diameter (P/D) ratio = 1.5, the cross sectional area of the bundle of tubes in the shell is:

$$A_{bundle} := \frac{A_{xs\_tubes}}{0.4}$$

$$A_{bundle} = \begin{pmatrix} 0.824 \\ 0.832 \\ 0.846 \\ 0.869 \\ 2.036 \\ 2.124 \end{pmatrix} m^2$$

The bundle diameter which corresponds to this bundle cross section is:

$$D_{bundle} := \left(\frac{A_{bundle} \cdot 4}{\pi} \right)^{0.5},$$

$$D_{bundle} = \begin{pmatrix} 1.024 \\ 1.029 \\ 1.038 \\ 1.052 \\ 1.61 \\ 1.644 \end{pmatrix} \text{m},$$

Using the schematic in **Figure E-1**. The factor by which the shell diameter is greater than the bundle diameter is (Figure E-1):

$$F_{spacing\_D} := \frac{0.20 + 0.57}{0.57}$$

$$F_{spacing\_D} = 1.351$$

The shell diameter is then:

$$D_{shell} := D_{bundle} \cdot F_{spacing\_D}$$

The shell radius is then:

$$R_{shell} := \frac{D_{shell}}{2}$$

$$R_{shell} = \begin{pmatrix} 0.692 \\ 0.695 \\ 0.701 \\ 0.711 \\ 1.087 \\ 1.111 \end{pmatrix} \text{m},$$

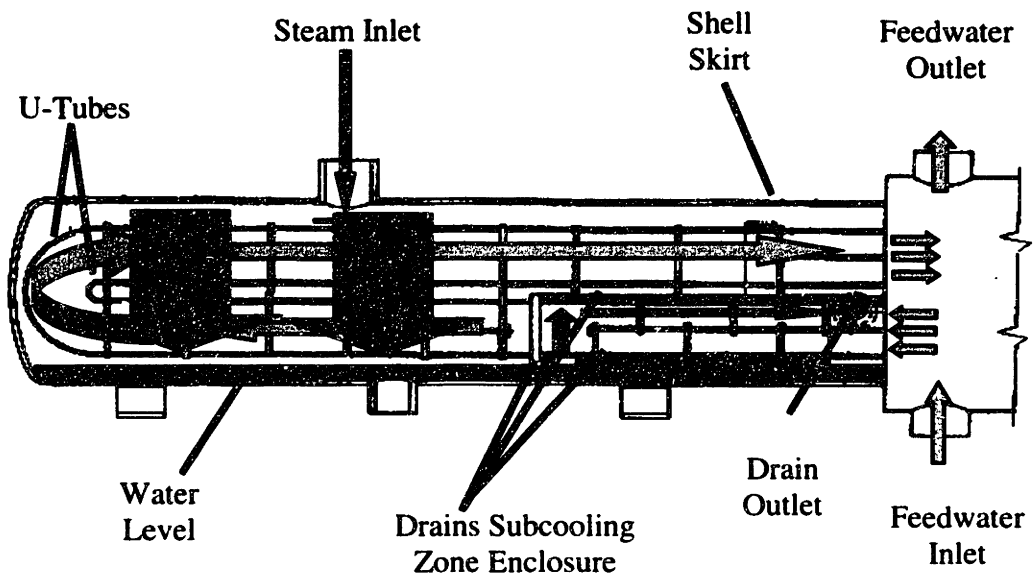

Figure E-1. Schematic of Feedwater Heater Used to Estimate Feedwater Shell and Tube Side Volumes (HEI, 1979).

The height of the water shown in the schematic as a fraction of the shell radius is given by (Figure E-1):

$$F_{spacing\_H} := \frac{0.11}{0.57}$$

$$F_{spacing\_H} = 0.193$$

The height of the water is then:

$$H_{water} := R_{shell} \cdot F_{spacing\_H}$$

$$H_{water} = \begin{pmatrix} 0.134 \\ 0.134 \\ 0.135 \\ 0.137 \\ 0.21 \\ 0.214 \end{pmatrix} m$$

The total length of the tubes is:

$$L_t := vel \cdot HTr\_Time$$

The fraction of the length of tubes for one pass over the width of the shell is (Figure E-1):

$$F_{spacing\_L} := \frac{5.35}{6.05}$$

$$F_{spacing\_L} = 0.884$$

The length of the shell is then:

$$L_{shell} := \frac{L_t}{2} \cdot F_{spacing\_L}$$

$$L_{shell} = \begin{pmatrix} 10.188 \\ 8.773 \\ 8.773 \\ 8.773 \\ 7.924 \\ 7.924 \end{pmatrix} m$$

Next the area fraction of the water in the cross section of the shell is computed based on the height of the water. First computing the angle between the vertical and the radius which intersect the shell at the height of the water is:

$$\theta_i := acos\left(\frac{R_{shell_i} - H_{water_i}}{R_{shell_i}}\right)$$

This area of the pie section for the two radii which intersect the shell at the height of the water is:

$$A_{piesection_i} := \pi \cdot \left(R_{shell_i}\right)^2 \cdot \frac{\theta_i}{2 \cdot \pi} \cdot 2$$

The area within this pie section that is taken up by steam not water is:

$$A_{2triangles_i} := \left(R_{shell_i} - H_{water_i}\right) \cdot \left[2 \cdot R_{shell_i} \cdot H_{water_i} - \left(H_{water_i}\right)^2\right]^{0.5}$$

The remaining area corresponds to the water area for the shell:

$$A_{water_i} := A_{piesection_i} - A_{2triangles_i}$$

$$A_{water} = \begin{pmatrix} 0.074 \\ 0.075 \\ 0.076 \\ 0.078 \\ 0.183 \\ 0.191 \end{pmatrix} m^2$$

The volume of the water in the shell is then the area of the water times the length of the shell:

$$Vol_{shell_i} := L_{shell_i} \cdot A_{water_i}$$

$$Vol_{shell} = \begin{pmatrix} 0.757 \\ 0.658 \\ 0.669 \\ 0.687 \\ 1.454 \\ 1.517 \end{pmatrix} m^3$$

Next, the volume of the drains cooling section is determined based on Figure E-1 and dimensions thus far determined. The cross sectional area of the drains cooling section covers a fraction of the length of one pass of the tube bundle. The cross sectional area of the drains cooling section is:

$$A_{xs\_dc} := \frac{A_{bundle}}{2}$$

The drains cooling section is a fraction of the length of the shell as is given by (Figure E-1):

$$F_{length\_dc} := \frac{2.4}{6.05}$$

$$F_{length\_dc} = 0.397$$

The length of the drains cooling section is then:

$$L_{dc} := L_{shell} \cdot F_{length\_dc}$$

$$L_{dc} = \begin{pmatrix} 4.042 \\ 3.48 \\ 3.48 \\ 3.48 \\ 3.144 \\ 3.144 \end{pmatrix} m$$

The volume of the drains cooling section is:

$$Vol_{shell\_dc_i} := A_{xs\_dc_i} \cdot L_{dc_i}$$

$$Vol_{shell\_dc} = \begin{pmatrix} 1.665 \\ 1.447 \\ 1.472 \\ 1.513 \\ 3.2 \\ 3.338 \end{pmatrix} m^3$$

Next, the volume of the tube section is determined based on Figure E-1 and dimensions thus far determined. The volume of the tubes is the product of the tube length and cross sectional area of a single pass of the tubes.

$$Vol_{tubes_i} := \frac{A_{xs\_tubes_i}}{2} \cdot L_{t_i}$$

$$Vol_{tubes} = \begin{pmatrix} 3.798 \\ 3.3 \\ 3.357 \\ 3.45 \\ 7.297 \\ 7.613 \end{pmatrix} m^3$$

E-2. Estimating the volume of the shells of the Moisture Separator Reheaters (MSR) for Kori Unit 3.

Based on Figure E-2 (Cohen, 1989), the radius in the schematic in inches is:

$$R_{Sch\_RH} := \frac{0.97 \cdot in}{2}$$

The highest level of the water in the MSR is at the edges as shown in the figure. In inches this level is:

$$L_{sch\_RH} := 0.73 \cdot in - R_{Sch\_RH}$$

$$L_{sch\_RH} = 0.245in$$

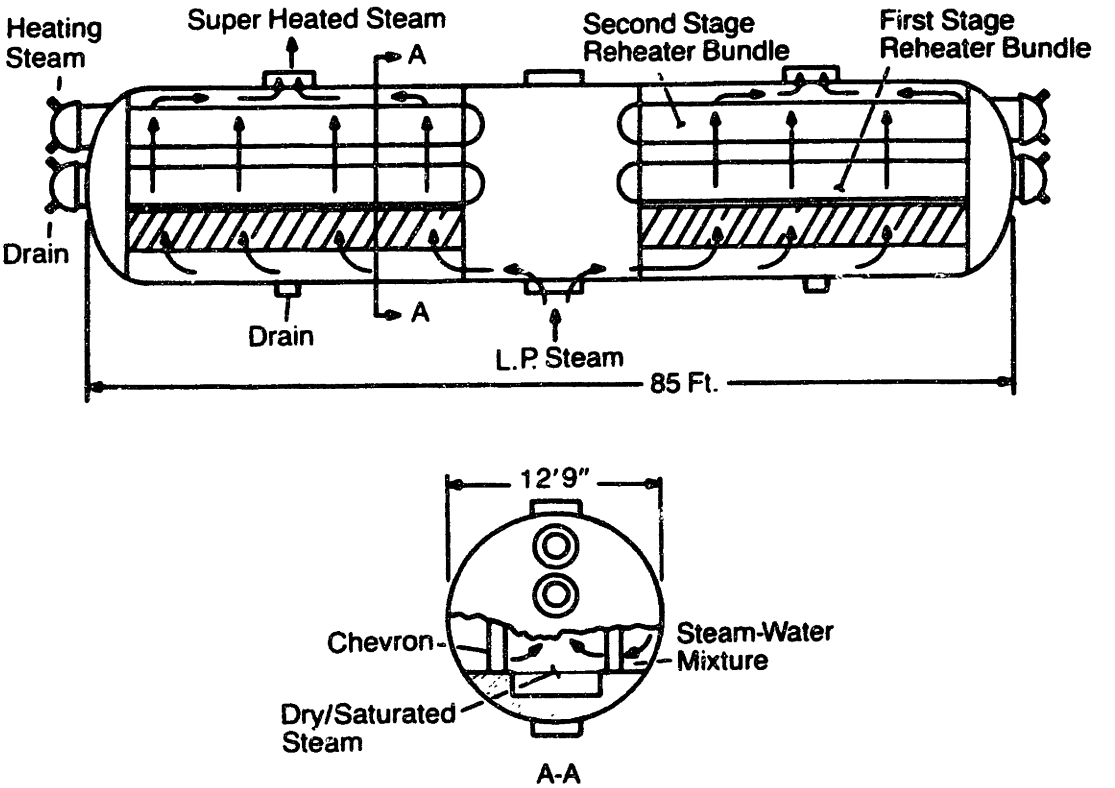

Figure E-2. Schematic of the MSR used to estimate the volume of the water in the shell of the MSR.

Using the Pythagorean theorem the half span of the water at the highest point is given by:

$$W_{sch\_RH} := \left(R_{Sch\_RH}^{2} - L_{sch\_RH}^{2}\right)^{0.5}$$

$$W_{sch\_RH} = 0.419\text{in}$$

The angle between the vertical and a radius which intersects the MSR shell at the upper water level is:

$$\theta := \operatorname{acos}\left(\frac{L_{sch\_RH}}{R_{Sch\_RH}}\right)$$

The area between two radii which intersect the shell at the level of the water is given by:

$$A_{piesection} := \pi \cdot R_{Sch\_RH}^{2} \cdot \frac{\theta}{2 \cdot \pi} \cdot 2$$

The area in between these radii in which water does not exist is the sum of that from the fraction above the maximum water level,

$$A_{2triangles} := \left(L_{sch\_RH}\right) \cdot \left(W_{sch\_RH}\right)$$

and the amount in the rectangular (box) area in the middle of the MSR (see Figure A-2).

$$A_{box} := 0.12\text{in} \cdot 0.4 \cdot \text{in}$$

The area of the water is then given by the total pie section area less these two areas:

$$A_{water} := A_{piesection} - A_{2triangles} - A_{box}$$

$$A_{water} = 0.094\text{in}^2$$

According to the figure the real MSR radius is:

$$\left(R_{real\_RH}\right) := \frac{12.75}{2} \cdot \text{ft}$$

The corresponding real cross sectional area is then:

$$A_{real\_RH} := \pi \cdot R_{real\_RH}^{2}$$

The real area of the water is then the same fraction of the real area of the reheater as the was found in square inches from the schematic.

$$A_{real\_water} := \frac{A_{water}}{\left(\pi \cdot R_{Sch\_RH}^{2}\right)} \cdot \left(A_{real\_RH}\right)$$

$A_{real\_water} = 1.515 m^2$

The total length of the reheater in the schematic in inches is:

$L_{sch\_RH} := 4.2 \cdot in$

The length occupied by water is that length below the heating stage tube bundles. In inches that is:

$L_{sch\_water} := 3.0 \cdot in$

From Figure E-2, the real MSR length is:

$L_{real\_RH} := 85 ft$

The real water length is then the same fraction in feet as would be found in inches from the schematic:

$$L_{real\_water} := \frac{L_{sch\_water}}{L_{sch\_RH}} \cdot L_{real\_RH}$$

$L_{real\_water} = 18.506 m$

The volume of the water in the MSR is then given by:

$Vol_{real\_water} := A_{real\_water} \cdot L_{real\_water}$

$Vol_{real\_water} = 28.033 m^3$

E-3. Estimating the volume of the water in the shell of the Steam Generator (SG) for Kori Unit 3.

The approximate volume of water in a Model F type Westinghouse Steam Generator is 50,000 kg (EPRI, 1985). The temperature of the water is taken as the average of the inlet temperature and the outlet temperature of the SG.

$Tin := 440F$

$Tout := 534 \cdot F$

$Tavg := \frac{Tin + Tout}{2}$

$Tavg = 487F$

The pressure is assumed to 1000 psi and the mass is multiplied by the specific volume of the liquid (stm_vcl) resulting in the volume of water:

$Vol_{SG} := 50000 \cdot kg \cdot stm\_vcl(1000, 487) \cdot \frac{ft^3}{lb}$

$Vol_{SG} = 62.634m^3$

In the SPPDP this volume is rounded to 60*m^3.

Appendix F. Raw Data Calculated for Kori Unit 3

The following parameters are those calculated based on the input of plant description of Kori Unit 3. They are the raw data input into the new FAC model and the result of the new FAC model is shown in the second column. In addition to these parameters, two others were input for the model, the alloying element content (=0.03%) and the time of operation (=1.11*10^5 hours).

Table F-1. Raw data for the Kori Unit 3 secondary plant calculated by the Secondary Plant Pipe Degradation Program and used as input to determine the Flow Accelerated Corrosion (FAC) rate.

Data Point #	FAC Wear[µg/cm ^2/hr]	Measured Wear [µg/cm^2 /hr]	Temper-ature [°C]	Liquid Velo-city [m/sec]	Geom-etry	Cold pH	Oxygen Conc [ppb]	Quality
1	16.702	15.462	106.105	2.820	0.160	9.388	6.474	0.000
2	31.315	13.955	106.105	2.820	0.300	9.388	6.474	0.000
3	21.454	21.234	143.185	2.912	0.160	9.388	5.354	0.000
4	40.225	22.022	143.185	2.912	0.300	9.388	5.354	0.000
5	24.586	9.690	158.098	1.965	0.150	9.362	3.194	0.000
6	26.223	5.842	158.098	1.965	0.160	9.362	3.194	0.000
7	70.993	17.664	158.098	1.965	0.300	9.362	3.194	0.000
8	32.673	13.885	158.950	3.920	0.160	9.362	3.020	0.000
9	60.309	24.386	158.950	3.768	0.300	9.362	3.020	0.000
10	224.43	20.167	158.950	4.239	0.750	9.362	3.020	0.000
11	33.764	41.169	158.950	4.239	0.160	9.362	3.020	0.000
12	63.308	45.365	158.950	4.239	0.300	9.362	3.020	0.000
13	33.764	20.631	158.950	4.239	0.160	9.362	3.020	0.000
14	33.552	26.589	184.492	4.363	0.160	9.362	2.345	0.000
15	62.905	63.099	184.492	4.363	0.300	9.362	2.345	0.000
16	25.736	8.044	226.457	4.623	0.160	9.362	1.160	0.000
17	48.227	66.298	226.457	4.623	0.300	9.363	1.160	0.000
18	36.048	57.489	226.457	3.790	0.230	9.363	1.160	0.000
19	33.659	45.898	279.001	30.308	0.230	9.365	5.862e-3	0.996
20	44.022	13.375	278.820	0.578	0.300	9.345	0.039	2.710e-4
21	92.213	13.074	229.410	2.799	0.160	9.350	3.017e-4	0.134
22	197.15	17.108	229.410	7.989	0.300	9.350	3.017e-4	0.134
23	32.345	14.650	189.723	1.248	0.160	9.368	0.272	0.000
24	60.637	19.287	189.723	1.248	0.300	9.368	0.272	0.000
25	24.691	22.903	230.980	0.435	0.150	9.339	0.014	0.000
26	92.064	25.035	221.862	0.695	0.160	9.343	4.074e-4	0.023
27	167.96	12.981	221.862	3.602	0.260	9.343	4.074e-4	0.023

28	87.884	12.263	230.981	1.452	0.160	7.000	0.000	0.919
29	123.00	20.608	194.771	2.622	0.160	7.000	0.000	0.932
30	110.09	13.816	192.412	2.732	0.140	7.000	0.000	0.933
31	50.306	16.922	187.301	0.278	0.300	9.418	0.178	0.000
32	53.747	8.044	188.493	0.258	0.160	8.947	3.501e-5	0.000
33	99.828	22.532	188.493	0.258	0.300	8.957	3.501e-5	0.000
34	106.97	11.335	188.493	1.173	0.300	8.967	1.435e-6	0.000
35	55.436	5.772	188.493	0.861	0.160	8.969	1.435e-6	0.000
36	40.850	9.898	186.432	2.290	0.160	9.300	7.274e-3	0.000
37	43.245	33.381	186.977	2.974	0.160	9.300	6.397e-3	0.000
38	40.536	20.840	186.977	2.974	0.150	9.300	6.397e-3	0.000
39	89.073	47.289	186.977	4.052	0.300	9.300	6.397e-3	0.000
40	43.238	19.588	186.977	2.974	0.160	9.300	6.397e-3	0.000
41	186.46	47.985	186.977	4.573	0.600	9.300	6.397e-3	0.000
42	93.229	17.803	186.977	4.573	0.300	9.300	6.397e-3	0.000
43	61.423	17.108	117.389	1.365	0.300	9.382	6.461e-3	0.000
44	171.75	22.694	111.706	5.895	0.160	9.382	1.315e-5	0.011
45	19.264	11.451	38.355	0.383	0.300	9.340	3.520e-4	0.000

Appendix G. Off Normal Chemistry Data

This appendix provides the contour plots of wear for all wear locations affected by both pH and oxygen concentration. The wear locations correspond to the first 18 listed in Appendix F.

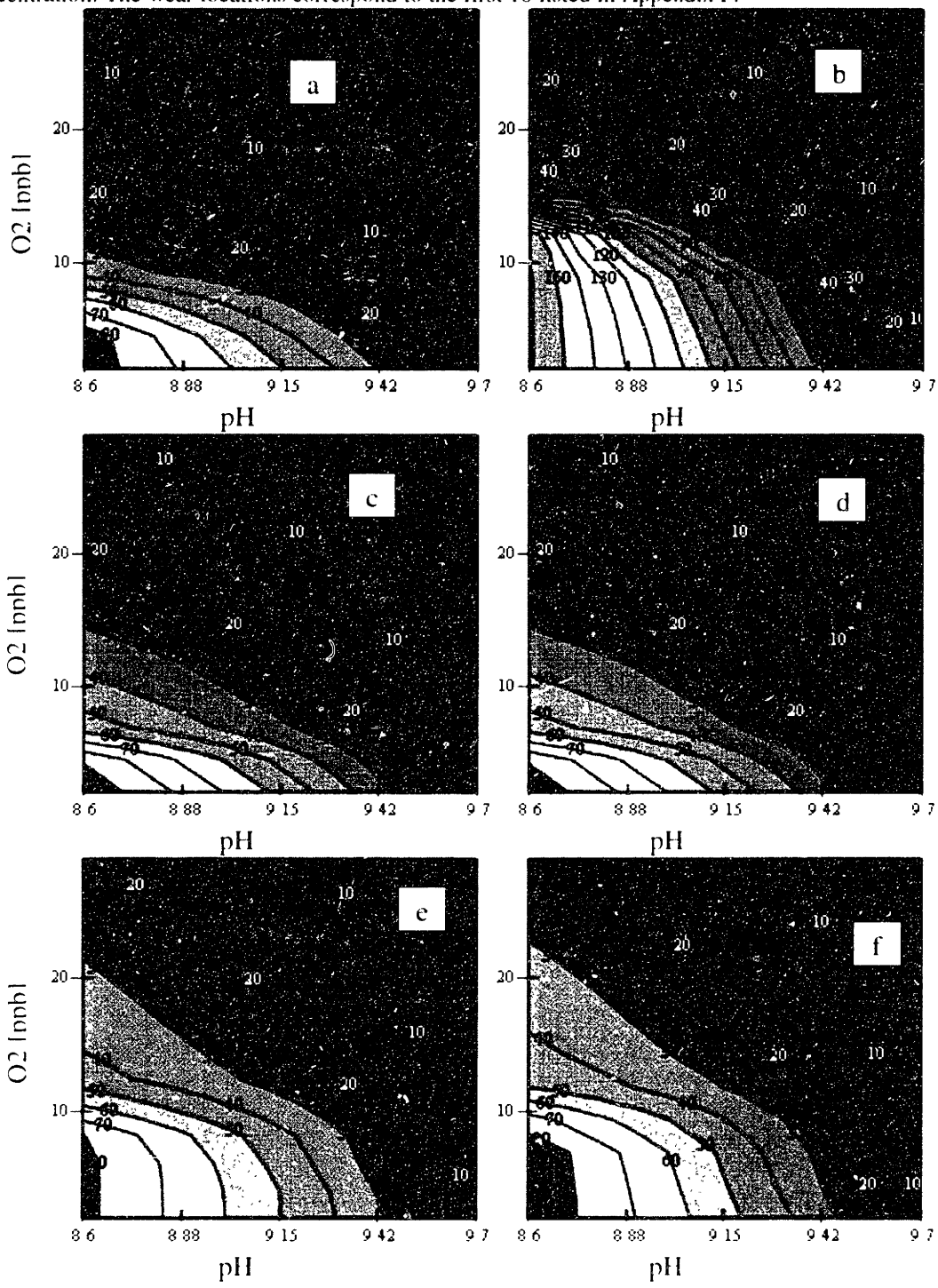

Figure G-1. Wear rate contours for off normal chemistry for wear locations 1 through 6: a) 1, b) 2, c) 3, d) 4, e) 5, f) 6 [microgm/cm^2/hr].

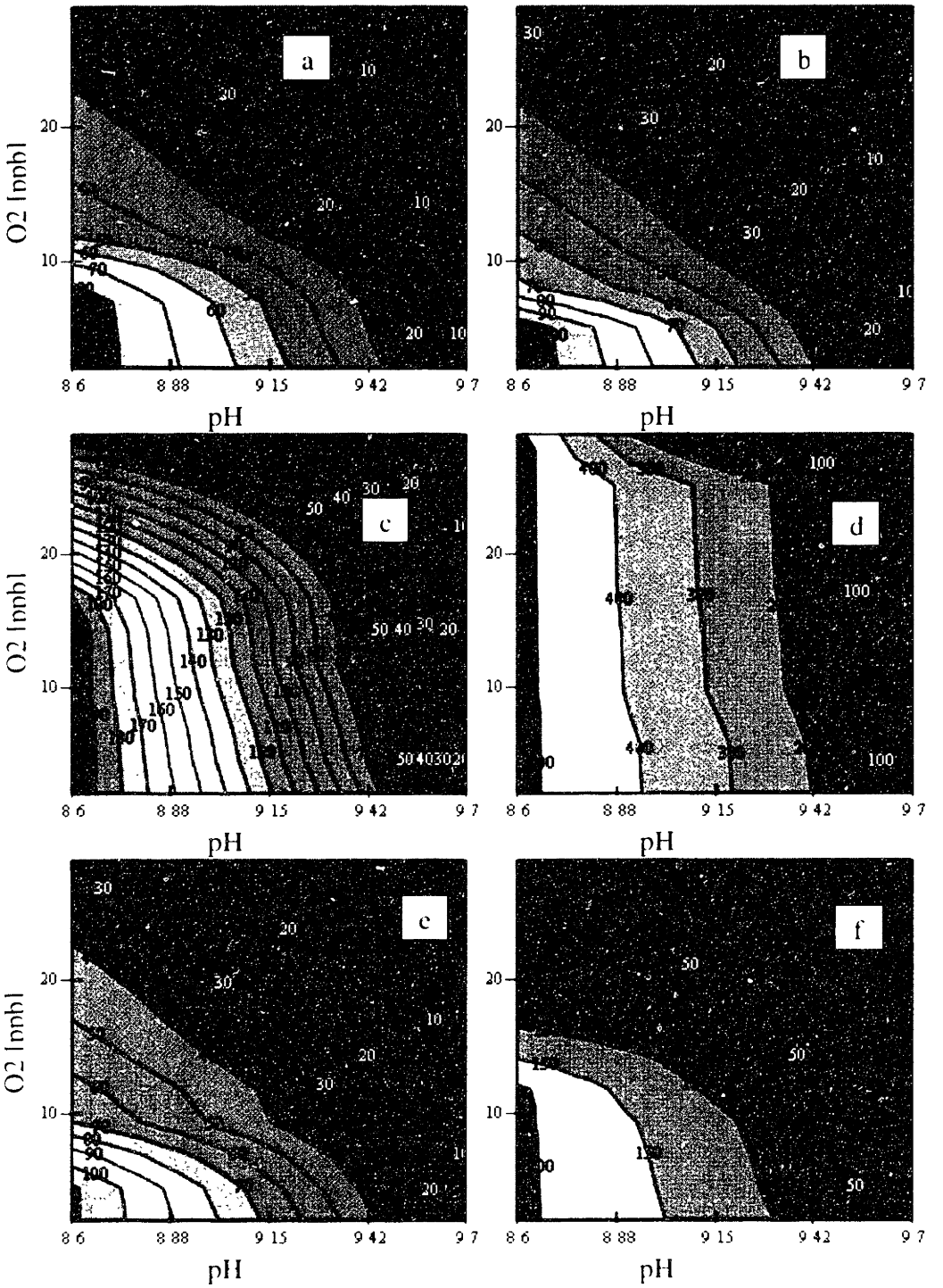

Figure G-2. Wear rate contours for off normal chemistry for wear locations 7 through 12: a) 7, b) 8, c) 9, d) 10, e) 11, f) 12 [microgm/cm^2/hr].

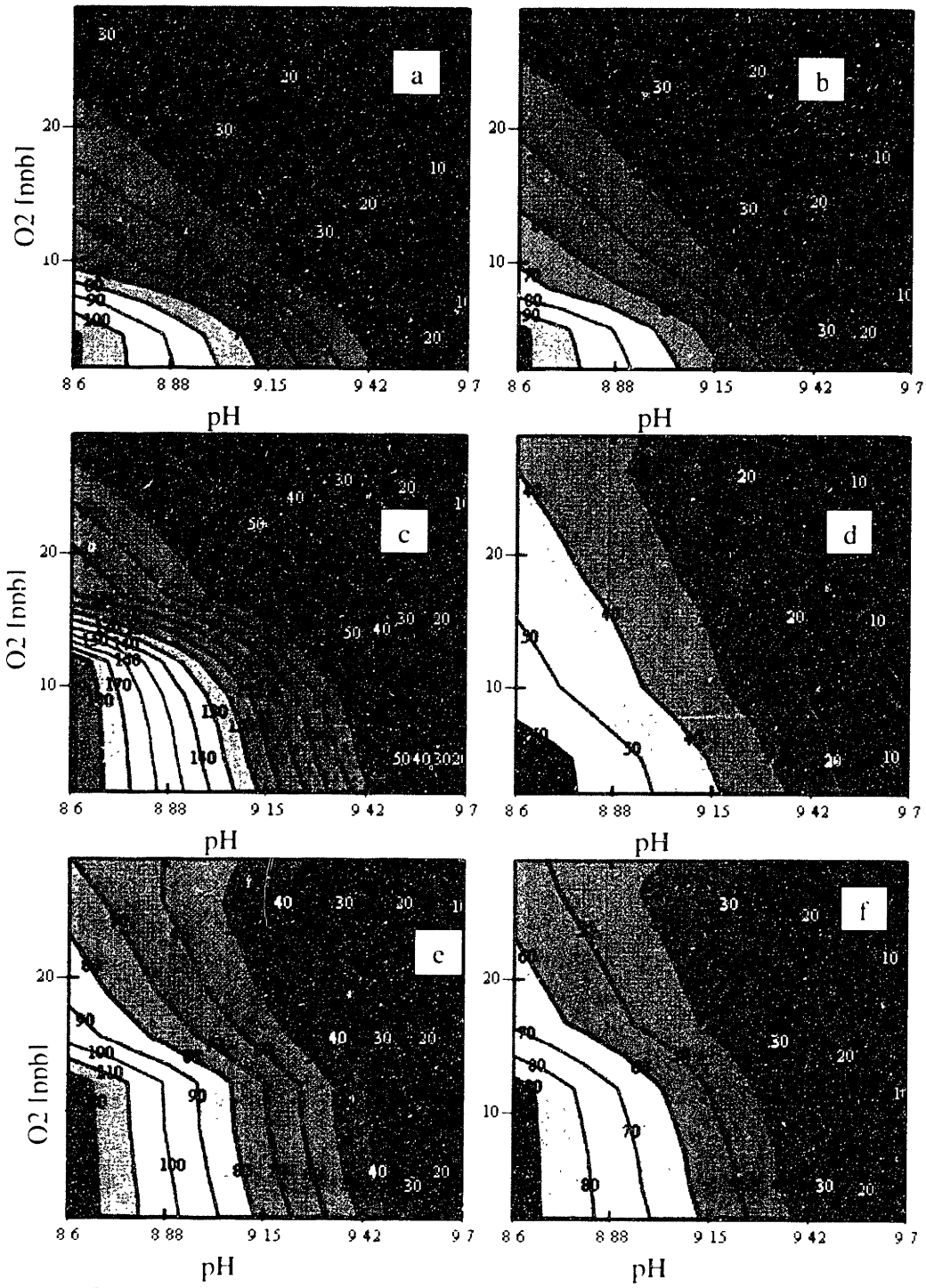

Figure G-3. Wear rate contours for off normal chemistry for wear locations 13 through 18: a) 13, b) 14, c) 15, d) 16, e) 17, f) 18 [microgm/cm^2/hr].

THESIS PROCESSING SLIP

FIXED FIELD: ill. _____ name _____

index _____ biblio _____

▶ **COPIES:** (Archives) Aero Dewey Barker Hum

Lindgren Music Rotch (Science) Sche-Plough

TITLE VARIES: ▶ ☐ _____

_____

_____

NAME VARIES: ▶ ☐ _____

_____

IMPRINT: **(COPYRIGHT)** _____

_____

▶ **COLLATION:** _____

_____

▶ **ADD: DEGREE:** _____ ▶ **DEPT.:** _____

▶ **ADD: DEGREE:** _____ ▶ **DEPT.:** _____

SUPERVISORS: _____

_____

NOTES:

_____ cat'r: _____ date:

page: F55

▶ **DEPT:** Nuc. Eng

▶ **YEAR:** 2001 ▶ **DEGREE:** Ph. D.

▶ **NAME:** VAN DER HILLM, Mark Jochum

_____